Strål säkerhets myndigheten

Swedish Radiation Safety Authority

2017:28

SSM's external experts' review of SKB's safety assessment SR-PSU - hydrogeology, geochemistry and bentonite

Main review phase

SSM perspective

Background

The Swedish Radiation Safety Authority (SSM) received an application for the expansion of SKB's final repository for low and intermediate level waste at Forsmark (SFR) on the 19 December 2014. SSM is tasked with the review of the application and will issue a statement to the government who will decide on the matter. An important part of the application is SKB's assessment of the long-term safety of the repository, which is documented in the safety analysis named SR-PSU.

Present report compiles results from SSM's external experts' reviews of SR-PSU during the main review phase. The general objective of these reviews has been to give support to SSM's assessment of the license application. More specifically, the instructions to the external experts have been to make an in depth assessment of the specific issues defined for the different disciplines.

Project information

Contact person SSM: Georg Lindgren

Contact persons and registration numbers for the different expert review contributions are given in the report.

Table of Contents

Strål säkerhets myndigheten

Swedish Radiation Safety Authority

2017:28

SSM's external experts' review of SKB's safety assessment SR-PSU - hydrogeology, geochemistry and bentonite

Main review phase

This report concerns a study which has been conducted for the Swedish Radiation Safety Authority, SSM. The conclusions and view-points presented in the report are those of the author/authors and do not necessarily coincide with those of the SSM.

Author: Joel Geier[1]
     [1]Clearwater Hardrock Consulting, Corvallis, Oregon, U.S.A.

Review of hydrogeological aspects of the safety assessment SR-PSU – Main review phase

Abstract

The Swedish Nuclear Fuel and Waste Management Co. (SKB) has presented the safety assessment SR-PSU in support of a proposed extension of the SFR facility for low- and intermediate-level radioactive waste, located near Forsmark, Sweden. This report presents findings of review of hydrogeological aspects of this safety assessment..

An inventory of key uncertainties in the discrete-fracture network (DFN) and shallow-bedrock aquifer (SBA) identifies the following as high priority for scoping calculations: (1) vertical hydraulic connection to the sea; (2) hydrogeological properties and extent of the SBA; (3) hydrogeological properties and lateral extension of probabilistic deformation zones; and (4) uncertainty in transmissivity values at deformation zone intercepts.

The three bedrock cases that were used as the basis for flow and transport modelling do not necessarily bound the uncertainties in bedrock properties that affect the dose and risk calculations for either the main scenario or for the high flow in the bedrock scenario. Scoping calculations are needed to establish more conservative bounds.

The upscaling from the DFN model to an ECPM representation using DarcyTools is based on a geometrical upscaling algorithm. Comparison with independent calculations indicates that the results obtained are consistent with the stated methodology. The results are likely conservative in terms of overall flows, but may underestimate the potential for focused flows to particular vaults.

The methodology for transferring boundary conditions as prescribed pressures between the different modeling scales is appropriate. However the regional-scale model has inconsistencies with the repository-scale and vault-scale models in terms of: (1) effective hydraulic conductivities of the backfilled rock vaults, and (2) local hydraulic conductivity of the bedrock. These inconsistencies imply additional uncertainty that should be accounted for in radionuclide transport calculations.

Calculated flows for present-day conditions are significantly higher in the model for SAR 08 than for SR-PSU, although better agreement is obtained for later times. The large discrepancies for present-day circumstances can be explained by the possibility that the older model's dynamic behavior was calibrated to indications of excess heads which are of doubtful reliability. However this also implies that resaturation times based on the older model have been underestimated.

Contents

1. Introduction

Since 1987 the Swedish Nuclear Fuel and Waste Management Co. (SKB) has operated an underground repository for low- and intermediate-level radioactive waste, the SFR, at a location near Forsmark, Sweden. In support of a proposed extension of this facility, SKB has presented a site descriptive model SDM-PSU which encompasses the bedrock volume hosting the existing SFR as well as the proposed extension (Figure 1.1) and a safety assessment, SR-PSU. This document presents findings from a review of hydrogeological aspects of SR-PSU, focusing on specific issues that were identified in an initial stage of review.

2. Review topics

2.1. Unevaluated uncertainties in hydrogeological models

The aim of this review topic is to assess the hydrogeological discrete fracture-network (DFN) and shallow bedrock-aquifer (SBA) models, focusing on the potential significance for the safety case of unevaluated uncertainties including stochastic variation.

The approach taken is to tabulate uncertainties in the DFN and SBA models, and their likely impacts based on how the models are used in the safety assessment, then to rank the uncertainties qualitatively, and comment on those that should be addressed by alternative conceptual models.

2.1.1. Vertical hydraulic connection to the sea

The role of seabed sediments in controlling the vertical hydraulic connection to the sea is mentioned by Öhman et al. (2012, p. 115): "*Reported excess head values prior to tunnel constructions are highly uncertain ..., but may also indicate a slow hydrogeological system, poorly vertically connected to the sea.*"

How addressed in SR-PSU

Alternative parameterizations for seabed sediments are not addressed in P-14-04.

Comments

This is a major conceptual and parametric uncertainty as it affects the inflows that have been used to evaluate the hydrogeological models, and their transient behaviour. Inflow data have not been used for a systematic calibration procedure, due to recognized limitations regarding baseline conditions prior to earlier stages of construction, as well as the role of "skin" effects around the tunnels, as explained by Öhman et al. (2013, p. 16). However inflow data have been used for comparative assessment of model variants that include different parameterizations of the hydraulic conductor domains, shallow-bedrock aquifer and near-tunnel skin, in what Öhman et al. (2013, p. 51-64) refer to as a "perturbation analysis."

Figure 1.1: Map of the Forsmark-SFR area showing the location of the existing SFR and the area that was prioritized for an extension of this facility. From Figure 1-1 of SKB-R-11-10.

The role of seabed sediments in regulating the inflows used in this evaluation is an important part of site understanding that has not been convincingly addressed. SSM has asked for complementary information regarding the connection to the sea (SSM2015-725-40 Point 4).

2.1.2. Extension of ZFM871

The uncertain extension of ZFM871 is mentioned by Öhman et al. (2012, p. 115-116):

 "*It is recommended that alternative extensions of ZFM871 are explored in the Safety Assessment. In the geologic model SFR v. 1.0, ZFM871 is terminated against three steeply dipping deformation zones: ... Hydrochemical classification of water types ... suggests extension beyond ZFMNNE0869 (KFR10) as well as ZFMNW0805B (KFR7A). The transient drawdown development in KFR7A ... and the high transmissivity in the possible deformation zone KFR10_DZ2 ... reinforce this suspicion. ... Two gently dipping structures are modelled at depth by Curtis et al. (2011) ...; these are not covered by borehole data and probably have minor significance for the SFR extension, owing to their deep location. ... The deterministic ZFM structures do not comprise a uniform population and cannot be compared against the HRD, as such. With exceptions of ZFM871, ZFMNNE0869, ZFMNNW1034, the Southern and Northern boundary belts, the general impression is that in the upper c. 200 m, deterministic structures do not differ significantly from*

the rock mass outside zones. This notion should be considered in context to the geologic modelling uncertainties in continuity and extent of zones inside the Central block ... and underlines the necessity of alternative conceptual interpretations."

How addressed in SR-PSU

An alternative model of the extension of ZFM871 was considered as part of a sensitivity study (SKBdoc 1395214). The impact of the uncertainty in ZFM871 extension was tested by including a variant with extended geometry as modelled by Holmén and Stigsson (2001a) and by Odén (2009). In the extended ZFM871 case, the northwest edge is assumed to outcrop below seafloor sediments.

According to SKBdoc135214 the extended geometry of ZFM871 produced only small increases in flow relative to the base case, has little effect on the base case. The average flow (over all of the vaults) increases by about 15% in SFR1 and by about 4% in the proposed extension. However inspection of Figure 5-14 of SKBdoc 1395214 indicates that stronger effects are seen for 1BLA in which the flows are increased by about 30%.

Comments

For most vaults the effects of an alternative interpretation of ZFM871 are minor. The strongest effect is for 1BLA for which an increase of about 30% in flow is seen.

2.1.3. Uncharacterized gently dipping structures

The potential existence of uncharacterized gently dipping structures is mentioned by Öhman et al. (2012, p. 115): "*Two gently dipping structures are modelled at depth by Curtis et al. (2011) ...; these are not covered by borehole data and probably have minor significance for the SFR extension, owing to their deep location.*"

How addressed in SR-PSU

This uncertainty is not addressed in the documents considered in this review.

Comments

This may not be significant for release paths, as argued by SKB. However for ongoing review it should be considered whether these structures could be important for geochemical stability (e.g. saline upconing).

2.1.4. Alternative conceptual models for ZFM structures

This topic concerns the possibility that alternative conceptual models for ZFM structures should be considered as distinct from the HRD, rather than indistinct from the HRD. This issue is mentioned by Öhman et al. (2012, p. 115-116): "*The deterministic ZFM structures do not comprise a uniform population and cannot be compared against the HRD, as such. With exceptions of ZFM871, ZFMNNE0869, ZFMNNW1034, the Southern and Northern boundary belts, the general impression*

is that in the upper c. 200 m, deterministic structures do not differ significantly from the rock mass outside zones. This notion should be considered in context to the geologic modelling uncertainties in continuity and extent of zones inside the Central block ... and underlines the necessity of alternative conceptual interpretations."

How addressed in SR-PSU

This uncertainty is not addressed in the documents considered in this review.

Comments

This is not likely to be significant for releases to biosphere. Treating ZFMs as distinct transmissive zones is likely conservative compared to treating them as more diffuse fracture networks.

2.1.5. Uncertainty due to lack of PSS measurements

This topic concerns the uncertainty in the DFN model, including the possibility of compartmentalised fracture transmissivity, due to lack of PSS (pipe-string system) measurements to complement PFL-f measurements.

This issue is mentioned by Öhman et al. (2012, p. 116): "*As no complementary PSS measurements have been performed within the SFR extension investigation, the hydrogeological analysis heavily relies on PFL-f data, which are representative of the flowing fracture system (and subject to hydraulic choking). Complementary PSS data are useful for the evaluation of compartmentalised fracture transmissivity, if it needs to be addressed. The old data set consists of short-term hydraulic packer data and hence includes compartmentalised transmissivity, but it covers a different part of the domain and is of a poorer quality.*"

How addressed in SR-PSU

This uncertainty is not addressed in the documents considered in this review.

Comments

Packer data from the older data set may be relevant to analyse even if of poorer quality, and from a different domain. SSM has asked for complementary information regarding this issue (SSM2015-725-40 Points 3 and 5).

2.1.6. Hydrogeological properties and extent of Shallow Bedrock Aquifer (SBA)

This issue together with the issue of unresolved probabilistic deformation zones is mentioned as a data gap by Öhman et al. (2012, p. 116): "*No interference tests have been specifically targeted to the interpreted SBA intercepts and Unresolved PDZs. Transient evaluation of a few selected packed-off pump tests targeting SBA*

intercepts and Unresolved PDZs may potentially shed some insight to their lateral extension."

Öhman et al. (2012, p. 116) also commented as follows on the characterization of the shallow bedrock aquifer: "*The PFL-f data in boreholes located close to the Northern boundary belt and ZFMNNW1034 indicate that SBA-structures do exist north of the Singö deformation zone, even if these seem to be of considerably less [significant] in relation to those modelled in SDM-Site Forsmark. .... The spatial extension of SBA-structures is uncertain, but borehole data (HFR101, KFR104 and KFR105) and SFR tunnel experiences suggest that these are of minor hydraulic significance in the Central block, below –60 m RHB 70. ... The old data set provides little guidance for interpretation of SBA-structures; most are short term measurements (a few minutes) and have no oriented fracture data.*"

How addressed in SR-PSU

This uncertainty is not addressed in the documents considered in this review. According to P-14-04, p. 27: "*As no SBA structures are in direct contact with disposal rooms in SFR 1 or SFR 3, variants of SBA structures are not addressed in the sensitivity analysis. Similarly to earlier TDs, all simulations include a fixed SBA variant, in which all 8 structures are included (SBA1 to SBA8).*"

A similar statement is given in SKBdoc 1395214 (TD08- SFR3 effect on the performance of the existing SFR1).

Comments

The consequences of the lack of analysis of SBA variants are difficult to assess due to the complicated dependence on details of geometry, properties, and hydraulic connections to other structures. SSM has asked for complementary information regarding this issue (SSM2015-725-40, Point 6).

2.1.7. Hydrogeological properties and lateral extension of unresolved PDZs

See preceding section where this is mentioned along with uncertainties regarding the shallow bedrock aquifer.

How addressed in SR-PSU

According to P-14-04, p. 27, "*The HRD represents the rock mass domain outside deterministic deformation zones and consists of stochastic realisations of connected [DFNs] and Unresolved PDZs (conceptually modelled as connected to deformation zones of the Southern and Northern boundary belts; Öhman et al. 2012).*"

Comments

Unresolved PDZs are treated by three stochastic realizations of geometry and properties which are linked to the corresponding HRD realizations. Selection of these three realizations is linked to the ad hoc selection of HRD realizations.

2.1.8. Uncertainty in transmissivity values of deformation zone intercepts based on older data.

Öhman et al. (2012, p. 116) commented as follows on use of older data: "*There also exists uncertainty in the geological modelling of deformation zone intercepts in the old data set (Appendix D), which propagates into an uncertainty in the assignment of hydraulic data. The old data set seem to result in higher transmissivity values of deformation zones (e.g. Figure 6-2e). The old data set is primarily used for conceptual understanding and as complementary data for the deformation zone parameterisation in the SFR near-field.*"

How addressed in SR-PSU

According to P-14-04, p. 27: "*The uncertainty in HCD transmissivity parameter-isation is demonstrated by elaborating four different concepts [homogeneous vs. heterogeneous, conditioning on borehole measurements, depth-trend alternatives, and anisotropic southern boundary belt].*"

Comments

None of the HCD variants appears to account for the possibility that the transmiss-ivities implied by the old data set could have been accurate. SSM has requested complementary information regarding this issue (SSM 2015-725-40, Point 5).

2.2. Selection of hydraulic rock domain realizations

The aims of this part of the review are to examine SKB's selection of the three specific hydraulic rock domain (HRD) realizations that were chosen for propagation to radionuclide transport models, and to evaluate whether these three high/low/intermediate-flow realizations are sufficient to bound the uncertainties that affect the dose and risk calculations.

2.2.1. Hydraulic rock domain realizations

The hydraulic rock domain (HRD) realizations used in the hydrogeological modelling on the regional scale consist of the following main components:

- Discrete-fracture network (DFN) models for the background rock (excluding deformation zones);
- Probabilistic deformation zones (PDZs).

The treatments of these components are summarized below.

Discrete-fracture networks in the background rock

The hydrogeological discrete-fracture network (DFN) model used in SR-PSU is specified in Appendix 5 of SKB (2013).

This model represents changes in characteristics of flowing fractures by dividing the SFR model domain into three depth intervals:

- Shallow domain: z > - 60 m
- Repository domain: -60 m $\geq$ z > -200 m
- Deep domain: -200 m $\geq$ z > -1100 m

where z is the elevation relative to the mean sea level (RHB 70 datum).

In each of these domains, five fracture sets are present. Three of these sets are steeply dipping and described by their nominal strike: East-West (EW), Northwest (NW), and Northeast (NE). A fourth set is gently dipping with variable strike (Gd), and a fifth set is subhorizontal (Hz).

SKB's parameterization of these fracture sets is summarized in Table 2.1. The distribution of orientations within each fracture set is described in terms of a Fisher distribution, which is defined in terms of a mean pole direction and a concentration parameter κ. For each fracture set, the orientation distribution is considered to be the same for all depth domains.

The volumetric intensity of fractures belonging to a given fracture set varies between domains. This is specified in terms of the fracture intensity parameter P_{32} (m^2/m^3), which is defined as fracture area per volume for a given interval in fracture size. The intensity is prescribed for a range of fracture sizes bounded by a minimum fracture radius $r_0 = 0.038$ m (taken as equal to the nominal borehole radius) and a maximum fracture radius, $r_{max} = 169$ m (based on the resolution level of the deterministic geological model which is estimated as 300 m, and calculating the radius of a disc-shaped fracture that has the same area as a square fracture of this size).

The variation of size for fractures within a given fracture set and depth domain is described by a probability distribution for fracture radius r, which is assumed to have the form of a power-law distribution with scaling exponent k_r. SKB (2013) note that k_r "is relatively uncertain, as it cannot be directly measured from borehole investigations," but also that "it has a strong influence on the connectivity of the fracture system."

Fracture transmissivity, T (m^2/s) is assumed to be a direct function of fracture radius, of the form:

$$T = a \cdot r^b$$

where a is the transmissivity of a one-metre radius fracture and b is a scaling exponent.

SKB has used two different approaches to estimate k_r in combination with the parameters a and b of the size-transmissivity relationship. This leads to two separate parameterizations for each domain, one based on a "connectivity analysis" and the other based on a "tectonic continuum" assumption.

The connectivity analysis as described by Öhman and Follin (2010b p. 26) is based on calibration of k_r to the intensity of connected fractures as determined from PFL-f data, along with the intensity of open or partly-open fractures as observed in boreholes. For an assumed value of k_r, fractures are simulated within a specified

volume around a central borehole until the linear frequency of fractures intersecting the borehole matches the observed frequency of open fractures. Then the connectivity of the resulting simulated network to hydraulic boundaries at some assumed distance is evaluated and compared with the linear frequency of PFL-f anomalies. The value of k_r is adjusted manually until the match to observations is judged to be adequate.

The tectonic-continuum approach is based on an alternative assumption that the discrete fractures on scales of meters or tens of meters belong to the same statistical population as the deterministically modelled deformation zones. With this assumption, the areal intensity of deformation zone traces as mapped at the surface constrains the value of k_r. The tectonic-continuum approach was evaluated by Öhman and Follin (2010b) only for the subvertical fracture sets. Öhman and Follin (2010b) state that "was done due to the recognized uncertainty in connectivity analysis for subvertical sets with a dataset based on predominantly subvertical boreholes." It could furthermore be noted that the sizes of subvertical deformation zones are better characterized by the site investigation methods than the sizes of the gently dipping or subhorizontal deformation zones that have orientations similar to the Gd and Hz sets.

According to Odén et al. (2014) the properties as listed in Table 2.1 are used throughout the SFR regional model area. They do not specify clearly which of the two parameterizations (connectivity analysis or tectonic continuum) is used as the primary model. SKBdoc 1395200 is referenced for details, but on p. 18 of this document which gives details of the methodology for generating DFN realizations, reference is simply made to Appendix 5 of SKB (2013), which lists both parameterizations. SKBdoc 1395200 mentions the connectivity analysis but does not refer to a tectonic-continuum parameterization at any point. From this it might be inferred that the connectivity-analysis parameterization has been used as the primary DFN parameterization, but this could not be confirmed based on the documents examined in this review.

Outside the regional SFR site-descriptive model area and the area modelled in SDM-Site (SKB, 2008), DFN models for the bedrock are based on the model setup described in Öhman and Follin (2010, Appendix A). The DFN model for these outlying areas is expected to have only minor influence on flows around the SFR facility, so it has not been considered in this review.

Unresolved Probabilistic Deformation Zones

The term "unresolved probabilistic deformation zones" refers to the potential existence on scales between the largest fractures considered by the DFN model of the HRD, and that of deformation zones that are treated deterministically in the site-descriptive model.

According to Odén et al. (2014) and Öhman et al. (2013), stochastic realisations of unresolved PDZs for the regional hydrogeological model are generated based on modelling procedures and properties described in Öhman et al. (2012, Appendix A).

Table 2.1: Parameters of DFN model, as specified in Table A5-1 of SKB (2013). P32 = fracture intensity (m^2/m^3); Tr = trend of mean pole (in degrees); Pl = plunge of mean pole (in degrees); κ = concentration parameter of univariate Fisher distribution (dimensionless); k_r = scaling exponent for fracture size distribution (dimensionless); a = transmissivity of a fracture of 1 m radius (m^2/s); b = scaling exponent for fracture transmissivity (dimensionless).

Set intensity		Orientation			Connectivity analysis			Tectonic continuum		
		(Fisher distribution)			Size	$(T = a\,r^b)$		Size	$(T = a\,r^b)$	
Set	P_{32}	Tr	Pl	κ	k_r	a	b	k_r	a	b
Shallow domain (z > -60 m RHB 70)										
Set	P_{32}	Tr	Pl	κ	k_r	a	b	k_r	a	b
EW	2.32	4.8	13.9	10.1	3.2	$2.1 \cdot 10^{-8}$	1.3	2.694	$1.6 \cdot 10^{-9}$	1.25
NW	0.99	233.8	7.2	13.7	3.2	$5.3 \cdot 10^{-8}$	1.3	2.626	$3.3 \cdot 10^{-9}$	1.2
NE	1.31	125.4	1.8	13.7	3.45	$1.8 \cdot 10^{-8}$	1.0	2.778	$1.2 \cdot 10^{-9}$	1.0
Gd	1.79	339.1	87	7.2	2.79	$2.1 \cdot 10^{-8}$	1.09	2.79	$2.1 \cdot 10^{-8}$	1.09
Hz	0.96	127.5	83.7	41.9	2.6	$9.8 \cdot 10^{-8}$	1.32	2.60	$9.8 \cdot 10^{-8}$	1.32
Repository domain (-60 ≥ z > -200 m RHB 70)										
Set	P_{32}	Tr	Pl	κ	k_r	a	b	k_r	a	b
EW	1.44	4.8	13.9	10.1	3.1	$2.1 \cdot 10^{-9}$	1.1	2.63	$7.9 \cdot 10^{-11}$	1.4
NW	0.81	233.8	7.2	13.7	3.0	$1.1 \cdot 10^{-8}$	1.1	2.596	$1.3 \cdot 10^{-9}$	1.1
NE	1.00	125.4	1.8	13.7	3.3	$2.2 \cdot 10^{-9}$	1.3	2.752	$8.6 \cdot 10^{-11}$	1.35
Gd	1.21	339.1	87	7.2	2.72	$4.0 \cdot 10^{-9}$	0.8	2.72	$4.0 \cdot 10^{-9}$	0.8
Hz	0.95	127.5	83.7	41.9	2.55	$8.5 \cdot 10^{-10}$	1.35	2.55	$8.5 \cdot 10^{-10}$	1.35
Deep domain (200 ≥ z > -1100 m RHB 70)										
Set	P_{32}	Tr	Pl	κ	k_r	a	b	k_r	A	B
EW	1.06	4.8	13.9	10.1	3.2	$3.6 \cdot 10^{-9}$	1.6	2.585	$7.1 \cdot 10^{-13}$	2.5
NW	0.67	233.8	7.2	13.7	3.15	$4.7 \cdot 10^{-9}$	1.13	2.597	$1.5 \cdot 10^{-10}$	1.31
NE	1.03	125.4	1.8	13.7	3.2	$1.9 \cdot 10^{-9}$	1.0	2.75	$1.6 \cdot 10^{-10}$	1.25
Gd	1.49	339.1	87	7.2	2.7	$2.7 \cdot 10^{-10}$	1.6	2.7	$1.4 \cdot 10^{-10}$	1.7
Hz	0.75	127.5	83.7	41.9	2.75	$1.9 \cdot 10^{-9}$	1.15	2.75	$1.3 \cdot 10^{-9}$	1.25

According to that report (Öhman et al., 2012, Appendix A, p. 129), the Unresolved PDZs are generated as stochastic planar features that are conditioned by their borehole intercept. The stochastic components are:

- Size (specified by side-length of a square feature),
- Location in 3D, and
- Orientation (strike and dip)

The transmissivity of each PDZ is treated as homogeneous.

According to Öhman et al. (2012) the orientation of the Unresolved PDZs is based on estimations from PFL-f data. Conditional simulation is used to ensure that the simulated PDZs conform to available observations regarding:

- Location and orientation at the observed borehole intercepts, and

- Absence of PDZs in other sections of the boreholes, tunnels in the existing SFR, and ground-surface traces longer than the 300 m length which is considered as the resolution of the deterministic deformation-zone model.

Additionally, Öhman et al. (2012) state that the simulated PDZs are required to be in direct contact with a hypothesised structural wedge located between the Northern boundary belt and deformation zone ZFMNNW1034.

2.2.2. Selection of realizations for propagation

According to Odén et al. (2014, p. 38), 99 realizations of the HRD model were generated, but then in order to reduce computational demands these were screened by a "statistical/geometric DFN analysis." Based on this screening process, three realizations were selected to represent a range of possibilities from "optimistic" to "pessimistic" (Öhman et al., 2014).

The screening process is documented in Section 4 of TD05 (SKBdoc 1395200). The procedure for a given realization as summarized in Tables 4-1 and 4-2 of that document is:

1. Generate a stochastic realization of the DFN model for a domain exceeding the SFR regional domain by at least 300 m.
2. Exclude all fractures with center coordinate outside the SFR regional domain.
3. Remove isolated fractures, i.e. fractures that are not connected directly or indirectly via a network to any of the following:
   - Deterministic deformation zones (HCDs);
   - Deterministic SBA-structure geometry;
   - Deterministic DFN outside the SFR Regional domain (excluding fractures located more than 300 m outside SFR regional domain);
   - Unresolved PDZ realisation corresponding to the DFN realization;
   - Tunnel geometry of the existing SFR1;
   - Tunnel geometry of the extension.
4. "Trim" and sample connected fractures intersecting disposal facilities in SFR 1 and L1B.

The reason for Step 2 in this process is not explained, but apparently this is to avoid overlapping with the "deterministic" DFN outside of the SFR domain (a single very large-scale realization of a regional DFN model generated previously with the CONNECTFLOW software), which would be appropriate.

The "trimming" in Step 4 is also not explained, except to list two different values of a variable T_{max} depending on the elevation z_{min} of the lowest corner of a given fracture:

$$z_{min} < -60 \text{ m} \quad : \quad T_{max} = 10^{-5.6} \text{ m}^2/\text{s} \ (\approx 2.5 \cdot 10^{-6} \text{ m}^2/\text{s})$$
$$z_{min} < -200 \text{ m} : \quad T_{max} = 10^{-6.5} \text{ m}^2/\text{s} \ (\approx 3.2 \cdot 10^{-7} \text{ m}^2/\text{s})$$

Presumably this is intended to limit the maximum transmissivity of fractures in certain depth zones.

"Sampling" of fractures involves identification of all fractures that intersect the underground openings that have transmissivity above some minimum value depending on whether the intersection is with the tunnels or the disposal facilities (vaults):

Tunnels : $T_{min} = 10^{-6}$ m^2/s

Vaults : $T_{max} = 10^{-7}$ m^2/s

Note that the combination of these "trimming" and "sampling" criteria (if the former has been interpreted correctly) implies that very large fractures that intersect the tunnels but which have one corner below $z = -200$ m would not be sampled, because their transmissivity would have been set to a value less than 10^{-6} m^2/s.

The sampled intersections between fractures and tunnels/or vaults, and the statistics of these intersections, were exported for further analysis. Realizations were ranked based on the number of fractures intersecting more than one tunnel in the existing SFR facility. According to TD05 (SKBdoc 139200, p. 19), "[t]his measure was believed to reflect the 'danger' of the realisation since hydraulic connections between different repository parts are undesirable and since there is a correlation between fracture size (large fractures more likely to intersect several repository parts) and fracture transmissivity."

Two realizations were selected based on the statistics of intersections with the SFR 1 disposal facilities:

- An "optimistic" realization, R18, which was one of six realizations that had no fracture intersecting more than one tunnel, and was also the realization that had the fewest fractures intersecting more than one tunnel when both SFR 1 and the proposed extension were taken into account.
- A "pessimistic" realization, R85, which was one of two realizations that had the largest number of fractures (7) intersecting more than one disposal room of SFR 1, and was also the realization that had the most fractures intersecting more than one tunnel when both SFR 1 and the proposed extension were taken into account.

The two chosen realizations, R18 and R85, were also among the realizations that ranked the lowest and highest, respectively, in terms of both the total number of tunnel intersections and the sum of the transmissivity of intersecting fractures.

Realization R85 was in fact ranked the highest by all of these measures. However from Figure 2.1 it can be seen that the sum of transmissivity of intersecting fractures is within a span of one order of magnitude for all 99 realizations that were analysed, and most of the realizations are within half an order of magnitude of the maximum value. Thus in terms of net transmissivity, the selected "pessimistic" realization, R85, does not show an overwhelming contrast with most of the other realizations. An additional HRD realization, R03, was selected based on an assessment that it was "pessimistic" for the SFR 3 vaults 4BLA, 5BLA and 2BMA, as well as SFR 1 vault 1BMA (Odén et al., 2014). The rationale for selecting this realization is not discussed in SKBdoc 1395200.

The resulting set of selected HRD cases are illustrated in Figure 2.2.
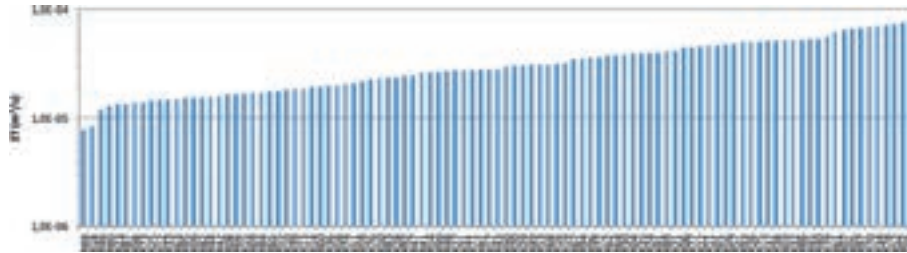
Figure 2.1: Realizations of the DFN model ranked by the sum of the transmissivity of stochastic fractures intersecting the rock vaults of SFR 1 and SFR 3. From Figure 4-5 of TD05 (SKBdoc 1395200).
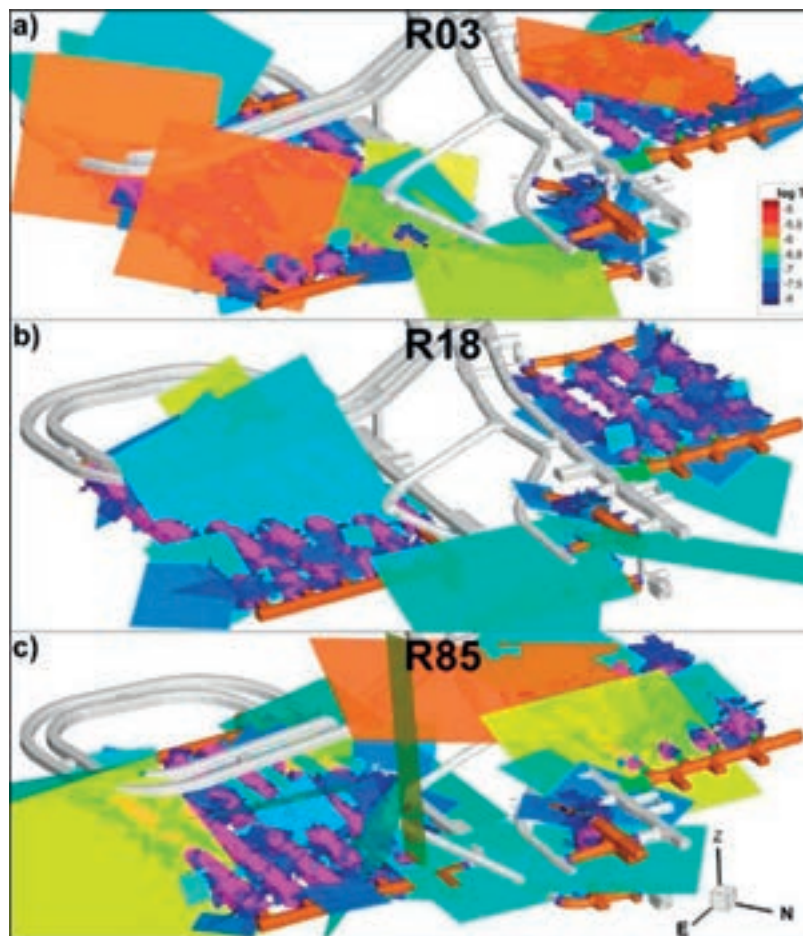
Figure 2.2: Transmissivity of stochastic fractures intersecting the rock vaults of SFR 1 and SFR 3: a) realization R03 (regarded as pessimistic for SFR 3), b) realization R18 (regarded as optimistic for SFR 1), and c) realization R85.(regarded as pessimistic for SFR 1 and overall).

2.2.3. Combination of HRD realizations in bedrock cases

The HRD realizations were combined with alternative representations and realizations of the hydraulic conductor domains (HCDs) to form a set of 17 bedrock calculation cases, as summarized in Table 2.2. A single representation of the shallow-bedrock aquifer (SBA) features was used for all bedrock cases.

Table 2.2: Bedrock cases studied in the sensitivity analysis (based on Tables 4-3 and 4-4 of Odén et al., 2013, R-13-25). R01 and R07 are two different realizations of a heterogeneous HCD model. R03, R18, and R85 are three different realizations of the DFN model for the HRD.

	HCD variant	Conditioning	Depth trend	Transmissivity variability	HRD
1	BASE_CASE1	**Yes**	**Yes**	Homogeneous	**R85**
2					R18
3	BASE_CASE2	**Yes**	**Yes**	Homogeneous, Anisotropic Southern boundary belt	**R85**
4	nc_DEP_HOM	No	**Yes**	Homogeneous	*R03*
5					**R85**
6	nc_NoD_HOM	No	No	Homogeneous	**R85**
7	CD_DEP_R01	**Yes**	**Yes**	**Heterogeneous, R01**	**R85**
8	nc_DEP_R01	No	**Yes**	**Heterogeneous, R01**	**R85**
9					R18
10	CD_DEP_R07	**Yes**	**Yes**	*Heterogeneous, R07*	**R85**
11	nc_DEP_R07	No	**Yes**	*Heterogeneous, R07*	**R85**
12					R18
13	nc_NoD_R01	No	No	**Heterogeneous, R01**	*R03*
14					**R85**
15					R18
16	nc_NoD_R07	No	No	*Heterogeneous, R07*	*R03*
17					**R85**

Based on the outcome of groundwater flow simulations for these 17 calculation cases during temperate climate conditions (Odén et al., 2014), three cases were selected based on calculated cross flows through the eleven disposal vaults in SFR 1 and SFR 3:

Bedrock case 1: A "base case" bedrock case with median disposal-facility cross flows, formed by combining a homogeneous depth trend for the HCD with the "pessimistic" HRD realization R85 for the HRD.

Bedrock case 11: A "high-flow" bedrock case with high disposal-facility cross flows, formed by combining a heterogeneous HCD realization with the "pessimistic" HRD realization R85.

Bedrock case 15: A "low-flow" bedrock case with low disposal-facility cross flows, formed by combining a heterogeneous HCD realization R01 with the "optimistic" HRD realization R18.

Bedrock case 1, which gives intermediate flows through all waste vaults, was selected as the base case for radionuclide transport calculations for the main scenario. The set of three bedrock cases are considered by Odén et al. (2014) to characterize the observed range of heterogeneity and conceptual uncertainty in bedrock parameterization.

The results used in the probabilistic radionuclide transport calculations were advective travel times and flow-related transport resistance values selected in pairs from the same realisations/particle tracks. These pairs of input data are available for 2000 AD, 2500 AD, 3000 AD, 3500 AD, 5000 AD and 9000 AD and are given in the Input data report, Section AMF number 11.

2.2.4. Adequacy of realizations to bound uncertainty

According to the Data Report (TR 14-10, p. 155), "*The delivered data represent different descriptions of the rock mass (Bedrock Cases). These cases cover the uncertainty in the description of the bedrock with one base case and two bounding variants.*" However the degree to which these cases cover the uncertainty in the description of the bedrock is debatable, for five main reasons.

First, conceptual uncertainty in the DFN model of the HRD has not been evaluated. According to SKBdoc 1395200, p. 18, "The DFN parameterisation is taken from Appendix 5 in SKB 2013. As represented in Table 2.1 of this review, that source includes two separate statistical models for fracture size and transmissivity, referred to as the "connectivity-analysis" and "tectonic-continuum" models. From SKBdoc 1395200, p. 9 apparently the "connectivity-analysis" model is the one that has been propagated for the HRD realizations used in the bedrock cases for SR-PSU, without comparing the results of the "tectonic-continuum" model as an alternative parameterization.

Second, the selection of HRD realizations was based only on the geometry and transmissivity of fractures that directly intersect with the tunnels and vaults, not the properties of the complete network by which these fractures are connected to the hydraulic boundaries. Such an evaluation would have required flow simulations or alternatively an equivalent-network analysis that takes the flow properties along network paths into account.

Third, in terms of net (summed) transmissivity for fractures intersecting the tunnels and vaults, the selected "pessimistic" realization, R85 is only marginally worse than many of the other realizations that were not evaluated by flow modelling. More than half of the other realizations had a net (summed) transmissivity within half an order of magnitude of that for R85. Lacking any further hydraulic analysis of the other 96 HRD realizations that were not propagated, at least half of them could be expected to produce flows of similar magnitude to those in R85. On this basis, R85 might be regarded as representing a "likely" case rather than a "pessimistic" case. If network effects were taken into account, some of those other realizations with similar net transmissivity could well produce higher flows through the vaults.

Fourth, only a single representation of the shallow-bedrock aquifer (SBA) features was used for all bedrock cases. Thus uncertainty in cross flows related to how fractures in the HRD realizations connect to different SBA representations was not explored.

Fifth, it was noted that the procedure for "trimming" and "sampling" fracture realizations in the connectivity analysis described in SKBdoc 1395200 might have resulted in omission of very large fractures that intersect the tunnels but have one corner below $z = -200$ m. This might not be a major effect but it adds further uncertainty to the interpretation of the connectivity analysis.

Due to these limitations, it is not clear that the three selected bedrock cases that were used to develop high-flow, intermediate-flow, and low-flow realizations are sufficient to bound the uncertainty associated with realistic variation in bedrock properties that affect the dose and risk calculations, for the main scenario. Therefore calculations based on simplified models are recommended to scope these uncertainties and establish more conservative bounds in relation to the main scenario. The realism and implications of a "high flow in bedrock" scenario, which

SKB regards as less realistic than the main scenario, are discussed in Section 2.4 of this review report.

2.2.5. Main findings concerning selection of realizations

The three bedrock cases that were used as the basis for flow modelling do not necessarily bound the uncertainties in bedrock properties that affect the dose and risk calculations. Conceptual uncertainty in the DFN model of the HRD, as reflected by two different statistical descriptions ("connectivity-analysis" and "tectonic-continuum" models) has not been evaluated. The selection of HRD realizations was based only on the geometry and net (summed) transmissivity of fractures that directly intersect the underground facility, without accounting for network flow effects. In terms of the net transmissivity of intersecting fractures, the "pessimistic" case R85 is not especially distinct from many other realizations that were propagated, and which could well produce higher cross flows depending on network effects. Effects of alternative SBA representations in combination with HRD realizations also were not evaluated.

Therefore scoping calculations are warranted to establish more conservative bounds on the uncertainties that affect the dose and risk calculations, considering plausible parametric variants in combination with different HCD and SBA models.

2.3. Upscaling of discrete-fracture network model

The hydrogeological models used in SR-PSU are all based on upscaling from a discrete-fracture model (DFN) to an equivalent-continuum porous medium (ECPM) representation. The aim of the review topic developed in this section is to assess the up-scaling of the DFN to ECPM models, and how this has impacted the hydrogeological results that are used in subsequent safety analysis steps.

2.3.1. Upscaling method used in SR-PSU

Upscaling from the DFN model to an ECPM for the hydrogeological models used in SR-PSU is performed using DarcyTools Version 3.4 (Svensson et al. 2010; Svensson 2010; Svensson and Ferry 2010). The method for generating grid cell hydraulic properties in DarcyTools (referred to as the GEHYCO algorithm) is essentially a geometrical upscaling method in which the grid cell properties are obtained by summing up the contributions of each individual fracture within a given grid cell, similar to that used for geometrical estimates in this review. As noted by Öhman et al. (2014) the ECPM conversion in Darcy Tools relies on several approximations, including the following two assumptions that pertain directly to hydraulic conductivity:

- All fractures inside a cell-wall control volume contribute to advection.
- The advection takes place over their full fracture surface area.

Furthermore only fractures within a specified size interval are included. The minimum fracture side length ranges from 2 to 16 m, depending on the fracture set and depth domain (as detailed in Appendix D of Öhman et al., 2014). According to Öhman et al. (2014), only the hydraulically connected subset of the fracture network is modelled. Details are provided in TD05 (SKBdoc 1395200), as discussed in Section 2.2. Because the summation for grid cells in DarcyTools takes into account only a subset of the fractures, the hydraulic conductivities calculated by DarcyTools should generally be lower than those obtained by the geometrical estimation method used here.

However, the DarcyTools algorithm as described by Svensson et al. (2010) does not take into account network effects that can limit the contributions of individual, connected fractures to the effective block-scale hydraulic conductivity. For example, some fractures that are connected to the main network might effectively be dead-end branches that do not contribute to net through-flow. Other low-transmissivity fractures might serve as bottlenecks that limit the effective contribution of higher-transmissivity fractures.

Although the code verification, validation and demonstration document for DarcyTools Version (Svensson, 2010) is stated to confirm the accuracy of the DarcyTools algorithm for upscaling DFN network properties, this statement seems to be based on the results for just one calculation case that does not necessarily represent the full range of network effects that could arise in a random DFN model.

Therefore the DarcyTools algorithm should generally be expected to produce higher K values than permeameter simulations such as SKB has used for modelling of the high-level waste repository at Forsmark.

The upscaled hydraulic conductivity data used in the models for SR-PSU are specified in Section 4.17 of the Input Data report (TR 14-12, AMF Number 84). The dataset is calculated using DarcyTools and is divided into two deliveries, one down to –170 m elevation and one down to –634 m elevation.

The hydraulic conductivities as used in the two models for the volume containing SFR 1 were compared graphically in Figure 3.21 of Abarca et al. (2013) as reproduced here in Figure 2.3. The usefulness of this graphical comparison is limited by slight differences in the color scales. However it appears that the volumes with hydraulic conductivity above 10^{-7} are somewhat more extensive in the COMSOL repository-scale model. This could be the result of using linear interpolation of values that differ by orders of magnitude, in mapping K values from the DarcyTools grid to the grid used in the COMSOL model.

This upward bias in the *K* field may account at least in part for the higher flows in the COMSOL repository-model for SFR 1 that were obtained in a benchmark comparison between DarcyTools and COMSOL. According to Table 4-2 of Abarca et al. (2013), the COMSOL model systematically yields higher total flows by 15% to 25% compared with DarcyTools.
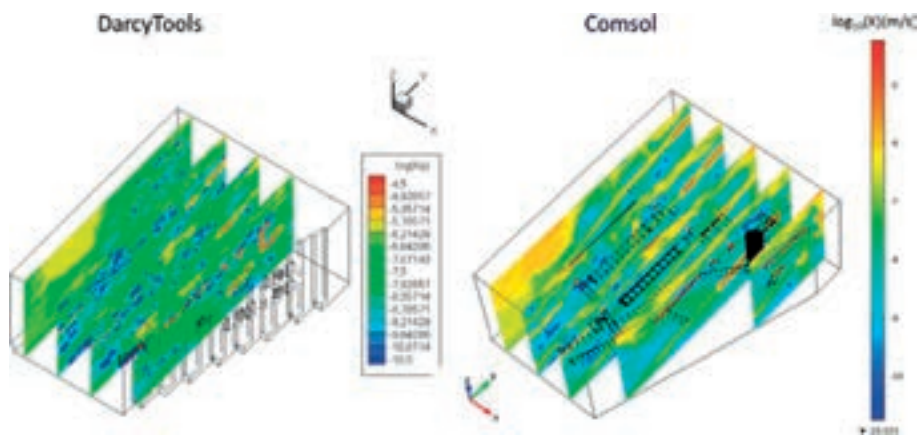

Figure 2.3: Rock hydraulic conductivity field represented in y-z planes in the DarcyTools regional-scale model and in the COMSOL repository-scale model of SFR 1. From Figure 3.21 of Abarca et al. (2013). Note that the color scales are not identical for the plots from the different models.

2.3.2. Independent estimates of hydraulic conductivity

As part of this review, the following approach has been used to evaluate the upscaling of hydraulic conductivity, based on independent methods of estimation:

- Apply an analytical formula for effective hydraulic conductivity tensors for the specified DFN statistical models, but with the simplifying assumption that fractures have an infinite extent;
- Carry out DFN simulations to calculate block-scale effective hydraulic conductivity tensors and their variability, based on a geometrical estimation method that accounts for finite fracture size but not network effects;

- Compare the estimates obtained by these two methods with the hydraulic conductivity fields produced by upscaling with the DarcyTools code used in hydrogeological modelling for SR-PSU;
- Examine how these upscaled values are applied to the different modelling scales used in SR-PSU; and
- Evaluate whether the hydraulic conductivity fields as applied are reasonable, and whether uncertainties in upscaling are adequately accounted for in the subsequent safety analysis steps.

The methods for analytical and geometrical upscaling are described in the following paragraphs.

Independent analytical estimates of hydraulic conductivity

For a fracture set with orientations described by a Fisher distribution, analytical expressions for the effective hydraulic conductivity tensor were developed by Geier (2012) based on the idealization that the fractures have infinite extent.

The hydraulic conductivity tensor $\mathbf{K}$ in a given reference coordinate system {x, y, z} is given by:

$$\mathbf{K} = \mathbf{A}\mathbf{K'}\mathbf{A}^T$$

where:

$$K' = \begin{bmatrix} K_t & 0 & 0 \\ 0 & K_t & 0 \\ 0 & 0 & K_p \end{bmatrix}$$

with:

$$K_t = \frac{\overline{T}}{P_{32}}\left[1 - \frac{\coth\kappa}{\kappa} + \frac{1}{\kappa^2}\right]$$

$$K_p = \frac{2\overline{T}}{P_{32}}\left[\frac{\coth\kappa}{\kappa} - \frac{1}{\kappa^2}\right]$$

being the components of hydraulic conductivity transverse and parallel, respectively, to the mean pole of the Fisher distribution, $\overline{T}$ is the mean transmissivity of the fracture set, and $\mathbf{A}$ is a rotation matrix:

$$A = \begin{bmatrix} \cos\theta_m\cos\phi_m & -\sin\phi_m & \sin\theta_m\cos\phi_m \\ \cos\theta_m\sin\phi_m & \cos\phi_m & \sin\theta_m\sin\phi_m \\ -\sin\theta_m & 0 & \cos\theta_m \end{bmatrix}$$

where θ_m is the angle from the z direction to the mean pole direction, and ϕ_m is the angle from a vector normal to the mean pole to the projection of the mean pole into the $x - y$ plane (see Geier, 2012 for further details). The superscript T denotes the matrix transpose.

The above formula requires an effective mean value of fracture transmissivity. As noted by Geier (2012) an area-weighted estimate of the mean transmissivity can be obtained from simulations as:

$$\langle \bar{T} \rangle_A = \frac{\sum_{i=0}^{N} A_i T_i}{\sum_{i=0}^{N} A_i}$$

where A_i is the area of the *i*th fracture, and T_i is the corresponding transmissivity.

For the DFN models used in SR-PSU, where there is a direct mathematical relationship between fracture radius and fracture transmissivity, and area-weighted estimate of mean transmissivity can also be calculated analytically, based the mathematical definition of the power-law distribution. This gives:

$$\langle \bar{T} \rangle_A = \frac{\int_{r_{min}}^{r_{max}} C r^{k_r+1} a r^b 2\pi r dr}{\int_{r_{min}}^{r_{max}} C r^{k_r+1} 2\pi r dr} = a \frac{(1-k_r)\left(r_{max}^{m+1-k_r} - r_{min}^{m+1-k_r}\right)}{(b+1-k_r)\left(r_{max}^{1-k_r} - r_{min}^{1-k_r}\right)}$$

in terms of the variables used in SKB's model.

Application of these formulae to the two alternative parameterizations of the DFN models of the HRD, as given in Appendix A5 of SKB (2013) and reproduced as Table 2.1 in this report, yields the tensor values as listed in Table 2.3.

Independent geometrical estimates of hydraulic conductivity

Block-scale estimates of the rock mass hydraulic conductivity **K** can also be produced using geometrical calculations based on stochastic simulations of the DFN model. In contrast to the foregoing analytical method, this approach accounts for the effects of finite fracture size and finite block scales, and produces estimates of spatial variability. However, as for the analytical method, the geometrical methods described here do not account for connectivity effects.

The basic approach in producing geometrical estimates of rock-mass hydraulic properties is to add up the contributions of individual fractures for 50 m and 100 m block scales. For these calculations, realizations of a 1000 m x 1000 m x 1000 m volume are used, and properties are calculated for blocks at different positions in the reference coordinate system.

The contribution of a single fracture *i* to the block-scale tensor **K** is calculated from Snow's law (Snow, 1969) which can be written in matrix form as:

$$K_i = \frac{T_i}{s_i}\left[I - n \otimes n\right]$$

where:

T_i = fracture transmissivity
s_i = effective fracture spacing
I = the identity matrix with components $I_{ii} = 1$; $I_{ij} = 0$ for $i \neq j$; $i,j = 1,2,3,$.
n = unit normal vector to fracture plane

and where $n \otimes n$ denotes the outer (tensor) product with components $n_i n_j$, for $i, j = 1, 2, 3$.

The effective fracture spacing s_i is taken as V/A_i where A_i is the area of the fracture that lies within the volume V of the rock block (the entire area of the fracture, if the fracture is entirely within the rock block).

The block-scale hydraulic conductivity tensor is then approximated as the sum of the contributions of each fracture that has some portion within the block volume V:

$$K = \sum_V K_i$$

This method of estimation was originally proposed by Oda (1985), and is implemented in the DFM discrete-feature modelling code (Geier, 2008 and subsequent version updates).

The geometrical estimates give an indication of block-scale variability, which is not available from the single value that is produced by the analytical formulae. Thus this method provides a relatively simple way to produce synthetic fields of hydraulic properties (**K** tensors and porosities) for groundwater flow models based on continuum concepts. However some limitations of the method are apparent from further examination of the results.

Table 2.3: Summary of analytical estimates of rock mass hydraulic properties.

Model	Domain	Hydraulic Conductivity Tensor Components K_{ij} (m/s)		
CA	Shallow	2.7809e-07	1.7498e-08	1.5347e-08
		1.7498e-08	2.6654e-07	1.2503e-08
		1.5347e-08	1.2503e-08	9.4027e-08
CA	Repository	1.8104e-08	5.1594e-09	7.9368e-10
		5.1594e-09	1.4764e-08	-1.1847e-09
		7.9368e-10	-1.1847e-09	1.9414e-08
CA	Deep	1.1429e-08	2.4010e-09	-9.6344e-11
		2.4010e-09	1.2409e-08	-2.5775e-10
		-9.6344e-11	-2.5775e-10	1.3226e-08
TC	Shallow	2.3131e-07	5.9079e-10	1.3203e-08
		5.9079e-10	2.2983e-07	1.6961e-08
		1.3203e-08	1.6961e-08	2.3772e-08
TC	Repository	7.4013e-09	9.0322e-10	1.5990e-10
		9.0322e-10	6.8325e-09	-8.7880e-11
		1.5990e-10	-8.7880e-11	3.6911e-09
TC	Deep	3.5083e-09	6.5141e-11	1.8664e-10
		6.5141e-11	3.3591e-09	1.8712e-10
		1.8664e-10	1.8712e-10	9.4746e-10

A drawback of this approximation is that it generally overestimates the block-scale hydraulic conductivity that would be obtained by an explicit block-scale DFN calculation. Not all fractures within a given volume will form part of the conductive "backbone" of the through-flowing network, and network tortuosity further reduces the effective hydraulic conductivity. However this approximation can be calculated with much less computational effort than is required for the more rigorous approach of permeameter simulations.

Values of hydraulic conductivity calculated by this method for the connectivity-analysis variant of the DFN model are presented graphically in Figures 2.4 through 2.7.

The first of these figures shows the geometric mean values of the directional values K_x, K_y, and K_z as a function of depth. It is evident that the vertical component K_z is lower than both of the horizontal components. Thus this DFN model leads to an anisotropic hydraulic conductivity field, which is more conductive in the horizontal directions than in the vertical direction by as much as a factor of 10 at shallow depths, but the degree of anisotropy decreases to a factor of about 2 at greater depths.

The next three plots show the variability of these components of hydraulic conductivity as a function of depth, characterized by the geometric mean and standard deviation, and by maximum and minimum values. It can be seen that the variability on a logarithmic scale is slightly larger for the horizontal components than for the vertical component. For each of the three components, the difference between the maximum value and the geometric mean is generally greater than the difference between the minimum value and the geometric mean, implying that anomalously high values are relatively rare compared with anomalously low values. This result can be expected due to the relative rarity of large fractures in the power-law distributions for fracture size, combined with the logarithmic correlation of fracture transmissivity to fracture size.
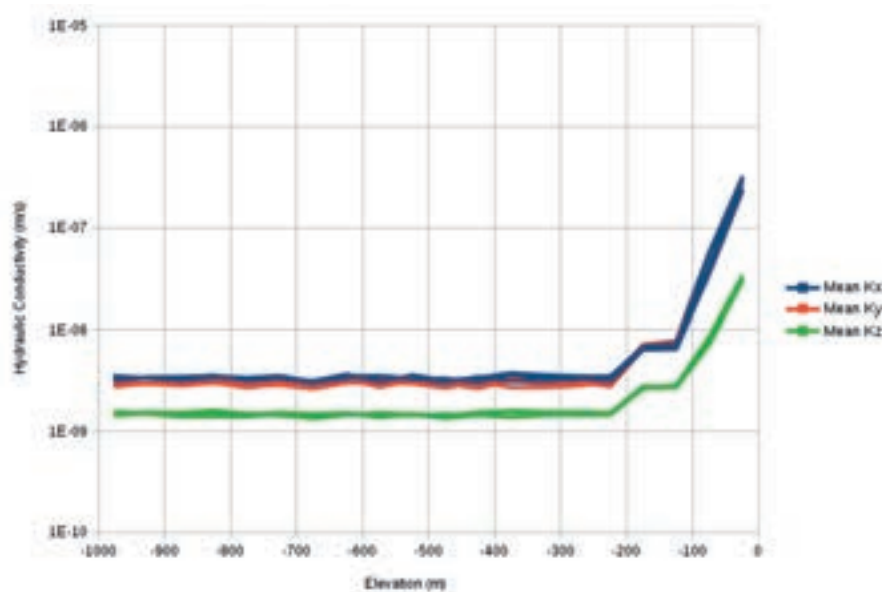

Figure 2.4: Geometric mean values of estimated hydraulic conductivities in the x, y, and z directions as a function of depth (elevation) of the center of the block, for a block scale of 50 m. Results are shown for three realizations of the connectivity-analysis version of the DFN model.
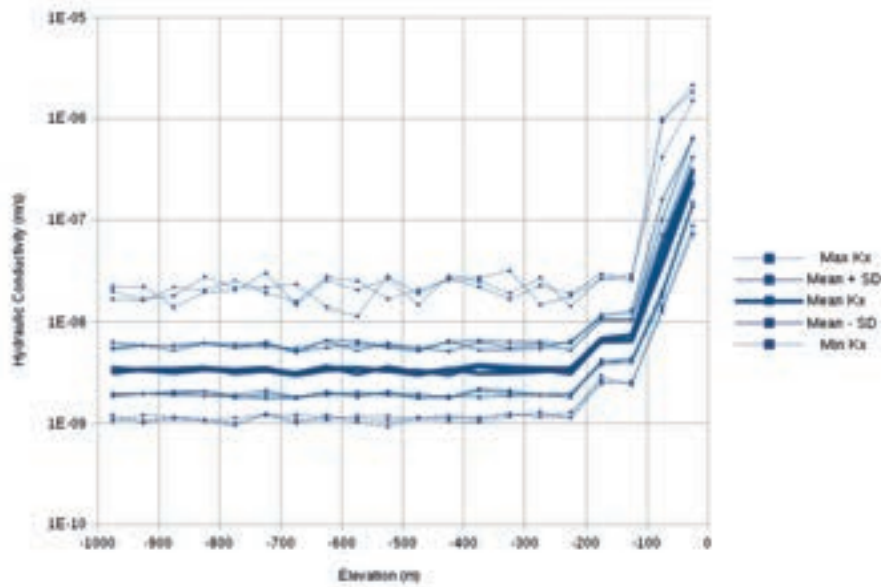
Figure 2.5: Geometric mean values and variabilities of hydraulic conductivities in the x directions as a function of depth (elevation) of the center of the block, for a block scale of 50 m. Results are shown for three realizations, with 400 blocks at each elevation. The uppermost and lowermost sets of lines show the maximum and minimum values, respectively. The middle set of thicker lines show the geometric mean values. The other two sets of lines show the mean value plus or minus one standard deviation on a logarithmic scale.

Figure 2.6: Geometric mean values and variabilities of hydraulic conductivities in the y directions as a function of depth (elevation) of the center of the block, for a block scale of 50 m. Results are shown for three realizations, with 400 blocks at each elevation. The uppermost and lowermost sets of lines show the maximum and minimum values, respectively. The middle set of thicker lines show the geometric mean values. The other two sets of lines show the mean value plus or minus one standard deviation on a logarithmic scale.
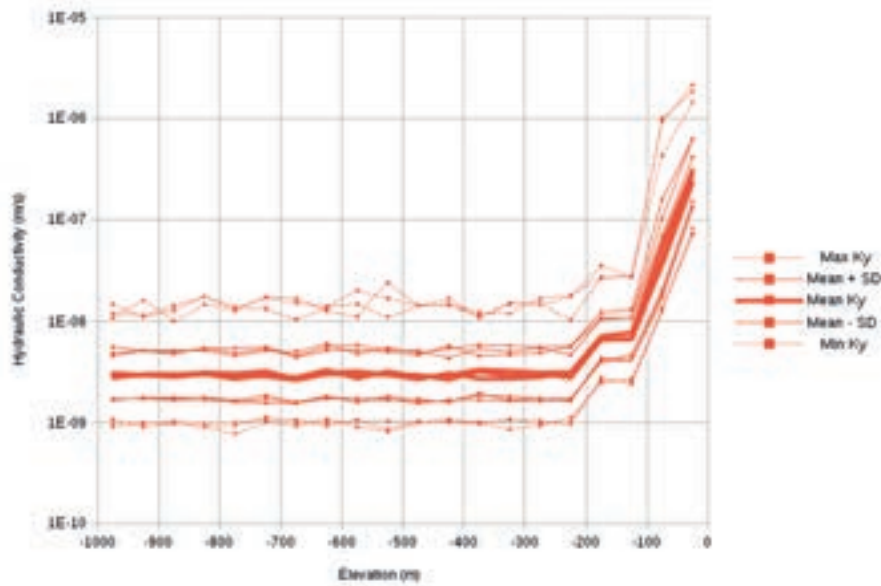
Figure 2.7: Geometric mean values and variabilities of hydraulic conductivities in the z directions as a function of depth (elevation) of the center of the block, for a block scale of 50 m. Results are shown for three realizations, with 400 blocks at each elevation. The uppermost and lowermost sets of lines show the maximum and minimum values, respectively. The middle set of thicker lines show the geometric mean values. The other two sets of lines show the mean value plus or minus one standard deviation on a logarithmic scale.
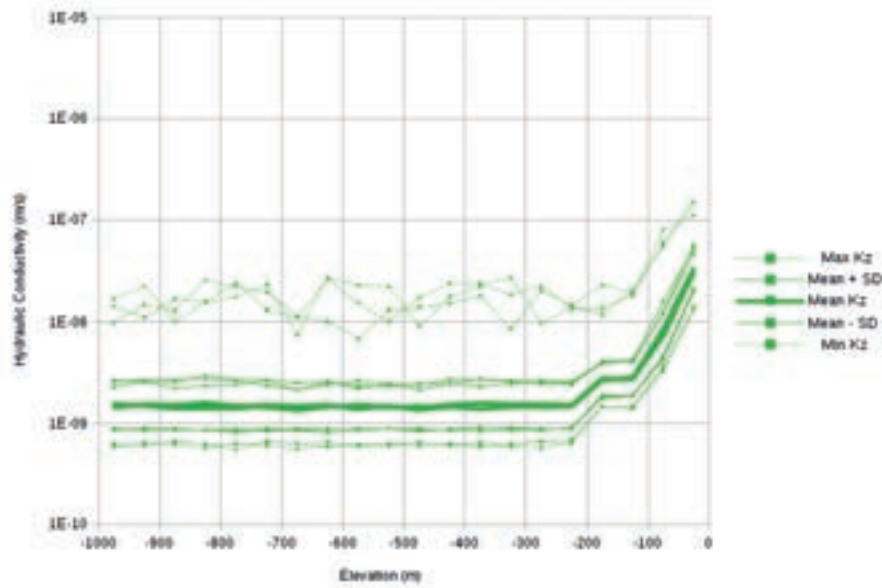
2.3.3. Comparison of upscaled hydraulic conductivities

The analytical and geometrical upscaling methods used for independent evaluation here are expected to be an upper bound on the hydraulic conductivities that would result from upscaling methods that take network effects into effect explicitly. The relationship among hydraulic conductivity values produced by these different methods of estimation should thus generally be:

$$K_{permeameter} \leq K_{DarcyTools} \leq K_{geometrical} \leq K_{analytical}$$

For the type of DFN models used in SR-PSU, in which fracture transmissivity is positively correlated to fracture size, the smaller fractures that are less likely to be connected across grid cell edges are also less likely to contribute significantly to the geometrical estimates. Hence it might be expected that:

$$K_{permeameter} \leq K_{DarcyTools} \approx K_{geometrical} \leq K_{analytical}$$

In other words, the geometrical estimates should provide a reasonable check on the values obtained by the DarcyTools estimate, even though both types of estimates are likely to be higher than the more rigorous approach of permeameter simulations.

The only tabular statistical presentation of the hydraulic conductivities found in the course of this review is Table 3-6 of Abarca et al. (2013). Table 2.4 lists the values from that presentation, including the volume-averaged, minimum and maximum

values of hydraulic conductivity, and compares these with the analytical and geometrical estimates as developed in Sections 2.3.2 and 2.3.3.

From Table 2.4 it is evident that the volume-averaged hydraulic conductivities calculated from the output of DarcyTools are both higher and more isotropic than those obtained by applying the analytical and geometrical estimation methods to the DFN models. It should be noted that these volume-averaged values based on DarcyTools output include the contribution of HCDs, which have not been included in the analytical and geometrical estimates based on the DFN models, as developed here.

By visual inspection of Figure 2.3 focusing on the typical values for the HRD at a given depth (i.e. excluding the higher-K linear zones that are presumably due to the HCDs), the magnitudes of hydraulic conductivity produced by DarcyTools are reasonably consistent with the geometrical estimates calculated for this review. Approximate agreement with these geometrical estimates should be expected based on the description of the algorithm used in DarcyTools.

Table 2.4: Characteristic values of rock hydraulic conductivity field calculated by DarcyTools and imported to COMSOL for use in repository-scale models, according to Table 3-6 of Abarca et al. (2013). Values calculated with the analytical method and geometrical methods as part of this review are also shown for comparison, for both the connectivity-analysis (CA) and tectonic-continuum (TC) parameterizations of the DFN model. The volume-averaged values of analytical estimates are averaged over the depth interval -250 m to -20 m considered by Abarca et al. (2013, Table 3-5). The values given for the geometrical method of estimation are the geometrical means for 50 m depth intervals that were chosen to lie entirely within the shallow, repository, and deep domains of the DFN model as specified in Table 2.1.

Method		K_x (m/s)	K_y (m/s)	K_z (m/s)
DarcyTools	Volume-averaged	1.57e-07	1.55e-07	1.44e-07
	Minimum	3.00e-11	3.00e-11	3.00e-11
	Maximum	1.06e-05	1.07e-05	1.06e-05
Analytical	Volume-averaged (CA)	5.69e-08	5.35e-08	2.85e-08
	Volume-averaged (TC)	4.18e-08	4.13e-08	6.06e-09
Analytical	Shallow (CA)	2.78e-07	2.67e-07	9.40e-08
	Shallow (TC)	2.31e-07	2.30e-07	2.38e-08
Geometrical	Shallow (CA)	2.93e-07	2.90e-07	3.29e-08
	Shallow (TC)	2.79e-07	2.78e-07	3.08e-08
Analytical	Repository (CA)	1.81e-08	1.48e-08	1.94e-08
	Repository (TC)	7.40e-09	6.83e-09	3.69e-09
Geometrical	Repository (CA)	6.53e-09	6.71e-09	2.74e-09
	Repository (TC)	7.89e-09	8.12e-09	2.89e-09
Analytical	Deep (CA)	1.14e-08	1.24e-08	1.32e-08
	Deep (TC)	3.51e-09	3.36e-09	9.47e-10
Geometrical	Deep (CA)	3.28e-09	2.90e-09	1.54e-09
	Deep (TC)	2.49e-09	2.36e-09	1.07e-09

2.3.4. Main findings concerning upscaling

The upscaling from the DFN model to an ECPM representation using DarcyTools produced results that appear to be consistent with what should be expected from the geometrical upscaling algorithm (GEHYCO) described in the DarcyTools documentation. This finding is based on comparison of geometrical estimates (obtained using the DFM code) with a graphical representation comparison of the generated hydraulic conductivity fields, and with volume-averaged quantities presented by Abarca et al. (2013).

The latter comparison is limited by inclusion of HCDs in the volumetric averages. A more direct comparison would require access to the hydraulic conductivity datasets as referenced in Section 4.17 of the Input Data report (TR 14-12, AMF Number 84).

The use of linear interpolation to assign hydraulic conductivities from DarcyTools to the COMSOL repository-scale models may have produced an upward bias in hydraulic conductivities, so that the repository-scale models have somewhat more extensive volumes of hydraulic conductivity $K > 10^{-7}$ m/s. This finding is also hampered by the limited basis for comparison of the K fields for DarcyTools and COMSOL representations (namely visualizations in which slightly different color scales are used). The same result can also be expected for the vault-scale models evaluated by Abarca et al. (2014), for which the same linear interpolation method was used.

This upward bias in the K field may account at least in part for systematically higher total flows through the COMSOL model domain for SFR 1 that were obtained in a benchmark comparison between DarcyTools and COMSOL. However the magnitude of the difference as reported by Abarca et al. (2013, Table 4-2) is only 15% to 25%. The effect on safety assessment calculations is likely to be conservative as slightly higher flows through the bedrock in the repository-scale models will lead to slightly more rapid advective transport of radionuclides.

This review has not quantitatively addressed the potential errors introduced by the geometrical upscaling algorithm (GEHYCO) in DarcyTools, in comparison with a an upscaling method that explicitly takes into account network effects such as the permeameter approach that SKB has used for modelling the high-level waste repository at Forsmark.

Qualitatively, it can be expected that the hydraulic conductivity field calculated by the permeameter method would be lower than that calculated by the GEHYCO algorithm. Thus such an approach would likely lead to lower overall flows through the SFR, compared to the presented approach. Thus the presented approach is likely to be conservative in terms of overall flows.

However, the GEHYCO method may also underestimate the heterogeneity of bedrock hydraulic conductivity. This means that the hydrogeological simulations may not adequately account for the possibility of higher flows being focused through some particular portion of the SFR. Hence it is recommended, for SSM's ongoing review, that scoping calculations should be carried out to assess the potential consequences of significantly higher flows through one or more particular vaults.

2.4. Construction of high flow in bedrock scenario

This review topic concerns SKB's method of constructing the high-flow-in-bedrock scenario, based on an independent assessment of the uncertainties and simplifications in the hydrogeological site-descriptive model, to assess whether SKB is justified in their argument that the probability of such elevated flows in all vaults is low.

Consequence calculations based on the high flow in bedrock scenario are presented in Section 9.3.2 of the main SR-PSU report (SKB, 2014). The results indicate that this scenario produces a modest but significant increase in dose especially in the time interval from 3000 to 20,000 AD (Main Report, Figure 9-17). However the calculated doses are still only about half of the level corresponding to the risk criterion.

2.4.1. Construction of the high flow in bedrock scenario

The *high flow in the bedrock* scenario is described in Section 7.6.2 of TR-14-01. The scenario is aimed to represent a deviation of the safety function *low flow in bedrock* from the assumptions of the main scenario, due to "uncertainties in the data used to describe the rock in the hydrogeological flow model."

The radionuclide transport calculations for this scenario are based on data calculated by the hydrogeological modelling for a particular realization of the DFN models for the HRD (bedrock case 11) that SKB considered as likely to produce high flows relative to other cases. These data include distributions of flow-related transport resistance F_r (Figure 2.8), advective travel times $t_{w,r}$ (Figure 2.9) and path lengths L_r (Figures 2.10).

Per a footnote on p. 214 of TR-14-01, the flow-related transport resistance is used together with the advective travel time to calculate the flow-wetted surface area a_w by the formula:

$$a_w = \frac{F_r}{t_{w,r}}$$

The path-length data apparently are not used directly in the radionuclide transport calculations.
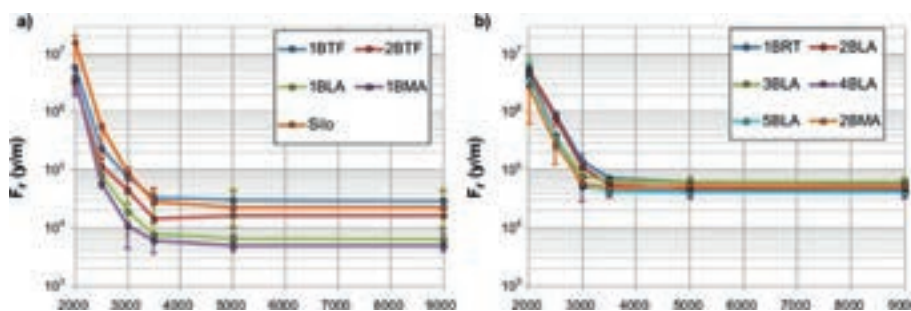

Figure 2.8: Median values of the flow-related transport resistances (F_r) for different waste vaults as a function of time (given in years AD on the x-axis): a) in SFR 1 and b) in SFR 3. The bars indicate the difference between the three bedrock cases selected to be representative for low, intermediate and high flow. From Figure 7-4 of TR-14-01.

Figure 2.9: Median values of the advective travel times ($t_{w,r}$) for different waste vaults as a function of time (given in years AD on the x-axis): a) in SFR 1 and b) in SFR 3. The bars indicate the difference between the three bedrock cases selected to be representative for low, intermediate and high flow. From Figure 7-5 of TR-14-01.
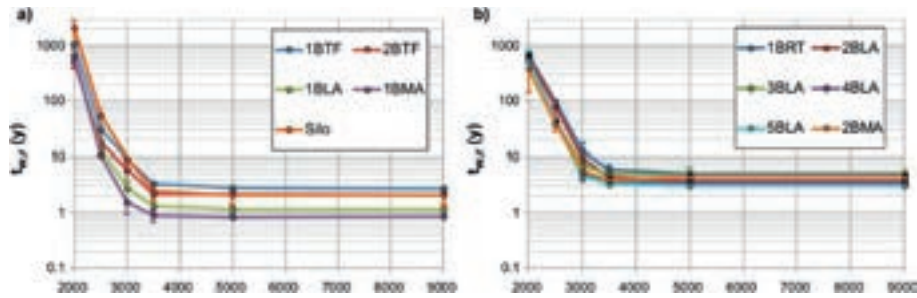

Figure 2.10: Median values of the path lengths (L_r) for different waste vaults as a function of time (given in years AD on the x-axis): a) in SFR 1 and b) in SFR 3. The bars indicate the difference between the three bedrock cases selected to be representative for low, intermediate and high flow. From Figure 7-6 of TR-14-01.
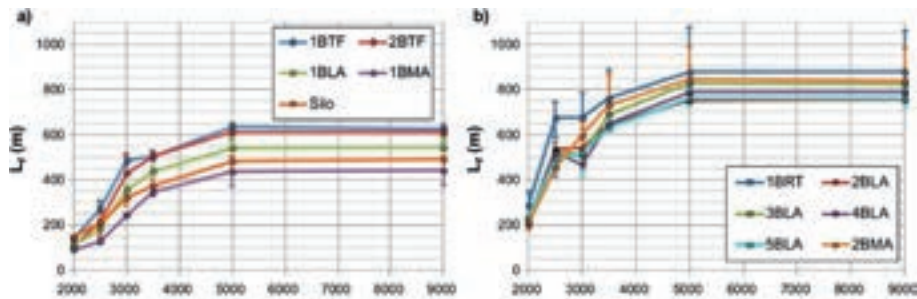
In the regional hydrogeological modelling (Odén et al. 2014), 17 bedrock cases have been included with different parameterisations of the deformation zones and fracture network. Data were produced for the following time steps: 2000 AD, 2500 AD, 3000 AD, 3500 AD, 5000 AD and 9000 AD.

According to TR-14-01, the detailed water flows inside the waste vaults were not calculated explicitly based on repository-scale or vault-scale hydrogeological models that incorporated the "high-flow" bedrock realization (bedrock case 11, composed as summarized in Table 2.2). Instead, the flows were obtained simply by scaling the water flows that were calculated for the main scenario.

The scale factor used for each vault is stated to be "the maximum quotient between the cross flow in all bedrock cases and the cross flow in the intermediate-flow case used in the main scenario (all time steps ≥ 2500 AD)." The intermediate-flow case is bedrock case 1, so in mathematical terms this scale factor for a given vault can be expressed as:

$$f_V = \max_{i,j}\left(\frac{Q_{V,i,j}}{Q_{V,1,j}}\right)$$

where $Q_{v,I,j}$ is the cross flow through vault V for the ith bedrock case and jth time step t_j such that $t_j \geq 2500$ AD.

There are 17 bedrock cases $i = \{1,2,\ldots,17\}$ as summarized in Table 2.2 and five time steps with $t_j \geq 2500$ AD, so the maximum quotient for each vault is taken over a total of $17 \cdot 5 = 85$ combinations of bedrock cases and time steps.

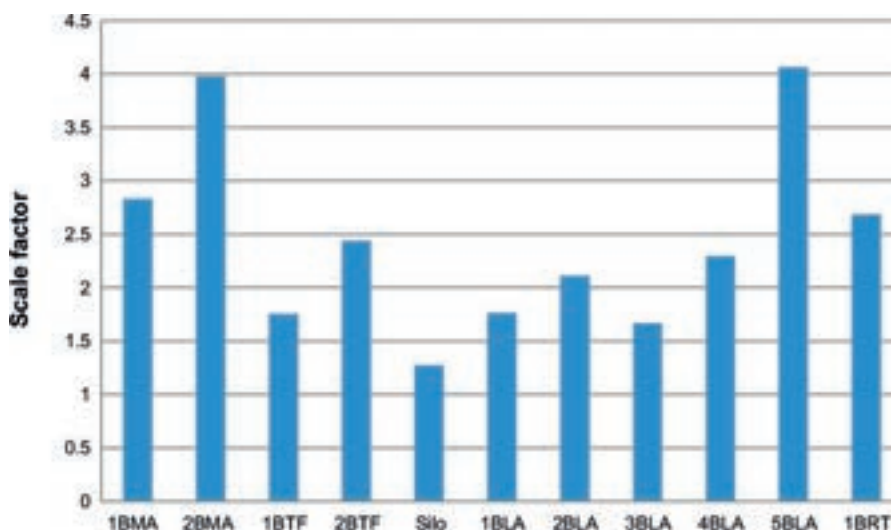The resulting scale factors are shown in Figure 2.11.

Figure 2.11: Scale factors for near-field flows for each waste vault used for the *high flow in the bedrock* scenario. Based on Figure 7-13 of TR-14-01.

The scale factors are then applied to the directional water flows through each vault for each concrete degradation state during the relevant time steps. The (x, y, z) directions of the flows in the vaults are maintained; only their magnitudes are increased by the relevant factor f_V.

All other data were the same as in the main scenario, including the partitioning coefficients for sorption. This is based on a judgment that accelerated chemical degradation of the concrete barriers is sufficiently cautiously treated in the main scenario.

2.4.2. Assessment of SKB's basis for constructing the scenario

The Main Report (TR-14-01) notes that some of the scale factors in Figure 2.11 result from calculation cases other than the "high-flow" bedrock case (bedrock case 11). Thus the total aggregated flow through the waste vaults in this scenario is higher than calculated in any of the bedrock cases.

SKB argues that this means that the combination of flowrates is "unphysical," as it does not correspond to a specific calculation case. This choice was intended to avoid underestimating the release from any of the waste vaults, in the *high flow in the bedrock scenario*. Based on this, they assert that the probability for the *high flow in the bedrock scenario* can be assumed to be considerably less than 10%.

However, the occurrence of higher flows for some vaults in cases other than bedrock case 11 implies that high flows can result from focusing of flow through a particular vault depending on stochastic properties of the HRD and HCD representations. This happens even within the limited set of 17 bedrock cases that have been evaluated.

As discussed in Section 2.2, it is not clear that the selection of bedrock cases has adequately bounded the flow to any given vault. There are residual uncertainties in the representation of the SBA, in the DFN statistical models for the HRD, and in terms of the hydraulic behaviour of the 96 out of 99 HRD realizations that were only evaluated in terms of geometric measures and a summation of transmissivities for intersecting fractures. Most of those 96 HRD realizations had net (summed) transmissivities within half an order of magnitude of the realization (R85) that was used for construction of the "high flow" bedrock case

Considering this last point in particular, the possibility cannot be discounted that a substantial percentage of the 96 HRD realizations that were not evaluated by flow simulations would yield higher flows to one or more of the vaults, even in excess of the scale factors in Figure 2.11. Therefore the assertion that the probability for the *high flow in the bedrock scenario* is "considerably less than 10%" is poorly supported by the evidence that has been presented.

2.4.3. Main findings concerning treatment of high flow in bedrock

SKB has not considered enough realizations of the DFN model for the HRD, or the main alternative parameterization of that model, or its combinations with alternative representations of HCDs and the SBA, to establish the probabilities and range of high flow. Scoping calculations as discussed in connection with the selection of bedrock calculation cases in Section 2.2 would help to establish more conservative bounds.

From the consequence calculations as presented in the main SR-PSU report (SKB, 2014), the high flow in bedrock scenario produces a significant increase in dose but this is still only about half of the level corresponding to the risk criterion. A more conservative formulation of this scenario could reduce that margin.

The potential interaction of engineered-barrier system (EBS) flow properties with properties of the HRD, as represented by DFN and ECPM models, has not been considered in this review. This topic would require an interdisciplinary approach to account for both hydrogeological processes and EBS processes, taking into account the effect of backfill properties.

2.5. Parameterizations and couplings

The hydrogeological modelling in support of SR-PSU was carried out on three different scales:

- Regional-scale modelling carried out with DarcyTools (Odén et al., 2014);
- Repository-scale modelling carried out with COMSOL Multiphysics (Abarca et al., 2013); and
- Vault-scale modelling carried out with COMSOL Multiphysics (Abarca et al., 2014).

The primary aim of the regional-scale modelling was to analyse the impacts of heterogeneity and uncertainties in bedrock parameterization on performance measures, specifically flows through the existing SFR 1 and the proposed extension (SFR 3) disposal rooms, the exit locations for conservative solute discharging from these disposal rooms, and flow-related transport properties associated with these discharge paths. The regional-scale model is also used to specify effective bedrock hydraulic properties and boundary conditions for the models on smaller scales.

The main objectives of the repository-scale model were (1) to estimate groundwater flow rates within the repository, and (2) to develop a system understanding focusing on the effects of barrier degradation, closure alternatives, and permafrost.

The vault-scale models were developed to address more specific questions concerning (1) the effects of concrete degradation of the 1BMA structure and (2) transport of solutes around the Silo. The smaller scale of the vault-scale models facilitated a larger number of simulations to address these issues.

The following section of this review gives an assessment of the relationships among the hydrogeological models for these different scales, including the linkage of boundary conditions and effective properties for the bedrock and disposal rooms (vaults). Key questions are whether the transfer of effective hydraulic parameters and boundary conditions between models for the different scales (regional-scale, repository-scale, and vault-scale) is appropriate, and whether consistency between these different scales is adequately maintained.

2.5.1. Parameterization of rock vaults

The parameterization of rock vaults in the DarcyTools regional-scale model is described by Odén et al. (2014, Section 3.3.4, R-13-25), who state that hydraulic conductivity values for tunnel plugs and silo barriers are taken from the intact plug case (Initial state report). A detailed representation is used for the silo, as shown in Figure 2.12. For the other vaults, the hydraulic conductivity is set to 10^{-5} m/s. The same value of 10^{-5} m/s is used to represent the backfilled sections of tunnels and ramps (other than those sections which are defined as plugs).
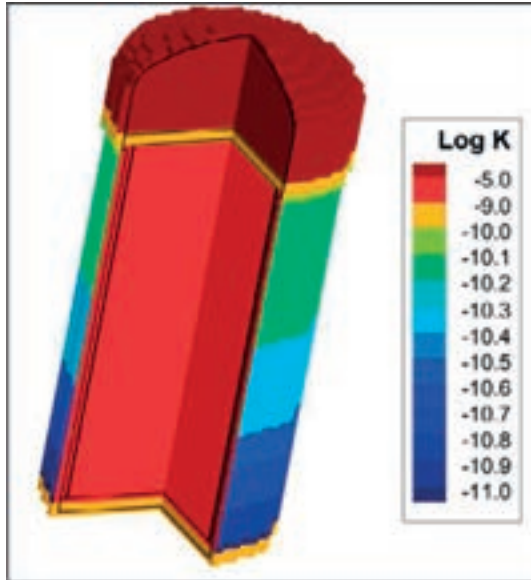
Figure 2.12: Parameterization of the silo in the regional-scale model. The vertical walls of the silo are represented with a single cell layer. From Oden et al (2014, Figure 3-9).

The representation of rock vaults and other underground openings in the COMSOL repository-scale models is detailed by Abarca et al. (2013, TR 13-08 Section 3.5). Table 2.5 compares the values of hydraulic conductivity for specific components in these model with those of the DarcyTools regional-scale model. The same values as used in the repository-scale model are also used in the base-case versions of the vault-scale models according to Tables 3-1 and 3-2 of Abarca et al. (2014).

The representation of the silo in the repository-scale model of SFR 1 (Figure 2.13) conforms closely to that in the regional-scale model. The parameterizations of the silo's bentonite walls and the top and bottom exterior layers also are in close agreement (Table 2.5). The waste in the silo interior is assigned a higher value of hydraulic conductivity in the repository-scale model, by more than two orders of magnitude. No explanation for this discrepancy was found in the course of this review. The concrete lid is treated as anisotropic in the repository-scale model, with a vertical component of hydraulic conductivity just 0.03 times the isotropic value used in the regional-scale model.
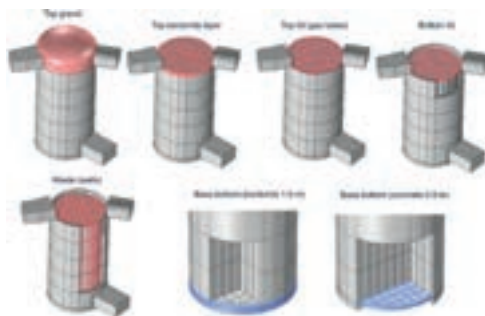

Figure 2.13: Representation of the silo in the repository-scale model. From Abarca et al (2013, Figure 3-6).

Table 2.5: Comparison of hydraulic conductivity values used in the regional-scale and repository-scale models for SR-PSU. Values for the regional-scale model (DarcyTools) are taken from Table 3-2 of Odén (2014) and accompanying text. Values for the repository-scale (COMSOL) model components are taken from Tables 3-3 and 3-4 of Abarca et al. (2013).

Regional-scale model		Repository-scale and vault-scale models		
Component	Hydraulic conductivity	Component		Hydraulic conductivity
SFR 1				
		Concrete backfill		$8.3 \cdot 10^{-9}$ m/s
1-2BTF	$1 \cdot 10^{-5}$ m/s	Waste (*)	K_x	$3.79 \cdot 10^{-9}$ m/s
			K_y	$6.65 \cdot 10^{-9}$ m/s
			K_z	$6.79 \cdot 10^{-9}$ m/s
1BLA	$1 \cdot 10^{-5}$ m/s	Waste		$1.0 \cdot 10^{-3}$ m/s
1BMA	$1 \cdot 10^{-5}$ m/s	Waste		$8.3 \cdot 10^{-7}$ m/s
		Sand layer		$1.0 \cdot 10^{-7}$ m/s
Silo interior	$5 \cdot 10^{-9}$ m/s	Waste		$8.3 \cdot 10^{-7}$ m/s
Ramp	$1 \cdot 10^{-5}$ m/s	Tunnel backfill		$1.0 \cdot 10^{-3}$ m/s
Silo exterior (lid)	$1 \cdot 10^{-5}$ m/s	Concrete lid with gas evacuation pipes	K_x, K_y	$8.3 \cdot 10^{-10}$ m/s
			K_z	$3.0 \cdot 10^{-7}$ m/s
Silo exterior	$1 \cdot 10^{-9}$ m/s	Top & bottom layers		$1.0 \cdot 10^{-9}$ m/s
Silo walls	$2.1 \cdot 10^{-10}$ m/s + $1.6 \cdot 10^{-12}$ s^{-1} z	Silo bentonite walls		$2.11 \cdot 10^{-10}$ m/s + $1.54 \cdot 10^{-12}$ s^{-1} z
Tunnels	$1.0 \cdot 10^{-5}$ m/s	Tunnels		$1.0 \cdot 10^{-3}$ m/s
SFR 3				
2BLA 3BLA 4BLA 5 BLA	$1 \cdot 10^{-5}$ m/s	Concrete Backfill		$8.3 \cdot 10^{-10}$ m/s $1.0 \cdot 10^{-3}$ m/s
2BMA	$1 \cdot 10^{-5}$ m/s	Waste		$8.3 \cdot 10^{-9}$ m/s
		Sand layer		$1.0 \cdot 10^{-7}$ m/s
		Gravel layer		$1.0 \cdot 10^{-3}$ m/s
1BRT	$1 \cdot 10^{-5}$ m/s	Grouted waste		$8.3 \cdot 10^{-9}$ m/s
Ramp	$1 \cdot 10^{-5}$ m/s			
Mechanical plug	$1 \cdot 10^{-6}$ m/s	Structural plug		$1 \cdot 10^{-6}$ m/s
Bentonite plugs in access tunnels	$1 \cdot 10^{-10}$ m/s	Sealed hydraulic bentonite section		$1 \cdot 10^{-12}$ m/s
Filter material	$1 \cdot 10^{-6}$ m/s			
Bentonite plugs in ramp	$5 \cdot 10^{-10}$ m/s			

* Homogenized values calculated with formulation of Holmén and Stigsson (2001) based on vault dimensions, configuration, and waste and concrete properties.

The net effect of these differences on flows in the vertical direction through the silo can be estimated by the effective hydraulic conductivity for these layers in series, calculated from:

$$K_{z,eff} = \frac{\sum h_i}{\sum \left(\frac{h_i}{K_i}\right)}$$

where h_i is the thickness of the ith layer and K_i is its hydraulic conductivity in the vertical direction. Using this equation with thicknesses of 0.9 m and 1.0 m for the bottom and top layers respectively, a height of 51.9 m for the waste, and 15 m for the average cap thickness (based on Figure 4-16 of the Main Report) in combination with the hydraulic conductivity values in Table 2.5 yields $K_{z,eff} = 5.6 \cdot 10^{-9}$ for the regional-scale model and $K_{z,eff} = 3.4 \cdot 10^{-8}$ m/s for the repository-scale model. Thus the representation of the silo in the repository-scale model is about 6 times as hydraulically conductive as that in the regional-scale model, for vertical flow through the silo.

The effective hydraulic conductivity through the silo in the horizontal direction is also greater for the repository-scale model than for the regional-scale model, because of the contrast in the waste domain while the vertical walls have consistent properties.

The 1BLA vault has the simplest representation in the repository-scale model (see Figure 2.14), as no flow barriers are considered to be present in this vault. A single value of hydraulic conductivity, equal to that of the backfill material ($1 \cdot 10^{-3}$ m/s), is assigned for the whole waste domain. This is two orders of magnitude higher than the value of $1 \cdot 10^{-5}$ m/s used for the 1BLA vault in the regional-scale model.
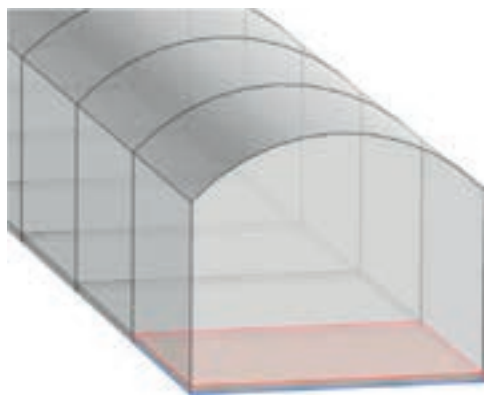

Figure 2.14: Representation of the 1BLA vault in the repository-scale model. From Abarca et al (2013, Figure 3-8).

For the 1BTF and 2 BTF vaults in SFR 1 (Figure 2.15), the waste domain includes longitudinal and transverse concrete walls that are not geometrically discretized in the repository-scale model. Abarca et al. (2013) used homogenized values of the hydraulic conductivities along the tunnel and perpendicular to the tunnels for the 1-2BTF waste domain, based on a homogenization formula proposed by Holmén and Stigsson (2001), in combination with an assumption that the hydraulic conductivity for the concrete backfill in the space between the waste and the rock walls is:

$$K_{grout} = 10 \cdot K_{concrete} \text{ with the constraint } K_{grout} \leq 10^{-3} \text{ m/s}$$

while the hydraulic conductivity of the waste is assumed to be:

$$K_{waste} = 1000 \cdot K_{concrete} \text{ with the constraint } K_{waste} \leq 10^{-3} \text{ m/s}$$

These formulae are used both for cases in which concrete is considered to be intact and when the concrete is degraded. According to Abarca et al. (2013), the upper limit for the hydraulic conductivity of the concrete backfill and waste of 10^{-3} m/s is to ensure that no hydraulic contrast exists in a vault when the concrete is completely degraded.

The resulting values of hydraulic conductivity for the repository-scale model representation of the 1-2BTF vaults, as seen in Table 2.5, are generally less than 10^{-8} m/s, which is three orders of magnitude less than the value used in the regional-scale model.
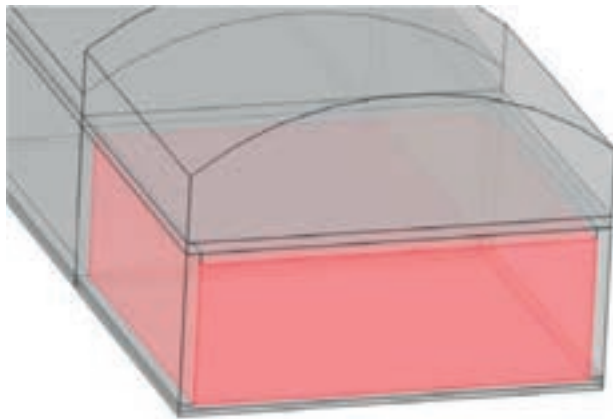

Figure 2.15: Representation of the 1BTF and 2BTF vaults (right) in the repository-scale model. The waste in the front section is represented by the pink-shaded volume. From Abarca et al (2013, Figure 3-7).

The 1BMA vault also has a more detailed representation in the repository-scale model, as shown in Figure 2.16. The hydraulic conductivity of the waste is again assumed to be:

$$K_{waste} = 1000 \cdot K_{concrete} \text{ with the constraint } K_{waste} \leq 10^{-3} \text{ m/s}$$

with the same upper limit to ensure that no hydraulic contrast exists in a vault when the concrete is completely degraded. The resulting values of hydraulic conductivity for the components of the 1BMA in the initial state for the repository-scale model are on the order of 10^{-7} m/s, which is two orders of magnitude less than the value used in the regional-scale model.

In SFR 3, the 2BMA vault is modeled with similar properties as for the 1BMA vault but with an additional high-conductivity gravel-layer at the base. Thus the contrast in effective hydraulic conductivity between the two models for the 2BMA vault should be slightly less than for the 1BMA vault.

For the 2-5BLA vaults in SFR 3, the backfill properties in both models are the same as for the 1BLA, so the contrast in effective hydraulic conductivity will be similar.
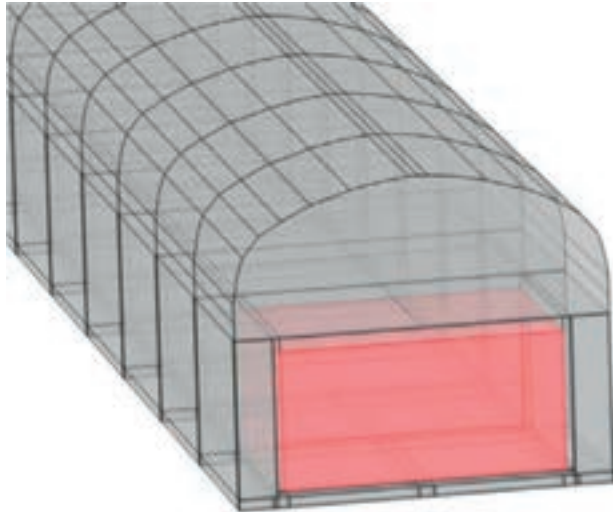
Figure 2.16: Representation of the 1BMA vault in the repository-scale model. The waste in the front section is represented by the pink-shaded volume From Abarca et al (2013, Figure 3-5).

2.5.2. Boundary conditions and couplings

Boundary conditions in regional-scale model

Boundary conditions for the regional-scale model using DarcyTools are summarized in Section 3.3 of Odén et al. (2014).

Specified-pressure boundary conditions are imposed at the upper surface of the model. For periods of periglacial conditions, this pressure is based on an assumption that the groundwater table is very close to the ground surface, due to the effects of permafrost. For periods of temperate climate conditions, the prescribed pressures for areas above the Baltic shoreline are calculated by a preliminary "recharge-phase" calculation.

As described by Öhman et al. (2014), the recharge-phase calculation uses a mixed flux and pressure surface condition which allows representation of unsaturated areas while also constraining the hydraulic heads so that they do not exceed the height of the topography (or of the surrounding topography, for local basins). An automated, iterative approach is used to adjust local recharge values until the excess-had errors converge to a level that is judged to be irreducible due to errors in the dynamic landscape model (RLDM) and mapping from the RLDM to the DarcyTools grid (SBKdoc 1395214 p. 47).

Allowing unsaturated conditions is especially important for a realistic representation of the effects of the SFR pier and islets east of the pier. In previous modelling of the SFR site (Holmén and Stigsson, 2001a,b) it was evident that treating the SFR pier as saturated resulted in unrealistic flow circulation patterns at the depth of the SFR.

The lateral boundaries of the model domain are chosen to coincide with topographical water divides for both present and future flow situations. The vertical sides are assigned no-flow boundary conditions. The bottom of the model is also assigned a no-flow boundary condition.

Taken together, as noted by Odén et al. (2014) these boundary conditions for the vertical sides and bottom mean that recharge, discharge and flows within the model are completely governed by climate-related processes prevailing on the top surface. This implies an assumption that there is no significant regional component of groundwater flow across the vertical boundaries, or regional discharge upward through the base of the model.

In connection with its high-level radioactive-waste disposal programme, SKB has sponsored other work that is relevant to evaluation of this assumption, namely a larger-scale regional model of northern Uppland (Holmén et al., 2003) and a more generalized evaluation and synthesis of modelling results for regional groundwater flow patterns (SKB, 2003). These studies concluded that local topography is a dominating factor in determining flow at depth, in the Swedish terrain and for the typical ratios of recharge to bedrock hydraulic conductivity.

As noted in a previous review of that work (SKI/INSITE memorandum 21 September 2004), the models used in those studies did not represent several commonly-observed characteristics of the bedrock in northern Uppland, including:

- Anisotropy and elevated hydraulic conductivity in the shallow (< 100 m deep) bedrock;
- Conductive subhorizontal fracture zones; and
- Tendency for recharge to be focused along low-topography areas that are correlated to fracture zones, with limited and seasonally-dependent recharge on elevated areas between these fracture zones.

However given the relatively shallow depth of the SFR in relation to the horizontal scale of the regional-scale model for SR-PSU, the consequences of regional flow passing under surface-water divides are likely to be minor.

Transfer of boundary conditions to repository-scale models

The use of the regional-scale flow model to prescribe boundary conditions for the repository-scale models for SFR 1 and SFR 3 is described in Section 4.2.1 of Abarca et al. (2013). Values of pressure calculated by the regional-scale model are extracted for points along the boundary of the repository-scale models, and then used as prescribed-pressure boundary conditions in the latter models. The equivalent hydraulic conductivity field for the bedrock as calculated by DarcyTools is also transferred to the COMSOL implementation of the repository-scale models. Thus the pressure field should be consistent with the bedrock hydraulic conductivity field, for each case considered.

The interface between the two codes is described in Sections 2.2.3 and 3.6 of Abarca et al. (2013). According to this, values of hydraulic conductivity from the grid used in DarcyTools are transferred by "a linear interpolation method" to the grid points in the discretizations for the repository-scale models.

As discussed in Section 2.3, the use of linear interpolation to assign hydraulic conductivities from DarcyTools to the COMSOL repository-scale models may have produced an upward bias in hydraulic conductivities, so that the repository-model has somewhat more extensive volumes of hydraulic conductivity $K > 10^{-7}$ m/s. This upward bias in the K field may account for systematically higher flows through the COMSOL model domain, by as much as 15% to 25% based on a benchmark comparison. The effect on safety assessment calculations is likely to be conservative

as slightly higher flows through the bedrock in the repository-scale models will lead to slightly faster advective transport of radionuclide.

Transfer of boundary conditions to vault-scale models

The vault-scale models using COMSOL (Abarca et al., 2014) are defined for volumes as shown in Figure 2.17.

The boundary conditions for each submodel are extracted in the form of pressure values extracted from the results of the base case of the repository-scale models for three different shoreline positions, as documented by Abarca et al. (2013). Pressures are extracted from the regional model along a set of planes that contain all facets of the vault-scale model boundaries, and then assigned to those facets.

The hydraulic conductivity for the bedrock portion of each vault-scale model is transferred directly from the regional-scale (DarcyTools) model. Linear interpolation is used to assign values to the vault-scale grids, as was done for the repository-scale models but in this case to a finer-scale grid.

Thus there can be differences in local values of bedrock hydraulic conductivity, compared with the repository-scale model from which the pressures used as boundary conditions were extracted. The use of linear interpolation to a finer-scale grid likely results in locally more smooth variations of the hydraulic conductivity field in the vault-scale models, compared to the repository-scale models.
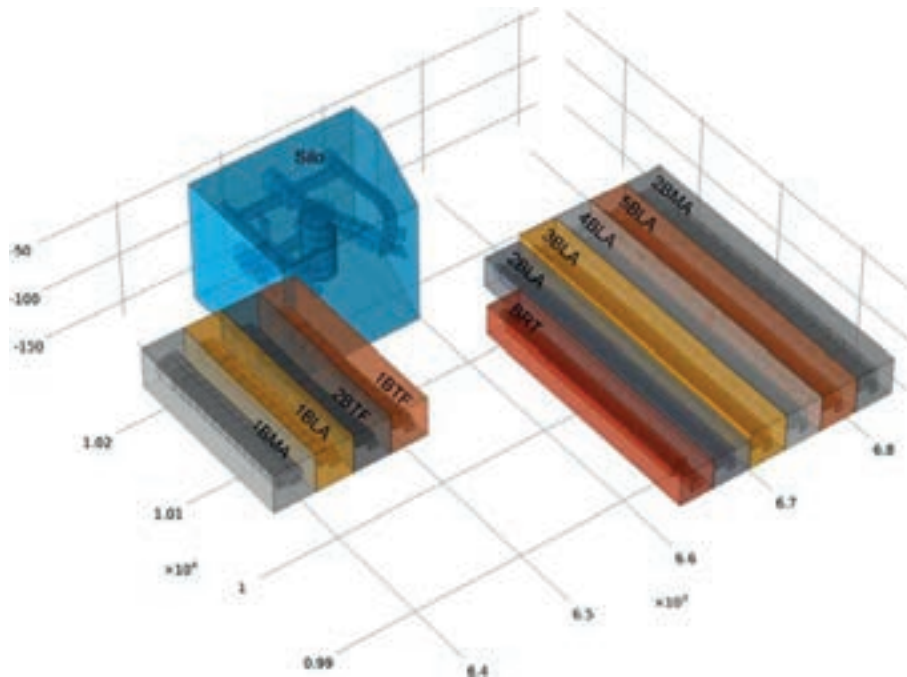
Figure 2.17: Subdomains treated with vault-scale models. From Abarca et al (2014, Figure 3-2).

A comparison of flowrates between the vault-scale models and the repository-scale models is described in Section 3.3 of Abarca et al. (2014). The flowrates calculated by the vault-scale models are listed in Table 2.6 along with the flowrates for the corresponding vaults in the regional-scale and repository-scale models as reported by Abarca et al. (2013).

In Table 2.6, percentages for comparing models were calculated directly from the flowrates listed here. The percentages listed in Table 4-3 of Abarca et al. (2013) for repository- vs. regional-scale models were not consistent with the reported flowrates in the case of Shoreline position 1, although the percentages for the other two shoreline positions were correct as verified here.

The percentages listed in Table 3-5 of Abarca et al. (2014) for comparing the vault-scale vs. repository-scale models could not be reconciled with the percentages that were calculated directly from the flowrates listed in Table 2.6. Perhaps the comparison of vault-scale vs. regional-scale models by Abarca et al. (2014) is based on a different calculation case of the repository-scale model for SFR 1 than the one used for the comparison of the repository-scale vs. regional-scale models by Abarca (2013). This possibility could not be checked directly as Table 3-5 of Abarca et al. (2013) does not list the repository-scale flowrates that were used for comparison.

According to Abarca et al., the flowrates calculated by the vault-scale models generally differ from the flowrates in the repository-scale model for SFR 1 by 26% or less. A separate comparison for the SFR 3 models produces much closer agreement (within 3%) for flows through the vaults. The general tendency is for lower flowrates in the vault-scale model relative to the repository-scale model.

Taken together, the differences in flowrates through the vaults calculated for different modeling scales as summarized in Table 2.6 indicate that the flowrates through vaults other than the silo and 2 BTF tend to be lower in the more detailed-scale models, and hence less conservative for predicting radionuclide fluxes. Part of this difference may be due to hydraulic properties for the vault backfill and waste components that conform more closely to the design specifications in the more detailed (COMSOL) models relative to the regional-scale (DarcyTools) model.

Table 2.6: Comparison of regional-scale, repository-scale and vault-scale models in terms of total flows through the SFR 1 vaults and the percentage difference in the total flows. Flowrates for comparing the repository-scale model to the regional-scale model are from Table 4-3 of Abarca et al. (2013). Flowrates for the vault-scale models are from Table 3-5 of Abarca et al. (2014). Q_{reg} = flow through vault calculated by regional-scale model; Q_{repo} = flow through vault calculated by repository-scale model; Qvs = flow through vault calculated by vault-scale model.

Shore line posi- tion	Vault	Q_{reg} m³/yr	Q_{repo} m³/yr	Q_{vs} m³/yr	Increase in repository- scale model vs regional- scale model	Flow increase in vault-scale model relative to repository- scale model	
						From Abarca et al. (2014)	Calcu- lated (2)
1	1BMA	0.05	0.04	0.041	–20%	–9.7%	–3%
	1BLA	0.14	0.13	0.126	–7%	–5.2%	–3%
	1BTF	0.04	0.03	0.027	–25%	–2.8%	–10%
	2BTF	0.07	0.05	0.048	–29%	1.8%	–4%
	Silo	0.0012	0.0017	0.004	42%	–8.4%	135%
	Total	0.30	0.25	0.246	–17%		–2%
2	1BMA	51.92	31.39	28.85	–40%	–5.1%	–8%
	1BLA	89.52	76.23	63.26	–15%	–3.0%	–17%
	1BTF	14.82	11.60	7.27	–22%	–6.9%	–37%
	2BTF	23.86	27.61	19.45	16%	–2.2%	–30%
	Silo	0.40	0.53	0.62	33%	–16.3%	17%
	Total	180.52	147.35	93.44	–18%		–19%
3	1BMA	99.61	69.39	62.35	–30%	–6.3%	–10%
	1BLA	187.26	162.83	143.32	–13%	–2.4%	–12%
	1BTF	36.19	28.83	16.43	–20%	–8.5%	–43%
	2BTF	52.41	62.65	40.29	20%	–7.3%	–36%
	Silo	1.45	1.99	1.16	37%	–26.3%	–42%
	Total	376.92	325.68	263.55	–14%		–19%

(1) Percentage calculated as $(Q_{repo} – Q_{reg})/Q_{repo}$; (2) Percentage calculated as $(Q_{vs} – Q_{repo})/Q_{rvs}$.

2.5.3. Main findings concerning parameterization and couplings

The regional-scale (DarcyTools) model has inconsistencies with the repository-scale and vault-scale (COMSOL) models in terms of:

- Effective hydraulic conductivities of the backfilled rock vaults, and
- Local hydraulic conductivity of the bedrock.

The first of these inconsistencies results from differences in parameterizations of the waste and backfill components for the vaults. The second inconsistency results from linear interpolation of hydraulic conductivity values that span orders of magnitude, in mapping these from the DarcyTools grid to the COMSOL grids for the more detailed-scale models. As the COMSOL models for the vault scale use different, finer grid geometries than those for the repository scale, the bedrock hydraulic conductivity fields also differ between these two modelling scales, with presumably a more smooth variation in the vault-scale models.

The resulting differences can be summarized as follows:

- Silo: The net effective hydraulic conductivities in both the vertical and horizontal directions through the silo are **higher** in the detailed-scale models than in the regional-scale model. For the vertical direction, the contrast is about a factor of six.
- 1-5BLA: The hydraulic conductivity is two orders of magnitude **higher** in the detailed-scale models than in the regional-scale model.
- 1-2BTF: The hydraulic conductivity is three orders of magnitude **lower** in the detailed-scale models than in the regional-scale model.
- 1BMA: The hydraulic conductivity is two orders of magnitude **lower** in the detailed-scale models than in the regional-scale model.
- 2BMA: The contrast in effective hydraulic conductivity should be slightly less than for the 1BMA vault due to the addition of a high-permeable layer of gravel.
- Bedrock: Overall effective hydraulic conductivity is **slightly higher** (by about 15% to 25% based on total flux through the repository-scale model domains) in the detailed-scale models than in the regional-scale model.

The contrasts in vault properties imply that for a given pressure gradient, the detailed-scale models can be expected to produce higher flows through the silo and all five of the BLA vaults, but lower flows through the BTF and BMA vaults. Conversely the pressure gradients calculated using the regional-scale model and applied to the repository-scale models may be too low across the silo and all five of the BLA vaults, but too high across the BTF and BMA vaults.

Based on the benchmark comparisons by Abarca et al. (2013 & 2014) the net effect of these differences is that the flowrates through vaults other than the silo and 2 BTF tend to be lower in the more detailed-scale models, and hence less conservative for predicting radionuclide fluxes from the vaults. Differences are typically on the order of 10% to 40% depending on the vault and time step considered.

The slightly higher bedrock conductivity would make groundwater velocities calculated from the repository-scale models slightly more conservative than those from the regional-scale model, by a factor of 15% to 25%.

The boundary conditions considered for the regional-scale model exclude the possibility of regional flow across surface-water divides, but can be regarded as appropriate given the relatively shallow depth of the SFR in relation to the horizontal scale of the regional-scale model. The treatment of the SFR pier and small islets near the SFR has been improved relative to previous modelling by allowing these to be unsaturated.

Boundary conditions are transferred both from the regional-scale model to the repository-scale models, and from the repository-scale models to the vault-scale, in terms of groundwater pressures. The methodology for doing this is appropriate, but inconsistencies in the hydraulic conductivity fields between each pair of modelling scales may introduce errors. This implies that additional uncertainty should be attached to fluxes and groundwater velocities estimated from this chain of models, on the order of the observed differences in groundwater flowrates between scales (i.e. on the order of a few tens of percent).

2.6. Agreement of flows in vaults for SAFE vs. SR-PSU

The aim of this section is to assess whether results from the hydrogeological analysis for SKB's previous SAFE project and safety assessment (SAR-08) agree with the results of SR-PSU in terms of flows in the vaults. This is motivated by the fact that some of the hydrochemical analysis in the near-field for SR-PSU is based on results from SAR-08.

The hydrogeological model used for SAR-08 (Holmén and Stigsson, 2001a) was based on an earlier structural geological model with fewer structures and homogeneous hydraulic conductivity, and was calibrated to 1997 data for inflows to SFR 1, which were 64% higher than the 2010 data used in the site descriptive model for SR-PSU (SKB, 2013).

As discussed by Odén et al. (2014, p. 46), the hydrogeological model of Holmén and Stigsson (2001a) also made an effort to represent "excess heads," based on transformations of pressure measurements made in boreholes drilled prior to construction of SFR 1, which indicated that the groundwater levels in the shallow bedrock could be higher than mean sea water level. In SR-PSU these excess heads were discounted based on an evaluation by Carlsson et al. (1987) who concluded that these were highly uncertain due to poor measurement and evaluation techniques, and that the reported excess head was too high or probably non-existent.

The flows through vaults predicted by the hydrogeological models for the two different safety assessments are compared in Table 2.7, based on the presentation of Odén et al. (2014). From this tabulation, the flows for nominally present-day conditions (2000 AD) are significantly higher in the model for SAR 08, by roughly two orders of magnitude for all of the vaults.

At 3000 AD, the flows through vaults predicted by the SR-PSU regional-scale model are within a factor of two of those predicted by the SAR 08 model, with no systematic difference. The exception is the Silo for which the SR-PSU flows are predicted to be almost an order of magnitude less than the SAR 08 flows. However the Silo accounts for only a small fraction of the total flow through the facility. The sum of flows through all vaults is in agreement between the two models, within 0.4%.

At 5000 AD, the flows through vaults as predicted by the SR-PSU regional-scale model are generally higher than those predicted by the SAR 08 model, except for the Silo for which the SR-PSU prediction of flow is only 28% of that predicted for SAR 08. For the 1-2BTF vaults the differences are minimal, but for 1BLA and 1BMA the flows predicted for SR-PSU are roughly twice as high as those for SAR 08.

Odén et al. (2014) suggest that the large differences between the two models at 2000 AD are mainly an artefact of the effort by Holmén and Stigsson (2001a) to represent excess heads, which have been discounted in the models for SR-PSU. The influence of excess heads was predicted by Holmén and Stigsson (2001a) to decrease with time, and to have only minor influence on flows after 3000 AD.

This is plausible as an explanation for the very large differences at 2000 AD, but does not explain the smaller but potentially significant differences (by a factor of 0.28 to 2) for flows at 5000 AD. These differences at later times might be a consequence of attributing a larger part of the present-day flows used for calibration, in SAR 08, to the dynamic response of the model of Holmén and Stigsson (2001a).

As a more general issue, the uncertainties related to time-dependent flow field evolution are not well understood. SR-PSU has used estimates of resaturation times based on the model of Holmén and Stigsson (2001a). If the flows for present-day circumstances were overestimated by this model by up to two orders of magnitude due to an erroneous interpretation of excess heads, this implies that the resaturation times predicted by that model – which have been used in other aspects of SR-PSU – are likely to be much too short.

Table 2.7: Comparisons of flows (in m^3/year) through vaults in SFR 1 calculated for SR-PSU using the regional-scale model versus flows through vaults reported in SAR-08 at three points in time. Based on Table 4-8 of Odén et al. (2014).

Vault	2000 AD		3000 AD		5000 AD	
	SAR-08	SR-PSU	SAR-08	SR-PSU	SAR-08	SR-PSU
1BTF	13	0.07	38	20.51	43	44.60
2BTF	12	0.07	33	22.35	41	47.81
1BLA	15	0.12	42	63.64	61	130.96
1BMA	4.8	0.09	50	57.86	65	112.56
Silo	0.6	0.0016	2.3	0.32	3.9	1.11
Total	45.4	0.35	165.3	164.68	213.9	337.04

3. Main Review Findings

The main review findings are summarized here in terms of the review topics covered in the preceding chapter.

3.1. Uncertainties in the DFN and SBA models

The following is a summary of key uncertainties in the DFN and SBA models, and their likely impacts based on how the models are used in the safety assessment. A qualitative assessment is given of the priority for further review.

Vertical hydraulic connection to the sea

The role of seabed sediments in controlling the vertical hydraulic connection to the sea is a major conceptual and parametric uncertainty, affecting model calculations of inflows to the existing facility and the proposed extension. In addition to the use of calculated inflows in the safety assessment, comparisons of these calculated inflows with measured inflows have been used to evaluate the relative performance of hydrogeological model variants (Öhman et al., 2013). Hence the uncertainty regarding seabed sediments may have also influenced the selection of variants regarding other components of the system. This is potentially an important part of site understanding that has not been convincingly addressed. SSM has asked for complementary information regarding the connection to the sea (SSM2015-725-40 Point 4).
Priority: High.

Extension of ZFM871

An alternative model of the extension of ZFM871 was considered as part of a sensitivity study (SKBdoc 1395214). For most vaults the effects of an alternative interpretation of ZFM871 are minor. The strongest effect is for 1BLA for which an increase of about 30% in flow is seen.
Priority: Low.

Uncharacterized gently dipping structures

The potential existence of uncharacterized gently dipping structures may not be significant for release paths, as argued by SKB. However for ongoing review it should be considered whether these structures could be important for geochemical stability (e.g. saline upconing).
Priority: Medium.

Alternative conceptual models for ZFM structures

This uncertainty has not been directly addressed by SKB, but it is not likely to be significant for releases to biosphere. Treating ZFMs as distinct transmissive zones is likely conservative compared to treating them as more diffuse fracture networks.
Priority: Low.

Uncertainty in DFN model due to lack of PSS measurements

The possibility of unresolved compartmentalized fracture transmissivity, due to lack of PSS (pipe-string system) measurements to complement PFL-f measurements, has apparently not been addressed in SR-PSU. Packer data from older data set may be relevant to analyse even if of poorer quality, and from a different domain. Compartmentalized fracture transmissivity is unlikely to have a strong effect on estimation of bulk flows through the waste storage vaults, but it could be significant for estimates of flow-connected porosity along radionuclide release paths through the bedrock.

Priority: Medium

Hydrogeological properties and extent of Shallow Bedrock Aquifer

The consequences of the lack of analysis of SBA variants in SR-PSU are difficult to assess due to the complicated dependence on details of geometry, properties, and hydraulic connections to other structures. Calculations using simplified models may be needed to scope the potential consequences.

Priority: High

Hydrogeological properties and lateral extension of unresolved PDZs

Unresolved PDZs have been treated by three stochastic realizations of geometry and properties which are linked to the corresponding HRD realizations. Selection of these three realizations is linked to the ad hoc selection of HRD realizations. In the three realizations used for analysis, none of the PDZs connect to the waste storage vaults. Therefore scoping calculations of their potential impact are still needed.

Priority: High

Uncertainty in transmissivity values of deformation zone intercepts based on older data

None of the HCD variants evaluated in SR-PSU appears to account for the possibility that the transmissivities implied by the old data set could have been accurate. Therefore scoping calculations should consider these older transmissivity values in bounding the consequences of uncertainty in HCD properties.

Priority: High

3.2. Selection of realizations for the bedrock model

The three bedrock cases that were used as the basis for flow modelling do not necessarily bound the uncertainties in bedrock properties that affect the dose and risk calculations. Conceptual uncertainty in the DFN model of the HRD, as reflected by two different statistical descriptions ("connectivity-analysis" and "tectonic-continuum" models) has not been evaluated. The selection of HRD realizations was based only on the geometry and net (summed) transmissivity of fractures that directly intersect the underground facility, without accounting for network flow effects. In terms of the net transmissivity of intersecting fractures, the "pessimistic" case R85 is not especially distinct from many other realizations that were propagated, and which could well produce higher cross flows depending on network effects. Effects of alternative SBA representations in combination with HRD realizations also were not evaluated.

Therefore scoping calculations are warranted to establish more conservative bounds on the uncertainties that affect the dose and risk calculations, considering plausible parametric variants in combination with different HCD and SBA models.

3.3. Upscaling from DFN to ECPM representation

The upscaling from the DFN model to an ECPM representation using DarcyTools produced results that appear to be consistent with what should be expected from the geometrical upscaling algorithm that is used. The comparison to upscaled properties developed in this review however is mainly limited to graphical comparisons and comparison of bulk properties which include HCDs in the volumetric averages. A more direct comparison based on the hydraulic conductivity datasets as referenced in Section 4.17 of the Input Data report (TR 14-12, AMF Number 84) is therefore recommended.

The use of linear interpolation to assign hydraulic conductivities from DarcyTools to the COMSOL repository-scale models appears to have produced an upward bias in hydraulic conductivities. This upward bias in the K field may account at least in part for systematically higher total flows through the COMSOL model domain for SFR 1 that were obtained in a benchmark comparison between DarcyTools and COMSOL. However the magnitude of the difference as reported by Abarca et al. (2013, Table 4-2) is only 15% to 25%. The effect on safety assessment calculations is likely to be conservative as slightly higher flows through the bedrock in the repository-scale models will lead to slightly more rapid advective transport of radionuclides.

This review has not quantitatively addressed the potential errors introduced by the geometrical upscaling algorithm in DarcyTools, in comparison with an upscaling method that explicitly takes into account network effects. The DarcyTools approach is likely to be conservative in terms of overall flows, but it may also underestimate the heterogeneity of bedrock hydraulic conductivity. This means that the hydrogeological simulations may not adequately account for the possibility of higher flows being focused through some particular portion of the SFR. Hence it is recommended that scoping calculations should be carried out to assess the potential consequences of significantly higher flows through one or more particular vaults.

3.4. Treatment of high flow in the bedrock

SKB has not considered enough realizations of the DFN model for the HRD, or the main alternative parameterization of that model, or its combinations with alternative representations of HCDs and the SBA, to establish the probabilities and range of high flow. Scoping calculations as discussed in connection with the selection of bedrock calculation cases would help to establish more conservative bounds.

The potential interaction of engineered-barrier system (EBS) flow properties with properties of the HRD, as represented by DFN and ECPM models, has not been considered in this review. This topic would require an interdisciplinary approach to account for both hydrogeological processes and EBS processes.

3.5. Parameterization and couplings

The regional-scale (DarcyTools) model has inconsistencies with the repository-scale and vault-scale (COMSOL) models in terms of:

- Effective hydraulic conductivities of the backfilled rock vaults, and
- Local hydraulic conductivity of the bedrock.

There are also inconsistencies in the bedrock hydraulic conductivity fields between the repository-scale and vault-scale models, with presumably a more smooth variation in the vault-scale models.

The resulting differences can be summarized as follows:

- Silo: The net effective hydraulic conductivities in both the vertical and horizontal directions through the silo are **higher** in the detailed-scale models than in the regional-scale model. For the vertical direction, the contrast is about a factor of six.
- 1-5BLA: The hydraulic conductivity is two orders of magnitude **higher** in the detailed-scale models than in the regional-scale model.
- 1-2BTF: The hydraulic conductivity is three orders of magnitude **lower** in the detailed-scale models than in the regional-scale model.
- 1BMA: The hydraulic conductivity is two orders of magnitude **lower** in the detailed-scale models than in the regional-scale model.
- 2BMA: The contrast in effective hydraulic conductivity should be slightly less than for the 1BMA vault due to the addition of a high-permeable layer of gravel.
- Bedrock: Overall effective hydraulic conductivity is **slightly higher** (by about 15% to 25% based on total flux through the repository-scale model domains) in the detailed-scale models than in the regional-scale model.

Based on the benchmark comparisons by Abarca et al. (2013 & 2014) the net effect of these differences is that the flowrates through vaults other than the silo and 2 BTF tend to be lower in the more detailed-scale models, and hence less conservative for predicting radionuclide fluxes from the vaults. Differences are typically on the order of 10% to 40% depending on the vault and time step considered.

The slightly higher bedrock conductivity would make groundwater velocities

calculated from the repository-scale models slightly more conservative than those from the regional-scale model, by a factor of 15% to 25%.

The boundary conditions considered for the regional-scale model exclude the possibility of regional flow across surface-water divides, but can be regarded as appropriate given the relatively shallow depth of the SFR in relation to the horizontal scale of the regional-scale model. The treatment of the SFR pier and small islets near the SFR has been improved relative to previous modelling by allowing these to be unsaturated.

The methodology for transferring boundary conditions as prescribed pressures between the different modeling scales is appropriate. However inconsistencies in the hydraulic conductivity fields between each pair of modelling scales may introduce errors. This implies that additional uncertainty should be attached to fluxes and groundwater velocities estimated from this chain of models, on the order of the observed differences in groundwater flowrates between scales (i.e. on the order of a few tens of percent).

3.6. Agreement of flows for SAR 08 vs. SR-PSU

The flows for nominally present-day conditions are significantly higher in the model for SAR 08, by roughly two orders of magnitude for all of the vaults.

For conditions 1000 years after present, the flows through vaults predicted by the SR-PSU regional-scale model are within a factor of two of those predicted by the SAR 08 model, with no systematic difference. The exception is the Silo for which the SR-PSU flows are predicted to be almost an order of magnitude less than the SAR 08 flows. The sum of flows through all vaults is in close agreement between the two models, within 0.4%.

At 3000 years after present, the flows through vaults as predicted by the SR-PSU regional-scale model are generally higher than those predicted by the SAR 08 model, except for the Silo for which the SR-PSU prediction of flow is only 28% of that predicted for SAR 08. For the 1-2BTF vaults the differences are minimal, but for 1BLA and 1BMA the flows predicted for SR-PSU are roughly twice as high as those for SAR 08.

The large discrepancies in flows for present-day conditions are attributed by SKB to an effort in the SAR 08 hydrogeological modelling to account for interpretations of excess heads, which have been discounted in the models for SR-PSU. This is plausible as an explanation for the very large differences at present-day, but does not explain the smaller but potentially significant differences (by a factor of 0.28 to 2) for flows 3000 years in the future.

SKB's explanation of the discrepancy between these models in terms of flows for present-day conditions also implies that the resaturation times predicted by the SAR 08 model – which have been used in other aspects of SR-PSU – are likely to be much too short.

4. Recommendations

Based on the inventory of uncertainties in the DFN and SBA models, the following issues are identified as high priority for further review and analysis including scoping calculations with simplified models:

- Vertical hydraulic connection to the sea;
- Hydrogeological properties and extend of Shallow Bedrock Aquifer;
- Hydrogeological properties and lateral extension of unresolved PDZs; and
- Uncertainty in transmissivity values of deformation zone intercepts based on older data.

Uncertainties of lesser priority include:

- Uncertainty in DFN model due to lack of PSS measurements (mainly of concern for porosity calculations);
- Uncharacterized gently dipping structures (possibly of concern for geochemical stability).

Scoping calculations are recommended to address additional issues that have not been adequately addressed by SKB's analysis. These include:

- Residual uncertainty due to the selection of just three DFN realizations for propagation based mainly on geometric (rather than hydrogeological) analysis, and failure to analyse alternative parameterizations;
- Related limitations in the *high flow in the bedrock scenario* due to the likelihood that the "high flow in bedrock" case chosen for analysis is not strongly distinguished from mid-ensemble cases;
- Residual uncertainty due to lack of consideration of alternative representations or realizations of the SBA model;
- Uncharacterized gently dipping structures (possibly of concern for geochemical stability).
- Potential for higher flows in one or more vault due to limitations of the method for upscaling from the DFN to an ECPM representations;

For radionuclide transport calculations, additional uncertainty (on the order of a few tens of percent) should be attached to fluxes and groundwater velocities estimated from the chain of hydrogeological models, due to potential errors introduced by transferring boundary conditions from models with inconsistent hydraulic conductivity fields.

The potential interaction of engineered-barrier system (EBS) flow properties with properties of the HRD, as represented by DFN and ECPM models, has not been considered in this review. This topic would require an interdisciplinary approach to account for both hydrogeological processes and EBS processes.

Resaturation times used in SR-PSU, based on the hydrogeological model used for SAR 08, should be carefully re-evaluated. SKB's explanation of discrepancies between these models, in terms of flows for present-day conditions, also implies that the resaturation times predicted by the SAR 08 model are likely to be much too short.

5. References

Abarca, E., Idiart, A., de Vries, L.M., Silva, O., Molinero, J., and von Schenk, H., 2013. Flow modelling on the repository scale for the safety assessment SR-PSU. SKB TR-13-08, Svensk Kärnbränslehantering AB.

Abarca, E., Silva, O., Idiart, A., Nardi, A., Font, J., and Molinero, J., 2014. Flow and transport modelling on the vault scale. Supporting calculations for the safety assessment SR-PSU. SKB R-14-14, Svensk Kärnbränslehantering AB.

Carlsson, L., Winberg, A., and Grundfelt, B., 1987. Hydraulic modelling of the final repository for reactor waste (SFR). Evaluation of the groundwater flow situation at SFR. SKB SFR 86-07, Svensk Kärnbränslehantering AB.

Geier, J., 2008. Discrete Feature Model (DFM) user documentation. SKI Report 2008:57, Swedish Radiation Safety Authority, Stockholm

Geier, J., 2012. Hydrogeological modelling of the Forsmark site. SSM Technical Note 2012:67, Swedish Radiation Safety Authority, Stockholm.

Holmén, J.G., 2005. SFR-1 Inverse modelling of inflow to tunnels and propagation of estimated uncertainties to predictive stages. SKB Report 05-74, Swedish Nuclear Fuel and Waste Management Co., Stockholm.

Holmén, J.G., 2007. SFR inverse modelling Part 2: Uncertainty factors of predicted flow in deposition tunnels and uncertainty in distribution of flow paths from deposition tunnels. SKB Report R-07-61, Swedish Nuclear Fuel and Waste Management Co., Stockholm.

Holmén, J.G., and Stigsson, M., 2001a. Modelling of future hydrogeological conditions at SFR. SKB R-01-02, Swedish Nuclear Fuel & Waste Management Co., Stockholm.

Holmén J. and, Stigsson, M., 2001b. Details of predicted flow in deposition tunnels at SFR, Forsmark. SKB R-01-21, Swedish Nuclear Fuel & Waste Management Co., Stockholm.

Holmén, J.G., Stigsson, M., Marsic, N. and Gylling, B., 2003. Modelling of groundwater flow and flow paths for a large regional domain in northeast Uppland: A three-dimensional, mathematical modelling of groundwater flows and flow paths on a super-regional scale for different complexity levels of the flow domain. SKB R-03-24, Swedish Nuclear Fuel & Waste Management Co., Stockholm.

Oda, M., 1985. Permeability tensor for discontinuous rock masses. *Geotechnique*, Vol. 35, No. 4, p. 483-495.

Odén, M., Follin, S., Öhman, J., and Vidstrand, P., 2014. SR-PSU Bedrock hydrogeology. Groundwater flow modelling methodology, setup and results. SKB R-13-25, Svensk Kärnbränslehantering AB, Stockholm.

SKB, 2003. Grundvattnets regionala flödesmönster och sammansättning – betydelse för lokalisering av djupförvaret, SKB R-03-01, Svensk Kärnbränslehantering AB, Stockholm.

SKB, 2008. SDM-Site site description of Forsmark at completion of the site investigation phase, SDM-Site Forsmark. SKB R-08-05, Swedish Nuclear Fuel and Waste Management Co., Stockholm.

SKB, 2013. Site description of the SFR area at Forsmark at completion of the site investigation phase, SDM-PSU Forsmark. SKB TR-11-04, Svensk Kärnbränslehantering AB, Stockholm.

SKBdoc 1395200: TD05-Effects in ECPM translation. SKB Promemoria (PM) publication. Version 1.0, 2013-05-16. Svensk Kärnbränslehantering AB, Stockholm.

SKBdoc 1395214: TD08- SFR3 effect on the performance of the existing SFR1. SKB Promemoria (PM) publication. Version 2.0, 2013-05-16. Svensk Kärnbränslehantering AB, Stockholm.

Snow, D. T., 1969. Anisotropic Permeability of Fractured Media, Water Resources Research Vol. 5, No. 6, p. 1273–1289, doi:10.1029/WR005i006p01273.

Svensson, U., 2010. DarcyTools version 3.4. Verification, validation and demonstration. SKB R-10-71, Svensk Kärnbränslehantering AB, Stockholm.

Svensson, U., and Ferry, M., 2010. Darcy Tools version 3.4. User's Guide. SKB R-10-72, Svensk Kärnbränslehantering AB, Stockholm.

Svensson, U., Ferry, M., and Kuylenstierna, H-O., 2010. DarcyTools version 3.4 – Concepts, methods and equations. SKB R-07-38, Svensk Kärnbränslehantering AB, Stockholm.

Öhman, J., Bockgård, N., and Follin, S., 2012. Site investigation SFR. Bedrock hydrogeology. SKB R-11-03, Svensk Kärnbränslehantering AB, Stockholm.

Öhman, J., and Follin, S., 2010a. Site investigation SFR. Hydrogeological modelling of SFR. Data review and parameterisation of model version 0.1. SKB P-09-49, Svensk Kärnbränslehantering AB, Stockholm.

Öhman, J, and Follin, S., 2010b. Site investigation SFR. Hydrogeological modelling of SFR. Model version 0.2. SKB R-10-03, Svensk Kärnbränslehantering AB, Stockholm.

Öhman, J., Follin, S., and Odén, M., 2013. Site investigation SFR. Bedrock hydrogeology – Groundwater flow modelling. SKB R-11-10, Svensk Kärnbränslehantering AB, Stockholm.

Öhman, J., Follin, S., and Odén, M., 2014. SR-PSU Hydrogeological modelling TD11 – Temperate climate conditions. SKB P-14-04, Svensk Kärnbränslehantering AB, Stockholm.

Coverage of SKB reports

The following reports have been covered in the review.

Table A1:1

Reviewed report	Reviewed sections	Comments
SKB P-09-49. Site investigation SFR. Hydrogeological modelling of SFR. Data review and parameterisation of model version 0.1.	All	Background reference for hydrogeological site data and models.
SKB P-14-04. SR-PSU Hydrogeological modelling TD11 – Temperate climate conditions.	All	Details of regional-scale hydrogeological modelling.
SKB R-07-38. DarcyTools version 3.4 – Concepts, methods and equations.		Used as background information on upscaling methodology.
SKB R-10-03 Site investigation SFR. Hydrogeological modelling of SFR. Model version 0.2.	All	Background reference for hydrogeological site modelling.
SKB R-10-71. DarcyTools version 3.4. Verification, validation and demonstration.	Appendices on verification/validation cases	Used as background information on upscaling methodology.
SKB R-10-72. Darcy Tools version 3.4. User's Guide.		Used as background information on upscaling methodology.
SKB R-11-03. Site investigation SFR. Bedrock hydrogeology.	All	Background on hydrogeological site descriptive model and parameterization.
SKB R-11-10. Site investigation SFR. Bedrock hydrogeology – Groundwater flow modelling.	All	Background reference for hydrogeological site modelling.
SKB R-13-25. SR-PSU Bedrock hydrogeology. Groundwater flow modelling methodology, setup and results.	All	Primary focus of review.

SKB R-14-14. Flow and transport modelling on the vault scale. Supporting calculations for the safety assessment SR-PSU.	All	Focused on set-up of repository-scale models and comparison to regional-scale model.
SKB TR-11-04. Site description of the SFR area at Forsmark at completion of the site investigation phase, SDM-PSU Forsmark.	Sections on structural geology and hydrogeology.	Background information for review.
SKB TR-13-08. Flow modelling on the repository scale for the safety assessment SR-PSU.	All	Focused on set-up of vault-scale models and comparison to repository-scale models.
SKB TR-14-01. Safety analysis for SFR. Long-term safety. Main report for the safety assessment SR-PSU.	Focused on sections on hydrogeological modelling and construction of scenarios and calculation cases.	Main reference for SR-PSU.
SKBdoc 1395200: TD05-Effects in ECPM translation. SKB PM Version 1.0	All	
SKBdoc 1395214: TD08-SFR3 effect on the performance of the existing SFR1. SKB PM Version 2.0	All	

Author: Joel Geier[1]
                [1]Clearwater Hardrock Consulting, Corvallis, U.S.A.

Hydrogeological assessment and calculations to support the review of SR-PSU

Abstract

Simplified 1-D models are used to scope the potential significance of hydrogeological issues that were identified in initial stages of review of a safety assessment for a proposed extension of an underground facility for low- and intermediate-level radioactive waste at Forsmark, Sweden.

Results indicate that the most significant controls on vault flows are the properties of the rock mass. High flows relative to the base case model can result either from high-transmissivity probabilistic deformation zones or relatively high-conductivity, equivalent-continuuum porous-medium blocks based on upscaled properties from a discrete-fracture network (DFN) model. The magnitude of the increase in vault flows could be up to a factor of 3 for SFR1 or a factor of 2.2 for SFR3. Alternative DFN parameterisations of the rock mass have much less significant effects on flows through vaults. Thus details of the DFN parameterisation are less important than the potential effects of spatial variability and stochastic uncertainty.

Deformation zone (HCD) transmissivities also affect flows significantly, but the effect is limited by the rock-mass properties. A full order-of-magnitude increase in HCD transmissivities, reflecting the uncertainty in older vs. newer data from HCD intercepts, results in only a 40% increase for flows to the SFR1 vaults, and a 70% increase for the vaults in the proposed new facility.

The influence of Baltic seabed sediments is negligible in the simplified model. Replacing a "skin" due to a meter-thick clay layer with a connection via fractured rock has no significant effect on flows to vaults. In SKB's supplementary calculations using a more complex 3-D model, more significant effects are seen due to the influence of localized clay deposits on constraining discharge locations, but the effects are still small in relation to those associated with rock mass and HCD properties.

Contents

1. Introduction

Since 1987 the Swedish Nuclear Fuel and Waste Management Co. (SKB) has operated an underground repository for low- and intermediate-level radioactive waste, the SFR, at a location near Forsmark, Sweden. In support of a proposed extension of this facility, SKB has presented a site descriptive model SDM-PSU which encompasses the bedrock volume hosting the existing SFR as well as the proposed extension (Figure 1.1) and a safety assessment, SR-PSU.

In an initial review phase by SSM, a series of review issues relating to hydrogeology were identified. A number of these issues were evaluated further in a subsequent analysis (Geier, 2016; SSM2016-3581). This document builds on the findings of that analysis specifically aiming to quantify, through the use of simplified models and bounding calculations, the significance of the hydrogeological issues for near-field flow and other key factors affecting safety analysis. The results of the estimations are used to assess the adequacy of the hydrogeological input data for specific scenarios that are evaluated in SR-PSU.

Figure 1.1: Map of the Forsmark-SFR area showing the location of the existing SFR and the area that was prioritized for an extension of this facility. From Figure 1-1 of SKB-R-11-10.

2. Analysis of selected issues

In preceding analyses in support of SSM's review of SR-PSU, the following aspects of the hydrogeological modelling were identified in previous analyses as issues that require a better quantitative understanding in terms of their impact on near-field flows:

- Vertical hydraulic connection to the sea

- Hydrogeological properties and extent of Shallow Bedrock Aquifer

- Hydrogeological properties and lateral extension of unresolved PDZs

- Uncertainty in transmissivity values of deformation zone intercepts based on older data

- Residual uncertainty due to the selection of just three DFN realizations for propagation based mainly on geometric (rather than hydrogeological) analysis, and lack of analysis of alternative parameterizations

- Related limitations in the high flow in the bedrock scenario due to the likelihood that the "high flow in bedrock" case chosen for analysis is not strongly distinguished from mid-ensemble cases

- Potential for higher flows in one or more vault due to limitations of the method for upscaling from the DFN to an ECPM representations

The effects of these issues on near field flows are expected to be important for evaluation of processes such as barrier degradation and chemical conditions in the near field.

These issues are evaluated mainly by application of simplified models of the hydrogeological system. The following subsections describe the simplified model of the system that was used, followed by the assessment of each specific issue making use of this approach and supporting bounding calculations.

2.1. Simplified modelling approach

The use of simplified models for bounding calculations and analysis of sensitivities follows the basic concepts set forth by Dverstorp et al. (1996). The approach uses elementary hydrological principles and very simple models comprising 1-D conductors either in series or in parallel.

The present application of simplified models focuses on estimating flowrates through waste vaults in the existing SFR1 facility and the proposed SFR3 facility, and the potential sensitivity of those flowrates to issues that have raised in previous review stages.

The simple model considers a basic recharge-discharge system as depicted in Figure 2.1. Flow to the repository (or a particular repository component, e.g. a specific waste vault) is considered to occur by recharge along a transmissive brittle deformation zone (hydraulic conductor domain or HCD in SKB's terminology), then by percolation through sparsely fractured bedrock (rock mass) to reach the repository, and from there discharging via the rock mass and a second deformation

zone that discharges to the surface (or seabed). The flow along this path is driven by the potential head difference between the recharge location and the discharge location (the difference in elevation, if both of the recharge and discharge locations are above sea level, or the elevation above sea level of the recharge point, if the discharge location is under the Baltic.
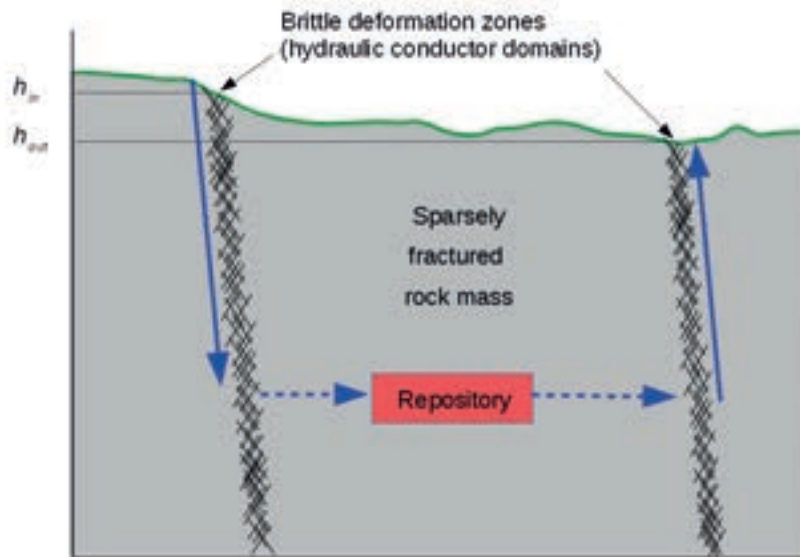

Figure 2.1: Conceptual model for the base case considered in the simplified model.

This system is idealized as an effectively one-dimensional series of segments as depicted in Figure 2.2. The main segments are:

- Regolith (in the recharge area);

- Deformation zone (in the recharge portion of the flow path);

- Rock mass between the recharge deformation zone and the repository;

- The repository components (vault or group of vaults);

- Rock mass between the repository and the discharging deformation zone;

- Deformation zone (discharging); and

- Regolith (in the discharge area)

For each of these segments, a set of alternative representations or parametrizations can be considered, as detailed below.
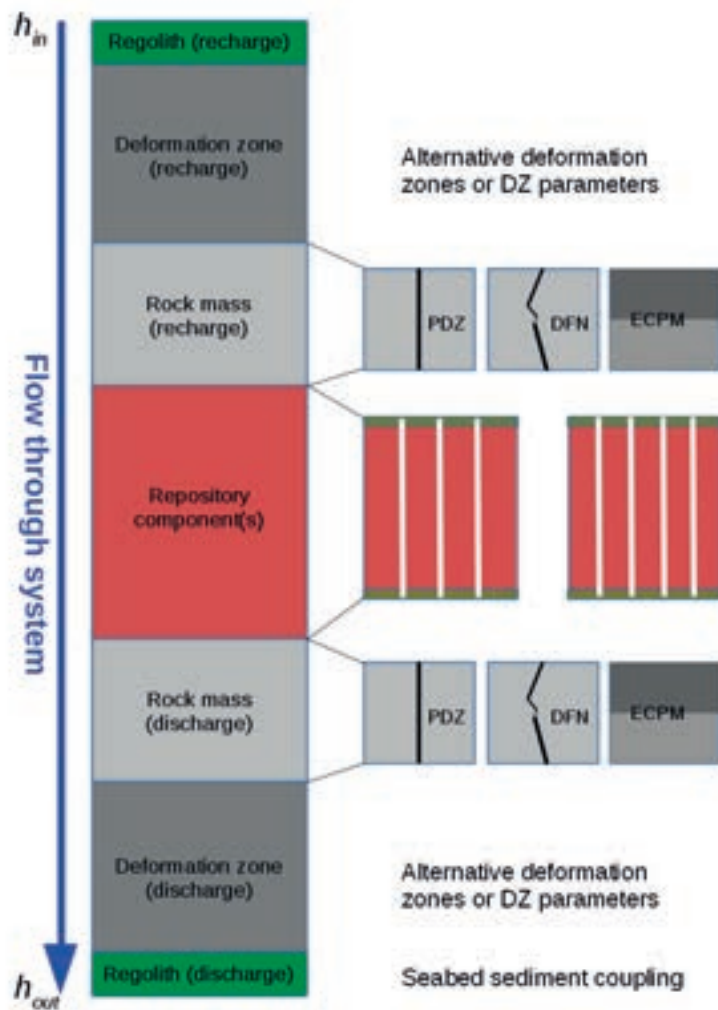
Figure 2.2: Simplified representation of flow system including key variants for the main flow path components.

Within each segment, the relationship between volumetric flowrate and potential head difference is considered to be linear:

$$Q = -C\Delta h$$

where:

Q = volumetric flowrate (L^3/T)

Δh = head difference between outlet and inlet ends of the segment (L)

The constant C, referred to here as the hydraulic conductance, has units of area per unit time (L^2/T).

For the case where a given segment is treated as a porous medium with hydraulic conductivity K in the direction of flow, this is given by:

$$C = KA/L$$

where A is the cross-sectional area through which flow takes place, and L is the distance, giving:

$$Q = - KA\Delta h/L$$

which can be recognized as the elementary form of Darcy's law.

When flow through a given segment is considered to take place via a tabular feature (such as a deformation zone, single fracture, or tabular aquifer) with a specified transmissivity T, the hydraulic conductance is:

$$C = Tw/L$$

where w is the nominal width of the tabular feature that participates in flow, giving:

$$Q = - Tw\Delta h/L$$

which is the conventional formula for one-dimensional flow through an aquifer of width w.

Flow through the series of segments that make up this simple model can be calculated as:

$$Q = C_{system} (h_{in} - h_{out})$$

where C_{system} is the effective conductance of the series of segments C_i:

$$C_{system} = \frac{1}{\sum_{i=1}^{N} \frac{1}{C_i}}$$

2.1.1. Regolith

Flow through the regolith segments in the simple model, on both the recharge and discharge ends, is considered to be vertical, with a conductance:

$$C = K_v A/\delta$$

where:

$K_v = $ vertical hydraulic conductivity [L/T]

$\delta = $ regolith thickness [L]

$A_r = $ recharge or discharge area [L^2]

The value of K_v depends on the type of regolith/sediments considered to be present at the recharge/discharge location. Values for K_v are taken from Table 2-3 of Bosson et al. (2010), as referenced by Odén et al. (2014) and reproduced here in Table 2.1.

For the base case of the simple model, the regolith in the recharge area is assumed to be coarse till (layer Z5 according to the notation of Bosson et al., 2010), as this is the most widespread flow-limiting layer across modern terrestrial areas of the site. The nominal thickness is assumed to be 5 m. The regolith in the discharge area is assumed to be clay (layer Z4) as this is the lowest-conductivity seabed layer in the characterization by Bosson et al. (2010). The nominal thickness is assumed to be 1 m.

Table 2.1: Directional hydraulic conductivities of regolith components from Tables 2-2 and 2-3 of Bosson et al. (2010). K_h is the horizontal hydraulic conductivity, and K_v is the vertical hydraulic conductivity.

Code	Layer	K_h (m/s)	K_v (m/s)
L1	Gyttja	$3 \cdot 10^{-7}$	$3 \cdot 10^{-7}$
L1	Peat	$1 \cdot 10^{-6}$	$1 \cdot 10^{-6}$
L2	Sand/gravel	$1.5 \cdot 10^{-4}$	$1.5 \cdot 10^{-4}$
L3	Clay	$1.5 \cdot 10^{-8}$	$1.5 \cdot 10^{-8}$
Z1	Surface layer till	$1.5 \cdot 10^{-4}$	$1.5 \cdot 10^{-5}$
Z1	Surface layer gyttja	$3 \cdot 10^{-7}$	$3 \cdot 10^{-7}$
Z1	Surface layer clay	$5 \cdot 10^{-6}$	$3 \cdot 10^{-7}$
Z1	Surface layer sand	$7.5 \cdot 10^{-4}$	$7.5 \cdot 10^{-5}$
Z1	Surface layer peat	$5 \cdot 10^{-6}$	$5 \cdot 10^{-7}$
Z1	Surface layer bedrock	$1 \cdot 10^{-7}$	$1 \cdot 10^{-7}$
Z2	Peat	$3 \cdot 10^{-7}$	$3 \cdot 10^{-7}$
Z3	Glaciofluvial deposit	$1.5 \cdot 10^{-4}$	$1.5 \cdot 10^{-4}$
Z4	Clay	$1.5 \cdot 10^{-8}$	$1.5 \cdot 10^{-8}$
Z5	Fine till	$5 \cdot 10^{-7}$	$5 \cdot 10^{-8}$
Z5	Coarse till	$7.5 \cdot 10^{-6}$	$7.5 \cdot 10^{-7}$
Z6	Fractured bedrock	$1.5 \cdot 10^{-6}$	$1.5 \cdot 10^{-6}$

2.1.2. Deformation zones

Deformation zones are treated as tabular features with a specified transmissivity value and width.

The inferred hydraulic properties of hydrogeologically significant deformation zones (or HCDs in SKB's nomenclature) are detailed in Table 4-3 of Öhman et al., 2014

(SKB P-14-04). As discussed by Odén et al. (2014), HCDs in SKB's models are treated as either homogeneous or heterogeneous, with two alternatives considered:

1) assuming the established HCD depth trend in SDM-Site Forsmark:

$$T(z) = T(0)\ 10^{z/k}$$

where T (z) is the flow model deformation zone transmissivity, z is the elevation (positive upwards), T (0) is the expected value of the transmissivity of the deformation zone at zero elevation, and k is the depth interval that gives an order of magnitude decrease of the transmissivity; the (transmissivity parameterisation is presented in SKB 2013, Appendix 6) versus,

2) no depth trend (transmissivity parametrization as presented in Öhman et al. (2014)

For the base case of this simple model evaluation, the latter alternative (no depth trend) is used. The transmissivity of the recharging zone is based on ZFMNNE0869 (as a relatively transmissive, large-scale deformation zone close to the repository). The transmissivity of the discharging zone is based on ZFMWNW0835 which has been identified by Öhman et al. (2014), along with ZFMENE3115, as one of two key deformation zones for the performance measures of SFR 3.

The length of the transport path along the deformation zones, for the base case model, is chosen to be equal to the depth of the SFR 3 vaults which are located at -120 m elevation according to Odén et al. (2014 SKB R-13-25 p. 28). The SFR 1 rock vaults are located at a shallower depth (–70 m elevation). For certain variants in which the two repository sections are treated separately, the effect of this lesser depth for SFR1 vaults is considered.

2.1.3. Rock mass representations

Three alternative representations are considered for flow through the rock mass:

- Direct connection via a single "probabilistic deformation zone" (PDZ), i.e. a minor deformation zone that was not represented as a deterministic feature in the site descriptive model;

- Network connection via a discrete-fracture network (DFN) composed of smaller-scale transmissive features, and

- Equivalent-continuum porous medium (ECPM) representations of the rock mass, parametrized in terms of a block-scale hydraulic conductivity;

In all of these representations, a key parameter is the length of the path L_{rm} through the rock mass, between the repository components and the recharging or discharging deformation zone.

Probabilistic Deformation Zones (PDZs)

The case of a direct connection via a PDZ can be considered as a bounding case. In the model of Öhman et al. (2012, Appendix A), the size of PDZs is considered to be

represented by a uniform distribution of square side lengths from 1 m to 1000 m. In this simplified model, only PDZs longer than L_{rm} need be considered as the class of PDZs that can form direct connections across this distance.

The transmissivity of each PDZ is treated as homogeneous. In this simplified model, the transmissivity of a PDZ is sampled randomly from the transmissivities evaluated from borehole intercepts as tabulated by Öhman et al. (2012, Tables A-1 and A-2). These values are reproduced here in Table 2.2. PDZs from the older data set for which the hydrological evidence was evaluated as "weak" by Öhman et al. (2012) are excluded from the dataset used in the simplified model. PDZs from the newer dataset were also excluded from the simplified model, if they were excluded by Öhman et al. (2012).

Table 2.2: Unresolved probabilistic deformation zone (PDZ) transmissivities and indications of confidence by Öhman et al. (2012, Tables A-1 and A-2).

Data Set	PDZ	$\log_{10} T$ (m^2/s)	Assessment of confidence
Old	KFR02_DZ2	-7.3	weak
Old	KFR03_DZ1	-6.0	possible
Old	KFR09_DZ2	-5.6	assumed splay
Old	KFR10_DZ2	-4.5	assumed extension
Old	KFR13_DZ1	-7.9	low T
Old	KFR13_DZ2	-7.5	low T
Old	KFR20_DZ1	-6.0	moderate
Old	KFR31_DZ1	-6.1	moderate
Old	KFR32_DZ1	-3.9	weak
Old	KFR37_DZ1	-6.0	strong
Old	KFR69_DZ1	-6.6	moderate
Old	KFR69_DZ2	-4.9	strong
New	KFR102B_DZ1	-6.1	included
New	KFR102B_DZ3	-5.3	included
New	KFR103_DZ1	-6.6	included
New	KFR103_DZ2	-5.0	included
New	KFR106_DZ1	-6.3	included
New	KFR106_DZ2	-5.8	included
New	KFR106_DZ4	-4.8	included
New	KFR106_DZ5	-4.8	included
New	KFR106_DZ6	-4.7	included
New	HFR106_DZ1	-4.5	included
New	KFR101_DZ3	-4.9	included
New	KFR101_DZ4	<-8	excluded
New	KFR101_DZ5	-8.3	excluded
New	HFR101_DZ2	-5.6	excluded

Discrete Fracture Network (DFN)

The possibility of discrete network connections via connected fractures in the rock mass is considered by a simplified representation of the hydrogeological DFN model used in SR-PSU, as specified in Appendix 5 of SKB (2013). The hydrogeological DFN model is defined for three depth intervals:

Shallow domain:	$z > -60$ m
Repository domain:	-60 m $\geq z > -200$ m
Deep domain:	-200 m $\geq z > -1100$ m

where z is the elevation relative to the mean sea level (RHB 70 datum). For this analysis, only the repository depth domain is considered, as being most relevant for the properties of the rock mass at repository depth. Two alternative parametrizations of this model were given by SKB (2013), referred to as the "Connectivity Analysis" (CA) and "Tectonic Continuum" (TC) variants.

SKB's DFN model is statistically parametrized in terms of an orientation distribution for each fracture set, together with a power-law model for fracture size (radius) and a logarithmic correlation of fracture transmissivity to fracture radius. For the 1-D representation considered in the simplified model for the present analysis, fracture orientation is not considered.

The method used to generate series of connected fractures to represent the main paths through a DFN is adapted from the approach described by Geier (2014). Connective paths are assumed to consist of the minimum number and length of fracture segments that are necessary to connect to the nearest point on the closest discharging HCD, subject to the constraints:

> (1) The first segment of the path is a fracture assumed to intersect the recharging or discharging HCD, with length equal to a fracture radius which is sampled from an assumed distribution, as explained below.

> (2) The second segment (and third, fourth, etc. segments if needed) are assumed to be of length equal to the remaining distance to connect between the HCD and the repository component, or the maximum fracture radius (whichever is less).

Based on previous analyses of similar DFN models for Forsmark, DFN connections through the rock mass are expected to take place mainly via connections between larger fractures on the scale of tens of meters or more, which although very sparse in the power-law models, are essential for percolation.

The simplified model for DFN connections via the rock mass considers only the largest fractures, with an arbitrary minimum radius of 20 m, ranging up to the maximum radius of 169 m as specified in SKB's hydrogeological DFN model.

The chance of a fracture participating in a percolating network can be expected to correlate positively to fracture radius. This at least partly offsets the tendency, with the power-law model, for the largest fractures to be relatively sparse. Direct

evidence of the frequency of fractures in this size range is not available from field data, and can only be inferred, e.g., by connectivity analysis.

Therefore, for the sake of simplicity, a uniform distribution is assumed for the size of fractures contributing to percolating networks. In order to maintain the inferred dependence of fracture transmissivity on fracture size for the different fracture sets, fractures are sampled randomly in proportion to the fracture set intensities as given in Table 2.3.

Table 2.3: Intensity, size and transmissivity distribution parameters of DFN model for the repository domain (-60 ≥ z > -200 m RHB 70) as specified in Table A5-1 of SKB (2013). P_{32} = fracture intensity (m²/m³); k_r = scaling exponent for fracture size distribution (dimensionless); a = transmissivity of a fracture of 1 m radius (m²/s); b = scaling exponent for fracture transmissivity (dimensionless).

Set		Connectivity analysis			Tectonic continuum		
Set	Intensity	Size	$(T = a\, r^b)$		Size	$(T = a\, r^b)$	
	P_{32}	k_r	a	b	k_r	a	b
EW	1.44	3.1	$2.1\cdot10^{-9}$	1.1	2.63	$7.9\cdot10^{-11}$	1.4
NW	0.81	3.0	$1.1\cdot10^{-8}$	1.1	2.596	$1.3\cdot10^{-9}$	1.1
NE	1.00	3.3	$2.2\cdot10^{-9}$	1.3	2.752	$8.6\cdot10^{-11}$	1.35
Gd	1.21	2.72	$4.0\cdot10^{-9}$	0.8	2.72	$4.0\cdot10^{-9}$	0.8
Hz	0.95	2.55	$8.5\cdot10^{-10}$	1.35	2.55	$8.5\cdot10^{-10}$	1.35

Equivalent Continuum Porous Medium

In a previous stage of the SFR-U review (Geier, 2017), the hydrogeological DFN model given by SKB (2013) was used to derive effective hydraulic conductivity values for both the CA and TC variants, on a 50 m block scale, in each of the three directions x (East-West), y (North-South), and z (vertical). These directional hydraulic conductivity values K_x, K_y, and K_z are used as for the ECPM representation of the rock mass in the simplified model.

The base case of the simplified model uses the geometrical mean values of K_x, K_y, and K_z to represent the rock mass in all components of the model. This includes rock mass segments of the recharge and discharge paths, as well as the rock mass associated with each vault (as discussed in Section 2.1.4).

For the calculation cases referred to as "permeameter" cases, a $\{K_x, K_y, K_z\}$ triplet for each rock mass segment in the simplified model is sampled randomly from the set of 1200 blocks within the repository depth range for which $\{K_x, K_y, K_z\}$ estimates were calculated by Geier (2017). Thus in these calculation cases, the rock mass segments of the recharge and discharge paths will have independent K values.

In all cases, a distinction is made between hydraulic conductivities in the vertical and horizontal directions. The vertical hydraulic conductivity is taken as $K_v = K_z$. The horizontal conductivity $K_h(\theta)$ in the direction with azimuth θ is calculated based on the assumption of a permeability ellipsoid with principal components aligned with the x, y, and z directions. This implies:

$$K_h(\theta) = [\cos^2\theta\, /\, K_x + \sin^2\theta/K_y]K_x K_y$$

In practice the block-scale hydraulic conductivities derived from the DFN model tend to be close to isotropic in the horizontal plane, with anisotropy ratios mainly in the range 0.9 to 1.1, so the effect of this calculation on the simplified model results is minor.

For calculating directional hydraulic conductivities of the rock mass parallel and transverse to the BMA, BLA, BRT, and BTF vaults, an azimuth of 30 degrees (N30E) is used, based on Figure 1-4 of the Initial State Report.

2.1.4. Repository components

Components of the repository are represented as simple 1-D conductors, considering either longitudinal flow along each vault (in the base case) or transverse flow (as variants). The following subsections describe the simplified models that were developed for individual vaults.

BMA Vaults

Dimensions for the intermediate-level waste vaults 1BMA and 2BMA are taken from the Initial State Report (SKB TR-14-02, Tables 4-1 and 5-1), as summarized in Table 2.4. For 2BMA the values for layout version 2.0 are used.
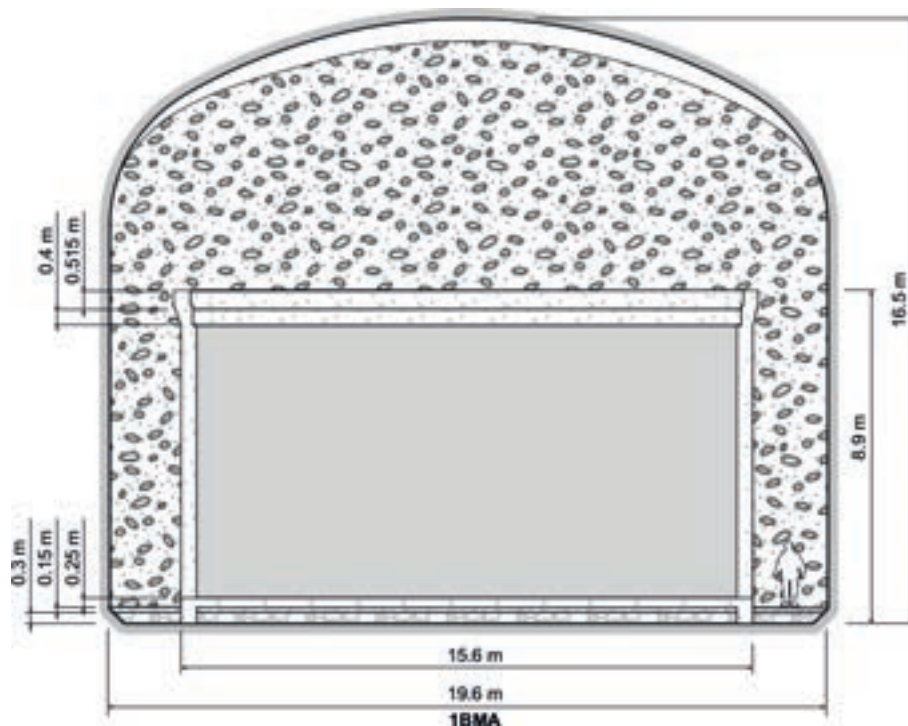
Figure 2.3: Cross section through waste-storage section of 1BMA. Based on Figure 4-3 of the Initial State Report (SKB TR-14-02).
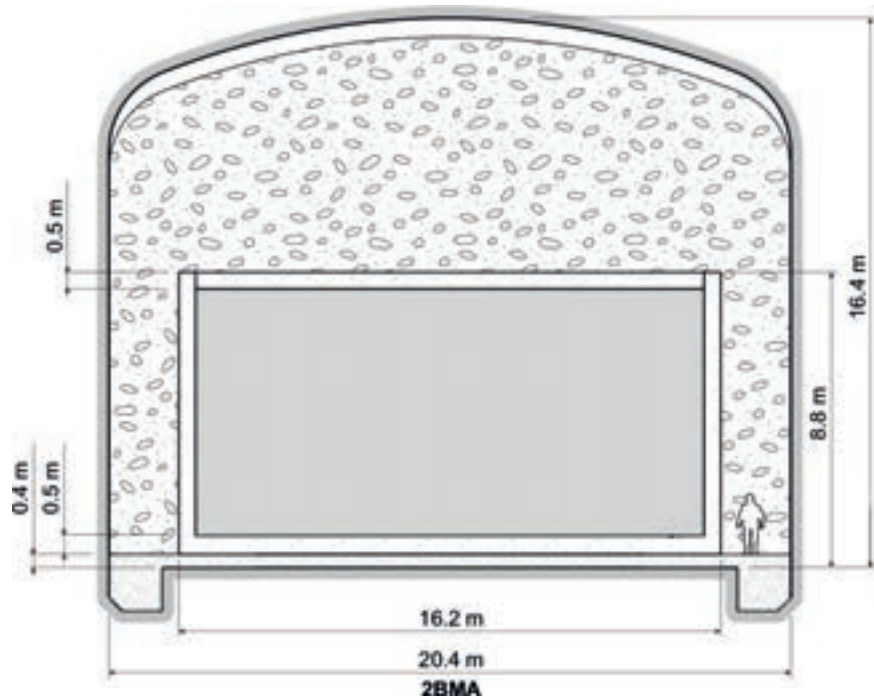
Figure 2.4: Cross section through waste-storage section of 2BMA (Layout 2.0). Based on Figure 5-2 of the Initial State Report (SKB TR-14-02). In this design, the waste vault lies atop a 0.4 m layer of macadam.

The simplified component model for longitudinal flow along each of these vaults is depicted in Figure 2.5.

For the section of the vault that contains the waste, there are three conductors in parallel, representing the floor, the waste vault, and the backfill (alongside and above the waste). The conductance of the floor is calculated as the sum of the conductances of the concrete and macadam layers, as well as (for 1BMA) the rock fill layer. The effect of the transverse concrete beams in 1BMA has not been accounted for.

The net effect of the two backfilled section at either end of the waste vault for flow is accounted for by a conductive segment placed in series with the waste-storage section. The conductance of this segment is calculated as:

$$C = \frac{K_{backfill} A_{vault}}{L_{vault} - L_{waste}}$$

where A_{vault} is the cross-sectional area of the vault. Finally the effect of bypass flow through the rock mass is accounted for by a parallel conductance equal to:

$$C = \frac{K_{rock} A_{rock}}{L_{vault}}$$

where A_{rock} is the cross-sectional area of an annulus of thickness d_{rock} of rock around the vault.
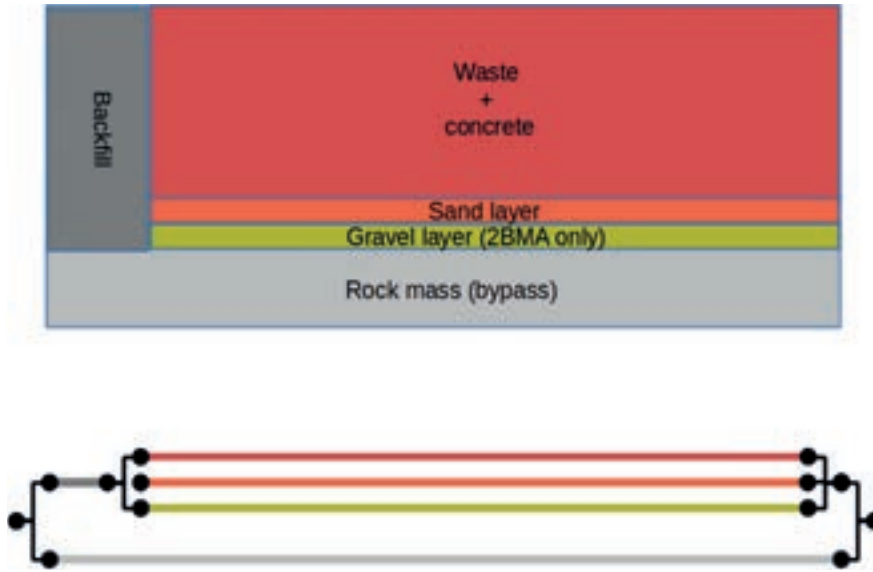

Figure 2.5: Simplified component model for 1BMA and 2BMA.

Table 2.4: Dimensions of the 1BMA and 2BMA vaults based on SKB TR-14-02, Tables 4-1 and 5-1. All dimensions are in meters.

Dimension	1BMA	2 BMA (Layout 2.0)
Vault length L_{vault}	160	275
Vault width w_{vault}	19.6	20.4
Maximum height H_{vault}	16.5	16.4
Average height h_{vault}	15.3	15.8
Length of inner zone	3.7	4.7
Waste length L_{waste}	139.85	246.3
Waste width w_{waste}	15.62	16.2
Waste height h_{waste}	8.215	8.4
Shotcrete thickness t_{shot}	0.05	0.05
Reinforced concrete floor thickness	0.25	0.5
Macadam thickness	0.15	0.4
Rock fill thickness	0.3	–
Thickness of coarse concrete below beams	0.5	–
Length of loading zone	15.2	24

BTF Vaults

Dimensions for the concrete tank vaults 1BTF and 2TF are taken from the Initial State Report (SKB TR-14-02, Tables 6-1 and 6-2), as summarized in Table 2.5. The dimensions of the two vaults are identical according to these tables.
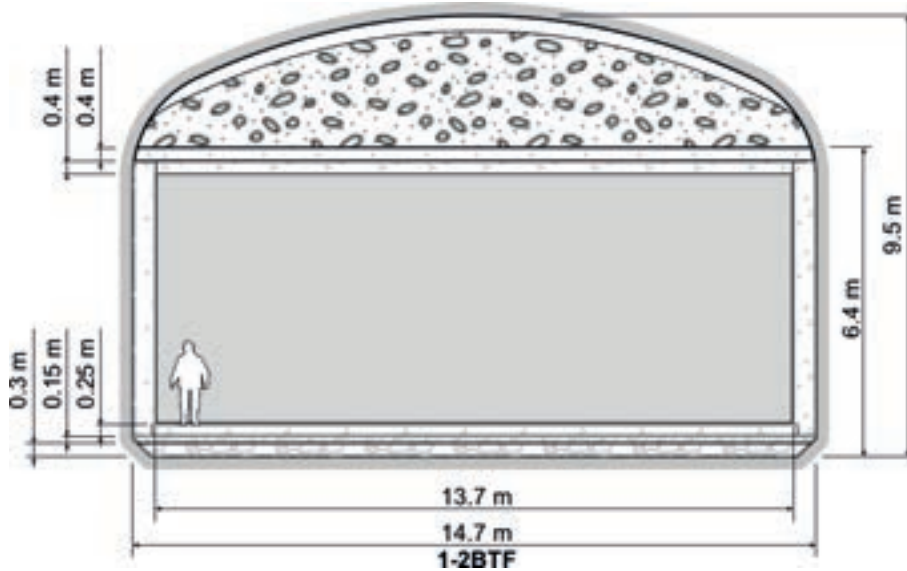

Figure 2.6: Cross section through waste-storage section of 1BTF. Based on Figure 6-3 of the Initial State Report (SKB TR-14-02).

The simplified component model for longitudinal flow along each of these vaults is depicted in Figure 2.7.

For the section of the vault that contains the waste, there are two conductors in parallel, representing the encased waste and the backfill above the waste. The conductance of the rock fill and macadam below the encased waste was not included in the base case calculations but is considered in a refined variant of the model.

As for the BMA vaults, the net effect of the two backfilled sections at either end of the waste vault for flow is accounted for by a conductive segment placed in series with the waste-storage section. The conductance of this segment is calculated as:

$$C = \frac{K_{backfill}A_{vault}}{L_{vault} - L_{waste}}$$

and the effect of bypass flow through the rock mass is accounted for by a parallel conductance equal to:
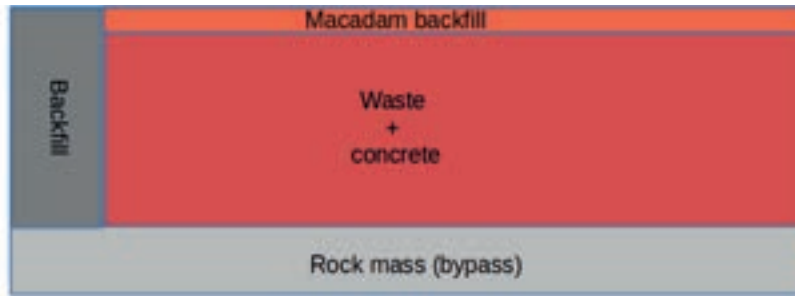
$$C = \frac{K_{rock}A_{rock}}{L_{vault}}$$

18

Figure 2-7: Simplified component model for 1BTF and 2BTF.

Table 2.5: Dimensions of the 1BTF and 2BTF vaults based on SKB TR-14-02, Tables 6-1 and 6-2, according to which these vaults have identical dimensions. All dimensions are in meters.

Dimension	1,2BTF
Vault length L_{vault}	160
Vault width w_{vault}	14.7
Maximum height H_{vault}	9.5
Average height h_{vault}	8.8
Shotcrete thickness t_{shot}	0.05
Length of inner zone	3.6
Inner wall thickness	0.3
Waste length L_{waste}	130
Waste width w_{waste}	13.7
Waste height h_{waste}	4.9
Inner lid thickness	0.4
Outer lid thickness	0.4
Thickness of grout between concrete tanks and rock wall	0.5
Floor width w_{floor}	13.9
Concrete floor thickness	0.25
Macadam thickness	0.15
Rockfill thickness	0.3
Thickness of coarse concrete below beams	0.5
Length of loading zone	25.8

Silo

The main components of the silo are illustrated in Figure 2.8. Dimensions used for calculating the properties of conductors in the simplified model are based on values given in Table 7-3 of the Initial State Report, as listed in Table 2-6.

The simplified representation for vertical flow is illustrated in Figure 2.9. Flow through the waste section of the silo is in parallel with the flow through the bentonite walls (expected to be minimal), and limited by series connections via the base and lid which are treated as conductors in series. Bypass flow via the rock mass is permitted as for the other vaults.

Table 2.6: Dimensions of the silo components SKB TR-14-02, Table 7-3. All dimensions are in meters.

Dimension	1,2BTF
Cupola diameter	31
Cupola height	15.7
External diameter of cylindrical part	29.4
Concrete base (cast coarse concrete + concrete plate)	0.3
Thickness of sand/bentonite (90/10) layer in base	1.5
Thin concrete layer	0.05
Reinforced floor thickness	0.9*
Outer diameter of cylindrical concrete structure	27.6
Height of cylindrical outer wall	52.55
Thickness of cylindrical outer wall	0.8
Top lid sand layer thickness	0.05
Thickness of reinforced lid with gas evacuation pipes	1
Thickness of sand above concrete lid	0.1
Thickness of sand/bentonite (90/10) layer in lid	1.5

* Value used in base case was 0.95 m which differs slightly from this value.
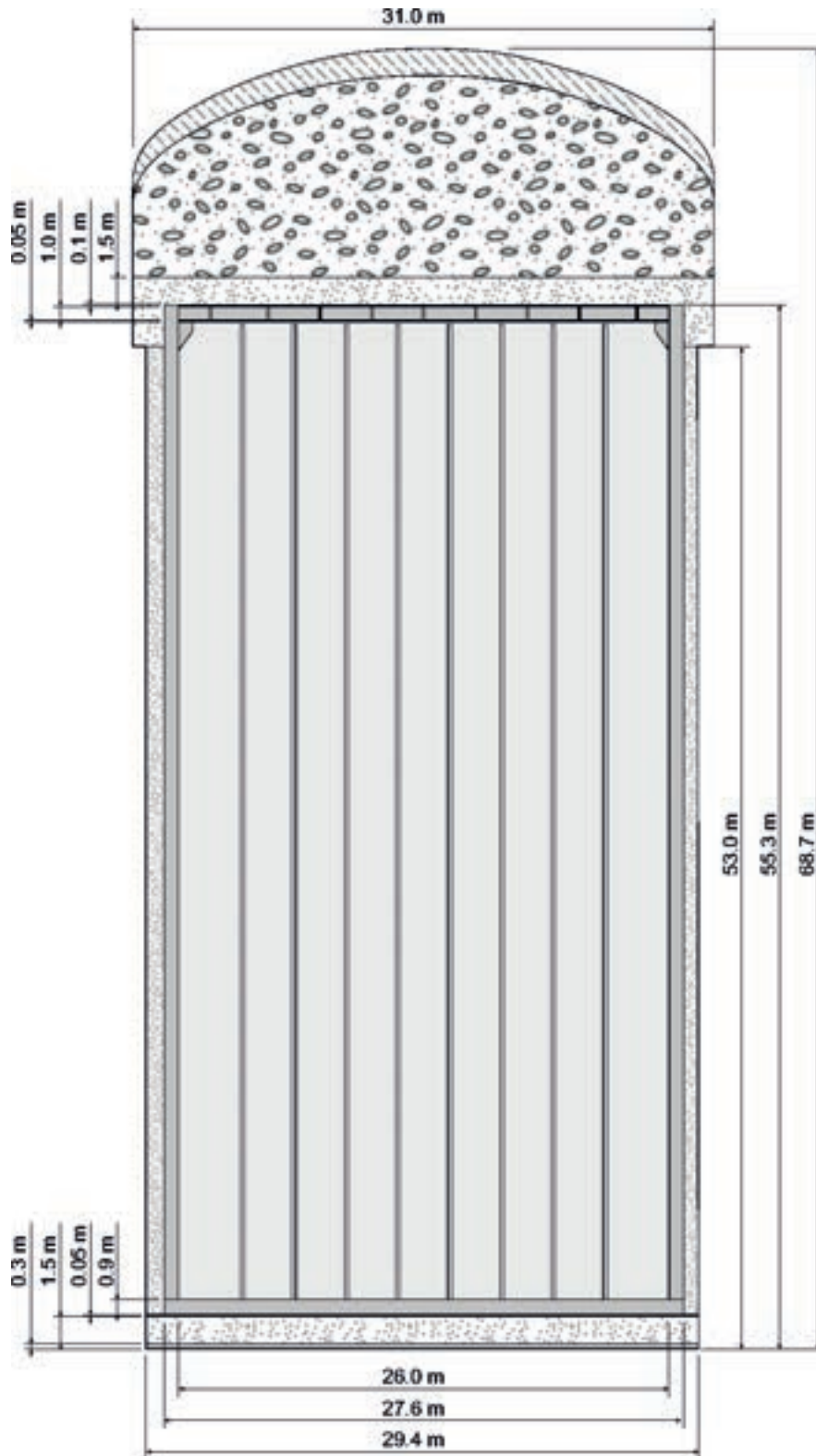
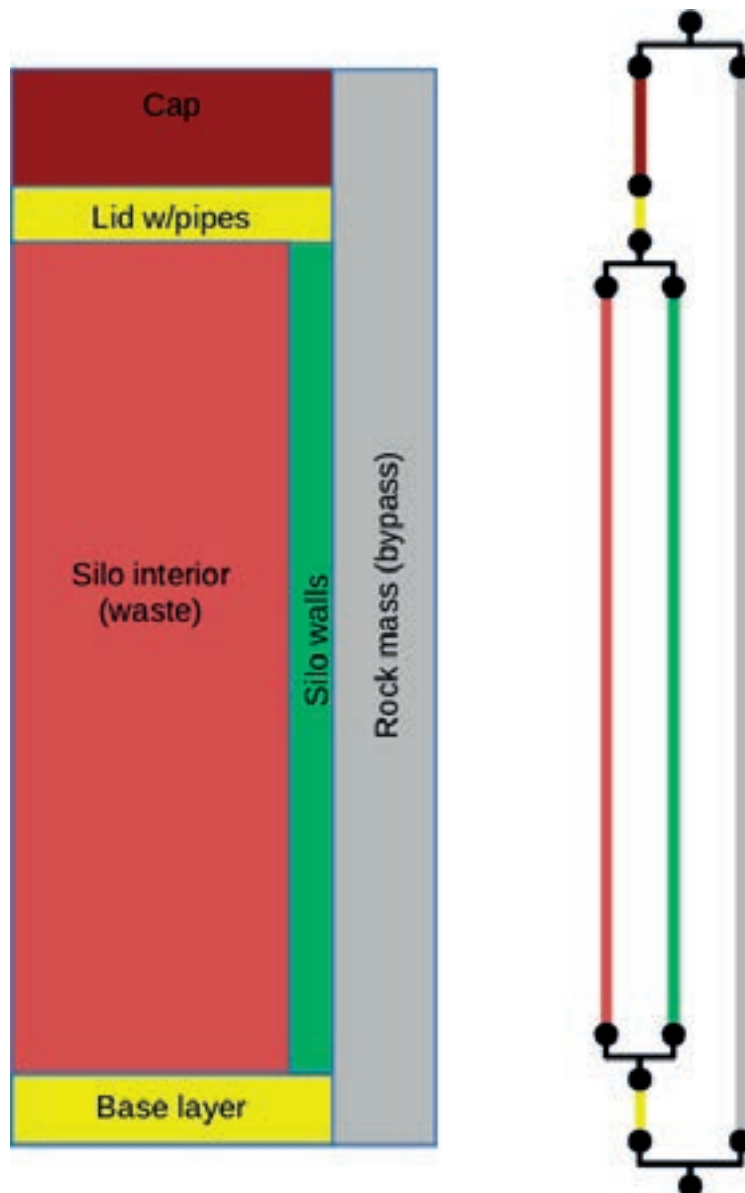**Figure 2-8:** Vertical section through silo. Based on Figure 7-3 of the Initial State Report.

Figure 2.9: Simplified model for vertical flow through the silo.

BLA Vaults

Dimensions for the low-level waste vaults 1BLA through 5BLA are taken from the Initial State Report (SKB TR-14-02, Tables 8-1 and 9-1). As shown by the cross-section diagram for 1BLA in Figure 2-10, the waste section of these vaults simply consists of waste containers stacked up, with no backfill.

The simplified component model for longitudinal flow along each of these vaults used in the base case is depicted in Figure 2-11.

For the section of the vault that contains the waste, there are two conductors in parallel, representing the floor and the waste vault. Flow through the non-backfilled open space is considered as part of the waste vault, based on the assumption that this volume of water will be in communication with the waste. The conductance of the floor is calculated as the sum of the conductances of the concrete and macadam layers, as well as (for 1BLA) the rock fill layer.

As for the BMA vaults, the net effect of the two backfilled section at either end of the waste vault for flow is accounted for by a conductive segment placed in series with the waste-storage section. The conductance of this segment is calculated as:

$$C = \frac{K_{backfill} A_{vault}}{L_{vault} - L_{waste}}$$

and the effect of bypass flow through the rock mass is accounted for by a parallel conductance equal to:

$$C = \frac{K_{rock} A_{rock}}{L_{vault}}$$
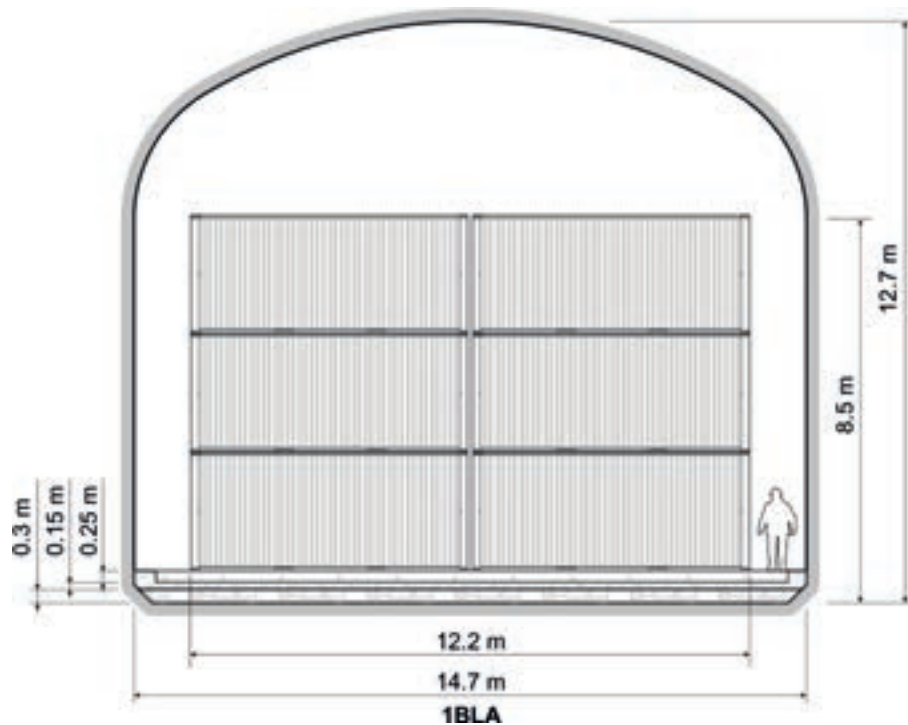
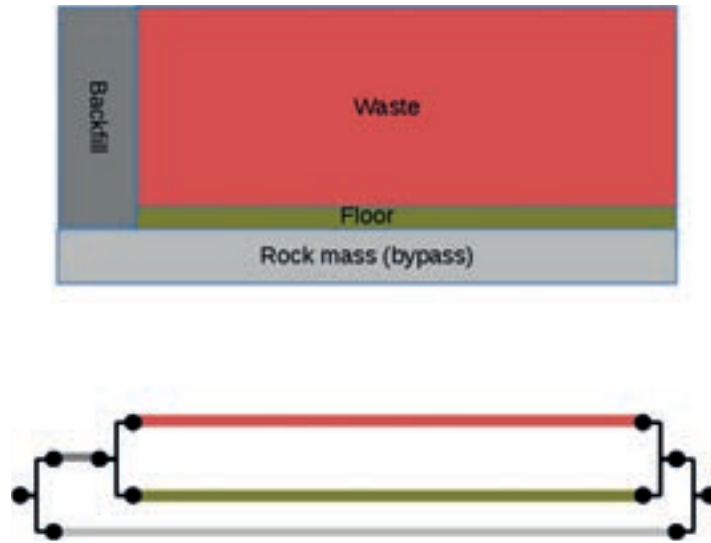**Figure 2.10:** Cross-section of waste-storage section of 1BLA (from the Initial State Report, Figure 8-2).

Figure 2.11: Simplified model of BLA vaults (for longitudinal flow cases).

Table 2.7: Dimensions of the BLA vaults based on SKB TR-14-02, Tables 8-1 and 9-1.. All dimensions are in meters.

Dimension	1BLA	2-5BLA (Layout 2.0)
Vault length L_{vault}	160	275
Vault width w_{vault}	14.7	17.9
Maximum height H_{vault}	12.7	14.1
Average height h_{vault}	11.8	13.5
Length of inner zone	3.7	8
Waste length L_{waste}	146.3	243
Waste width w_{waste}	12.2	12.2
Waste height h_{waste}	7.8	7.8
Shotcrete thickness t_{shot}	0.05	0.05
Floor width	13	14
Concrete floor thickness	0.25	0.5
Macadam thickness	0.15	0.4
Rockfill thickness	0.3	–
Length of loading zone	10	24

BRT Vault

BRT dimensions (in meters) are based on SKB TR-14-02 Table 10-1. Properties are calculated by methods analogous to those for the other vaults.
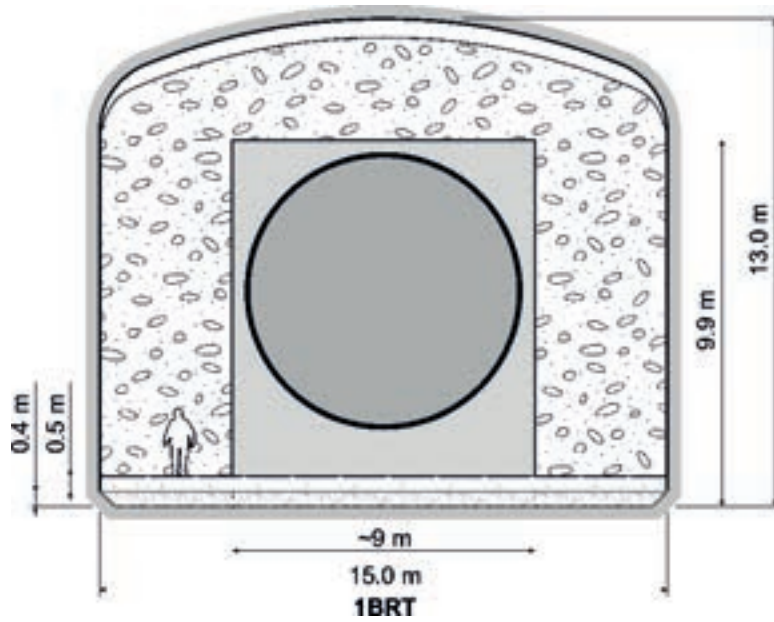
Figure 2.12: Cross-section of waste-storage section of BRT (from the Initial State Report, Figure 10-3).

Table 2.7: Dimensions of the BRT vault based on SKB TR-14-02, Table 10-1, for Layout version 2.0. All dimensions are in meters.

Dimension	BRT (Layout 2.0)
Vault length L_{vault}	240
Vault width w_{vault}	15.0
Maximum height H_{vault}	13.0
Average height h_{vault}	12.5
Length of inner zone	31.5
Waste length L_{waste}	207
Waste width w_{waste}	8.6
Waste height h_{waste}	9
Shotcrete thickness t_{shot}	0.05
Floor width	12.8
Concrete floor thickness	0.5
Macadam thickness	0.4
Length of loading zone	1.5

Hydraulic conductivities of vault components

Hydraulic conductivity values used for repository components in the base case of the simplified model are based on the values listed by Abarca et al. (2013), as summarized in Table 2.4.

For the silo wall, due to self-compaction the hydraulic conductivity is expected to be decrease linearly with depth according to Öhman et al. (2012), who gave the following formula:

$$K = 2.11\text{e-}10 \text{ m/s} + (1.54\text{e-}12 \text{ s}^{-1})\, z$$

where z is the elevation. The silo extends from –64 to –133 m RHB 70 Öhman et al. (2012, p. 44). In the simplified model, the mean value is calculated by setting:

$$z = -(64 \text{ m} + 133 \text{ m})/2 = -98.5 \text{ m}$$

which is the midpoint of the silo. This yields:

$$K = 2.11\text{e-}10 \text{ m/s} + (1.54\text{e-}12 \text{ s}^{-1})(-98.5 \text{ m}) = 6.39\text{e-}11 \text{ m/s}$$

The thickness of rock mass contributing to bypass flow around each vault is arbitrarily set to $d_{rock} = 20$ m

Table 2.4: Base case hydraulic conductivities (in m/s) from Abarca et al (2013, Tables 3-3 and 3-4).

Component	Material	Direction (if not isotropic)	Hydraulic conductivity (m/s)
Tunnels	Backfill		1.00e-03
Plugs	structural plug		1.00e-06
Plugs	bentonite section		1.00e-12
BTF	concrete backfill		8.30e-09
1BMA	concrete beams		8.30e-10
1,2BTF	waste	horizontal (x)	3.79e-09
1,2BTF	Waste	horizontal (y)	6.65e-09
1,2BTF	Waste	vertical	6.79e-09
1BLA	Waste		1.00e-03
1,2BMA	waste		8.30e-07
BRT	Waste		8.30e-09
Silo	top layer (cap)		1.00e-09
Silo	bottom layer (base)		1.00e-09
Silo	interior waste		8.30e-07
Silo	Lid	vertical	8.30e-10
Silo	Lid	horizontal	3.00e-07
Silo	vertical wall		6.39e-11
General	construction concrete		8.30e-10
General	macadam		1.00e-03

2.2. Base case of simplified model

The head difference driving flows for this base case is $\Delta h = 5$ m. This is approximately representative of the topographic differential for a situation at a future point when the Baltic has retreated beyond the location of the repository, and the dominant recharge-discharge path runs from an HCD outcropping near the present-day coastline, to a second HCD outcropping just beyond the repository. Note that the model is linear with respect to Δh, so the effects of increasing or decreasing Δh by a given factor can be obtained by simply scaling these flowrates by a the same factor.

Results for the base case of the simplified model are compared with SKB's results for SR-PSU in Figure 2.13.

Results are shown for two versions of the base case, representing two contrasting assumptions about flow is partitioned among the vaults:

(1) Each vault responds individually, as part of a distinct recharge-discharge path;
(2) Vaults in each section of the repository (SFR1 vs. SFR2-3) respond as groups of conductors in parallel.

For most vaults, the results for these two different assumptions bracket the flowrates calculated in SKB's model for times approximately 1000 years after present (3000 CE), at which point the Baltic has retreated sufficiently for the assumed value of Δh to be realistic. The exceptions are 1-2BTF and 2BMA, where SKB's calculations exceed the simplified model results by less than a factor of 2.
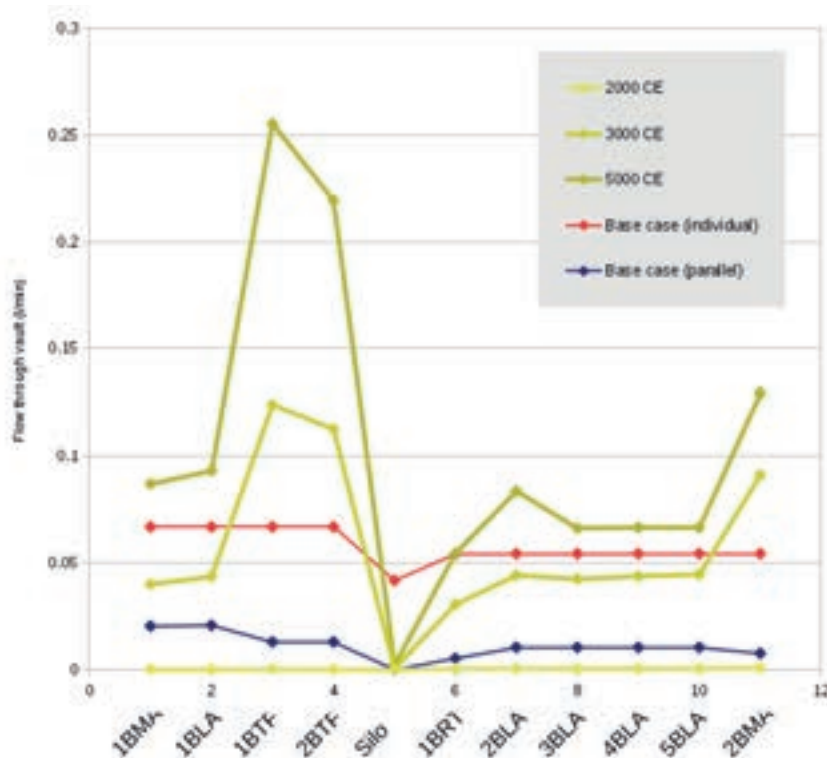
Figure 2.13: Comparison of simplified model base case results in terms of flowrates through waste vaults, versus flowrates calculated for SR-PSU for for three different times from the present through 7000 years after present. The red points show flowrates for the case where each individual vault is considered separately. The blue points show flowrates for the case where each of the vaults within each section of the repository are treated as conductors in parallel.

2.3. Vertical hydraulic connection to the sea

The role of seabed sediments in controlling the vertical hydraulic connection to the sea is mentioned by Öhman et al. (2012, p. 115): "*Reported excess head values prior to tunnel constructions are highly uncertain ..., but may also indicate a slow hydrogeological system, poorly vertically connected to the sea.*" However alternative parameterizations for seabed sediments were not addressed in SKB's calculations for SR-PSU. SSM has asked SKB for complementary information regarding the connection to the sea (SSM2015-725-40 Point 4). SKB's response is discussed in section 3.4.1.

Uncertainty regarding the vertical hydraulic connection to the sea could affect the inflows that have been used to evaluate the hydrogeological models, and their transient behaviour. Inflow data have not been used for a systematic calibration procedure, due to recognized limitations regarding baseline conditions prior to earlier stages of construction, as well as the role of "skin" effects around the tunnels, as explained by Öhman et al. (2013, p. 16). However inflow data have been used for comparative assessment of model variants that include different parameterizations of the hydraulic conductor domains, shallow-bedrock aquifer and near-tunnel skin (Öhman et al., 2013, p. 51-64).

In the simplified model used in the present analysis, the base case assumes that the regolith in the discharge area is a 1 m thick layer of clay (layer Z4), with $K_v = 1.5\times10^{-8}$ m/s. The importance of seabed sediments was tested by a "no Baltic skin" variant in which the hydraulic conductivity of this layer was assigned the same hydraulic conductivity as the shallow fractured bedrock (layer Z6), with $K_v = 1.5\times10^{-6}$ m/s.

Results for this "no Baltic skin" case show that the difference with the base case is negligible. These results are compared numerically in Table 2.5. The differences are generally less than 0.3%, and thus too small to be evident in a graphical presentation.

Table 2.5: Comparison of flowrates (in liters/min) between the base-case model and the "no Baltic skin" variant, for the two different assumptions regarding flow partitioning among vaults.

Vault	Individual Base case	Individual no Baltic skin	Parallel Base case	Parallel no Baltic skin
1BMA	0.06688	0.06708	0.02031	0.02037
1BLA	0.06688	0.06708	0.02074	0.02080
1BTF	0.06687	0.06707	0.01292	0.01295
2BTF	0.06687	0.06707	0.01292	0.01295
Silo	0.04172	0.04180	0.00001	0.00001
1BRT	0.05430	0.05443	0.00520	0.00521
2BLA	0.05432	0.05445	0.01039	0.01042
3BLA	0.05432	0.05445	0.01039	0.01042
4BLA	0.05432	0.05445	0.01039	0.01042
5BLA	0.05432	0.05445	0.01039	0.01042
2BMA	0.05431	0.05444	0.00757	0.00758

2.4. Unresolved Probabilistic Deformation Zones

Uncertainty regarding the lateral extent and hydraulic properties of unresolved probabilistic deformation zones (PDZs) is mentioned as a data gap by Öhman et al. (2012, p. 116): "*No interference tests have been specifically targeted to the interpreted SBA intercepts and Unresolved PDZs. Transient evaluation of a few selected packed-off pump tests targeting SBA intercepts and Unresolved PDZs may potentially shed some insight to their lateral extension.*"

In SR-PSU, unresolved PDZs are treated by three stochastic realizations of geometry and properties which are linked to the corresponding HRD realizations. Selection of these three realizations is linked to the ad hoc selection of HRD realizations.

In the simplified model for the present analysis, the potential effect of PDZs was scoped by considering the case where flow through the rock mass, both along the recharge and discharge paths, occurs through single features with transmissivities representative of PDZs.

The transmissivity values for the PDZs were drawn from the logarithmic values given by Öhman et al. (2012), as listed in Table 2.2. Two approaches were considered: (1) random sampling from this table of of values and (2) selection of the maximum value. The latter approach is more conservative and was therefore used to scope the maximum plausible effect of unresolved PDZs providing high-transmissivity paths through the bedrock.

Results of this calculation case are compared with the base-case results in Table 2.6 and Figure 2.14 (together with results of another case related to deterministic HCDs, discussed in the next section). Direct connections through the rock mass via high-transmissivity PDZs could potentially increase flows to vaults in SFR1 by a factor of 3, and flows to vaults in SFR3 by a factor of 2.2, relative to the base case.

Table 2.6: Comparison of flowrates (in liters/min) between the base-case model and the PDZ and high-transmissivity HCD variants, for the two different assumptions regarding flow partitioning among vaults.

| Vault	Individual Base case	Individual PDZ	Individual High-T HCD	Parallel Base case	Parallel PDZ	Parallel High-T HCD
1BMA	0.06688	0.20454	0.02867	0.02031	0.06215	0.09438
1BLA	0.06688	0.20454	0.02927	0.02074	0.06344	0.09438
1BTF	0.06687	0.20446	0.01823	0.01292	0.03951	0.09437
2BTF	0.06687	0.20446	0.01823	0.01292	0.03951	0.09437
Silo	0.04172	0.07192	0.00001	0.00001	0.00002	0.05099
1BRT	0.05430	0.11974	0.00875	0.00520	0.01147	0.09136
2BLA	0.05432	0.11980	0.01749	0.01039	0.02292	0.09139
3BLA	0.05432	0.11980	0.01749	0.01039	0.02292	0.09139
4BLA	0.05432	0.11980	0.01749	0.01039	0.02292	0.09139
5BLA	0.05432	0.11980	0.01749	0.01039	0.02292	0.09139
2BMA	0.05431	0.11977	0.01273	0.00757	0.01669	0.09138
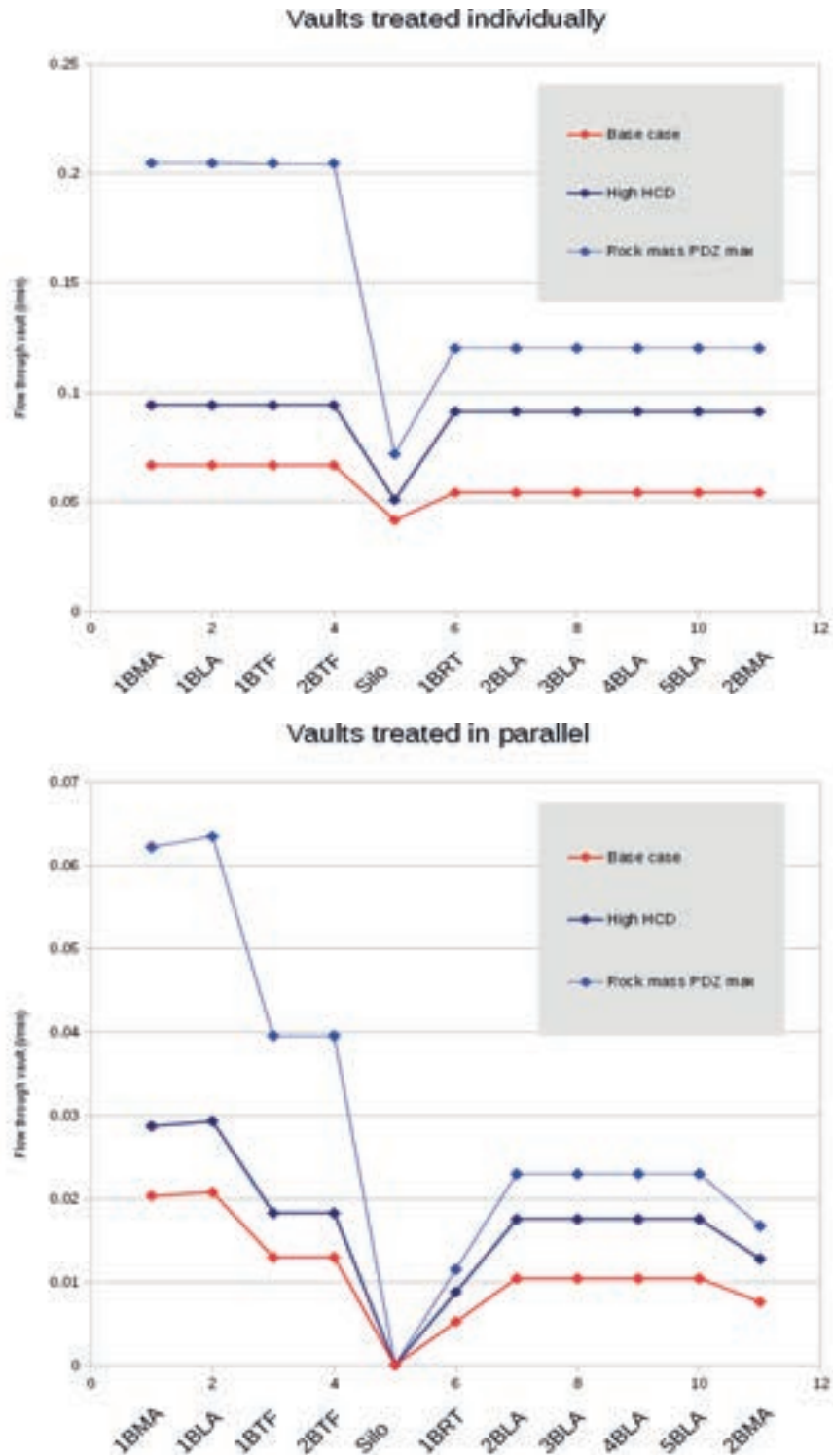
Figure 2.14: Comparison of calculation cases representing (light blue) an order-of-magnitude increase in HCD transmissivities and (dark blue) connections to the repository via probabilistic deformation zones (PDZs), relative to the base case of the simplified model (red). The upper plot shows flowrates for the case where each individual vault is considered separately. The lower plot shows flowrates for the case where each of the vaults within each section of the repository are treated as conductors in parallel.

2.5. Transmissivity of deformation zone intercepts

According to Öhman et al. (2012, p. 117) the deformation zone intercepts assessed based on older data tended to have higher interpreted transmissivities than those based on newer data. Figure 6-2 from Öhman et al. (2012, p. 102) indicates that the difference between transmissivities for HCD intercepts in the older and newer data sets for the SFR is roughly an order of magnitude (lower for the newer data set).

The sensitivity of results to this uncertainty is evaluated by considering an order-of-magnitude increase in HCD transmissivities in the simple model, for both the recharge and discharge paths.

The results as shown in Figure 2.14 are an increase in flowrates, relative to the base case, by roughly 40% for the SFR1 vaults by 70% for the vaults in the proposed new facility. The greater effect for the latter is a consequence of its greater depth, as this implies a longer path through HCDs and thus a proportionally greater distance over which HCD transmissivity limits flow, in this simplified model.

2.6. Alternative rock mass parameterizations and realizations

SKB's analysis of fracture data yielded two alternative DFN parameterizations, referred to as "tectonic-continuum" and "connectivity-analysis" models, but only the latter parameterization was propagated to the SR-PSU safety analysis. Within that parameterization, only three DFN realizations were selected for propagation, based mainly on geometric (rather than hydrogeological) analysis. Thus there is residual uncertainty both due to lack of analysis of alternative parameterizations and due to the limited number of realizations considered.

This limitation of the analysis furthermore affects the construction of the "high flow in bedrock" scenario due to the likelihood that the calculation case chosen for analysis is not strongly distinguished from mid-ensemble cases.

To assess these uncertainties using the simplified model, the rock mass portions of the system were modelled using hydraulic conductivity values based on multiple realisations of both of the alternative DFN parameterizations.

Equivalent-continuum, porous-medium (ECPM) hydraulic conductivities on a 50 m scale were calculated for both of the DFN parameterizations, using the modelling approach and tools described in a previous review report (Geier, 2017). The method for upscaling from DFN fractures to ECPM is based on geometrical formulae as proposed by Oda (1985), rather than actual network simulations, but is conceptually and mathematically the same as the geometrical upscaling method used in the main modelling approach used by SKB in SR-PSU (Svensson et al., 2010).

For each of the two DFN parameterisations, multiple realisations were evaluated to calculate ECPM estimates of the directional hydraulic conductivities (K_x, K_y, K_z) on a 50 m block scale, for 1200 simulated blocks at repository depth, where x, y, and z respectively denote the values in the East-West, North-South, and vertical directions. The distributions of these values are compared in Figure 2.15, as distributions plotted in terms of the geometric mean value of the directional conductivities for each block, i.e.,

$$K_g = (K_x \, K_y \, K_z)^{1/3}$$

The distributions are similar in terms of the overall spread of values. The connectivity-analysis model has a slightly lower median value of K_g, with slightly more low-K_g blocks relative to the tectonic-continuum model, but also a slightly higher number of blocks with $K_g > 2\times10^{-7}$ m/s.
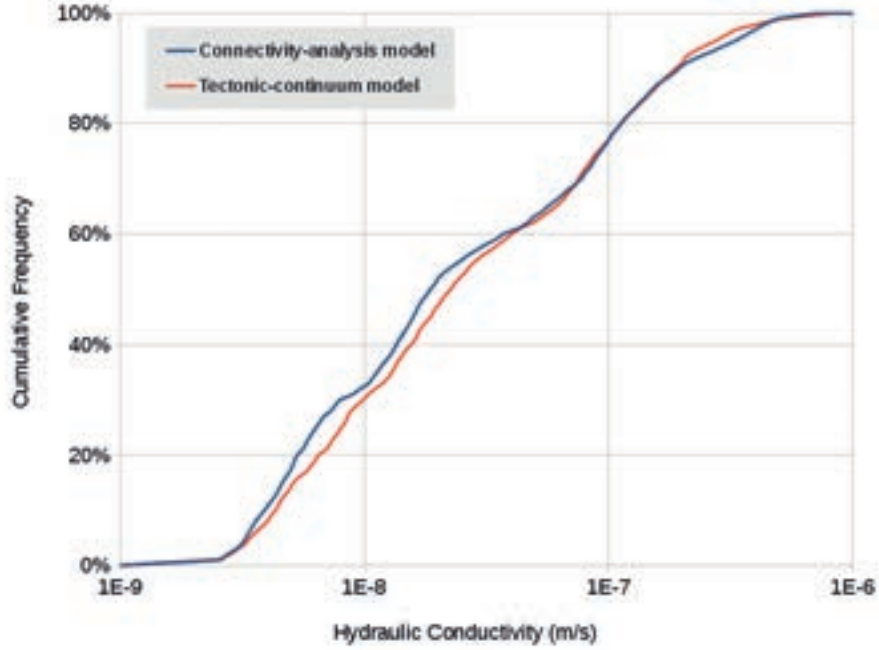

Figure 2.15: Cumulative distributions of hydraulic conductivity at repository depths, calculated by geometric upscaling for 50 m scale blocks, for the two DFN parameterizations (connectivity-analysis and tectonic-continuum models). Hydraulic conductivity values for this plot are calculated as the geometric mean of the directional conductivities for each block.

These estimates of (K_x, K_y, K_z) were then sampled randomly for each realization of the corresponding variants of the simplified model.

For vertical flow-path segments, the effective hydraulic conductivity is taken to be:

$$K_{eff} = K_z$$

For horizontal flow-path segments (e.g. parallel or perpendicular to the vaults), the effective hydraulic conductivity is calculated from K_x and K_y based on the assumption of an effective hydraulic conductivity tensor with principal components in the cardinal directions, using the formula:

$$K_{eff} = K_x K_y \left(\frac{\cos^2 \theta}{K_x} + \frac{\sin^2 \theta}{K_y} \right)$$

where θ is the azimuth of the flow direction.

Simplified model calculations were carried out by this method for 100 realizations of K_{eff} values drawn from each of the two DFN parameterizations.

The results are shown in Table 2.7 and Figure 2.16. The differences between the connectivity-analysis model and the tectonic-continuum model are very slight. For both models, the maximum increase in flow relative to the base case is roughly a factor of 3 for the vaults in SFR1, and a factor of 2.2 for the vaults in SFR3. Thus the maximum flows resulting from connections via relatively high-conductivity portions of the bedrock, with an ECPM representation based on the DFN models, is similar to the effect of direct connections through the rock mass via PDZs.

The connectivity-analysis model produces a slightly wider range of flowrates for a given vault. This can be explained in terms of the observations from Figure 2.15, that the connectivity-analysis model has a slightly more low-K_g blocks relative to the tectonic-continuum model, but also a slightly higher number of high- K_g blocks with $K_g > 2 \times 10^{-7}$ m/s.

Table 2.7: Comparison of flowrates (in liters/min) between the base-case model and the two variants based on sampling upscaled hydraulic conductivities from the connectivity-analysis (CA) and tectonic-continuum (TC) variants of the DFN parameterization, for each of the two different assumptions regarding flow partitioning among vaults.

| Vault	Individual Base case	Individual CA variant maximum	Individual TC variant maximum	Parallel Base case	Parallel CA variant maximum	Parallel TC variant maximum
1BMA	0.06688	0.2015	0.1998	0.0203	0.06123	0.06067
1BLA	0.06688	0.2015	0.1998	0.0207	0.06241	0.06202
1BTF	0.06687	0.2015	0.1998	0.0129	0.03903	0.03857
2BTF	0.06687	0.2015	0.1998	0.0129	0.03970	0.03867
Silo	0.04172	0.1785	0.1896	0.00001	0.00056	0.00090
1BRT	0.05430	0.1187	0.1181	0.0052	0.01137	0.01137
2BLA	0.05432	0.1188	0.1182	0.0104	0.02274	0.02262
3BLA	0.05432	0.1188	0.1182	0.0104	0.02274	0.02260
4BLA	0.05432	0.1188	0.1182	0.0104	0.02275	0.02259
5BLA	0.05432	0.1188	0.1182	0.0104	0.02272	0.02259
2BMA	0.05431	0.1187	0.1181	0.0076	0.01654	0.01645
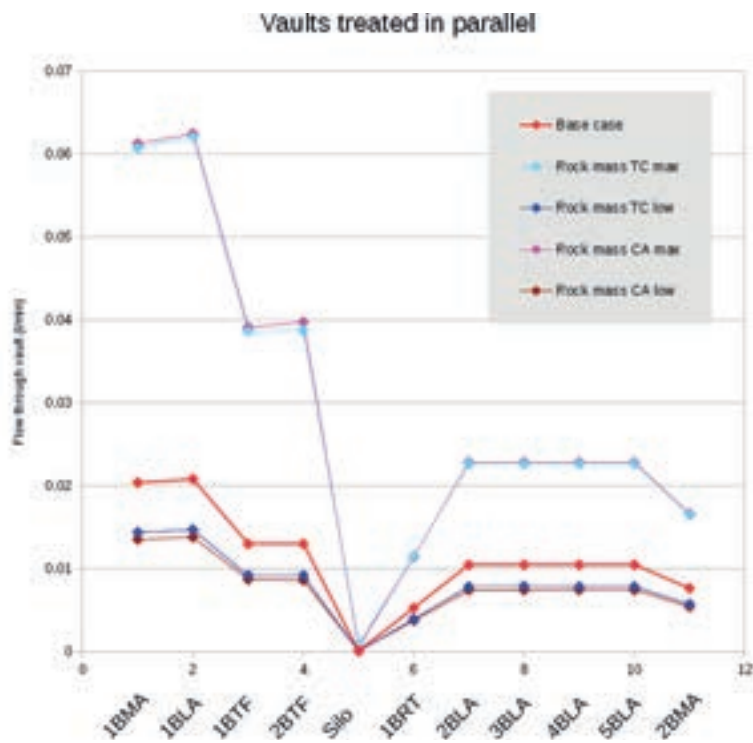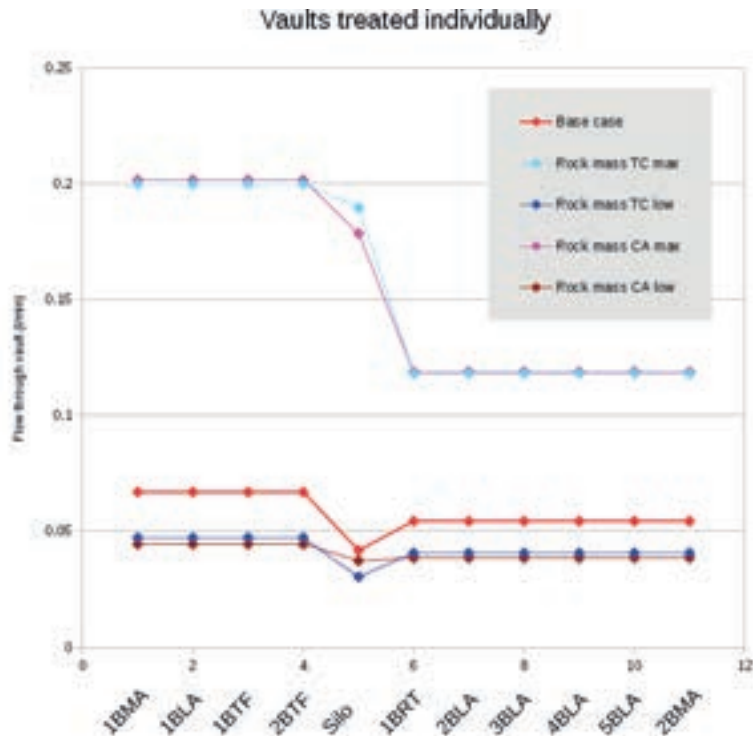
Figure 2.16: Comparison of calculation cases representing two different parameterizations of the rock mass, tectonic continuum (TC) and connectivity analysis (CA), as compared with the base case. The upper plot shows flowrates for the case where each individual vault is considered separately. The lower plot shows flowrates for the case where each of the vaults within each section of the repository are treated as conductors in parallel. In each plot the upper and lower lines for each parameterisation represent the maximum and minimum values from a set of 100 realizations.

3. Discussion

3.1. Main results from simplified model

The main results from the simplified model are summarized in Table 3.1, and compared in Figure 3.1 with the flows predicted by SKB's modelling for present-day and future temperate-period conditions.

The vault flows calculated using this simple 1D representation of the hydraulic system are reasonably comparable in magnitude to those calculated by SKB using much more complex 3D models, for future situations where the Baltic has receded beyond the present location of the SFR and its proposed extension. This builds confidence that the simplified model is useful as a reasonable and transparent basis for checking sensitivity of vault flows to main components of the hydraulic system.

The most significant controls on vault flows in the evaluated system are the properties of the rock mass, whether high-transmissivity probabilistic deformation zones (PDZs) or relatively high-conductivity ECPM blocks with properties calculated from the DFN model. Both of these are more significant for the relatively shallow SFR1 repository than for the deeper proposed expansion, because the part of the recharge-discharge path through the rock mass is proportionally longer for the shallower facility than for the deeper facility.

Deformation zone (HCD) transmissivities also affect flows significantly, but the effect is limited by rock-mass properties. A full order-of-magnitude increase in HCD

Table 3.1: Factor of increase (or decrease) in calculated flowrates relative to the base case for the main variants, for the situation where flow along the recharge-discharge path is evaluated for each individual vault.

Vault	No Baltic skin	High-T HCD	PDZ	DFN (CA) maximum	DFN (CA) minimum
1BMA	1.003	1.41	3.06	3.01	0.66
1BLA	1.003	1.41	3.06	3.01	0.66
1BTF	1.003	1.41	3.06	3.01	0.66
2BTF	1.003	1.41	3.06	3.01	0.66
Silo	1.002	1.22	1.72	4.28	0.89
1BRT	1.002	1.68	2.21	2.19	0.71
2BLA	1.002	1.68	2.21	2.19	0.71
3BLA	1.002	1.68	2.21	2.19	0.71
4BLA	1.002	1.68	2.21	2.19	0.71
5BLA	1.002	1.68	2.21	2.19	0.71
2BMA	1.002	1.68	2.21	2.19	0.71

transmissivities, reflecting the uncertainty in older vs. newer data from HCD intercepts, results in only a 40% increase for flows to the SFR1 vaults, and a 70% increase for the vaults in the proposed new facility. The greater effect for the proposed new facility is due to its greater depth, as this implies a longer path through HCDs and thus a proportionally greater distance over which HCD transmissivity limits flow, in this simplified model.

An alternative DFN parameterisation of the rock mass ("tectonic continuum" model vs. "connectivity analysis" model) has only a very minor effect on flows through vaults.

Combinations of high-transmissivity HCDs, and rock mass with either high hydraulic conductivities or high-transmissivity connections via PDZs, could lead to more extreme flows.

The influence of Baltic seabed sediments is negligible in the simple formulation. Replacing a "skin" due to a meter-thick clay layer with a connection via fractured rock has no significant effect on flows to vaults.

Differences between and among SKB hydrogeological model representations of vaults vs. engineering specifications may affect the relative magnitude of flows through different vaults. The potential role of unfilled gaps (without backfill) has not been analysed.

Combinations of geosphere variations with alternative parametrizations of degraded/cracked barriers have not been evaluated.
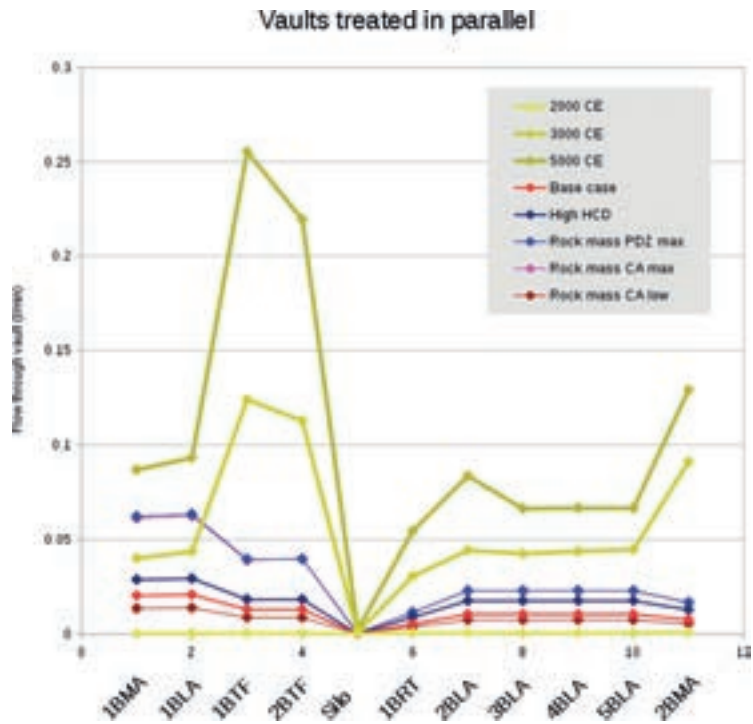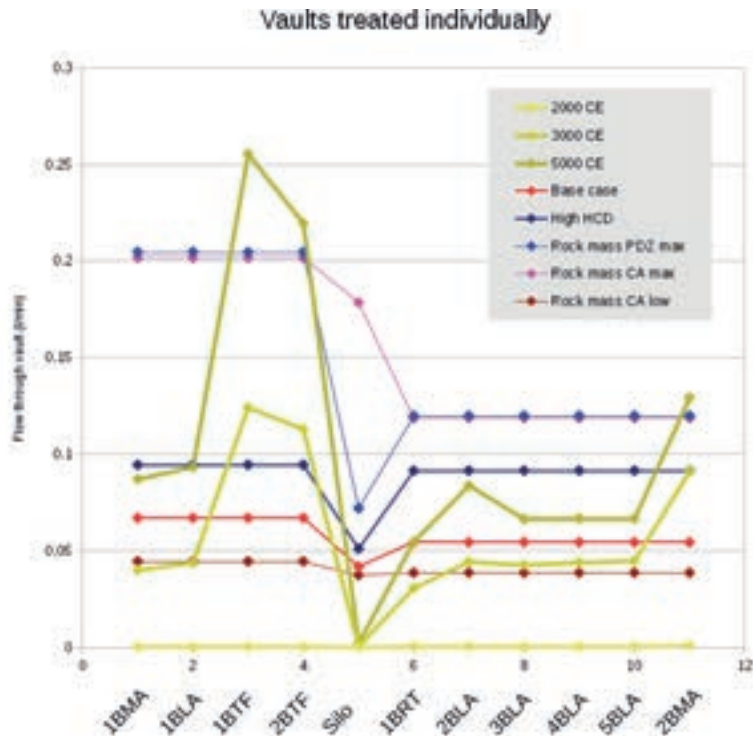
Figure 3.1: Comparison of results for the most significant calculation cases considered in the simplified-model analysis. The upper plot shows flowrates for the case where each individual vault is considered separately. The lower plot shows flowrates for the case where each of the vaults within each section of the repository are treated as conductors in parallel. In each plot the upper and lower lines for each parameterisation represent the maximum and minimum values from a set of 100 realizations.

3.2. Upscaling methodology for DFN models

The geometric upscaling methodology used in SR-PSU to derive ECPM properties from DFN models has not been evaluated directly in the simplified modeling for this review. A direct evaluation would require explicit network-flow simulations for the DFN models, both on the block scale and on the repository scale.

The upscaling issue is discussed in complementary information provided by SKB in a memorandum (SKB Document ID 1578373, p. 83). The authors do not present results from explicit network-flow simulations for comparison. Instead they present results based on versions of the DarcyTools model in which upscaling is performed for successively finer grids (4 m and 2 m). They argue that these refined ECPM grids come closer to approximating the irregular connectivity of the DFN model realizations that were used as the basis for flow and transport calculations in SR-PSU.

The main results of these calculations with refined ECPM grids are shown in Figure 3.2. Flows are generally reduced relative to the values calculated for the coarser grid. This reduction in flow is explained by a reduction in the artificially increased hydraulic conductivity caused by the DarcyTools upscaling method, as the grid (cell) size is reduced. This is a reasonable argument and the results support SKB's contention that the geometrical upscaling method is conservative for the purpose of predicting flows through vaults.

Corresponding transport calculations (with a particle-tracking method), evaluated in terms of the distributions of transport resistance F (Figure 3.3) show that the refined versions of the model produce an increase in the frequency of paths with lower transport resistance (mainly in the range 2×10^3 yr/m to 3×10^3 yr/m for SFR1 and 4×10^3 yr/m to 1×10^4 yr/m for SFR3).

This type of shift is consistent with expectations for a more discrete representation of the fracture network. Although the shift is modest (e.g. the 10th percentile value of F for SFR1 is decreased by 20% at worst), larger shifts could be expected for a fully discrete representation. The analysis furthermore is limited to a single realization.

Thus this complementary analysis by SKB has not fully bounded the consequences of their upscaling method, in conservative terms. Consequences of a greater decrease (e.g. a 50% decrease in the 10th percentile value of F for SFR1, and corresponding decreases up to the median value) should be considered to determine if the results for safety assessment could be sensitive to the ECPM upscaling method.
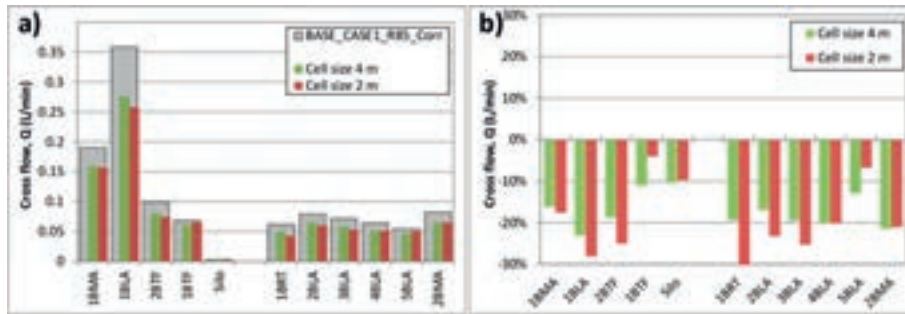
Figure 3.2: Effect of finer discretization of ECPM grid on calculated cross flows to vaults, based on the DarcyTools upscaling method. The comparison is shown (a) in absolute terms and (b) in terms of changes relative to the coarser ECPM model used for SR-PSU. From SKBdoc 1578753, Figure 3-38.
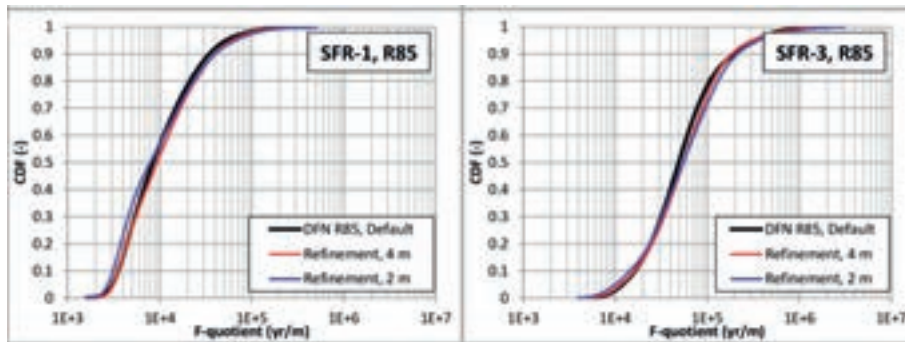

Figure 3.3: Effect of finer discretization of ECPM grid on transport resistance *F*, based on the DarcyTools upscaling method for (left) SFR-1 and (right) the proposed SFR-3. From SKBdoc 1578753, Figure 3-38.

3.3. Shallow Bedrock Aquifer

Uncertainty regarding the hydrogeological properties and extent of Shallow Bedrock Aquifer (SBA) structures was not addressed in the original set of documents supporting the SR-PSU safety case. According to Öhman et al. (2014), p. 27: "*As no SBA structures are in direct contact with disposal rooms in SFR 1 or SFR 3, variants of SBA structures are not addressed in the sensitivity analysis. Similarly to earlier TDs, all simulations include a fixed SBA variant, in which all 8 structures are included (SBA1 to SBA8).*" A similar statement was given in SKBdoc 1395214.

This cannot be directly addressed with the simplified modelling approach employed in this review, due to the intrinsic three-dimensional aspects and the complicated dependence on details of geometry, properties, and hydraulic connections to other structures. SSM asked for complementary information regarding this issue (SSM2015-725-40, Point 6).

In response, SKB has provided a sensitivity analysis (SKBdoc 1578373, p. 78-80). The sensitivity analysis considers a case in which the SBA structures are entirely

omitted from the 3-D model. The results in terms of flows to vaults are shown in Figure 3.4.

The results show that the SBA structures as implemented in the base case for SR-PSU do not have a significant effect on flows for SFR1. This is explained by the fact that the SBA structures (as interpreted) were not associated with flow paths for SFR1.

For the planned extension, SFR3, removing SBA structures results in a reduction in cross flows, despite that SBA structures were intentionally avoided in the localisation of the extension. The largest effect is seen for 2BMA, where removing the SBA features results in a 31% reduction in flow. This effect is attributed to the relative proximity of 2BMA to structures SBA1-6 and the wedge between NNW1034 and NW0805.

The effects on release locations are also minor for most vaults. The main effect of the SBA structures is to direct more particles upward to biosphere object 157_2, rather than to the more remote biosphere objects 157_1 and 116. For the vault most strongly affected by the SBA structures, 2BMA, this effect is seen for approximately 10% of the released particles.

From this it can be concluded that the SBA structures, as interpreted in the base case model for SR-PSU, have only a minor effect on cross flows and discharge paths.

The sensitivity of these results to possible extensions of the SBA structures, or to alternative interpretations of their properties, has not been evaluated. If the SBA structures extend beyond their current interpreted positions, or if their transmissivity is higher than the values estimated from limited field data, presumably the effects could be in the direction opposite to the effects of removing these structures, i.e., cross flows might increase in SFR3 and discharge might be concentrated more strongly in the closest biosphere object.

The magnitude of such effects cannot be evaluated from the complementary information provided by SKB. However considering that the consequences of increasing transmissivity and connectivity in the upper part of the model will be limited by the flow resistance of the deeper part of the model, the magnitude of the effects on flows would likely not be significantly larger than the magnitudes observed for the sensitivity case considered. Hence considering an increase in flowrates for SFR3 vaults by about one third should be sufficient to scope the consequences for the safety case.
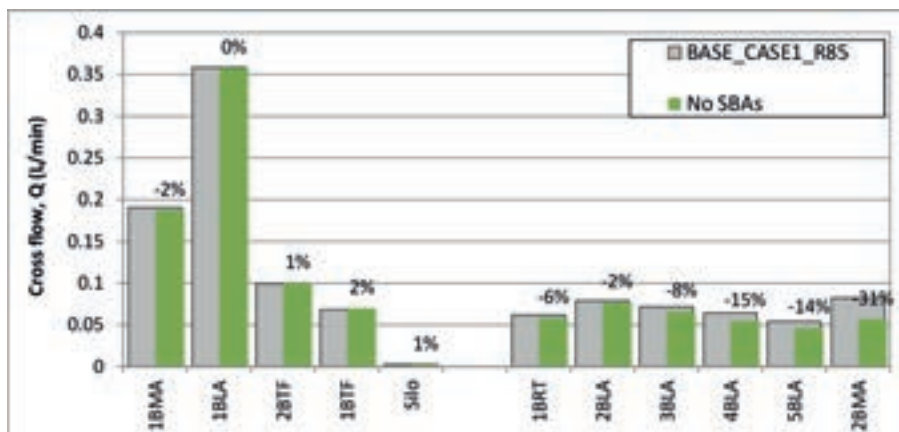
Figure 3.4: Effect on disposal-room cross flows of excluding deterministically modelled Shallow Bedrock Aquifer features. The comparison is based on the base case, 5000 AD, but without SBAs. From SKBdoc 1578753, Figure 3-35.

3.4. Comparison of simplified model results with complementary information

Supplementary modelling results provided as complementary information by SKB (SKB document 1578373) provide further insights into the sensitivity of the flow and transport calculations with respect to parameterisations of the HSD (regolith), the HCD (fracture zones), and HRD (rock mass) domains. These results are discussed in the following paragraphs.

3.4.1. HSD parameterisation

Results of complementary simulations by SKB to assess alternative HSD parameterisations are presented in p. 43-56 of SKB document 1578373. Five variants were considered in addition to the base case. The calculation cases for these HSD variants are numbered 2 through 6 (the authors use 1 to refer to the base case):

- HSD case 2 is a homogenous HSD (both terrestrial and seabed).

- HSD cases 3 and 4 involve, respectively, a uniform decrease and a uniform decrease in HSD hydraulic conductivity (both terrestrial and seabed).

- HSD case 5 considers a decrease in vertical hydraulic conductivity due to a hypothesized "bedrock-surface choking" effect.

- HSD case 6 considers an order-of magnitude decrease in the hydraulic conductivity of seabed sediments.

HSD case 6 is the one that bears the closest relation to the alternatives regarding Baltic "skin" that have been considered here using the simplified model, as it considers a reduction in the hydraulic conductivity in seabed sediments independent of terrestrial sediments.

SKB's complementary results indicate that decreasing the hydraulic conductivity of clay deposits above the repository can result in slightly increased flows through the repository, by up to 28% for 1BMA, 17% for the Silo and 15% for 1BLA, but to a lesser degree for other vaults. This increase is attributed to forcing discharge locations farther out from shore to locations where the seabed has more permeable sediments, with the results that higher hydraulic heads are maintained in the area just upstream of the repository. These effects of spatially heterogeneous sediments cannot be represented in the simplified 1-D model, in which the only function of these clays is to increase resistance to flow.

The effects of the other HSD variants on flows through vaults generally fall within a factor of 0.5 to 1.25 of the values for the base case. Thus the effects of all of the variants considered are within the range of factors 0.5 to 1.3.

3.4.2. HCD parameterisation

A "conservative HCD" variant was considered in SKB's supplementary calculations with results as presented in parameterisations are presented in p. 57-58 of SKB document 1578373. This variant substitutes transmissivity estimates based on older data from SDM-PSU for 10 of the 40 HCDs in the base-case model, mainly those close to SFR1 for which data were obtained earlier. The factor of increase in transmissivity for these zones varies from just 1.3 to 12.6, as detailed in Table 3.2. For the other zones, there was no change in values.

This "conservative HCD" variant produces an increase in flows to most of the vaults in SFR1, except for 1BLA where a 22% decrease is predicted. The maximum increase is 77% for 1BTF, with increases of 7% to 9% for the other SFR1 vaults. The change in total flow through SFR1 is practically unchanged (within 1%) so the changes reflect a redistribution of flow away from 1BLA and into the other vaults, due to the modified contrasts between HCDs.

For SFR3 the effects of the "conservative HCD" variant are much less. All vaults in SFR3 see slightly higher flows but the increase is only 1% to 6%, with 1BRT and 3BLA showing the greatest effect, and 2BMA and 5BLA showing the least effect.

The lesser effect on SFR3 relative to SFR1 can be attributed to the fact that the "conservative HCD" variant considers changes mainly in HCDs that are close to SFR1, with comparatively little influence on SFR3. Thus this case is less conservative (but possibly more realistic) than the high-T HCD variant considered with the simplified model. However the maximum increase in flow predicted by the simplified model (68%) is close in magnitude to that for the "conservative HCD" variant (77%).

Table 3.2: HCDs with increased transmissivities in "conservative HCD" variant. Based on Table 1-1 of SKB document 1578373.

Zone	Base case log $T_{eff}(0)$	Conservative HCD log $T_{eff}(0)$	Factor of increase
ZFM871	-5.2	-4.8	2.5
ZFMNE0870	-6.3	-6.2	1.3
ZFMNE3118	-6.6	-6.2	2.5
ZFMNW0002	-4.6	-3.6	10.0
ZFMNW0805a	-4.7	-4.3	2.5
ZFMNW0805b	-5.5	-4.7	6.3
ZFMWNW0001	-3.9	-2.9	10.0
ZFMWNW0813	-5.9	-5.7	1.6
ZFMWNW1035	-5.0	-4.0	10.0
ZFMWNW3259	-5.3	-4.2	12.6

3.4.3. HRD parameterisation

A variant of the DFN model for the HRD in the SFR regional domain is described in p. 6-7 and with results presented in p. 58-63 of SKB document 1578373. Although described as an "alternative parameterisation" of the DFN model, this variant is based on the same "connectivity analysis" DFN parameterization as was used for the SR-PSU base case. The difference is only in the assumed form of correlation between fracture size and transmissivity, with the new variant considering the case of imperfect correlation (called "semi-correlated" in SKB's nomenclature) rather than perfect correlation.

The effect of assuming imperfect rather than perfect correlation between fracture size and transmissivity is a roughly a 10% reduction in net flow through the facility, with changes of -30% to +15% for individual vaults, depending on the stochastic realization of the transmissivity values (for a single realization of the network geometry). Thus the effects of this variant on flows through vaults fall well within the bounding values calculated with the simplified model.

4. Conclusions

The most significant controls on vault flows in the simplified model are the properties of the rock mass, whether high-transmissivity probabilistic deformation zones (PDZs) or relatively high-conductivity ECPM blocks with properties calculated from the DFN model. A conservative assessment of the potential effects of these rock mass features indicates that the maximum increase on vault flows relative to the base case is approximately a factor of 3 for SFR1, and a factor of 2.2 for SFR3. These high-flow cases result from considering the maximum effects of PDZs or rock-mass variability, as sampled from multiple realisations of the DFN model.

An alternative DFN parameterisation of the rock mass ("tectonic continuum" model vs. "connectivity analysis" model) has only a very minor effect on flows through vaults. Likewise a variation with respect to the assumed form of correlation of fracture transmissivity to fracture size, considered in supplementary calculations by SKB, has only minor effects when applied to a single realization of the DFN geometry. Thus details of the DFN parameterisation are found to be less important than the potential effects of spatial variability, or the corresponding uncertainty represented by differences between stochastic realizations of DFN geometry.

Deformation zone (HCD) transmissivities also affect flows significantly, but the effect is limited by rock-mass properties. A full order-of-magnitude increase in HCD transmissivities, reflecting the uncertainty in older vs. newer data from HCD intercepts, results in only a 40% increase for flows to the SFR1 vaults, and a 70% increase for the vaults in the proposed new facility. A more limited and localized increase in transmissivities of HCDs near the SFR1 facility, evaluated in supplementary calculations by SKB, predicts little effect on flows for the proposed SFR3 extension and lesser but comparable increases in flows for SFR1.

The influence of Baltic seabed sediments is negligible in the simple formulation. Replacing a "skin" due to a meter-thick clay layer with a connection via fractured rock has no significant effect on flows to vaults. In SKB's supplementary calculations using a much more complex 3-D model, more significant effects are seen due to the influence of localized clay deposits on constraining discharge locations. The maximum increase in vault flows caused by these clay deposits is 28% for 1BMA, 17% for the Silo and 15% for 1BLA, and less for the other vaults.

Combinations of high-transmissivity HCDs, and either high rock-mass conductivities or high-transmissivity connections through the rock mass via PDZs, could lead to more extreme flows.

Neither the simplified model nor SKB's supplementary information provide direct information about the potential increases in flows through vaults, if the shallow bedrock aquifer (SBA) structures are more extensive or have higher transmissivities than have been assumed in SKB's base-case model. However, based on SKB's evaluation of a case in which SBA features were removed from the base-case model, an increase in vault flows by about one third should be sufficient to account for the uncertainty that propagates from this uncertainty to performance assessment calculations.

5. References

Abarca, E., Sampietro, D., Miret, M., von Schenk, H., 2013, Flow modelling on the repository scale for the safety assessment SR-PSU. SKB TR-13-08, Svensk Kärnbränslehantering AB.

Bosson, E., Sassner, M., Sabel, U., and Gustafsson, L-G., 2010. Modelling of present and future hydrology and solute transport at Forsmark. SR-Site Biosphere. SKB R-10-02, Svensk Kärnbränslehantering AB.

Dverstorp, B., Geier, J. and Voss, C., 1996. Simple evaluation of groundwater flux and radionuclide transport at Äspö (SITE-94). SKI Report 96:14, Swedish Nuclear Power Inspectorate, Stockholm, Sweden.

Geier, J., 2014. Assessment of flow-related transport parameters for performance assessment calculations for canister positions in the KBS-3 repository at Forsmark. SSM Technical Note 2015:40.

Geier, J., 2017. Review of hydrogeological aspects of SR-PSU – main review phase. SSM report 2017:xx (this volume), Strålsäkerhetsmyndigheten.

Odén, M., Follin, S., Öhman, J., and Vidstrand, P., 2014. SR-PSU Bedrock hydrogeology. Groundwater flow modelling methodology, setup and results. SKB R-13-25, Svensk Kärnbränslehantering AB, Stockholm.

Oda, M., 1985. Permeability tensor for discontinuous rock masses. Geotechnique, Vol. 35, No. 4, p. 483-495.

SKB, 2013. Site description of the SFR area at Forsmark at completion of the site investigation phase, SDM-PSU Forsmark. SKB TR-11-04, Svensk Kärnbränslehantering AB, Stockholm.

SKB docID 1395214 ver. 2, 2013. TD08 – SFR 3 effect on the performance of the existing SFR 1. Svensk Kärnbränslehantering AB, Stockholm.

SKB docID 1578373, 2017. TD15 Complementary simulation cases in support of SR-PSU. Svensk Kärnbränslehantering AB, Stockholm.

SSM2015-725-40, Begäran om komplettering av ansökan om utökad verksamhet vid SFR – hydrogeologi. Strålsäkerhetsmyndigheten, Stockholm.

Svensson, U., Ferry, M., and Kuylenstierna, H-O., 2010. DarcyTools version 3.4 – Concepts, methods and equations. SKB R-07-38, Svensk Kärnbränslehantering AB, Stockholm.

Öhman, J., Bockgård, N., and Follin, S., 2012. Site investigation SFR. Bedrock hydrogeology. SKB R-11-03, Svensk Kärnbränslehantering AB, Stockholm.

Öhman, J., Follin, S., and Odén, M., 2013. Site investigation SFR. Bedrock hydrogeology – Groundwater flow modelling. SKB R-11-10, Svensk Kärnbränslehantering AB, Stockholm.

Öhman, J., Follin, S., and Odén, M., 2014. SR-PSU Hydrogeological modelling. TD11 – Temperate climate conditions. SKB P-14-04, Svensk Kärnbränslehantering AB.

Coverage of SKB reports

Following reports have been covered in the review.

Table A1:1

Reviewed report	Reviewed sections	Comments
SKB P-14-04. SR-PSU Hydrogeological modelling TD11 – Temperate climate conditions.	All	Set-up and parameterization of regional-scale hydrogeological models.
SKB R-13-25. SR-PSU Bedrock hydrogeology. Groundwater flow modelling methodology, setup and results.	All	General account of hydrogeological models used in SR-PSU
SKB R-14-14. Flow and transport modelling on the vault scale. Supporting calculations for the safety assessment SR-PSU.	All	Set-up and parameterization of repository-scale models
SKB TR-13-08. Flow modelling on the repository scale for the safety assessment SR-PSU.	All	Set-up and parameterization of vault-scale.
SKB TR-14-01. Safety analysis for SFR. Long-term safety. Main report for the safety assessment SR-PSU.	Focused on sections on hydrogeological modelling and construction of scenarios and calculation cases.	Main reference for SR-PSU.
SKB TR-14-02. Initial State Report.	Focused on descriptions of vault geometry and materials.	Used for comparison with modeling reports.
SKB document 1578373.	All	

3

Authors: R. Metcalfe[1], S. J. Benbow[1], J. C. Wilson[1], D. Savage[2]
[1]Quintessa Limited, Henley on Thames, UK
[2]Savage Earth Associates, Bournemouth, UK

Review of geochemical aspects of SR-PSU – Main review phase

Abstract

This report contributes to the Strålsäkerhetsmyndigheten's (SSM's) Main Review Phase of the SR-PSU safety assessment, which has been submitted by Svensk Kärnbränslehantering AB (SKB). This safety assessment supports SKB's licence application to extend its final repository for low- and intermediate-level waste at Forsmark (SFR) in the municipality of Östhammar, Sweden.

During its initial review phase of the SR-PSU, SSM commissioned three reports from its consultants (2016:08, 2016:09 and 2016:12) that identified several geochemical issues for further review in the main review phase. The present document provides more in-depth reviews of the following issues arising from these earlier reports:

- the potential for fracture armouring in concrete components of the engineered barrier system (EBS) by secondary minerals produced as inflowing groundwater interacts with porewater in the cementitious concrete matrix;
- the potential for Ca-bearing minerals in cement within the EBS to be replaced by Fe(II)-bearing minerals, with consequent implications for the cement's chemical buffering capability and longevity; and
- conservatism in the radionuclide retardation model in the SR-PSU assessment, taking account of the approach to selecting K_d values and the combined retardation effect of sorption and rock matrix diffusion.

Were it to occur along fractures in concrete that remain conductive with respect to groundwater, potentially armouring could cause relatively low-pH water to contact the wastes. In this case, corrosion of the barrier system's metal components might not be passivated to the extent expected by SKB. Additionally, the solubilities of certain radionuclides in the groundwater might be greater than SKB anticipate. Each of these processes might cause a higher flux of radionuclides from the SFR than assessed in the SR-PSU.

In the present study, a number of coupled models were developed to investigate the effects of armouring. These models simulated the inflow of groundwater to a vault, via a fracture in a concrete wall. The simulations all revealed a tendency for the fracture to self-seal by the precipitation of Mg-rich secondary minerals.

Among the coupled simulations a modelling case was implemented to investigate the possibility that brucite ($Mg(OH)_2$) precipitation might occur 'upstream' of the cement, in the backfill. This process, if it occurs, would remove some of the Mg from the groundwater entering the concrete fractures. Such removal could potentially reduce the amount of fracture clogging that might be expected, brucite being a major predicted clogging phase. However, the modelling demonstrates that a fracture is still likely to be clogged by precipitation of solid phases within it, even if dissolved Mg precipitates as brucite before water reaches the fracture. In this case the solids precipitated clogging the fracture are likely to comprise carbonate minerals such as calcite and secondary aluminosilicates.

The extent to which the cement in the walls of a fracture buffers the pH of groundwater flowing through the fracture depends upon the degree to which the fracture fills with minerals and the diffusivity of the armouring layer. The model results show that the smaller the thickness of armouring and the smaller the

diffusivity of the armouring layer compared to that of the cement matrix, the further along the fracture will relatively low-pH water penetrate. The smaller thickness is required to maintain a significant advective contribution to transport, while the smaller diffusivity is required to limit upstream buffering of fracture porewater by cement interactions. The greatest perturbation of pH from values in the cement matrix is given by model variant cases in which there is a small relative diffusivity of the armouring layer (10^{-3}), when a continuously open fracture is assumed (the fracture porosity is limited to 0.1). In these cases, there would be a possibility that pore waters with pH ~11 could enter the vault from a fracture in the cement. However, even in these cases the decreased pH at downstream locations only reduces to around 10.8 after 10,000 years.

The modelling suggests that there would be no significant safety-relevant impacts on the chemical buffering capability of the cement in the SFR vaults over the assessment time frame considered here of 10,000 years.

In the SR-PSU, SKB has apparently given no consideration to the possibility that Fe may combine with solid phases present in cementitious barriers, thereby potentially altering the chemical buffering capability of these barriers and their longevity. It is important to assess whether such Fe-uptake could be significant and, if so, what implications there might be for the safety assessment.

To explore the potential for Fe(II) release from iron/steel corrosion to result in decreasing pH in cement pore fluids, the following tasks were undertaken:

- steel corrosion processes were reviewed;
- iron compounds associated with cement were reviewed; and
- thermodynamic modelling was undertaken.

The thermodynamic modelling included: a review of the pH conditions associated with buffering by different cement solids and steel corrosion products; the aqueous solubility of iron/steel corrosion products; the potential for Fe-rich cement solids to form in cement and the effect of adding dissolved Fe(II) to cement pore fluid on pH.

Overall, although data on Fe(II) behaviour in cement are lacking, thermodynamic modelling suggests little potential for Fe(II) to replace Ca in cement to any significant extent. Such replacement as does occur would not suppress hyperalkaline conditions.

SKB has modelled retardation of radionuclides in the geosphere by a combination of:

- rock matrix diffusion; and
- sorption on minerals within the rock matrix, which contact radionuclides as due to rock matrix diffusion.

SKB use linear distribution coefficients (K_d values) to represent sorption. The K_d values used are based on the data acquired by SKB to support its SR-Site safety assessment for the proposed Spent Fuel (SF) repository at nearby Forsmark. In the SR-Site assessment 'transfer factors' were used by SKB to adjust laboratory sorption data to in-situ conditions. A similar approach was used for the SR-PSU assessment. SKB assumed that all the transfer factors used in the SR-Site assessment, except for the chemical transfer factor, f_{chem}, are also valid for the sub-surface conditions around the SFR. However, SKB specified different f_{chem} values

because the groundwater chemistry around the SFR repository is different to that in the deeper proposed SF repository site.

The K_d approach does not accurately represent actual sorption mechanisms and uncertainties associated with applying the approach are large. However, for the far-field, SKB's analysis provides confidence that the limitations of the K_d approach does not have adverse consequences for the demonstration of safety; overall safety is much more influenced by sorption in the near-field than in the far-field. These conclusions are supported by SKB's findings that:

- Removing sorption in the rock matrix from the global warming variant of the main scenario ('Loss of barrier function – no sorption in bedrock' scenario) increases peak doses from 8.2 µSv to 10.4 µSv, still below the dose criterion of 14 µSv.
- In contrast, removing sorption in the repository near-field from the global warming of the main scenario ('Loss of barrier function – no sorption in the repository') causes the peak dose to increase by a factor of 5 to 41.4 µSv,

However, SKB has not demonstrated that its treatment of radionuclide retardation in the geosphere is truly conservative. Neglecting sorption on fracture-filling minerals is not conservative with respect to retardation by rock matrix diffusion, because radionuclides are permitted to enter the rock matrix more readily than if sorption on fracture-filling minerals does occur.

SKB's analysis of the bedrock's barrier function considers only uncertainties in sorption. Within the set of analysed scenarios, there is apparently little consideration of the impact of uncertainties in rock matrix diffusion. The absence of sorption in the 'Loss of barrier function – no sorption in bedrock' scenario' presumably causes diffusing radionuclides to penetrate more rapidly and / or to greater depth within the rock matrix than in the other scenarios. The retardation provided by rock matrix diffusion is therefore enhanced compared to the other scenarios in which sorption in the matrix occurs. This raises the question as to the relative importance of rock matrix diffusion and sorption in the rock matrix as retardation mechanisms. Specific questions are:

- If rock matrix diffusion and sorption are both neglected, then would the dose criterion be exceeded?
- If the answer is yes, then how much would rock matrix diffusion need to be diminished from that attained in the main scenario, for the dose criterion to be exceeded?

None of the reviewed documents provide details of the matrix diffusion depth attained in any of the scenarios, or of the rate of radionuclide uptake by this mechanism. It therefore cannot be judged how important this effect may be. To answer these questions, it would be helpful for SKB to present additional cases in which rock matrix diffusion is diminished in order.

Contents

1. Introduction

1.1. Purpose

The Swedish Radiation Safety Authority (SSM) received an application for the expansion of SKB's final repository for low and intermediate level waste at Forsmark (SFR) on the 19 December 2014. SSM is tasked with the review of the application and will issue a statement to the government for its consideration in due course. An important part of the application is SKB's assessment of the long-term safety of the repository, which is documented in the safety analysis named SR-PSU. SSM's review is divided into an initial review phase and a main review phase. The work presented here forms part of the main review phase. The general objective of the assignment is to evaluate the adequacy of the results of SKB's geochemical analysis in SR-PSU for the subsequent steps in the safety analysis. Moreover, it is of importance to assess if SKB has shown that they have an adequate general understanding of the geochemistry at the site and its evolution over time. This review and assessment considers the overall quality of supporting data, the appropriateness of the conceptual models, the credibility of the calculations and SKB's interpretation of the results. Emphasis has been upon aspects that are likely to have the largest influence on repository performance.

During its initial review phase of the SR-PSU, SSM commissioned several reports from its consultants: 2016:08, 2016:09 and 2016:12. These initial reviews identified several geochemical issues for further review in the main review phase. The present document provides more in-depth reviews of SKB's treatment of three of these issues:

- **Investigation of the potential for 'armouring' of fractures in concrete (Section 4)**. The interface between fractures and the concrete matrix could become armoured through the precipitation of carbonates or other minerals. This could act to isolate the cement from the fracture pore water, limiting the concrete leaching process and its pH-buffering effect, and allowing lower-pH groundwaters to more rapidly penetrate deeper into the fractures. This could have consequences for the corrosion passivation property of the concrete, possibly leading to corrosion of steel reinforcement bars ('rebars') near the lower pH groundwaters whose volumetric expansion could lead to additional cracking. Additionally, the altered physical properties of the fracture-concrete matrix interface and the lower pH environment could hinder sorption and thus affect the transport and retention properties of any radionuclides that are released from the waste form.

- **Investigation of potential for replacement of Ca- with Fe(II)-bearing minerals (Section 5)**. Lowering of pH due to extensive anaerobic metal corrosion and the replacement of Ca-bearing solids, such as portlandite, with Fe(II)-bearing solids could tend to inhibit ongoing passivation of steel corrosion reactions in the near-field, thereby enhancing concrete degradation rates in the near-field compared to those assumed by SKB, through damage associated with the corrosive expansion of rebars.

- **Investigation of K_d values and representation of retardation in the radionuclide transport model for the SR-PSU assessment (Section 6)**. Retardation of radionuclides is represented by a combination of sorption and rock matrix diffusion. The former process is modelled using the simplifying assumption that it can be described by linear, equilibrium partitioning of radionuclides between aqueous and solid phases (i.e. the "K_d" approach). Rock matrix diffusion assumes that the matrix pore space between water-conducting fractures is fully accessible to diffusing solutes. Sorption is assumed to occur only in the rock matrix and not on minerals within / lining the water-conducting fractures. The question arises as to whether the overall representation of retardation is in fact conservative.

1.2. Background information

The report TR-14-01 (SKB, 2014a) is the main report for the safety assessment, describing the initial groundwater chemistry in Section 4.8 (page 122-128), the reference evolution in Section 6 for the first 1 ka after closure (Sections 6.3.6, 6.3.7, and 6.3.8 describe geochemical evolution, chemical evolution of the waste domain and evolution of the engineered barriers respectively), with a similar arrangement of descriptions for the temperate climate domain after 1 ka (Section 6.4), and periods of periglacial climate domain after 1 ka (Section 6.5). Scenarios are described in Section 7, with a 'less probable' scenario of relevance being 'accelerated concrete degradation' in Section 7.6.3 (calculational results for this scenario in Section 9.3.3).

The Conclusions Section of TR-14-01 (page 364 and following) has the following relevant statements defining the functions and geochemical requirements of the natural and engineered barriers:

- '*the rock also provides a stable chemical environment, including anaerobic conditions which contribute to protecting reducing conditions at repository depth. Reducing conditions imply that iron corrodes only slowly and that the mobility of certain safety critical radionuclides (particularly radioisotopes of uranium) is low*'. (page 370).
- '*For the Silo, the pH-buffering function of the concrete and the grout keeps gas production due to microbial activity and iron corrosion low. The choice of concrete as an engineering material also ensures good sorption properties*'. (page 371).
- '*For 1BMA and 2BMA vaults, the long-term evolution of the flow-limiting ability of the concrete structure is associated with a transformation of cement minerals, and the flow-limiting function is maintained for at least 20,000 years*'. (page 371).
- '*For 1BTF and 2BTF vaults, the pH-buffering function of the concrete and the grout keeps gas production due to microbial activity and iron corrosion low. The choice of concrete as an engineering material provides good sorption*'. (page 371).
- '*For the BRT vault, the function of the concrete is to limit the water flow in and around the RPVs and to maintain high pH conditions in order to limit corrosion of steel. Limited corrosion delays the release of the surface contamination on the inside of the RPVs, as well as the release of neutron activation products*'. (page 372).
- '*Sorption of radionuclides has been shown to be the main mechanisms controlling retardation in the repository. Sorption occurs mainly on the*

> *cementitious materials in barriers and waste packages. The sorption depends on the amount of available concrete surfaces, but also on the chemical composition of the water in the repository. The importance of sorption is strongly related to the chemical characteristics of individual radionuclides, including their redox state*'. (page 373).

- '*The pH in BMA is maintained at such a level that microbial degradation of C-14-containing waste is kept so low that release of C-14 as methane gas will not be a dominant transport pathway*'. (page 377).

Geochemical aspects of the evolution of the site is described in Chapter 5 of TR-14-05 (SKB, 2014b). The following key processes are described: advection and mixing of solutes; diffusion of solutes; speciation and sorption; rock-water interactions in the rock matrix; water-rock interactions in fractures; microbial processes; degradation of grout; colloidal processes; methane hydrate formation; salt exclusion; and earth currents.

Chemical processes in waste and waste packaging are discussed in Sections 3.5 and 4.4 of TR-14-03 (SKB, 2014c). For the most part, these are fundamental descriptions of relevant processes as related to conditions in SFR and are thus analogous to FEP descriptions. These processes are: advection; diffusion; sorption/uptake; colloid formation and transport; dissolution, precipitation and recrystallisation; degradation of organics; water uptake/swelling; microbial processes; metal corrosion; and gas formation and transport.

The equivalent report for the engineered barrier system is TR-14-04 (SKB, 2014d) and has a similar layout and text content as TR-14-03 described above.

The FEP report for SR-PSU is TR-14-07 (SKB, 2014e) and provides direct links to the processes defined above in the 'Waste and Waste Packaging' (TR-14-03) and 'Engineered Barriers' (TR-14-04) process reports described above.

Detailed modelling of the evolution of the degradation of concrete in the BMA vaults is described in the report by Höglund (2014; R-13-40). This includes modelling of both physical and chemical processes and is in much greater detail than similar studies published previously by SKB (e.g. Gaucher et al., 2005; Cronstrand, 2007). This report by Höglund is the mainstay for the understanding of concrete degradation as presented in the main report (TR-14-01).

A more simplistic and conservative assessment of the degradation of concrete is presented in the report by Cronstrand (2014) which treats the near-field as a mixing tank and deals with advection and equilibrium reactions only to model pH evolution with time. Cronstrand (2014) states that his approach is a '*coarse and conservative method exclusively applied to provide the global average pH evolution*'. He notes that substantial local deviations are expected due to the inhomogeneous character of the waste compartments, flow path restrictions etc. Höglund's report on the other hand (Höglund, 2014), is more detailed and presents a series of analytical and numerical reactive transport models focused on investigating physical and chemical processes that cause fractures and chemical degradation in concrete barriers, and the impact of fractures on the long-term performance of SFR. His report also provides data on hydraulic conductivities, effective diffusivities and porosities of the concrete barriers and addresses the issue of fractures in SFR barriers explicitly for the first time.

2. Site conditions

2.1. Groundwater

Hydrochemical data for the SFR site are presented in chapter 8 of the site description report (SKB, 2011) and in more detail in Nilsson et al. (2011), with water-rock modelling described in Gimeno et al. (2011) and details of fracture mineralogy in Sandström and Tullborg (2011) and Sandström et al. (2011). These studies describe four major groundwater types at SFR (Figure 2-1; Table 2-1):

1. Local Baltic Seawater type;
2. Littorina type water with a glacial component;
3. Brackish-glacial water type, and
4. Mixed brackish water (transition type).

SKB believes that the distribution of the different groundwater types shows that the major deformation zones have served as important groundwater flow pathways over long periods of geological time while single discrete fractures in rock volumes between zones generally contain older and more isolated groundwater. The steeply dipping geological structures have facilitated the drawdown of modern Baltic Seawater which has been observed since excavation and construction of the SFR commenced some twenty years ago.
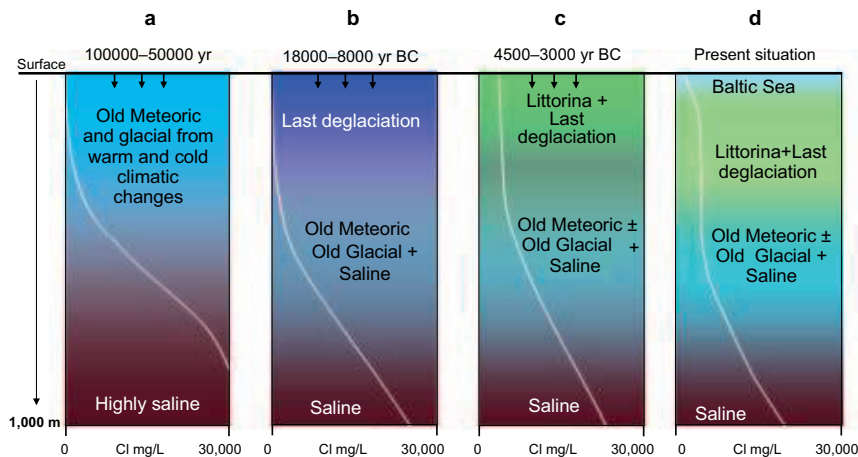

Figure 8-2. Sketch showing tentative salinities and groundwater type distributions versus depth down
Figure 2-1: Salinities and groundwater types vs depth to 1000 m for the transmissive deformation zones at SFR (from SKB, 2011). From left to right: a) situation prior to the last deglaciation, b) last deglaciation and intrusion of Late Weichselian meltwater, c) Littorina Sea water penetration caused by density intrusion, and d) the present-day situation with possible penetration of local Baltic Sea water. The white line shows chloride concentration versus depth.

Table 2-1: Groundwater types in SFR – composition, reactions/processes and origin. From SKB (SKB, 2015a).

Groundwater type	Composition/ characteristics	Dominant reactions and processes	Origin
Local Baltic	Chloride 2,500–3,500 mg/L $\delta^{18}O$ −9 to −7.5‰ V-SMOW Na-(Ca)-(Mg)-Cl-SO_4 type Cl/Mg weight ratio < 27	Ion exchange and micro-biological reactions in the bedrock have resulted in decreased concentrations of Mg, K, Na and SO_4^{2-} as well as enrichment of Ca and HCO_3^- compared with Baltic Sea water.	It is unclear whether the Baltic Sea water was present at all in the deformation zones before the construction of the tunnels in SFR. It is more probably a modern component that has been introduced due to the drawdown caused by tunnels.
Littorina with a glacial component	Chloride 3,500–6,000 mg/L $\delta^{18}O$ −9.5 to −7.5 ‰ V-SMOW Na-Ca-(Mg)-Cl-SO_4 type Cl/Mg weight ratio < 27	The Na/Ca ratio is lower than the marine ratio. These changes are caused by ion exchange, but also by dilution with glacial meltwater.	Compared with the original Littorina water, it has been diluted (lower Cl and $\delta^{18}O$ values) with glacial meltwater.
Brackish-glacial	Chloride 1,500–5,000 mg/L $\delta^{18}O$ < −12.0 ‰ V-SMOW Na-Ca-Cl type Cl/Mg weight ratio > 32	An old mixture of different, mainly non-marine ground-waters.	This is the oldest groundwater type and the amounts of post-glacial components are very small. It is a mixture of primarily glacial meltwater (last deglacia-tion or older) and brackish non-marine water (pre-glacial). It probably contains components of old meteoric water prior to last deglaciation as well.
Mixed-brackish (transition type)	Chloride 2,500–6,000 mg/L $\delta^{18}O$ −12.0 to −9.5‰ V-SMOW Na-Ca-(Mg)-Cl-(SO_4) type	Natural or artificial mixing of the three different ground-water types above.	Significant mixing of the brackish- glacial and the two brackish marine groundwater types (mostly the Littorina type) has caused this ground water of transition type. It is more common during the last two decades, according to data from long time series which suggests artificial mixing due to the presence of the repository.

Some key geochemical features of the rock-groundwater system described by SKB are:

- Most of the SFR groundwaters seem to be in equilibrium or slightly oversaturated with respect to calcite.
- The main source of sulphur in the SFR groundwaters is the intrusion of past (Littorina) and present (Baltic) seawaters, which have mixed with the earlier resident groundwaters. Like the Forsmark groundwaters, all the SFR groundwaters are undersaturated with respect to gypsum and celestite and in equilibrium with respect to barite, calcite and fluorite.
- The potentiometric Eh measurements in the SFR groundwaters provide both positive and negative values. Reducing conditions (Eh values between −140 and −190 mV) are in line with those measured in the Forsmark groundwaters and are apparently caused by the occurrence of an iron phase with an intermediate crystallinity and/or by ferrous clay minerals, both of which have been identified.
- The redox capacity provided by the fracture minerals in the hydraulically conductive fractures is mainly found in Fe (II) present in chlorite and clay minerals (e.g. corrensite, a mixed-layer smectite-chlorite mineral) and to some extent in the less abundant sulphides (mainly pyrite). It is unclear however, which mineral assemblage may control redox conditions at depth.

Geochemical evolution of the SFR repository system is discussed in Section 6.3.6 of TR-14-01 and is firmly linked with climatic and shoreline changes shifting groundwater flow patterns. The brackish groundwater type has been chosen by SKB

as the reference composition of the first 1000 years of evolution (Table 2-2, left-hand side), with high pH conditions from the degradation of the engineered barriers affecting downstream from the repository. SKB goes onto state (SKB, 2015b; top of page 154):

> '*The durability of the near-field system is highly dependent of the longevity of the engineered barriers in the repository as they are affected by chemical reactions that take place when the barriers come into contact with the groundwater and waste. The chemical evolution of the barriers is also of importance for sorption and for the release of radionuclides and other species*'.

Interaction of the groundwater with cementitious barriers will contribute to an increase of the pH in the water in the repository. Note that the bulk of the concrete-groundwater modeling carried out by Höglund (2014) used the composition shown on the right-hand side of Table 2-2 and a 'freshwater' composition as shown in Table 2-3. Cronstrand's pH evolution modeling (Cronstrand, 2014) used three different groundwater compositions (Table 2-4).

Table 2-2: Composition of penetrating brackish/saline water and range of variation of the relevant parameters during the temperate climate domain when the repository is situated beneath the surface of the sea. Concentrations in mg/L (Auqué et al., 2013; Tables 4.1 and 4.2). Data from an earlier safety assessment employed by Höglund (2013) for concrete-groundwater modeling are also shown for comparison (right-hand side).

	Composition	Range of variation Samples from SFR down to −200 m	Earlier safety assessment SFR 1 (Höglund 2001)
pH	7.3	6.6–8.0	7.3 (6.5–7.8)
Eh	−225	−100 to −350	Red. (−100 to −400)
Cl	3,500	2,590–5,380	5,000 (3,000–6,000)
SO_4^{2-}	350	74–557.2	500 (20–600)
HCO_3^-	90	40–157	100 (40–110)
Na	1,500	850–1,920	2,500 (1,000–2,600)
K	20	3.8–60	20 (6–30)
Ca	600	87–1,220	430 (200–1,600)
Mg	150	79–290	270 (100–300)
SiO_2	11	2.6–17.2	5.66

Table 2-3: Groundwater composition proposed for the fresh water period (i.e. following the salt water period) and the associated variation interval (as used by Höglund (2014), derived from Höglund (2001).

Parameter	Fresh water period		
(mg/l)	Proposed	Min	Max
HCO_3^- (alkalinity)	300	170	540
SO_4^{2-}	50	3	110
Cl^-	45	5	1,000
Na^+	100	20	200
K^{+*}	4	0.2	10
Ca^{2+}	35	25	140
Mg^{2+}	9	3	10
pH	7.49	6.7	8.7
Eh (mV)	Reducing	−400	−100
Si as SiO_2(aq)	5.9		
Electrical balance %	−0.08%		

* Proposed value= rounded "Allard standard water" (Höglund et al. 1997). Min and max values are taken from measure-

Table 2-4: Groundwater compositions used for the pH evolution modeling (from Cronstrand, 2014).

Element	Saline groundwater (mol/kgw)	Temperate-periglacial water (mol/kgw)	Glacial derived water (mol/kgw)
C	1.48E–3	4.92E–3	6.40E–4
Ca	1.50E–2	1.25E–3	2.96E–4
Cl	9.87E–2	5.36E–3	8.19E–6
K	5.12E–4	1.28E–4	1.65E–5
Mg	6.17E–3	4.94E–4	1.04E–6
Na	6.53E–2	7.83E–3	4.35E–6
S	3.64E–3	5.21E–4	1.25E–5
Si	1.83E–4	2.00E–4	2.13E–4

2.1.1. Salinity

The degree of salinity of the groundwater at the SFR site will control to a large extent the rate and amount of degradation of the concrete engineered barriers (degradation is enhanced under more saline conditions) and also the ambient pH of near-field pore fluids. This will impact upon not only the timing of release of radionuclides from concrete vaults, but also their solubility and sorption behaviour (in general pH > 10 is desirable for safety-relevant time periods).

SKB (2011; top of page 188) notes that the range in chloride concentration of the SFR groundwaters is small (1500 to 5500 mg/L Cl⁻) compared with the Forsmark site investigation area (50 to 16,000 mg/L Cl⁻). Moreover, SKB goes on to state that present-day groundwater chemistry at SFR is influenced by drawdown to the tunnel, which will be important in some of the sampled sections where inflow of Baltic Sea water can be expected. The most saline groundwater is generally found at intermediate depths (100-200 m) and is of the brackish marine Littorina type. The more dilute brackish water found at shallow depths (~100 m) is of local Baltic type, and the most dilute waters (1600 mg/L Cl⁻) are of brackish-glacial type at about 240 m depth (SKB, 2011; foot of page 190).

Regarding changes to salinity during operation of SFR, SKB observes that most of the changes showed a slightly decreasing chloride concentration between 1986 and 2000 followed by a nearly stable period until 2010, with the greatest changes in groundwater pressure and inflow to the boreholes and the tunnel system occurring soon after construction (SKB, 2011; paragraph beneath bullet points on page 200).

Unlike Forsmark investigations, waters in the rock matrix ('pore waters') at SFR have not been sampled (SKB, 2011; section at foot of page 198) which makes it difficult to assess past natural variations of groundwater salinity.

SKB has produced a schematic diagram of the distribution of water types at SFR, here reproduced as Figure 2-2. The precise location of deep saline water at SFR is hypothetical in Figure 2-2 since there are no data from boreholes deeper than -400 m elevation.
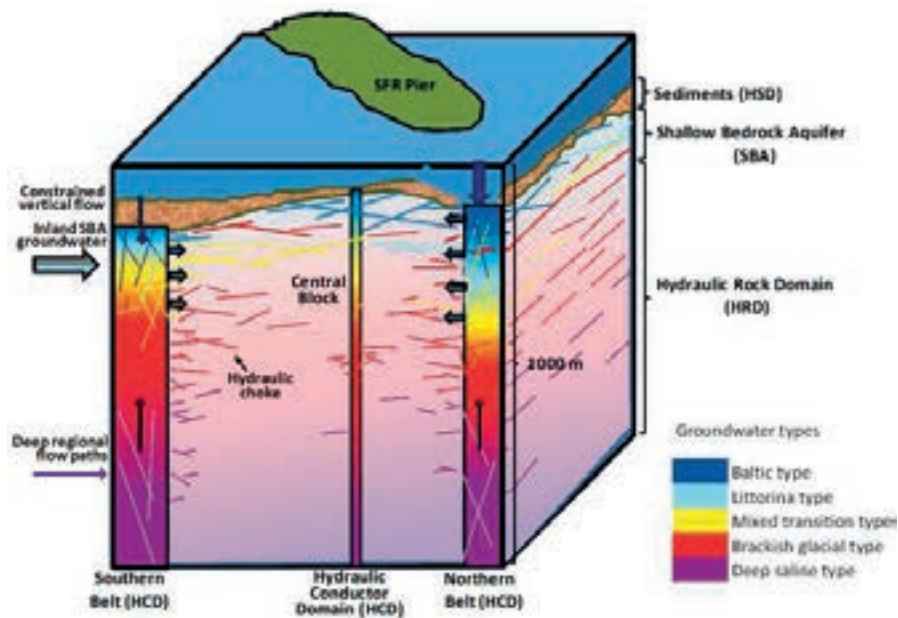

Figure 2-2: Conceptual block model (0–1000 m depth) integrating the major hydrogeological and hydrogeochemical features of the investigated SFR rock volume. The different groundwater types are indicated by the colour scheme displayed on the right side. The deep saline groundwater which is indicated by lilac is not present as a dominant groundwater type in the SFR rock volume. From SKB (SKB, 2011; page 203).

2.1.2. pH buffering

The solubility and sorption of many radionuclides are sensitive to pH due to its role in affecting aqueous speciation.

Calcite is seen to be a major control upon pH in groundwaters at the SFR site (e.g. Gimeno et al., 2011; Section 4.1, page 39):

14

'*Calcite is one of the most abundant minerals in fracture fillings in these sites and it plays an integral role in the pH-buffering of the recharge groundwaters. CO_2 partial pressure (usually referred as PCO_2 in this document) is another relevant parameter for understanding the evolution of the carbonate system and for evaluating possible uncertainties in measured pH values*'.

This statement implies that calcite somehow acts alone in the pH buffering process, yet in the paragraph preceding the text above, states:

'*The available mineralogical information for the fracture fillings present in the SFR bedrock, indicates that, together with chlorite, calcite is one of the most abundant fracture filling minerals and is widely distributed at all examined depths (reaching 520 m.a.s.l.) without significant variations with depth (Sandström and Tullborg 2011). Clay minerals, mainly mixed layer smectite-illite and illite, also appear in dominant amounts in open fractures*'.

Calcite is not an essential mineral of the rocks constituting the repository host rock at SFR, but is a product of water-rock reaction over geological time by reactions such as the irreversible weathering of the calcic component of plagioclase feldspar (anorthite, $CaAl_2Si_2O_8$) to form clays (here represented by illite, as observed in fracture-fillings at Forsmark):

$$3 \text{ anorthite} + 2\,K^+ + 3\,HCO_3^- + H^+ \rightarrow 2 \text{ illite} + 3 \text{ calcite}$$
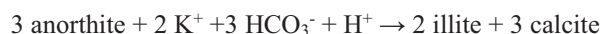
Savage et al. (Savage et al., 1999a; Savage et al., 1999b) showed that the pH buffer capacity of solid carbonates alone is much less than that of aluminosilicate minerals in water-rock systems. Moreover, calcite is such a small part of the mineralogical system at SFR that from mass balance constraints, it is highly unlikely to constitute a significant pH buffer.

2.1.3. Carbonate system

The carbonate system is important for radionuclide migration in that the solubility and sorption of most actinides are sensitive to the amounts of bicarbonate ion in groundwater. It is thus important to understand controls (reactions) of PCO_2 in groundwater.

Groundwaters at SFR are shown to have PCO_2 values greater than that required for equilibrium with the atmosphere (log $PCO_{2,\ bars}$ = -3.5) (Gimeno et al., 2011; Section 4.1.3) and range up to log $PCO_{2,\ bars}$ = -2.0.

Nilsson et al. (2011) (bottom of page 98) state:

'*high and variable HCO_3^- values are the result of the biological activity during infiltration of marine waters through the seabed sediments*'.

In other words, oxidation of organic matter in seabed sediments by dissolved sulphate leads to the production of bicarbonate (and elevated PCO_2) and mineral sulphides (e.g. Andrews et al., 1996).

2.1.4. Redox conditions

The solubility and sorption behaviour of many radionuclides (especially actinides) is sensitive to redox activity, with lower Eh tending to lower element solubility. Understanding the controls of redox in the far-field is thus key to the modelling of the migration and retardation of many radionuclides.

SKB's assessment of redox conditions at SFR are somewhat uncertain, with measured reducing Eh values ranging between -140 and -190 mV and oxidising values between +30 and +110 mV (SKB, 2011; foot of page 182). The reducing conditions are ascribed to either 'an iron phase' (sic) of indeterminate crystallinity, or by 'ferrous clay minerals'. 'Redox capacity' is ascribed to the presence of chlorite and Fe-bearing clay minerals in fracture fillings.

Although SKB considers that major variations in hydrochemical conditions can be attributed mainly to mixing of groundwater types, heterogeneous reactions between minerals and groundwater are relied upon to provide stable redox conditions. This assessment by SKB seems somewhat inconsistent, since the equilibration (dissolution-precipitation) of sheet silicates such as biotite (the dissolution of which is considered a source of fluoride in SFR groundwaters – foot of page 106 of Nilsson et al., 2011), chlorite and clay minerals will contribute solutes other than reduced iron to groundwaters.

SKB's position regarding Eh is similar (SKB, 2014b; page 138, 6th paragraph):

> '*The bedrock content of reducing substances such as sulphide, divalent iron and manganese is vital for maintaining reducing conditions in the groundwater. The reducing capacity available in the rock matrix at SFR exists mainly in the Fe(II)-bearing biotite, chlorite, amphibole, pyrite and magnetite. Biotite is, by far, the main reducing mineral in the rock matrix at SFR (Sandström and Stephens 2009, Curtis et al. 2011, Sidborn et al. 2010)*'.

2.2. Fracture minerals

Regarding groundwater interaction with the rocks, SKB (Sandström and Tullborg, 2011, Abstract; Nilsson et al., 2011, page 27) report that there are no major differences between the fracture mineralogy of the investigated borehole sections from SFR and the fracture mineralogy of the Forsmark site investigation area.

Sandström and Tullborg (2011) report that the most common fracture minerals are mixed layer clay (smectite-illite), illite, chlorite, calcite, quartz, adularia and albite. Other minerals identified in the borehole sections include laumontite, pyrite, barite, chalcopyrite, hematite, Fe-oxyhydroxide, muscovite, REE-carbonate, allanite, biotite, asphaltite, galena, sphalerite, arsenopyrite, uranium phosphate, uranium silicate, Y-Ca silicate, monazite, xenotime, harmotome and fluorite.

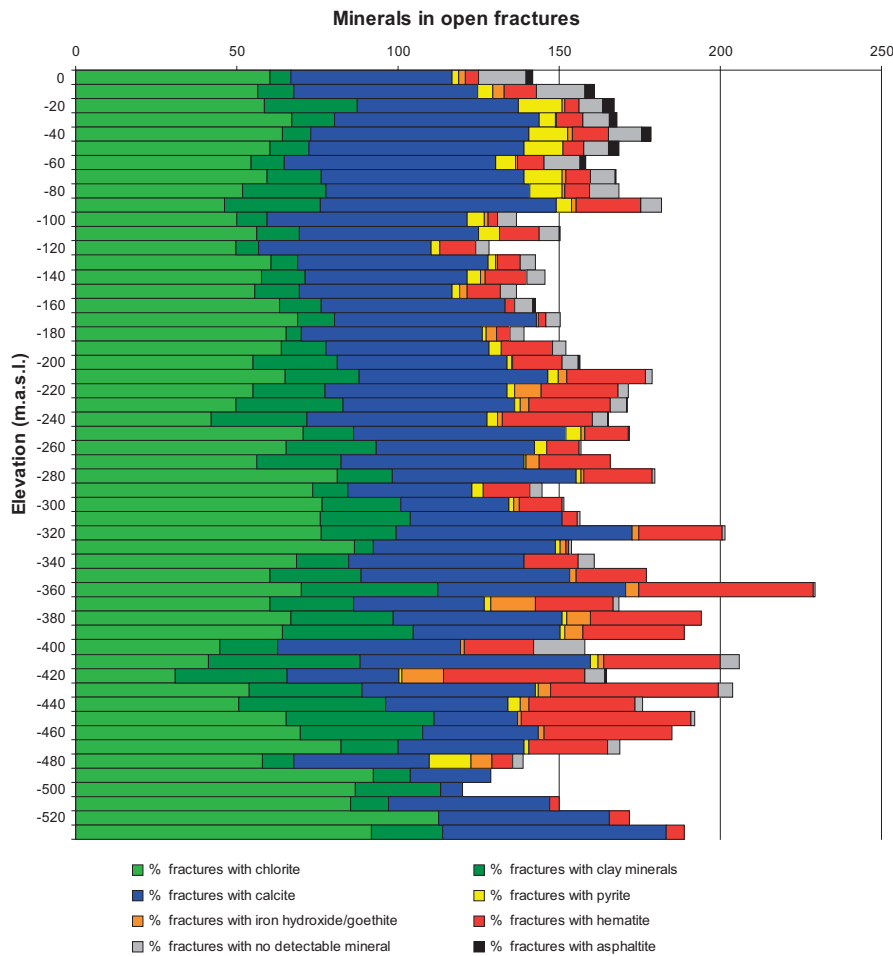The depth distribution of fracture minerals in open fractures are shown here in Figure 2-3.

Minerals in open fractures

Figure 5-1. Depth distribution of fracture minerals in all mapped open fractures from SFR.
Figure 2-3: Depth distribution of fracture minerals in all mapped open fractures from SFR.
From Sandström and Tullborg (2011).

Sandström and Tullborg (2011) report that there are no indications of significant inflow of oxygenated waters, such as oxidation and/or dissolution of sulphides, that have been identified in the SFR fracture systems. However, in water conductive zones, occurrences of Fe-oxy-hydroxides indicate that oxidising conditions have prevailed, at some period, in parts of the fracture system. This observation agrees with the observations from the Forsmark site investigations. No signs of a redox transition zone were detected, also in agreement with observations of the redox system at Forsmark. No samples were investigated from above –57 m.a.s.l. by Sandström and Tullborg. However, based on the drill core mapping, pyrite is only absent in water conductive fractures in the upper 10 metres indicating prevailing reducing conditions. Iron hydroxide is present at depths down to about –500 m.a.s.l.

Sandström and Tullborg (2011) state that there are no major differences evident between the fracture mineralogy of the sampled SFR drill cores and samples investigated during the Forsmark site investigation in that the four fracture mineral generations distinguished within the Forsmark site investigation are also found at SFR. However, some differences have been observed:

- barite and uranium minerals are more common in the SFR fractures.

- Clay minerals like mixed layer illite-smectite and illite dominate at SFR in contrast to Forsmark where corrensite (mixed-layer chlorite-smectite) is the most common clay mineral.
- REE-carbonates which were not identified in the samples from the Forsmark site investigation occur on many of the analysed fracture surfaces at SFR.

Nilsson et al. (2011), page 27, report that 'Generation 4' (i.e. most recent) fracture fillings consist predominantly of clay minerals and thin precipitates of calcite in hydraulically conductive fractures; minor occurrences of pyrite and goethite are also found. They believe that precipitation probably occurred at low temperatures (< 50 °C) during a prolonged period, possibly since the late Palaeozoic until present, by groundwater circulation.

There are many references to the apparent stability of calcite in fractures in the bedrock at SFR (e.g. SKB, 2014b; page 147, 4th paragraph):

   'no evidences for calcite dissolution in the upper parts of the bedrock have been found '.

However, evidence from SEM investigations carried out by Sandström et al. (2011) clearly show features of calcite that are attributable to dissolution (Figure 2-4) which challenges the statement above that calcite is stable in the ambient rock-groundwater system.
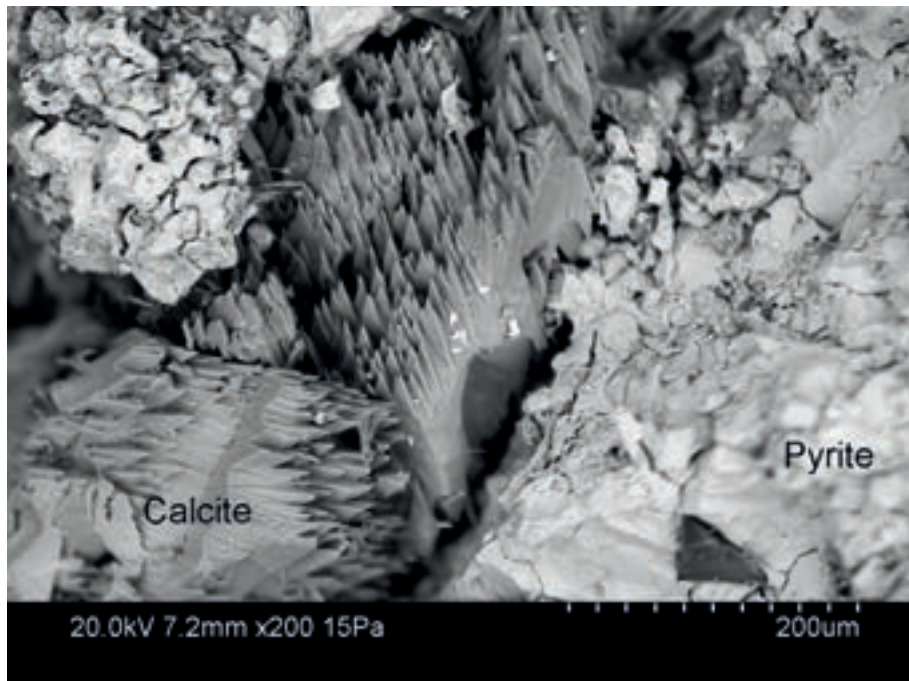

Figure 2-4: Backscattered electron image of calcite and pyrite crystals (from Sandström et al., 2011; page 47). Etching of calcite due to dissolution is clearly visible.

2.3. Retardation properties

2.3.1. Influence of chemical conditions

'Favourable water chemistry' is identified as an important feature for the engineered barrier/groundwater system in that sorption (of radionuclides) is heavily dependent on the composition of the pore water (SKB, 2015a; top of page 135). The most important parameters are deemed to be pH, redox potential, and the concentrations of complexing agents. pH is desired to be higher than 10.5 which generally guarantees favourable sorption conditions for important cations. Anions are assumed to sorb poorly to cementitious materials in the entire relevant pH range. A low redox potential leads to a slower release of important radionuclides. Consequently, 'good retention' has been defined as a safety function for the EBS, with the following safety function indicators (SKB, 2015a; Table 5-3, page 137):

- pH in concrete barriers (1–2BMA, 1–2BTF, silo, BRT),
- redox potential in concrete barriers (1–2BMA, 1–2BTF, silo, BRT),
- concentrations of complexing agents in concrete barriers (1–2BMA, 1–2BTF, silo),
- available specific surface area for sorption in concrete barriers (1–2BMA, 1–2BTF, silo, BRT).

The chemically-relevant aspect of the geosphere is 'good retention', which is controlled by reducing conditions at repository depth. The relevant safety function indicator defined by SKB is:

- redox potential.

Sorption data used in SR-PSU are described in the radionuclide transport report (SKB, 2015a) and the input data report (SKB, 2014g). For the rock matrix, the data are based on the same assumptions made for the SR-Site geosphere K_d report (Crawford, 2010, Crawford, 2013). In other words, the rock surrounding the SFR repository is geochemically similar to the one surrounding the planned KBS-3 repository (e.g. based on a reference granite to granodiorite, metamorphic medium grained rock type). This rock type is selected as it is dominant within the domains of both the planned KBS-3 repository and the current and planned SFR repository.

Regarding variation with groundwater composition, the K_d values were based on speciation calculations performed with the SFR groundwater compositions reported by Auqué et al. (2013). These compositions are that for 'brackish' groundwater (as shown here in Table 2-2), early and late periglacial groundwaters (as shown here in Table 2-5), and a 'glacial-derived' groundwater (as shown here in Table 2-6),

The radionuclide transport report also includes the possibility of a high pH plume from the repository given its content of cement and concrete materials. In Crawford (2013), a method is presented to scale the rock matrix K_d values depending on the amount of influence from the repository Ordinary Portland Cement (OPC) water. For the crushed rock data, the assumption is made that the influence is high enough (e.g. repository water around the backfill at a pH > 10).

Table 2-5: Proposed composition of the fresh groundwater around the repository during temperate and periglacial climate domains (early periglacial left-hand reference composition; late periglacial right-hand reference composition) when the repository is not covered by the sea. From SKB (2014f).

	Reference composition	Range	Reference composition	Range
	Not extending for more than approximately 40,000 years		Extending for more than 40,000 years	
pH	7.4	6.6–8.3	7.6	6.6–8.3
Eh (mV)	–210	–135 to –300	–250	–135 to –300
Cl (mg/L)	190	16–503	90	5–357
SO_4^{2-} (mg/L)	50	25–163	40	17–110
HCO_3^- (mg/L)	300	300–500	200	120–324
Na (mg/L)	180	65–400	110	38–250
K (mg/L)	5	5–15	3	2–5.3
Ca (mg/L)	50	24–105	30	7–48
Mg (mg/L)	12	7–24	6	2–13
SiO_2 (mg/L)	12	2–21	10	12–31

Table 2-6: Proposed composition of the glacial-derived groundwater expected to reach the repository during a glacial climate domain. From SKB (2014f).

	Composition	Range
pH	9.3	9.0 – 9.6
Eh (mV)	+400	+900 to –290
Cl (mg/L)	0.5	0.5–178.0
SO_4^{2-} (mg/L)	0.5	0.1–5.8
HCO_3^- (mg/L)	22.7	17.0–150.0
Na (mg/L)	0.17	0.17–130.0
K (mg/L)	0.4	0.14–3.6
Ca (mg/L)	6.8	6.6–21.0
Mg (mg/L)	0.1	0.05–2.0
SiO_2 (mg/L)	12.8	7.9–14.5

2.3.2. Sorption on clay minerals

The SR-PSU radionuclide transport report focuses on sorption in the bulk rock matrix, but SKB describes an approach to model retention of radionuclides by ion exchange and surface complexation on sheet silicates in the radionuclide transport report for SR-Site (SKB, 2010a, page 210 and following).

The SR-Site radionuclide transport report states that data derived for the bentonite buffer have been used to quantify the potential for sorption of radionuclides by ion-exchange and surface complexation on chlorite and the clay mineral group although rescaled to match the approximate range of cation exchange capacities (CEC) estimated for the fracture minerals. These data were defined for a reference bentonite porewater ('RPW') deemed appropriate for both non-saline and mildly saline conditions, as well as a reference saline porewater of a much higher salinity ('HSPW'). Although derivation of K_d values 'from scratch' for illite and smectite clay mixtures and specific groundwater compositions using thermodynamic modeling might give a more accurate assessment, SKB believes the simplified approach outlined above is appropriate for the current purpose. The uncertainty and variability of groundwater composition implies that a more sophisticated modeling

approach may not necessarily reduce data uncertainty to any great extent over that already implicit in the recommended data ranges.

The data corresponding to the RPW water composition were used by SKB as a reference case. The purpose was to facilitate the discussion of the relative merits of different modelling assumptions regarding risk assessment, so that only a small subset of radionuclides was selected for this analysis. These were chosen partly because their importance in safety assessment but mainly owing to their differing geochemical behaviour. The rescaled fracture mineral K_d values used as a basis for the transport calculations used by SKB are given in Table 2-7.

Table 2-7: Estimated K_d data for chlorite (CEC ≈ 5 meq 100 g^{-1}) and clay minerals taken as a group (CEC ≈ 20 meq 100 g^{-1}, assuming illite as an approximate analogue). The data are based on the corresponding values for MX-80 bentonite (CEC ≈ 85 meq100 g^{-1}), although rescaled relative to the CEC of the indicated fracture minerals. The best estimate K_d value is assumed to be the median. From SKB (2010a).

Element (Redox state)	Best estimate K_{ds} (m³/kg)	Lower limit K_{ds} (m³/kg)	Upper limit K_{ds} (m³/kg)
Chlorite			
Am(III)	3.6	0.59	22
Cs(I)	$5.3 \cdot 10^{-3}$	$1.2 \cdot 10^{-3}$	$3.3 \cdot 10^{-2}$
Ni(II)	$1.8 \cdot 10^{-2}$	$1.8 \cdot 10^{-3}$	$1.9 \cdot 10^{-1}$
Ra(II)	$2.6 \cdot 10^{-4}$	$4.7 \cdot 10^{-5}$	$1.6 \cdot 10^{-3}$
U(IV)	3.7	0.21	65
U(VI)	0.18	$2.9 \cdot 10^{-2}$	1.1
Clay mineral group (assuming Na-illite as an analogue)			
Am(III)	14	2.4	89
Cs(I)	$2.1 \cdot 10^{-2}$	$4.7 \cdot 10^{-3}$	0.13
Ni(II)	$7.1 \cdot 10^{-2}$	$7.1 \cdot 10^{-3}$	0.78
Ra(II)	$1.1 \cdot 10^{-3}$	$1.9 \cdot 10^{-4}$	$6.4 \cdot 10^{-3}$
U(IV)	15	0.85	262
U(VI)	0.71	0.12	4.2

3. EBS conditions

3.1. 1BMA

SSM requested that SKB carry out further investigations of the physical and chemical concrete degradation processes that impact the concrete throughout the lifetime of the barriers. Additionally, fractures have been observed in the 1BMA barriers during two site inspections. Fractures may affect several of the key parameters used in the groundwater flow modelling (hydraulic conductivity) and radionuclide transport modelling (hydraulic conductivity, effective diffusivity and sorption capability) for the SFR site. This means they have a direct bearing on the safety assessment. SKB plans to repair the 1BMA barriers, but there are clearly important questions remaining over the extent to which these fractures would impact on performance, as well as any further fractures that form during the operational or post closure periods.

1BMA is an operational vault in the SFR repository for low and intermediate level radioactive waste at Forsmark. It is used for storage of waste with lower activity level than the waste stored in the Silo repository and for waste packages that are unsuitable for deposition in the Silo due to the geometry of the packages, their mechanical properties (e.g. swelling), or their chemical composition. The vault consists of a concrete structure divided into 13 large compartments and two small compartments, see Figure 3-1. The vault is built like a large box with separating walls creating the compartments. The concrete walls and floor structures are made of in-situ cast reinforced concrete. To keep the molds in place during casting penetrating form rods made from steel were used. The supporting concrete structures rest on solid rock and the bottom of the compartments rests on a gravel layer on the excavated bottom. The walls and roof of the vault are lined with shotcrete to stabilise the rock during the operating phase.

Figure 3-2 shows a schematic view of the concrete barriers, the concrete molds containing the waste and the concrete grout around the concrete constructions in the 1BMA vault. During closure, the empty voids outside the concrete barriers in the 1BMA vault will be backfilled with sand or gravel. Ninety percent of the volume above the concrete constructions, under the rock ceiling, will be filled with macadam (crushed rock that has been sieved to the size fraction 16–32 mm). Dimensions of the 1BMA vault and concrete constructions are presented in Table 3-1.
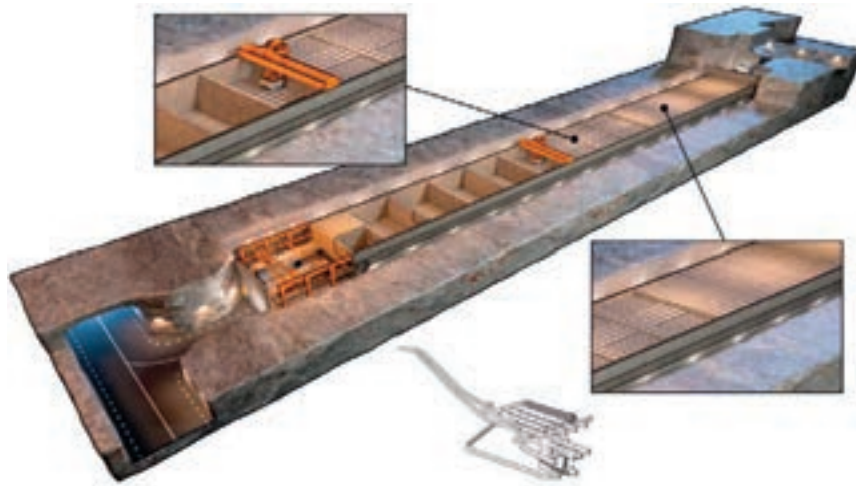
Figure 3-1: Illustration of 1BMA during the operating phase (from Höglund, 2014). The upper detail shows the emplacement of waste packages with the overhead crane, the lower detail shows the concrete lid. In addition, there is a view of SFR 1 with the position of 1BMA highlighted.
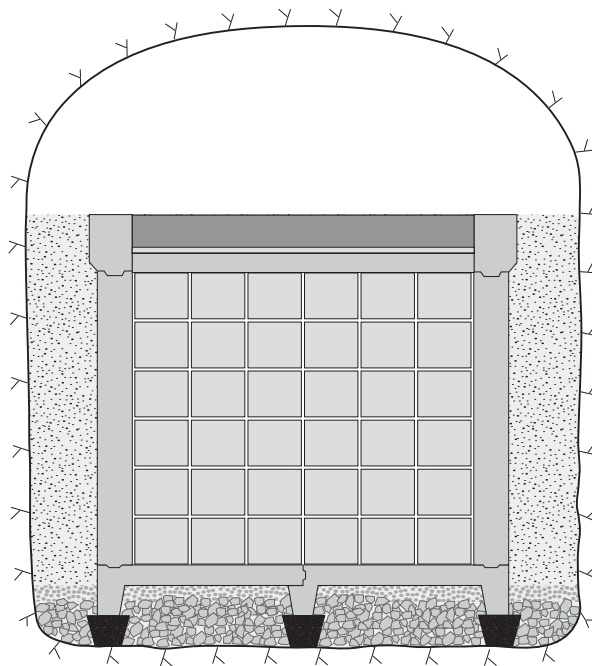

Figure 3-2: Illustration of the different concrete barriers, concrete molds and macadam (crushed rock) backfill in the 1BMA vault. Figure is not to scale. From Höglund (2014).

Table 3-1: Approximate dimensions of the 1BMA vault and concrete constructions. From Höglund (2014).

1BMA vault	Dimensions
Vault	
Length	160 m
Rock wall height	16.5 m
Width	19.6 m
Concrete structures	
Length	140 m
Height	8.915 m
Width	15.62 m
Empty void or sand filled slot	1–2 m
Reinforced concrete lid[1]	0.5 m
Cast concrete lid[1]	0.05 m
Concrete plank[1]	0.4 m
Side walls	0.4 m
Concrete bottom	0.25 m
Compartment wall	0.4 m
Macadam	0.15 m
Rock fill	0.3 m
Large compartments	
Number	13
Inner length	9.9 m
Inner width	14.82 m
Small compartments	
Number	2
Inner length	4.95 m
Inner width	7.2 m

[1] Total thickness of the lid should be 0.915 m (i.e. the sum of reinforced lid + cast concrete + concrete plank).

3.2. Cement and concrete

3.2.1. Compositions employed by Höglund (2014)

The cement used for concrete walls at SFR etc. is Degerhamn cement (Table 3-2). The mixing proportions used for concrete components and concrete grout in SFR are presented in Table 3-3 (from Höglund 2001). The ballast material is selected to comply with Swedish standards on resistance to alkali-silica reactions. The chemical composition of the ballast material is presented in Table 3-3.

The porosity of the concrete barriers in 1BMA has been calculated by Höglund (2014) from the mixing proportions in Table 3-3 and a simple hydration model presented by Höglund (1992). The results are presented in Table 3-5 (from Höglund, 2001). The stated porosity refers to the total porosity of the concrete, taking into account the presence of significant amounts of ballast that has been assumed to be non-porous. Höglund (2013) reports recent analyses of concrete samples from 1BMA that indicate a somewhat higher porosity than the calculated results shown in Table 3-5. The experimental values are in the range 16.5–16.9 % with a variation of +/– 2%. The reason for such discrepancy between calculated and

experimental values could result from the assumed W/C-ratio and the assumed density of the ballast material (which constitutes ~70 % of the material).

The composition of the hydrated cement minerals in the concrete due to the initial hardening of the concrete has been calculated and is presented in Table 3-6 (from Höglund, 2001).

Table 3-2: Chemical composition of Degerhamn cement, including both the oxide composition and the corresponding clinker mineral composition (from Höglund, 2014).

Component	Content % by weight
Ca	64
SiO_2	21
Al_2O_3	3.5
Fe_2O_3	4.6
MgO	0.7
K_2O	0.62
Na_2O	0.07
SO_3	2.2
Cl	< 0.1
Free $CaCO_3$	0.9
Corresponding clinker components	
Tricalcium silicate, C_3S	64.4
Dicalcium silicate, C_2S	10.9
Tricalcium aluminate, C_3A	2.0
Tetracalcium aluminate ferrite, C_4AF	13.9
Calcium sulphate (gypsum), $C\hat{s}H_2$	3.7
Alkali hydroxides, $N + K$	0.7

Table 3-3: Mixing proportions for concrete structures in 1BMA in SFR, amounts given in kg m^{-3}. From Höglund (2014).

Component	Construction concrete (Jacobsen and Gjörv 1987, SKB 2014c)	Concrete grout (SKB 2014c)
Degerhamn anläggningscement	350	325
Water	164.5	366
Ballast	1,829 (total) 0–8 mm 920 kg/m^3 8–16 mm 374 kg/m^3 16–32 mm 535 kg/m^3	1,302
Additives (anti-foaming, cellulose)	0.5% Sika Plastiment BV-40 0.05–0.2% Sika Retarder	6.5
Air	–	2.5% by volume
W/C ratio	0.47 (0.46–0.49)	1.125

Table 3-4: Chemical composition of the ballast material, 'Baskarpsand', used in the 1BMA concrete. From Höglund (2014).

Component	Content % by weight
SiO_2	78.8
Al_2O_3	11.6
Fe_2O_3	1.21
CaO	1.12
MgO	0.28
K_2O	3.86
Na_2O	3.09
Loss on ignition at 1,000°C (LOI)	0.48
Proportion of free quartz	43
Sintering temperature	1,250°C

Table 3-5: Porosity of the 1BMA construction concrete calculated using the hydration model by Höglund (1992). From Höglund (2014).

Type of pores	Porosity (m^3/m^3)
Capillary pores	0.03
Gel pores	0.047
Contraction pores	0.022
Total porosity	0.099

Table 3-6: Composition of hydrated cement used in SFR. Composition calculated using the hydration model by Höglund (1992) from the chemical composition of the SFR cement and the mixing proportions stated in Table 3-3. From Höglund (2014).

Hydrate	Amount kmol/m^3 concrete	Fictive concentration kmol/m^3 pore water
C_3FH_6	0.1008	1.020
C_3AH_6	0.02397	0.2424
Monosulphate	0.09613	0.9722
Ettringite	0	0
CSH-gel (Ca/Si=1.8)	1.225	12.39
Portlandite	1.036	10.48
Brucite	0.06079	0.6149
KOH	0.04607	0.4660
NaOH	0.007903	0.07993
$CaCO_3$	0.06295	0.6367
Porosity	0.099	m^3/m^3 concrete

3.2.2. Compositions employed by Cronstrand (2014)

Cronstrand (2014) employed a slightly different composition, being that used previously by this author (Cronstrand, 2007; Table 3-7). Cronstrand represents calcium silicon hydrates (CSH) by three distinct mineral phases, CSH_1.6, CSH_1.2 and CSH_0.8, with decreasing Ca/Si ratios to reflect incongruent dissolution. Cronstrand notes that in contrast to cement, concrete contains ballast, which reduces its buffer capacity. Cronstrand represents ballast by quartz which is assumed to dissolve according to the rate equations in Rimstidt and Barnes (1981). The assumed mineral distribution for 1 kg concrete and 1 kg cement respectively is given in Table 3-8 and Table 3-9.

Table 3-7: Composition of hydrated Degerhamn cement employed by Cronstrand (2014).

Phase	Formula	M (g/mol)
CSH	$Ca_{1.60}SiO_{3.6}:2.58H_2O$	196.3
Portlandite	$Ca(OH)_2$	74.1
Ettringite	$Ca_6Al_2(SO_4)_3(OH)_{12}:26H_2O$	1,255.1
C3AH6	$Ca_3Al_2(OH)_{12}$	378.3
Hydrotalcite	$Mg_4Al_2O_7:10H_2O$	453.4
Magnetite	Fe_3O_4	231.5
Quartz	SiO_2	60.1

Table 3-8: Solids comprising 1 kg of concrete (Cronstrand, 2014).

Phase	n (mol)	(g)
CSH	0.446	87.5
Portlandite	0.431	32.0
Ettringite	0.010	12.6
C3AH6	0.028	10.5
Hydrotalcite	0.004	1.8
Magnetite	0.021	4.9
Ballast (Quartz)	16.642	850.7

Table 3-9: Solids comprising 1 kg of cement (Cronstrand, 2014).

Phase	n (mol)	(g)
CSH	2.986	586.1
Portlandite	2.890	214.1
Ettringite	0.067	84.3
C3AH6	0.186	70.3
Hydrotalcite	0.027	12.1
Magnetite	0.143	33.1

3.3. Concrete degradation

An assessment of the evolution of pH in SFR has been reported by Cronstrand (2014), who modeled the system as a homogeneous mixing tank, and considered advective flow and thermodynamic equilibrium between different solid materials. In this study, except for in 1 BLA, the pH is predicted to be maintained above 12 throughout the initial 10,000 years. The combination of higher flow rates and low content of cement and concrete leads to a more dramatic pH evolution for BLA than the other repository parts. *Cronstrand emphasises that his report is intended to be a pessimistic assessment of pH evolution.*

Höglund (2014) provides a more comprehensive description of a series of analytical and numerical reactive transport models focused on investigating physical and chemical processes that cause fractures and chemical degradation in concrete barriers, and the impact of fractures on the long-term performance of SFR. The report also provides data on hydraulic conductivities, effective diffusivities and porosities of the concrete barriers, and addresses the issue of fractures in SFR barriers.

3.3.1. Fractures

Höglund (2014) presents a detailed review of fracture mechanisms in concrete. According to Höglund (2014), fractures may affect several of the key parameters used in the groundwater flow modelling (hydraulic conductivity) and radionuclide transport modelling (hydraulic conductivity, effective diffusivity and sorption capability) for the SFR site. The main results presented by Höglund are:

- Fractures increase the hydraulic conductivity and effective diffusivity of the barriers. Shrinkage of the concrete, as it dries during the operational phase and cools during re-saturation with groundwater, will induce fractures. Fractures increase the leaching of calcium and other important chemical components from the concrete, thereby increasing the porosity of the adjacent concrete, and ultimately leading to a widening of the fractures.
- A reactive front of the potentially deleterious minerals ettringite and thaumasite that can lead to gradual deterioration of the concrete will propagate through the different concrete barriers in the period between 2

and 10 000 ka after closure. Chloride intrusion will cause depassivation of steel components of the barriers (reinforcement bars and form ties) and result in corrosion.

- Corrosion of reinforcement will lead to fracture formation in the concrete and spalling of the surface layer, the fractures will gradually become wider as corrosion progresses.
- Corrosion of form ties that fully penetrate the concrete walls leads to fracture formation and will eventually result in fully penetrating fractures that may extend to the edges of the concrete walls and floors.
- The barrier function will decrease with time, but the new 2BMA design will degrade much more slowly than the current 1BMA.

Höglund (2014) produces some results for concrete with fully penetrating fractures shown in Figure 3-3. His calculations assume a hydraulic conductivity KI of 10^{-11} ms^{-1} in intact concrete. The effect of surface roughness is neglected in these calculations. Different cases of the fracture width (aperture) b, and the fracture spacing d, are given in the figure. An important observation is that the overall hydraulic conductivity is much more sensitive to the fracture aperture width than to the fracture spacing. Hence, even for large spacings, the presence of wide fractures has a large impact on the overall hydraulic conductivity of the concrete structures.

Höglund (2014) also investigated the overall diffusivity of concrete with fully penetrating fractures. His results calculated for concrete with fully penetrating fractures are shown in Figure 3-4. The calculations assume an effective diffusivity DeI (effective diffusivity in intact concrete) of 3×10^{-12} m^2 s^{-1} in intact concrete and a 0.4 m thick concrete barrier (L). The effect of surface roughness is neglected in these calculations. Different cases of the fracture width (aperture) b, and the fracture spacing d, are given in the figure.   The results show that the overall effective diffusivity is much less sensitive to the presence of fractures, even large fractures, than the corresponding impact on the overall hydraulic conductivity presented in the above paragraph. The reason for this is that the ratio D_0/D_{eI} is much smaller than the ratio K_f/K_I. D_0 = diffusivity in bulk water; K_f = hydraulic conductivity of fractures in concrete (m s^{-1}); K_I = hydraulic conductivity of intact concrete (m s^{-1}).
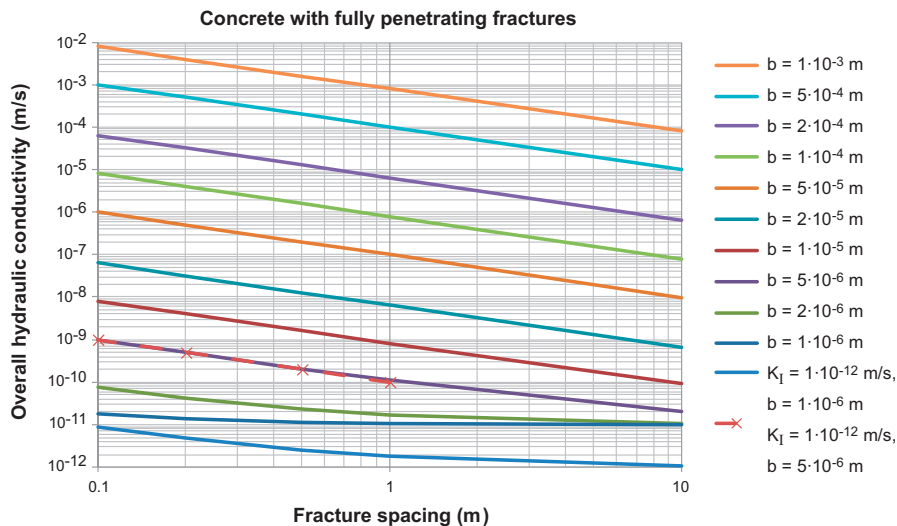

Figure 3-3: Example calculations for the impact of fully penetrating fractures on the hydraulic conductivity of a concrete barrier. From Höglund (2014).
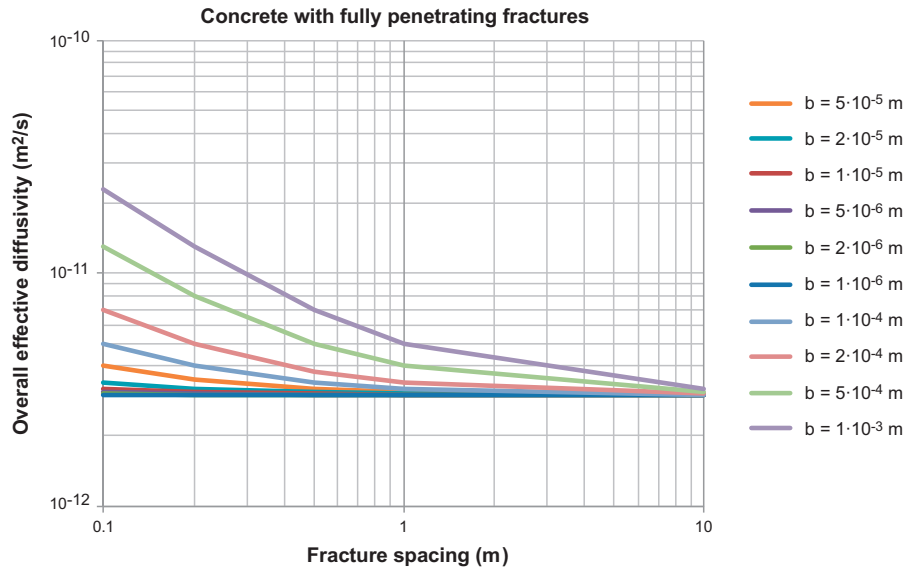
Figure 3-4: Example calculations for the impact of fully penetrating fractures on the effective diffusivity of a concrete barrier. From Höglund (2014).

Höglund (2013) goes on to estimate the overall hydraulic conductivity of the 1BMA concrete structures, taking into account the actual fractures observed and characterised during the inspection (Table 3-10). Using these data and applying his model, the overall hydraulic conductivity of the concrete structures in the 1BMA vault is estimated to $5.2 \cdot x\ 10^{-5}$–$1\ x\ 10^{-4}$ m s^{-1} for the bottom and western long side wall and $1.1\ x\ 10^{-4}$–$2.2 \cdot x\ 10^{-4}$ m s^{-1} for the bottom and eastern long side wall based on the results of the inspection in year 2000. For comparison, he assumed that the hydraulic conductivity of intact concrete is $1 \cdot x\ 10^{-11}$ m s^{-1}. A surface roughness factor of 0.5–1 was assumed in the calculations.

A corresponding calculation based on the reported results of the inspection undertaken in 2011 shows an overall hydraulic conductivity of the concrete walls in 1BMA of $2.6 \cdot x\ 10^{-4}$–$5.3\ x \cdot 10^{-4}$ m s^{-1}. The data assumed for the calculations are shown in Table 3-10.

The results show that very high values for the overall hydraulic conductivity are expected for the concrete structures in the 1BMA vault based on the results of the inspected section.

Table 3-10: Compilation of observed fractures in the 1BMA vault concrete structures. IpX denotes Inspection point nr X. From Höglund (2014).

Fracture Id/ Inspection point	Fracture length l_i (m)	Fracture aperture width b_i (m)
Inspection 2011 (only fracture aperture widths are given in the report, lengths assumed based on comparison with inspection data from 2000 and photos.)		
Ip1+Ip2	9.8	$1.1 \cdot 10^{-3}$
Ip3	9.8	$4.5 \cdot 10^{-4}$
Ip4	17.1	$1.8 \cdot 10^{-3}$
Ip5	0.5	$3.0 \cdot 10^{-4}$
Ip6	1.2	$1.5 \cdot 10^{-3}$
Ip6	7	$1.6 \cdot 10^{-3}$
Ip7	5.5	$2.5 \cdot 10^{-4}$
Ip9	1	$2.5 \cdot 10^{-4}$
Ip10	1	$2.1 \cdot 10^{-4}$
Ip11	1	$3.0 \cdot 10^{-4}$
Ip12+Ip16	2	$3.0 \cdot 10^{-4}$
Ip13	2	$1.5 \cdot 10^{-4}$
Ip14	2	$3.0 \cdot 10^{-4}$
Ip15	1.5	$3.0 \cdot 10^{-3}$
Ip17	11.8	$1.4 \cdot 10^{-3}$
Inspection 2000 Western long side		
1	2.5	$5.0 \cdot 10^{-4}$
2	4	$1.1 \cdot 10^{-3}$
3	3.5	$5.0 \cdot 10^{-4}$
4	1.5	$2.0 \cdot 10^{-3}$
5	1.2	$2.0 \cdot 10^{-3}$
6	7	$7.9 \cdot 10^{-4}$
7	4	$5.0 \cdot 10^{-4}$
8	1.5	$2.0 \cdot 10^{-3}$
9	3	$3.0 \cdot 10^{-4}$
Inspection 2000 Eastern long side		
10	1.5	$2.0 \cdot 10^{-3}$
11	2.5	$5.0 \cdot 10^{-4}$
12	4	$1.0 \cdot 10^{-3}$
13	4	$3.6 \cdot 10^{-4}$
14	1.5	$3.0 \cdot 10^{-3}$
15	4	$5.0 \cdot 10^{-4}$
16	4	$5.0 \cdot 10^{-4}$
17	4	$5.0 \cdot 10^{-4}$
18	4	$5.0 \cdot 10^{-4}$
19	4	$2.0 \cdot 10^{-3}$
20	7	$5.0 \cdot 10^{-4}$
21	1.2	$1.0 \cdot 10^{-3}$

3.3.2. Carbonation reactions

Höglund (2014) reports that laboratory experiments have shown that the degradation depth of concrete in groundwater is highly dependent on the carbonate concentration of the external solution. If the external groundwater contains dissolved carbon dioxide, precipitation of calcite might be expected. Moreover, he recognizes that exposure to carbonate may result in lowering of the pH in the concrete and chloride intrusion is known to result in initiation of corrosion of reinforcement bars and other steel components in the concrete constructions which are initially passivated by the high pH. Höglund (2014) goes onto state that a study by Moranville et al. (2004) showed that the leaching depth of concrete decreases by a factor of 5 when the external water is in equilibrium with atmospheric CO_2, due to the sealing produced by calcite precipitation at the cement-water interface.

The analysis of leaching of concrete by groundwater presented by Höglund (2014; Section 5) is informative, but focuses upon removal of Ca^{2+} from portlandite and/or CSH gel, and excludes carbonation effects. It is thus unclear from Höglund's analysis how 'armouring' of fractures by the formation of solid carbonates (aragonite, calcite) would impede concrete degradation and/or have deleterious effects upon radionuclide retention (decreased pore fluid pH; decreased sorption). Also, it is not clear if the exclusion of carbonation from the consideration of concrete degradation processes is a pessimistic assumption.

The more detailed (combined) analysis of the effects of chloride, sulphate and carbonate in Section 5.2 is more realistic, but carbonation is considered here by Höglund to consist of the formation of monocarbonate rather than calcite.

In Section 7 (2-D modelling of 1BMA vault with brackish groundwater), during the period 500–5 000 years, Höglund (2014) shows that calcite precipitates primarily in the macadam fill at the left-hand upstream side close to the rock wall that limits the increase of dissolved carbonate. The maximum impact on the porosity due to precipitation of calcite during the first 5 ka is a reduction of the porosity in the macadam from 30 to 27 %. During the remaining simulation period (10–100 ka) calcite precipitation takes place in the macadam fill (reaching a lowest porosity of 19 % at 100 ka) and on the outside of the concrete wall at the left side, as well as above the concrete lid, where the carbonate in groundwater meets calcium leached from the concrete constructions. The porosity is estimated by Höglund (2014) to change from 11 to 4.7 % after 100 ka due to calcite precipitation in the most exposed parts of the concrete constructions. Hence, the precipitation of calcite is not expected to result in extensive blocking of the porosity. In the concrete structures, calcite replaces monocarboaluminate which decomposes with simultaneous formation of Friedel's salt. The formation of Friedel's salt requires the supply of chloride ions from the saline groundwater.

3.3.3. Redox

Redox is viewed by SKB to be of high importance in the safety assessment (bottom of page 159 of TR-14-01) and SKB considers that if the system responds to the Fe-magnetite system, and considering the evolution of pH due to degradation of the concrete barriers, the redox potential would be about –0.7 V at pH =12.5. This could be achieved within 5 years of repository closure.

Redox evolution in SFR is discussed in detail in a paper by Duro et al. (2014). They consider that corrosion of the steel-based material present in the repository keeps the system under reducing conditions for long time periods. Their simulations considered both the presence and the absence of microbial activity. In the initial stages after the repository closure, they found that the microbially-mediated oxidation of organic matter rapidly causes the depletion of oxygen in the system. The system is thereafter kept under reducing conditions, and hydrogen is generated due to the anoxic corrosion of steel. The times for exhaustion of the steel vary from 5 ka to more than 60 ka in the different vaults, depending on the amount and the surface area of steel. After the complete corrosion of steel, they believe that the system would still maintain a high reducing capacity, due to the magnetite formed as a steel corrosion product. Simulations assuming the presence of oxic water due to glacial melting, intruding the system 60 ka after repository closure, indicate that magnetite is progressively oxidised, forming Fe(III) oxides. The time at which magnetite is completely oxidised varies depending on the amount of steel initially present in the waste package.

However, it should be noted that there is uncertainty regarding magnetite being the 'end-point' of anaerobic corrosion of steel at low temperatures. Some authors (e.g. Reardon, 1995; Wilkin et al., 2003; Phillips et al., 2000) believe that the transformation of $Fe(OH)_2$ (initial corrosion product) to magnetite (theoretical long-term corrosion product) is unlikely at temperatures less than 100 °C. This would imply much higher concentrations of Fe^{2+} in the near-field due to buffering by $Fe(OH)_2$ solubility with the potential for its substitution for Ca^{2+} in Ca-hydroxides and C-S-H, thus lowering the long-term pH of the near-field. This uncertainty is not acknowledged by Duro et al. (2014) or elsewhere in the SR-PSU documentation.

Of course, the attainment of such reducing conditions in the repository implies a sharp redox front with the geological barrier where the redox state may be maintained at the relatively more oxidising conditions of hematite-magnetite equilibrium. Therefore, chemically-reducing fluids (containing hydrogen and organic acids) migrating from the repository will tend to destabilize redox-sensitive mineral such as Fe-oxides and clays in the geosphere.

3.4. Interaction between EBS materials

There is an in-depth discussion of the corrosion of metals in waste packages in the waste packaging process report (SKB, 2014c; Section 3.5.9, page 147 and following; Section 4.4.7, page 197 and following), but there is no discussion of the fate of ferrous iron and how it may impact upon concrete degradation in particular. This is also absent from the modelling described by Höglund (2014). Indeed, towards the base of page 171, it is stated:

'*Iron is present in low concentrations in groundwater, unless the conditions are very reducing. Iron is a constituent of concrete and may appear in various minerals including iron hydroxides, hydrotalcite-Fe, iron-substituted ettringite etc. Iron also appears in large amounts in the waste and waste packaging, as well as in reinforcement and other steel construction details. Iron in the form of metal that may undergo corrosion*

and form dissolved or solid reactions products have not been considered in the present modelling but could be addressed in future studies'.

And again, on page 251:

'*SFR contains other steel components embedded in concrete, such as grouted waste drums and steel in concrete-conditioned waste, which is outside the scope of this report. The corrosion of these may also affect the performance of SFR and may need to be considered in future studies*'.

All iron present in cement and concrete is fully oxidised to the ferric form, but under the chemically-reducing, post-closure conditions of SFR, ferrous iron would be thermodynamically preferred. It is a moot point whether ferric iron in the cement could be reduced by microbiological activity associated with hydrogen released from anaerobic corrosion, but there will be substantial amounts of ferrous iron available from the anaerobic corrosion of steel.

Consequently, it could be considered that ferrous iron derived from steel corrosion could play an important role in the degradation of cement and concrete in the SFR. Although the solubility of Fe^{2+} in near-field pore fluids is limited at high pH, the inventory of iron in the repository EBS materials is large and it is conceivable that Fe^{2+} could play a similar role to that of Mg^{2+} in groundwater, by substituting for Ca^{2+} in portlandite and other Ca-bearing solids. This would serve to lower the ambient pH of pore fluids from 12.5 (equilibration with portlandite) to ~9 (equilibration with $Fe(OH)_2$). This type of reaction has not been hypothesised previously (by any WMO), but could conceivably occur because of the very reducing conditions associated with the anaerobic corrosion of steel and the likely enhanced solubility of ferrous iron.

There are concerns that the description of the process of corrosion of metal components in SFR by SKB is constrained to a large degree by reported performance of such materials in the sub-aerial (surface) environment where 'rust' (ferric oxyhydroxides of one form or another) dominates (see discussion on pages 48-49 of Höglund, 2013). It is not clear, for example, that 'rust' (or even magnetite) would form in a chemically-reducing geological environment (e.g. text on page 255 of Höglund, 2014). Consideration should therefore be given to the evaluation of how metal corrosion processes may be different in the long-term sub-surface. It may be, for example that steel corrosion is initiated under oxic conditions (e.g. before repository closure) and then proceeds anoxically. It is not clear that the large collection of published work on steel corrosion in concrete in surficial environments is relevant to deep geological disposal.

4. Potential for armouring of fractures in cement

4.1. Issues investigated

SKB's analysis of leaching of concrete by groundwater is presented by Höglund (Höglund, 2013, Section 5). The analysis assumes various scenarios for cement leaching, including diffusion-limited degradation of intact or weathered concrete, advection-controlled degradation of hydraulically-conductive concrete, and advection-controlled degradation caused by groundwater flow through fractures in the concrete. In each case, analytical solutions for the leaching of Ca ions from the concrete are presented, which are based on various simplifying assumptions. An additional simplified model is presented that considers the effect of intrusion of dissolved salts (chloride, carbonate and sulphate), but the model does not consider the formation of calcite. Salt intrusion has the potential to lower pH and thus deleteriously affect the corrosion passivation property of the cement.

Realistic estimates of cement degradation rates and the pattern of their evolution are important, since they will impact upon radionuclide retention in the EBS, longevity of engineered features, the patterns and timescales associated with the development of near-field heterogeneities and the extent to which a high-pH plume enters the near-field.

The scenarios that might be expected lead to the most significant deviation from the as-emplaced high-pH, diffusion-limited, transport environment in the concrete are those scenarios that include some fracturing of the concrete. This can include either fully-penetrating advective fractures or partially penetrating fractures in which solute transport continues to be diffusion-limited. These cases should be investigated in more detail than that presented by SKB (Höglund, 2013), particularly to assess the potential for feedbacks caused by physico-chemical interactions to affect the evolution around the interface between the fracture and the concrete matrix.

One possibility is that the interface will become 'armoured' through the precipitation of carbonates (and potentially other solids). This could act to isolate the cement from the fracture pore water, limiting the concrete leaching process and its pH-buffering effect, and allowing lower-pH groundwaters to penetrate deeper into the fractures more rapidly. This could have consequences for the corrosion passivation property of the concrete, possibly leading to corrosion of rebars near the lower pH groundwaters. Volumetric expansion of the rebars could lead to additional cracking. Moreover, the altered physical properties of the fracture-concrete matrix interface and the lower pH environment could hinder sorption and thus affect the transport and retention properties of any radionuclides that are released from the waste form.

4.2. Approach to investigating issues

Reactive-transport models of the fracture-matrix system were constructed, based on groundwater compositions, cement assemblages and concrete fracture dimensions consistent with SKB's specifications. The set of potentially-forming secondary minerals was assessed by appealing to the cement literature and evidence from

natural analogues. Alternative models of fracture-matrix interactions were considered, including assumptions of neoformation 'in the matrix' and 'on the fracture surface' to determine if any realistic assumptions could be found that lead to significantly different evolution of the pH plume in the fracture-matrix system.

4.3. Conceptual model

Prior to the development of detailed models of the fracture-matrix system, a simplified 'preliminary' model was constructed in which a 0.5m thick section of concrete was reacted with groundwater as a fixed boundary condition (Figure 4-1). A geometric approach was taken to model discretisation, because this approach is more efficient computationally as smaller cells near the expected alteration are included. The width of the smallest cell in contact with the groundwater boundary is 0.01m. This smallest grid cell size was imposed because preliminary modelling (Section 4.9.1) suggested that pore clogging would occur due to precipitation of secondary minerals. Due to the coupling of transport with the evolution of the mineral assemblage in the model (diffusion reduces with porosity, as described in Section 4.5), rates of transport will reduce to zero as the porosity in any cell becomes completely clogged, which effectively halts the simulation as no further groundwater ingress is possible. The depth of 0.01m was chosen to be representative of the depth over which clogging of matrix porosity might be expected to lead to a complete loss of diffusivity into the cement, since compete clogging over smaller scales (such as 1mm scales) might not be expected to lead to a complete loss of transport due to the heterogeneity of the media. However, in the numerical model, transport would be halted for any clogging layer thickness, and timescales for clogging in very small cells would be rapid, leading to the model revealing little of the possible cement alteration beyond the clogged region.
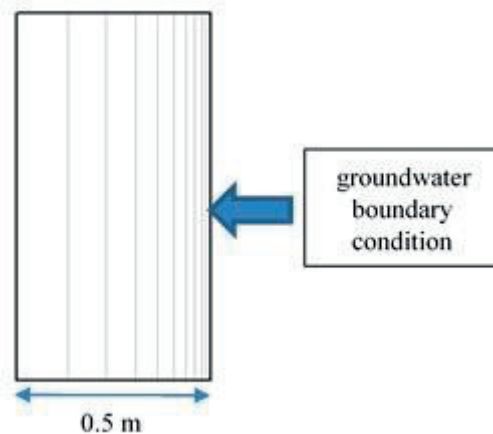
Figure 4-1: Conceptual model for simple 'preliminary' 1D model of concrete-water interaction (diffusive transport only).

The conceptual geometry considered in the fracture-matrix models is shown in Figure 4-2. Incoming groundwater is advected through the fracture and diffusively mixes with matrix porewaters, leading to mineral precipitation and dissolution in the matrix and the possibility of development of an armouring layer in the fracture. It is assumed that there is no flow in the matrix.

If formed, the armouring layer will inhibit the diffusive transfer of solutes between the open fracture and the matrix. The thickness of the armouring layer will evolve

with time as secondary minerals precipitate and dissolve in the fracture. The thickness will also vary in space and will be likely to be thickest in upstream regions where fresh incoming waters mix with matrix porewaters. Further along the fracture, incoming waters will be expected to be buffered more and will therefore be expected to react less.
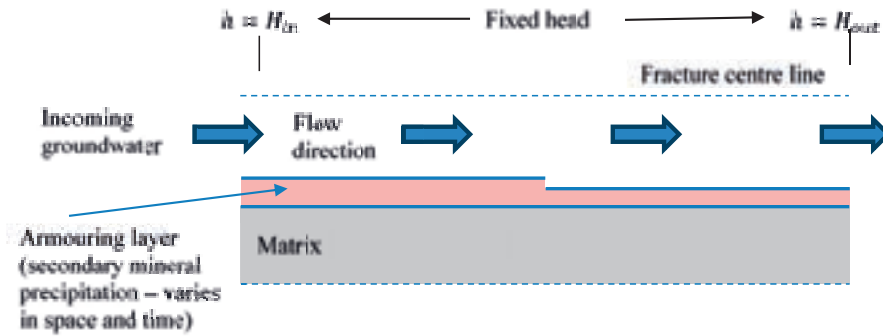

Figure 4-2: Conceptual geometry of fracture including armouring layer. The position of the armouring layer varies with time and the thickness of the layer will vary along the fracture.

The discretisation of the geometry as a grid, and the transport processes on the grid are shown in Figure 4-3. In the grid, the cell locations are fixed for all time. Therefore, if an armouring layer develops, fracture cells that originally contained only open fracture regions will eventually contain both open fracture (with a reduced aperture) and a region of armouring layer, as shown in
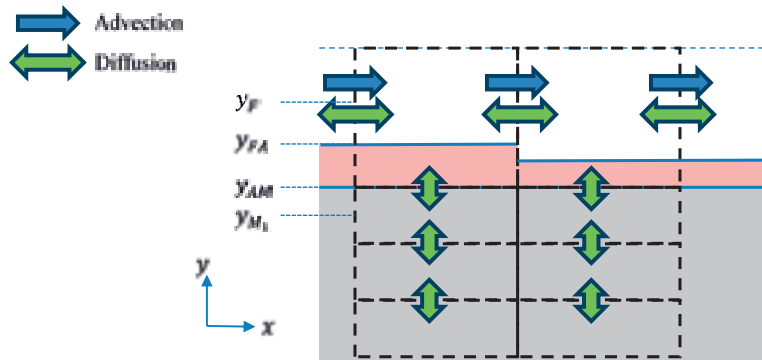
Figure 4-4. Advection and diffusion are modelled in the fracture. In the matrix, only diffusion perpendicular to the fracture is simulated.
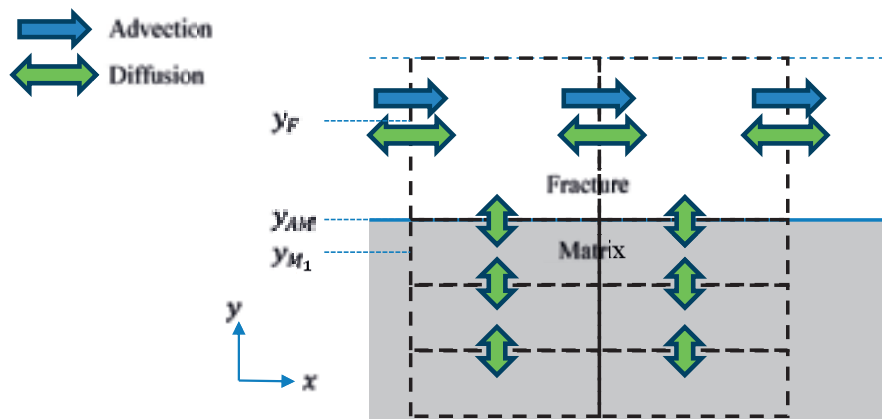
Figure 4-3: Discretisation of conceptual geometry into grid cells at t_0. Dotted-black lines show grid cell boundaries. Transport processes are shown: advection only takes place in the fracture cells (1-D flowline); diffusion occurs in the fracture cells, and perpendicularly in the matrix cells. Overall discretisation is 1.5-D due to omission of diffusion interactions in the x-direction in the matrix.
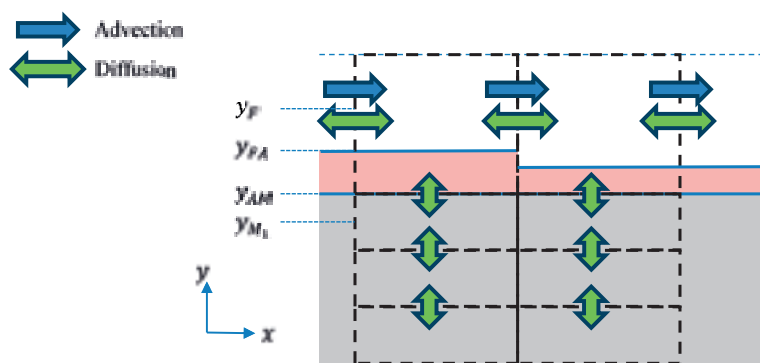
Figure 4-4: Discretisation of conceptual geometry into grid cells at $t > t_0$ when an armouring layer is assumed to have developed. 'Fracture cells' now include regions of both open fracture and armouring layer.

The model focuses on interactions between the fracture and the matrix. As the fracture surface becomes armoured:

- Diffusion between the fracture and matrix becomes inhibited; and
- The open fracture aperture is reduced, leading to a reduction in flow rate and advection.

The model, however, assumes that diffusion within the fracture is always possible; i.e. that the fracture never becomes so clogged as to completely halt the diffusion of solutes along the fracture pathway. This is because, in the model the fracture is represented as a 1-D feature, whereas in the true system, it may be a 2-D feature, which may, for some time, allow for diffusion around any locally clogged regions. Thus, if the fracture surface becomes fully armoured along its length, leading to a loss of buffering capacity from the matrix, then the expected behaviour in the model is that the incoming groundwater will eventually travel through the fracture either by

advection and diffusion (if the fracture surfaces are fully armoured everywhere, but the fracture remains open) or by diffusion (if the fracture surface is fully armoured everywhere and the open fracture aperture reduces to zero at any point). If it is believed that the fracture can clog sufficiently to become impassable by diffusion, then any evolution in the system after the time of complete clogging at a single location in the fracture should be discarded.

The conceptual model described above has been implemented using the QPAC general purpose modelling software (Quintessa, 2013) and its reactive transport module. The QPAC model solves for the evolving concentrations and fluxes of aqueous solutes, concentrations of mineral species and porosity in the fracture and matrix regions of the system.

4.4. Chemical model

4.4.1. Cement and concrete data

An idealised and concrete composition (Table 4-1Table 4-) was generated using data from Cronstrand (2014). Volume % data were generated based on reported proportions of solid masses using molal volume and molecular mass data from the thermodynamic database 'Thermoddem', version 1.01 (Blanc et al., 2012). Magnetite (present in small amounts) was excluded from the model. A reference porosity value of 0.11 was taken from SKB (2014f).

Table 4-1: Idealised SFR Concrete Compositions.

Solid	Concrete
	vol.%
C-S-H gel	8.72
Portlandite	3.30
Ettringite	1.65
C3AH6	0.96
Hydrotalcite	0.21
Quartz	74.17
Porosity	11.0
Total	100

4.4.2. Thermodynamic data

Thermodynamic data (equilibrium constants for hydrolysis reactions, molal volume and masses) were taken from version 1.01 of the 'Thermoddem' database produced in Geochemist's Workbench format (Blanc et al., 2012). This database was used as it includes a wide range of cement solids and rock-forming minerals.

4.4.3. Potential cement alteration products

Potential cement alteration products were identified via literature review and thermodynamic modelling. Primary and secondary minerals/solids and compositions (as in Thermoddem version 1.01) are given in Table 4-2. In the Thermoddem database, version 1.01, C-S-H gel is represented by three discrete end-members with different Ca/Si ratios. The highest Ca/Si ratio composition (CSH_1.6) is included as the primary C-S-H gel composition, with lower Ca/Si end-members being included to allow for the simulations of cement leaching. There are several potential alteration pathways, including carbonation, i.e. the formation of carbonate minerals (e.g. Taylor, 1990; Purser et al., 2013); magnesium attack (resulting in brucite formation or formation of other magnesium-bearing solids, commonly associated with seawater-cement or seawater-brine interaction (Buenfield and Newman, 1986); sulphate attack, with alteration to minerals such as ettringite, gypsum and thaumasite (e.g. Taylor, 1990; Crammond, 2002; Thaumasite Expert Group 2002; MacPhee and Barnett, 2004) and chloride attack resulting in the formation of minerals such as Friedel's salt or Kuzel's salt (Balonis et al., 2010, and references therein).

In addition to cement leaching, carbonation and sulphate/magnesium/chloride attack, the interaction of cement with rock forming minerals is likely to cause a zone of alteration forming at cement-rock or cement-clay interfaces. The alteration it likely to include several aluminosilicate minerals and calcium aluminium-silicate-hydrate (C-A-S-H) phases (e.g. Savage et al., 2002; Savage et al., 2007; Savage et al., 2010; Savage 2011). At the time of modelling, there was a lack of data for C-A-S-H gels, therefore only representative clays, framework silicates (such as zeolites) and poorly-crystalline silica (amorphous silica) were included in the reactive transport simulations. The minerals chosen were considered representative, as there is a very wide range of compositions within the mineral groups of interest (e.g. Chipera and Apps, 2001) and the reliance on estimated thermodynamic data for many zeolite compositions also results in a degree of uncertainty in which specific compositions are of most relevance (e.g. Savage et al., 2007; Arthur et al., 2011).

Table 4-2: Summary of primary and potential secondary solids (using cement solids from Cronstrand, 2014).

Solid	Composition
Primary Concrete Solids	
Portlandite	$Ca(OH)_2$
CSH (1.6)	$Ca_{1.60}SiO_{3.6}:2.58H_2O$
Ettringite	$Ca_6Al_2(SO_4)_3(OH)_{12}:26H_2O$
C3AH6	$Ca_3Al_2(OH)_{12}$
Hydrotalcite	$Mg_4Al_2O_7:10H_2O$
Quartz (inert)	SiO_2
Possible Alteration Products	
CSH (1.2)	$Ca_{1.2}SiO_{3.2}:2.06H_2O$
CSH (0.8)	$Ca_{0.8}SiO_{2.8}:1.54H_2O$
Calcite	$CaCO_3$
Dolomite	$CaMg(CO_3)_2$
Friedel's salt	$Ca_4Al_2Cl_2O_6:10H_2O$
Thaumasite	$CaSiO_3CaSO_4CaCO_3:15H_2O$
Gypsum	$CaSO_4:2H_2O$
Brucite	$Mg(OH)_2$
Sepiolite	$Mg_4Si_{6O15}(OH)_2:6_HO$
Analcime	$Na_{0.99}Al_{0.99}Si_{2.01}O_6:H_2O$
Gismondine	$Ca_2Al_4Si_4O_{16}:9H_2O$

Chabazite	$Ca(Al_2Si_4)O_{12}:6H_2O$
Scolecite	$CaAl_2Si_3O_{10}:3H_2O$
Straetlingite	$Ca_2Al_2SiO_2(OH)_{10}:2.5H_2O$
Ca-Heulandite	$Ca_{1.07}Al_{2.14}Si_{6.86}O_{18}:6.17H_2O$
Na-Heulandite	$Na_{2.14}Al_{2.14}Si_{6.86}O_{18}:6.17H_2O$
Ca-Clinoptilolite	$Ca_{0.55}(Si_{4.9}Al_{1.1})O_{12}:3.9H_2O$
Na-Clinoptilolite	$Na_{1.1}(Si_{4.9}Al_{1.1})O_{12}:3.5H_2O$
Ca-Phillipsite	$Ca_{0.5}AlSi_3O_8:3H_2O$
Na-Phillipsite	$NaAlSi_3O_8:3H_2O$
ZeoliteP(Ca)	$Ca_2Al4Si_4O_{16}:9H_2O$
Illite (Al)	$K_{0.85}Al_{2.8}5Si_{3.15}O10(OH)_2$
Na-Beidellite	$Na_{0.34}Al_{2.34}Si_{3.66}O_{10}(OH)_2$
Ca-Beidellite	$Ca_{0.17}Al_{2.34}Si_{3.66}O_{10}(OH)_2$
Na-Saponite	$Na_{0.33}Mg_3Al_{0.33}Si_{3.67}O_{10}(OH)_2$
Ca-Saponite	$Ca_{0.17}Mg_3Al_{0.34}Si_{3.66}O_{10}(OH)_2$
$SiO_{2(am)}$	SiO_2

Thermodynamic modelling using the Thermoddem database, version 1.01, suggests that potential secondary aluminosilicate minerals include: Ca-zeoliteP, chabazite, gismondine, vermiculite, saponite, beidellite and straetlingite. It is assumed that the cement porefluid evolves to become richer in dissolved aluminium and silica as cement reacts with intruding groundwater (Figure 4-5). In addition to zeoliteP, chabazite, and gismondine, a range of other representative zeolite minerals were included as potential secondary alteration products based on Savage et al. (2007) and Savage (2011). Note that K-feldspar has been considered as a potential product of cement-rock interaction, but it's absence in the Thermoddem database, version 1.01, has led to it being omitted from the models presented herein.
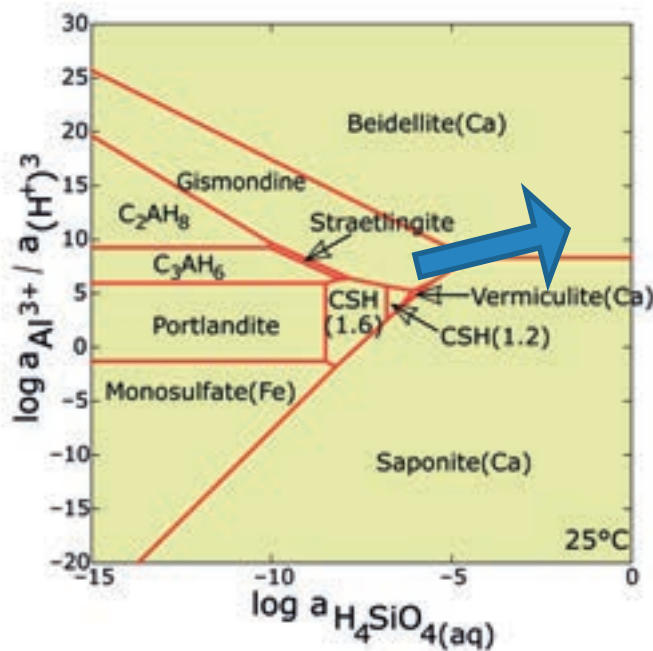
Figure 4-5: Activity diagram showing potential reaction pathway occurring due to cement-groundwater interactions. Constructed using the Act2 module of Geochemist's Workbench (Bethke, 2008) and v1.01 of the Thermoddem database version 1.01, . Ca^{2+} buffered by

Portlandite, SO_4^{2-} buffered by ettringite, Mg^{2+} buffered by hydrotalcite, Fe^{2+} buffered by magnetite, Cl^- buffered by Friedel's salt, $\log f\ O_{2(g)}$ = -69, $\log a\ Na^+$ = -1.3, T = 25 °C, P = 1 bar.

Although less commonly discussed in the literature than C-S-H gel, M-S-H (Magnesium Silicate-Hydrate) gel may form in magnesium-rich systems and it may be a candidate cement alteration product in environments with relatively higher dissolved magnesium concentrations. Experimental work also suggests that Magnesium-Silicate-Hydrate (M-S-H) could form due to interaction of cement with Mg sulphate solutions (e.g. Santhanam et al., 2002). Thermodynamic data are sparse for M-S-H gel, so sepiolite (a magnesium-rich clay mineral) was included as a proxy in the model, as spectroscopic analyses of the material suggests that M-S-H bonding environments are similar to those of magnesium-rich clay minerals (Brew and Glasser, 2005).

4.4.4. Water compositions

Reactive transport modelling focussed on the reference 'brackish/saline' water during the temperate climate domain when the repository is situated beneath the surface of the sea (Auqué et al., 2013) (Table 4-3). The solute concentrations associated with this composition were also used by Cronstrand (2014) for pH modelling.

Table 4-3: Reported and re-equilibrated compositions of brackish/saline water (and selected mineral saturation index values, SI). Model compositions 1 and 2 were generated using Geochemist's Workbench (SpecE8 module), in Model 1, the concentration of Al is set as kaolinite equilibrium; in Model 2, total dissolved carbon corresponds to calcite equilibrium and dissolved silica is set as quartz equilibrium.

	Reported	Model 1	Model 2
T (deg. C)	25	25	25
pH	7.3	7.3	7.3
pe	-3.804	-3.804	-3.804
Eh (V)	-0.225	-0.225	-0.225
IS	0.12468	0.12468	0.124556
log f O2	-69.109	-69.109	-69.109
log f CO2	-2.506	-2.506	-2.644
mol/kg			
Cl	9.780E-02	9.780E-02	9.780E-02
S (total)	3.609E-03	3.609E-03	3.609E-03
C (TIC)	1.461E-03	1.461E-03	1.062E-03
Na	6.464E-02	6.464E-02	6.463E-02
K	5.067E-04	5.067E-04	5.067E-04
Ca	1.483E-02	1.483E-02	1.483E-02
Mg	6.114E-03	6.114E-03	6.114E-03

Si	1.814E-04	1.814E-04	1.816E-04
Al (kaol)	-	3.76E-09	3.757E-09

Mineral	SI	SI	SI
Calcite	0.138	0.138	0.000
Quartz(alpha)	-0.001	-0.001	0.000
Kaolinite	-	0.000	0.000

An initial cement porewater composition was produced using the SpecE8 module of Geochemist's Workbench, assuming cement solid/mineral buffering (Table 4-4). Note that the composition assumes that alkalis have been leached, leaving Na and K concentrations similar to those of the intruding groundwater. The initial Cl⁻ concentration was set at Friedel's salt equilibrium, as this solid would be supersaturated into the initial cement pore fluid if measured groundwater Cl⁻ concentration was used, thereby promoting rapid alteration throughout the cement from t = 0.

Table 4-4: Model initial concrete porewater composition.

	Parameter	Assumption
T (deg. C)	25	
pH	12.585	charge balance
Eh (V)	-0.5377	
log f O2	-69.109	groundwater value
log f CO2	-13.139	calculated
Conc. (mol/kg)		
Cl	4.047E-02	Friedel's salt
S (VI)	1.661E-05	ettringite buffer
C (TIC)	8.475E-06	calcite buffer
Na	6.458E-02	reported
K	5.063E-04	reported
Ca	1.458E-02	portlandite buffer
Mg	2.534E-09	hydrotalcite buffer
Si	3.099E-06	CSH(1.6)buffer
Al	6.004E-05	C3AH6 buffer

The equilibration calculations undertaken to produce the model water compositions allowed relevant secondary aqueous species to be identified for inclusion in detailed

models. The 'basis' species included in Thermoddem, version 1.01, are: Cl^-, Na^+, Ca^{2+}, Mg^{2+}, SO_4^{2-}, HCO_3^-, K^+, Al^{3+}, $H_4SiO_{4(aq)}$, H^+. Secondary species (occurring in calculations at concentrations > 1e-15 molal) are: AlO_2^-, $HAlO_{2(aq)}$, $NaAlO_{2(aq)}$, $Al(OH)_2^+$, $Al(OH)^{2+}$, $AlH_3SiO_4^{2+}$, $KAlO_{2(aq)}$, $AlSO_4^+$, $CO_{2(aq)}$, CO_3^{2-}, $CaOH^+$, $CaCO_{3(aq)}$, $Ca(HCO_3)^+$, $CaSO_{4(aq)}$, $CaCl^+$, $CaCl_{2(aq)}$, $HCl_{(aq)}$, $KCl_{(aq)}$, $KAlO_{2(aq)}$, KSO_4^-, $KOH_{(aq)}$, $MgCl^+$, $MgSO_{4(aq)}$, $Mg(HCO_3)^+$, $MgCO_{3(aq)}$, $MgOH^+$, $NaSO_4^-$, $NaHCO_{3(aq)}$, $NaCO_3^-$, $NaOH_{(aq)}$, $HSiO_3^-$, $H_2SiO_4^{2-}$, $Si_2O_2(OH)_5^-$, $Si_2O_3(OH)_4^{2-}$, HSO_4^-, OH^-.

In Geochemist's Workbench (and reactive transport models) the 'Helgeson B-dot' method (an extended Debye-Hückel approach) is use for mean solute activity calculation. The B-dot model has activity coefficients for charged ions given by

$$\log \gamma_i = \frac{-Az_i^2 \sqrt{I}}{1+a_i^\circ B \sqrt{I}} + \dot{B}I \qquad \forall i \in S \text{ with } z_i \neq 0.$$

The coefficients A, B and $\dot{B}$ vary with temperature and are provided as lookup tables in the standard database files. The parameter a_i° is the size (diameter) of the ion, which is also available in the standard databases, and values for B in the databases are usually such that a_i° is specified in angstroms (10^{-10} m). The B-dot model was used in preference to the Davies equation and other approaches for mean solute activity calculations in reaction-transport modelling as it has the capacity to accurately model activity-concentration relationships in solutions of relatively high ionic strengths, reportedly being reasonably accurate to an ionic strength of ~1 mol/kg, or even up to ~3 mol/kg for NaCl-dominated water compositions (Bethke, 2008; Helgeson, 1969).

4.4.5. Kinetic data

The reactive transport simulations include a kinetic treatment of mineral dissolution/precipitation reactions, using a routinely-applied Transition State Theory (TST) -based approach (e.g. Aagaard and Helgeson 1982) represented by (Palandri and Kharaka, 2004):

$$\frac{dS}{dt} = A(S)\left(k_1(a_{H+})^{n_1} + k_2 + k_3(a_{H+})^{n_3} + k_4(f_{CO_2})^{n_4}\right)\left(1 - \frac{Q}{K}\right) \qquad (4-1)$$

where S is the quantity of a solid of interest (mol), t is time (s), $k_{1,2,3,4}$ are the rate constants (mol/m²/s) for acid, neutral, base and carbonate mechanisms, $A(S)$ is the mineral reactive surface area (m²), n is a dimensionless catalysis constant for acid (n_1), base (n_3) and carbonate-dependent rates (n_4), Q is the ion activity product for the solid of interest, a_{H+} is the activity of the hydrogen ion, f_{CO_2} is the CO_2 fugacity, and K is the equilibrium constant for the mineral. Apart from $A(S)$ and k, these parameters are dimensionless. The mineral's reactive surface area is a function of the mineral abundance, its specific surface area, A_{sp} (m²/g) and its molecular weight, W (g/mol), and is given by $A(S) = A_{sp} W S$.

The compilation by Palandri and Kharaka (2005) was used as the primary source of kinetic data (k and n values) for silicate and carbonate minerals. Additional data required for other minerals were taken from the published peer-reviewed literature (Table 4-5). Approximate rates of dissolution reactions for cement solids were taken from Baur et al., (2004). Where data were unavailable for a specific k term in Equation (4-1, the value of that term was set to zero. The calculated dissolution rates

under such circumstances are more uncertain than in cases where all terms in the equation are constrained by experimental data.

Where data were completely unavailable, an analogue approach was used, whereby values for the solid phase of interest were assumed to be comparable to those measured for a similar substance. Specific surface area data (Table 4-5) are either reported values or were calculated based on geometric assumptions (spherical grains of 1 or 0.25 μm diameter for minerals considered to be more crystalline or very poorly crystalline, respectively).

Table 4-5: Kinetic data.

Solid	Acid log k_1 mol/m²/s	n_1 -	Neutral log k_2 mol/m²/s	Base log k_3 mol/m²/s	n_3 -	Carbonate log k_4 mol/m²/s	n_4 -	Notes	A m²/g	Notes
Primary Solids										
Portlandite	-	-	-12	-	-	-	-	-	9.8	Ettringite analogue
CSH (1.6)	-	-	-12	-	-	-	-	Baur et al. (2004)	41	BET Data (Baur et al., 2003)
Ettringite	-	-	-12	-	-	-	-	Baur et al. (2004)	9.8	BET Data (Baur et al., 2003)
C3AH6	-	-	-12	-	-	-	-	Ettringite analogue	9.8	Ettringite analogue
Hydrotalcite	-	-	-12	-	-	-	-	Ettringite analogue	9.8	Ettringite analogue
Magnetite	-	-	-10.78	-	-	-	-	Palandri and Kharaka (2004)	9.8	Ettringite analogue
Secondary Solids										
CSH (1.2)	-	-	-12	-	-	-	-	Baur et al. (2004)	41	BET Data (Baur et al., 2003)
CSH (0.8)	-	-	-12	-	-	-	-	Baur et al. (2004)	41	BET Data (Baur et al., 2003)
Calcite	-0.3	1	-5.81	-	-	-3.48	1.0	Palandri and Kharaka (2004)	2.2	1 μm diameter spheres
Dolomite	-3.19	0.5	-7.53	-	-	-5.11	0.5	Palandri and Kharaka (2004)	2.1	1 μm diameter spheres
Friedel's salt	-	-	-12	-	-	-	-	Ettringite analogue	9.8	Ettringite analogue
Thaumasite	-	-	-12	-	-	-	-	Ettringite data used as analogue	9.8	Ettringite analogue
Gypsum	-	-	-2.79	-	-	-	-	Palandri and Kharaka (2004)	10.4	0.25 μm diameter spheres
Brucite	-4.73	0.5	-8.24	-	-	-	-	Palandri and Kharaka (2004)	10	0.25 μm diameter spheres

Solid	Acid log k_1 mol/m²/s	n_1	Neutral log k_2 mol/m²/s	Base log k_3 mol/m²/s	n_3	Carbonate log k_4 mol/m²/s	n_4	Notes	A m²/g	Notes
Sepiolite	-5.7	0.8	-12.4	-	-	-	-	Lizardite analogue	12	0.25 µm diameter spheres BET data (Savage et al., 2001)
Analcime	-	-	-	-13.9	0.36	-	-	Savage et al. (2002)	0.25	
Gismondine	-	-	-	-16.4	0.36	-	-	Clinoptilolite analogue	10.1	clinoptilolite analogue
Chabazite	-	-	-	-16.4	0.36	-	-	Clinoptilolite analogue	10.1	clinoptilolite analogue
Scolecite	-	-	-	-16.4	0.36	-	-	Clinoptilolite analogue	10.1	clinoptilolite analogue
Straetlingite	-	-	-	-16.4	0.36	-	-	Clinoptilolite analogue	10.1	clinoptilolite analogue
Ca-Heulandite	-	-	-	-16.4	0.36	-	-	Clinoptilolite analogue	10.1	clinoptilolite analogue
Na-Heulandite	-	-	-	-16.4	0.36	-	-	Clinoptilolite analogue	10.1	clinoptilolite analogue
Ca-Clinoptilolite	-	-	-	-16.4	0.36	-	-	Murphy et al. (1996) (H+ dependency data for analcime).	10.1	Murphy et al. (1996)
Na-Clinoptilolite	-	-	-	-16.4	0.36	-	-	Murphy et al. (1996) (H+ dependency data for analcime).	10.1	Murphy et al. (1996)
K-Clinoptilolite	-	-	-	-16.4	0.36	-	-	Murphy et al. (1996) (H+ dependency data for analcime).	10.1	Murphy et al. (1996)
Ca-Phillipsite	-	-	-	-16.4	0.36	-	-	Clinoptilolite analogue	10.1	clinoptilolite analogue
Na-Phillipsite	-	-	-	-16.4	0.36	-	-	Clinoptilolite analogue	10.1	clinoptilolite analogue
K-Phillipsite	-	-	-	-16.4	0.36	-	-	Clinoptilolite analogue	10.1	clinoptilolite analogue
ZeoliteP(Ca)	-	-	-	-16.4	0.36	-	-	Clinoptilolite analogue	10.1	clinoptilolite analogue

47

48

Solid	Acid		Neutral	Base		Carbonate		Notes	A m²/g	Notes
	log k_1 mol/m²/s	n_1 -	log k_2 mol/m²/s	log k_3 mol/m²/s	n_3 -	log k_4 mol/m²/s	n_4 -			
Illite (Al)	-11.78	0.5 6	-15	-20.07	-0.55	-	-	Wilson et al. (2017), refitted data from Kohler et al. (2003)	130	BET data (Kohler et al., 2003)
Illite (Mg)	-11.78	0.5 6	-15	-20.07	-0.55	-	-	Wilson et al. (2017), refitted data from Kohler et al. (2003)	130	BET data (Kohler et al., 2003)
Na-Beidellite	-12.37	0.3 5	-14.54	-15.66	-0.18	-	-	Wilson et al. (2017), refitted data from Kohler et al. (2003)	111	BET Data (Rozalen et al., 2008)
Ca-Beidellite	-12.37	0.3 5	-14.54	-15.66	-0.18	-	-	Wilson et al. (2017), refitted data from Kohler et al. (2003)	111	BET Data (Rozalen et al., 2008)
K-Beidellite	-12.37	0.3 5	-14.54	-15.66	-0.18	-	-	Wilson et al. (2017), refitted data from Kohler et al. (2003)	111	BET Data (Rozalen et al., 2008)
Na-Saponite	-12.37	0.3 5	-14.54	-15.66	-0.18	-	-	Wilson et al. (2017), refitted data from Kohler et al. (2003)	111	BET Data (Rozalen et al., 2008)
Ca-Saponite	-12.37	0.3 5	-14.54	-15.66	-0.18	-	-	Wilson et al. (2017), refitted data from Kohler et al. (2003)	111	BET Data (Rozalen et al., 2008)
K-Saponite	-12.37	0.3 5	-14.54	-15.66	-0.18	-	-	Wilson et al. (2017), refitted data from Kohler et al. (2003)	111	BET Data (Rozalen et al., 2008)
Na-Vermiculite	-12.37	0.3 5	-14.54	-15.66	-0.18	-	-	Wilson et al. (2017), refitted data from Kohler et al. (2003)	111	BET Data (Rozalen et al., 2008)
Ca-Vermiculite	-12.37	0.3 5	-14.54	-15.66	-0.18	-	-	Wilson et al. (2017), refitted data from Kohler et al. (2003)	111	BET Data (Rozalen et al., 2008)
SiO$_{2(am)}$	-	-	-12.77	-	-	-	-	Palandri and Kharaka (2004)	9.23	0.25 µm diameter spheres

4.5. Transport equations with a time-dependent armouring layer

The transport of aqueous solutes is governed by the advective-diffusive transport equation:

$$\frac{\partial}{\partial t}(\theta\rho c) = \nabla \cdot (\rho D_e \nabla c - \rho \boldsymbol{q} c). \tag{4-2}$$

Here, c (mol/kg) is the solute molality, $\theta(x,y)$ (-) is the porosity of the media, ρ (kg/m^3) is the density of water, $D_e(\theta)$ (m^2/s) is the effective diffusivity of the solute and $\boldsymbol{q}(\theta)$ (m/s) is the Darcy velocity.

Rates of advection and diffusion are dependent upon porosity, which varies in time due to mineral dissolution and precipitation. The dependence of effective diffusion upon porosity is represented by the linear Archie's law:

$$D_e(\theta) = \frac{\theta}{\theta_0} D_e^0, \tag{4-3}$$

where D_e^0 (m^2/s) is the reference effective diffusivity at reference porosity θ_0 (-). Conceptually, in the model precipitation of secondary minerals in the fracture cells is assumed to take place on the fracture surface, and therefore, the evolving aperture of the fracture can be calculated from the amount of mineral that has precipitated in the fracture cell.

If the concentration at time t (s) of mineral j in a fracture cell with initial volume (before commencement of any armouring) V_F^0 (m^3) is denoted $C_{F,j}$ (mol/m^3), then the total volume, V_P (m^3), of precipitated mineral in the fracture cell at time t is given by:

$$V_P(t) = V_F^0 \sum_j C_{F,j}(t) M_{V,j}, \tag{4-4}$$

where $M_{V,j}$ (m^3/mol) is the molar volume of mineral j.

If the area of intersection of the fracture cell with the matrix is denoted A_F (m^2) then the thickness, w_A (m), of the precipitated layer at time t is given by:

$$w_A(t) = \frac{V_p(t)}{A_F}. \tag{4-5}$$

If the initial aperture of the fracture is w_F^0 (m), then the fracture aperture, w_F (m), in the cell at time t is given by:

$$w_F(t) = w_F^0 - w_A(t). \tag{4-6}$$

Diffusive transport between the fracture and the matrix will be impeded by the presence of an armouring layer. Initially, when no armouring layer is present, diffusion into and out of the fracture will depend only on the effective diffusivity of the solute in the water within the fracture and the matrix. However, as an armouring layer develops, solutes diffusing between the fracture and the matrix will also have to diffuse through the armouring layer, which will pose an increasing diffusive

barrier as the armouring layer grows in thickness. The degree to which armouring impedes this process is determined as follows.

The model calculates solute molalities at the centre of each grid cell. Rates of diffusive transport between cells can be determined analytically by introducing solute concentrations at interface locations between cells. If c_{AM} (mol/kg) is used to denote the concentration of the solute at the interface between the armouring layer and the matrix (at location y_{AM} using the notation in Figure 4-3), then the rate of diffusion of solute into the matrix is given by:

$$F_{M_1} = \rho D_{eM_1} \frac{c_{AM} - c_{M_1}}{y_{AM} - y_{M_1}}. \tag{4-7}$$

Here, subscripts M_1 denote the first cell in the matrix, so that c_{M_1} is the solute concentration at the centre of the first cell in the matrix, which has y-coordinate y_{M_1}. D_{eM_1} denotes the effective diffusivity in the same cell, which will depend on the evolved porosity θ_{M_1} in the cell. The flux F_{M_1} of solute into the cell has units mol/m^2/s.

The location y_{AM} is assumed to be fixed in the model, regardless of whether any mineral precipitation or dissolution has taken place in the fracture, and therefore assumes that no cannibalisation or significant dissolution of the matrix has occurred, so that the interface between the armouring layer and the matrix is distinct and does not move with time.

In the fracture cell, when the armouring layer has thickness $w_A > 0$, the cell is effectively composed of two composite media: open fracture and armouring material. Only a single cell is used to represent the composite media, with the solute concentration taken to represent the solute in the centre of the open fracture region and the mineral concentration taken to represent the mineral in the armouring layer.

The flux of solute from the centre of the open fracture to the armouring layer/matrix interface can be written as:

$$F_F = \rho \widetilde{D_{eF}} \frac{c_F - c_{AM}}{y_F - y_{AM}}. \tag{4-8}$$

Here, c_F (mol/kg) is the solute molality in the centre of the open fracture, y_F is the mid-point of the open fracture (which equals to 1/4 of the evolved aperture, since the model simulates half of the fracture), which varies as the thickness of the armouring layer evolves, and $\widetilde{D_{eF}}$ (m^2/s) is the effective diffusivity of the solute in the fracture cell along the path from y_F (the centre of the open fracture) to y_{AM} (the interface of the armouring layer and the matrix).

Mass conservation is maintained by equating the flux of solute leaving the fracture cell with the flux of solute entering the matrix, and therefore:

$$F_F - F_{M_1} = 0. \tag{4-9}$$

This equation can be solved to determine the interface concentration c_{AM}, which can then be substituted into the equation for F_F (or F_{M_1}) to evaluate the solute flux between the fracture and the matrix. The resulting flux is equivalent to that between the points y_F and y_{M_1} through a medium whose effective diffusivity is given by the

harmonic average of the two diffusivities $\widetilde{D_{eF}}$ and D_{eM_1}, weighted by the relative length of the pathway through the fracture cell and the matrix cell.

The same approach can be used to determine an appropriate time-dependent value for the effective diffusivity $\widetilde{D_{eF}}$ of the composite media of the open fracture and evolving armouring layer. If D_{eF} and D_{eA} (m²/s) are used to denote the effective diffusivity of the open fracture and armouring layer material respectively, then:

$$\widetilde{D_{eF}}(t) = \left(\frac{1 - f(t)}{D_{eF}} + \frac{f(t)}{D_{eA}}\right)^{-1}, \tag{4-10}$$

where:

$$f(t) = \frac{w_A}{w_F^0}. \tag{4-11}$$

4.6. Hydraulic evolution with a time-dependent armouring layer

Advection is assumed to only take place in cells in the fracture pathway (Figure 4-3), where initially the porosity (i.e. the volume fraction of void in the total cell volume) is taken to be unity, representing an open fracture. As an armouring layer develops, the aperture of the fracture will decrease, leading to a decrease in the porosity of the fracture cells (
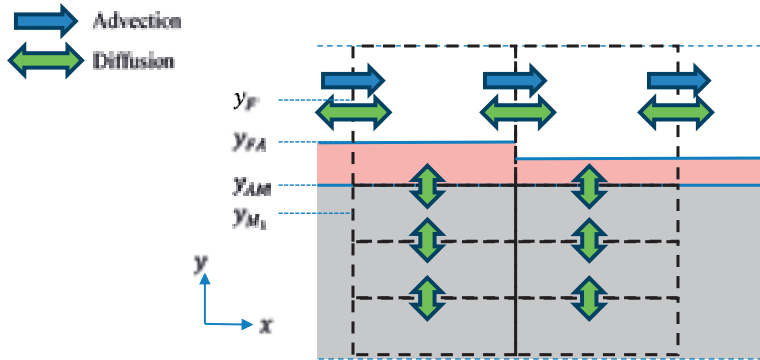
Figure 4-4). The decrease in aperture following armouring will lead to reduced transmissivity.

If an idealised planar fracture is assumed, and if it is further assumed that all mineral precipitation/dissolution in the fracture that modifies the fracture aperture is slow with respect to the transient terms in the water flow equations, then steady state flow conditions can be assumed in the fracture, and the flow can be modelled with the Navier-Stokes equations for incompressible flow:

$$\frac{\partial p}{\partial x_i} - \mu \nabla u_i = 0, \quad \text{for } i = x, y, z. \tag{4-12}$$

Here, p (Pa) is the pressure in the pore fluid and $u = \left(u_x, u_y, u_z\right)$ (m/s) is the velocity at each point in the fracture. μ (Pa s) is the viscosity of the fluid.

If it is assumed that flow is parallel to the x-coordinate axis, then $\partial p / \partial y = \partial p / \partial z = 0$ and so (4-12) reduces to:

$$\frac{\partial p}{\partial x} - \mu \frac{\partial^2 u_x}{\partial y^2} = 0. \qquad (4\text{-}13)$$

Here it is assumed that the y-coordinate is in the direction of the fracture aperture (i.e. the fluid velocity is only assumed to vary across the fracture aperture), and it will also be assumed that the origin of the y-coordinate is at the centre of the open fracture.

Since the first term in (4-13) only depends on x and the second term only depends on y, it is clear that:

$$\frac{\partial p}{\partial x} = C = \mu \frac{\partial^2 u_x}{\partial y^2} = 0, \qquad (4\text{-}14)$$

where C (Pa/m) is a constant.

If the fracture flow path is assumed to be of length L (m), with upstream and downstream pressure P_{in} and P_{out} (Pa) respectively, then it must be the case that:

$$p = P_{in} + Cx, \qquad (4\text{-}15)$$

$$C = \frac{P_{out} - P_{in}}{L}, \qquad (4\text{-}16)$$

and

$$u_x(y,t) = \frac{C}{2\mu}\left(y^2 - \left(\frac{w_F(t)}{2}\right)^2\right). \qquad (4\text{-}17)$$

This is the standard Poiseuille result for planar flow. Figure 4-6 shows an example flow calculation based on equation (4-17) for a fracture with initial aperture 1mm that reduces to 0.5mm after precipitation of secondary minerals. The imposed pressure gradient C is -2.5×10⁻⁹ Pa/m and the fluid viscosity is taken to be 1×10⁻⁶ Pa s.
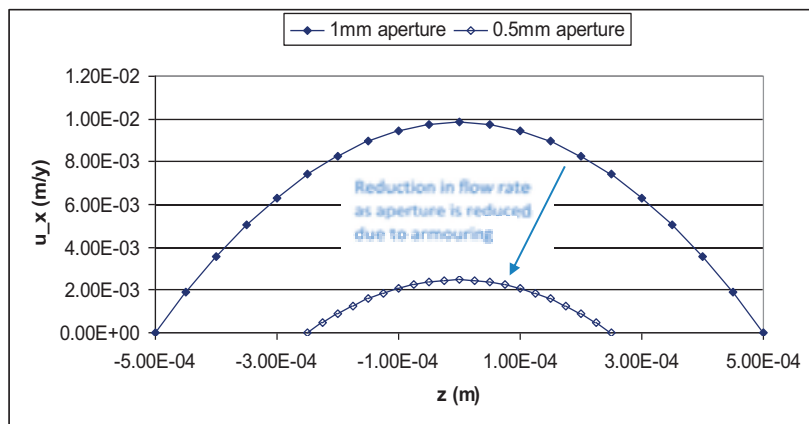
Figure 4-6: Example variation in flow when aperture reduces from 1mm to 0.5mm.

The volumetric flux of water through the fracture can be obtained by integrating (4-17) over a plane in the fracture, perpendicular to the flow direction, and of width W (m), to obtain:

$$Q = W \int_{-w_F/2}^{w_F/2} u_x \, dy$$

$$= A \frac{w_F^2}{12} \frac{P_{in} - P_{out}}{L\mu}. \tag{4-18}$$

Here, $A = W w_f$ (m^2) is the area of the plane through which the volumetric flow rate Q (m^3/s) arises. This result can be compared with an equivalent Darcy velocity q (m/s) in the fracture to obtain the equivalent fracture permeability k (m^2), if:

$$Q = Aq = -A \frac{k\rho g}{\mu} \nabla h. \tag{4-19}$$

then it is clear that:

$$k = \frac{w_F^2}{12}. \tag{4-20}$$

This is the same well-known result that is assumed by Höglund (2014) (Equation 6-6).

Equation (4-20) therefore provides an aperture-dependent permeability rule that can be applied to obtain a time-dependent permeability in the fracture as the open fracture aperture evolves due to armouring with secondary minerals. This is used in the model to solve for the instantaneous Darcy velocity. The upstream and downstream hydraulic heads will be assumed to remain constant throughout the evolution.

4.7. Armouring model implementation details

The model of inhibited diffusion between the fracture and matrix due to armouring of the fracture surface described in Section 4.5 is implemented directly in the model. The value of D_{eA} (m^2/s), the effective diffusivity of the armouring layer material, is defined in the model in terms of the initial matrix diffusivity (before alteration), D_{eM}^0 (m^2/s), as:

$$D_{eA} = \alpha D_{eM}^0. \tag{4-21}$$

Test calculations with the model suggest that, for fracture apertures of 1 mm and initial flow rates of 0.1 m/y, the fracture tends to clog with armouring material relatively rapidly (on the order of 50 years) for values of $\alpha \geq 10^{-3}$. Thus, to achieve a more prolonged armouring effect in the model, a default value of $\alpha = 10^{-4}$ has been chosen.

Additionally, a diffusion-blocking armouring layer thickness can also be set in the model to completely inhibit fracture-matrix diffusion once a sufficiently thick armouring layer has developed. This does not prevent continued fracture clogging at the location, since diffusion of mixed fracture-matrix porewaters from

neighbouring fracture cells can continue, which can act to prolong the precipitation of armouring material.

To stabilise the model should cell porosities approach zero (when the usual harmonic averaging approach to the determination of the diffusive flux would lead to a singular problem), a scaling of the diffusive flux is implemented to reduce fluxes to zero when the porosity in any matrix cell approaches a small critical value θ_{crit}. For the purposes of the modelling a value of $\theta_{crit} = 10^{-3}$ has been chosen.

4.8. Model parameterisation

4.8.1. Base case

A base case model has been set-up, with geometry and hydraulic properties parameterised as described in Table 4-6. The geochemical model is as described in Section 4.4.

Table 4-6: Parameterisation of base case model.

Property	Value
Fracture Aperture	10^{-3} m
Fracture length	0.5 m
Initial flow rate in fracture	1.89×10^{-3} m/y
Reference diffusivity in matrix	3×10^{-12} m^2/s (reference porosity 0.11)
α in D_{eA} formula (equation (4-21))	10^{-3}
Armouring diffusion-blocking thickness	2.5×10^{-4} m (equivalent to half-blocking of aperture)
Depth of matrix	10^{-1} m

The fracture aperture of 10^{-3} m is in the range observed in the 1BMA vault inspections in 2000 and 2011, the largest of which was 3×10^{-3} m and the smallest 1.5×10^{-4} m (Höglund, 2014, Table 6-1). The fracture length of 0.5 m is a notional length in the order of the dimensions of the side walls of the 1BMA structure (which are 0.4 m – Höglund (2014, Table 2-1)).

The initial flow rate in the fracture is the same as that assumed in modelling by Höglund (2014, e.g. Figure 5-16). Höglund also quotes a flux of 2.5×10^{-2} m/y, which is considered in variant cases (see below).

The matrix diffusivity is the same as that taken by Höglund (2014, p103) for the concrete walls in the 1 BMA vault. A linear Archie's law is used to simulate the variation of matrix diffusivity as the matrix porosity evolves.

The relative diffusivity of the armouring layer to the intact concrete (α) is chosen to be small to maximise the possibility of an armouring layer providing a diffusive barrier that isolates the matrix from the fracture. Larger values are considered in variant cases (see below).

The armouring diffusion blocking thickness is chosen to be one quarter of the fracture aperture, so that the blocking effect begins when the fracture is half-filled with armouring products, since it is assumed that identical precipitation occurs on opposing fracture surfaces. Precipitation of armouring material can continue beyond this time, but only due to diffusive interactions with mixed cement/fresh waters arising in neighbouring cells in the grid.

The simulated depth of matrix of 0.1 m implies an assumption of similar-sized fractures repeating every 20 cm in the concrete, although considerations of bulk flows through structures are not considered in the modelling. The assumption is also consistent with greater fracture separations in cases where alteration fronts in the matrix do not penetrate the full 10 cm simulated depth.

4.8.2. Variant cases

Variant 1

This variant case tests sensitivity of the evolution to the relative diffusivity of the armouring layer to the intact concrete (α). A value of $\alpha = 10^{-1}$ is chosen, meaning that the armouring layer is assumed to be 0.1 times as diffusive as the intact concrete. All other parameters are as in the base case (Table 4-6).

Variant 2

In this variant case, it is assumed that some porosity always remains open in the fracture, for example due to continued mechanical degradation and movement of the vault wall structure. A notional porosity of 0.1 is assumed to always be available in the fracture, so that advection of solutes will occur for the duration of the simulation (albeit at a reduced rate due to the decreased transmissivity of the narrowed fracture aperture- see Figure 4-6). All other parameters are as in the base case (Table 4-6).

Variant 3

The variant case combines variant cases 1 and 2, so that a larger relative diffusivity of the armouring layer to the intact concrete is assumed, while it is also assumed that the fracture remains partially open, with a porosity of 0.1. All other parameters are as in the base case (Table 4-6).

Variant 4

In this variant case, the assumption of an always open porosity from variant case 2 is combined with a faster initial flow rate of 2.5×10^{-2} m/y (see above). All other parameters are as in the base case (Table 4-6).

Variant 5

This variant case combines variant case 3 with the faster initial flow rate assumed in variant case 4. All other parameters are as in the base case (Table 4-6).

A summary of the variant cases is given in Table 4-7.

Table 4-7: Summary of variant cases. Differences from the Base Case are highlighted with grey background.

Case	Relative diffusivity of armouring layer α (-)	Initial Flow rate (m/y)	Fracture remains open (porosity=0.1)
Base	10^{-3}	1.89×10^{-3}	No
Variant 1	10^{-1}	1.89×10^{-3}	No

Variant 2	10^{-3}	1.89×10^{-3}	Yes
Variant 3	10^{-1}	1.89×10^{-3}	Yes
Variant 4	10^{-3}	2.5×10^{-2}	Yes
Variant 5	10^{-1}	2.5×10^{-2}	Yes

4.8.3. Spatial discretisation

A geometrically-spaced grid is used to represent the fracture pathway, and a matrix leg perpendicular to each fracture cell. This arrangement allows the fracture region close to the inflowing fracture boundary and the matrix regions close to the fracture to be more refined, while maintaining a relatively small overall number of cells. The geometrical spacing of the grid cells in the fracture is listed in Table 4-8 and the spacing of each cell in the matrix legs is shown in Table 4-9.

Table 4-8: Locations of geometrically-spaced fracture cells.

Fracture cell name	Cell midpoint (m)	Cell width (m)
S1__fracture_S1_4__0	0.005	0.010
S1__fracture_S1_4__1	0.017	0.013
S1__fracture_S1_4__2	0.032	0.018
S1__fracture_S1_4__3	0.053	0.024
S1__fracture_S1_4__4	0.080	0.032
S1__fracture_S1_4__5	0.117	0.042
S1__fracture_S1_4__6	0.166	0.060
S1__fracture_S1_4__7	0.231	0.075
S1__fracture_S1_4__8	0.318	0.099
S1__fracture_S1_4__9	0.434	0.132

Table 4-9: Locations of geometrically-spaced matrix cells. There is one matrix leg per fracture cell.

Cell midpoint depth into matrix (m)	Cell width (m)
2.5×10^{-4}	5×10^{-4}
9.05×10^{-4}	8.1×10^{-4}
1.965×10^{-3}	1.31×10^{-3}
3.68×10^{-3}	2.12×10^{-3}
6.46×10^{-3}	3.44×10^{-3}
1.097×10^{-2}	5.58×10^{-3}
1.828×10^{-2}	9.03×10^{-3}
3.01×10^{-2}	1.46×10^{-2}
4.92×10^{-2}	2.37×10^{-2}
8.03×10^{-2}	3.84×10^{-2}
	0.1

The QPAC model solves for solute concentrations (molalities) at the centre of each cell and on the interfaces between cells, meaning that there are approximately twice as many grid variable locations for solute species in the model as there are grid cells. Mineral (solid) species concentrations are assumed to be constant over each grid cell. If N_C is the number of grid cells, N_A is the number of aqueous (solute) species and N_M is the number of mineral species in the model, then the overall number of unknowns is approximately $N_C(2N_A + N_M)$. In the model, $N_C = 110$, $N_A = 46$ and $N_M = 35$, resulting in approximately 14,000 unknowns.

The small size of the fracture (1 mm) compared to the depth into the matrix that is simulated (10 cm) makes 2-D visualisation of the results difficult. To make useful visualisation possible, some output plots use an 'abstract' view of the grid, where all

grid cells are plotted with equal size, and connectivity between grid cells is indicated by arrows. An example is shown in
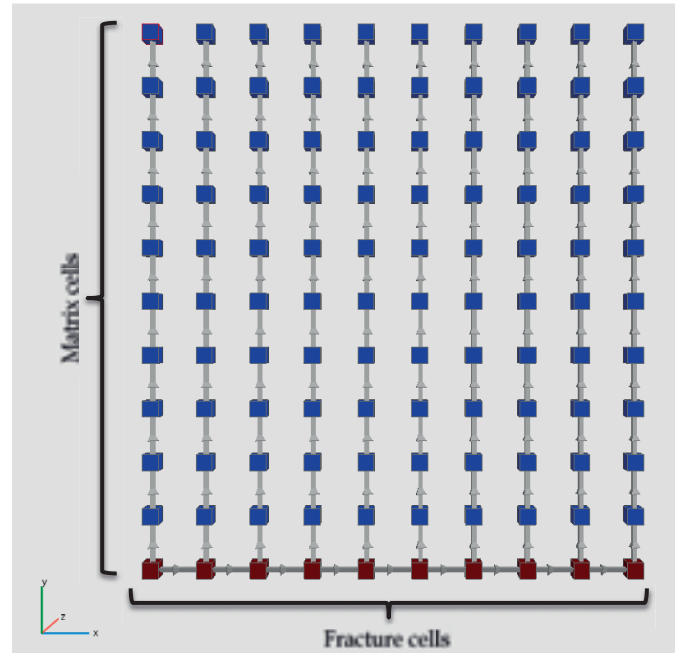
Figure 4-. The arrows showing the cell connectivity allows the 1-D nature of the matrix legs to be seen.
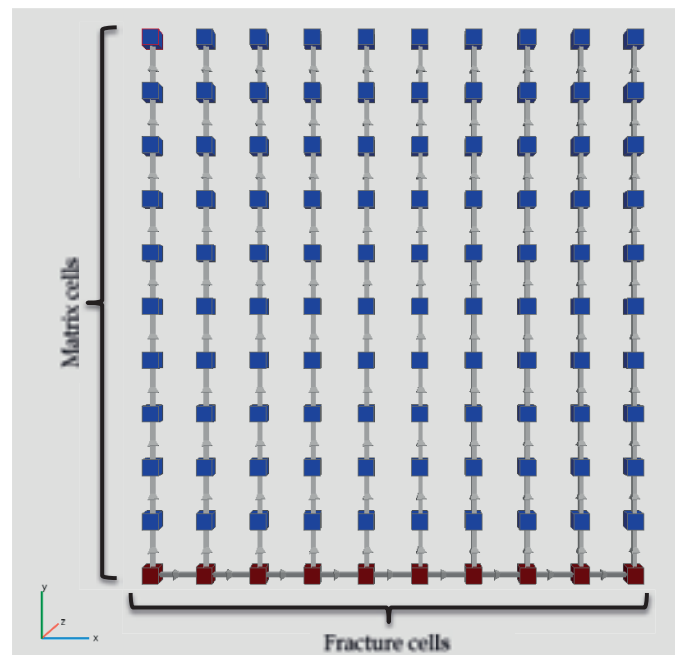
Figure 4-7: Abstract grid view, where all grid cells are plotted with equal size, and connectivity between grid cells is indicated by arrows.

4.9. Results

4.9.1. Preliminary 1-D model

The distribution of solid phases at key times is shown in Figure 4-8 and Figure 4-9. The model shows dissolution of primary cement solids, followed by the precipitation of alteration products, mainly calcite, hydrotalcite, Friedel's salt, brucite, Na-vermiculite and Na-saponite, with pore clogging of the 1cm thick outermost concrete cell being complete by ~4000 years. The primary cement solids present outermost concrete cell in contact with groundwater were almost completely replaced by alteration products (thaumasite, ettringite and brucite) with Friedel's salt penetrating the concrete to greater depth (Figure 4-8). By 500 years, the alteration zone characterised by Friedel's salt precipitation (and smaller volume of hydrotalcite) had penetrated ~0.2m into the concrete from the groundwater boundary (Figure 4-8). Between 100 and 500 years, thaumasite present in the outermost concrete cell as an alteration product had been replaced as calcite and brucite continued to precipitate (Figure 4-8), with all primary cement solids having been dissolved. Na-vermiculite precipitated in the second model cell from the groundwater boundary by this time. Between 500 years and 1000 years (Figure 4-9), brucite and calcite continued to precipitate in the outermost model cell, with the addition of a relatively small volume of Na-vermiculite. Alteration of primary cement solids (mainly portlandite and C_3AH_6) and precipitation of Friedel's salt also continued to occur between 500 and 1000 years.
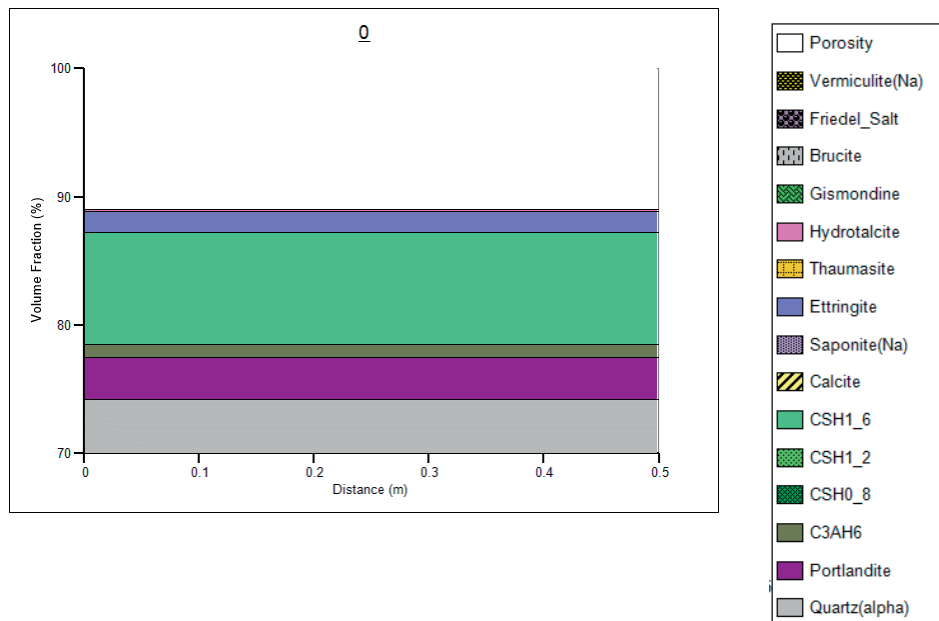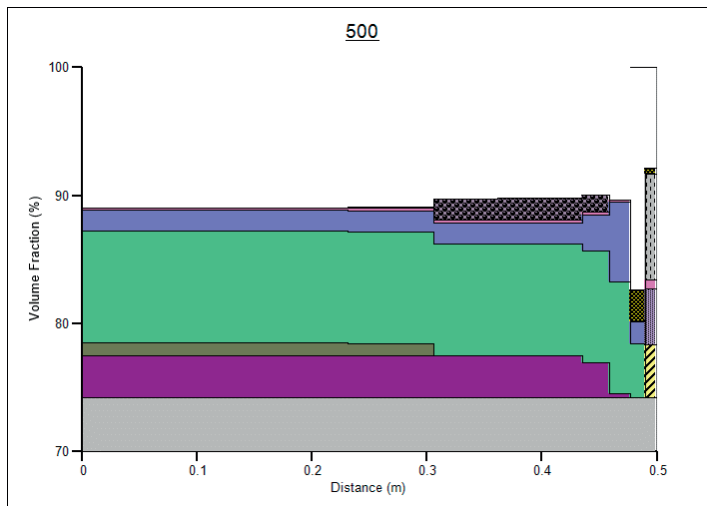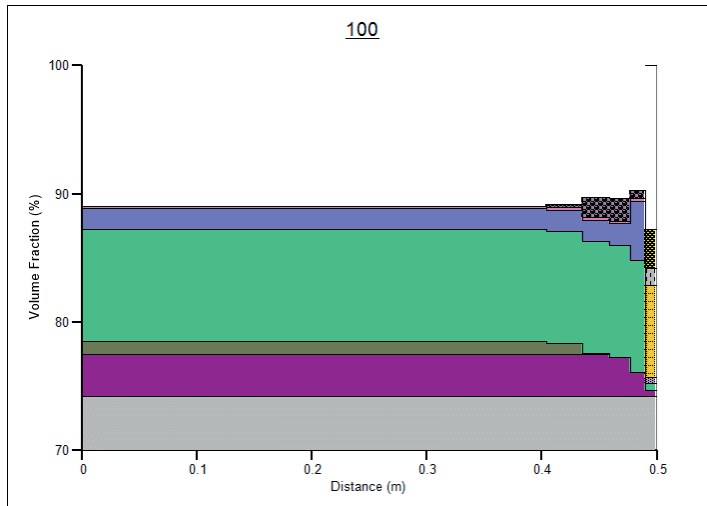
Figure 4-8 Volume fraction diagrams for preliminary 1D model at 0, 100 and 500 years. Groundwater boundary at 0.5 m. Note that the y-axis range has been reduced to show alteration of cement solids more clearly.
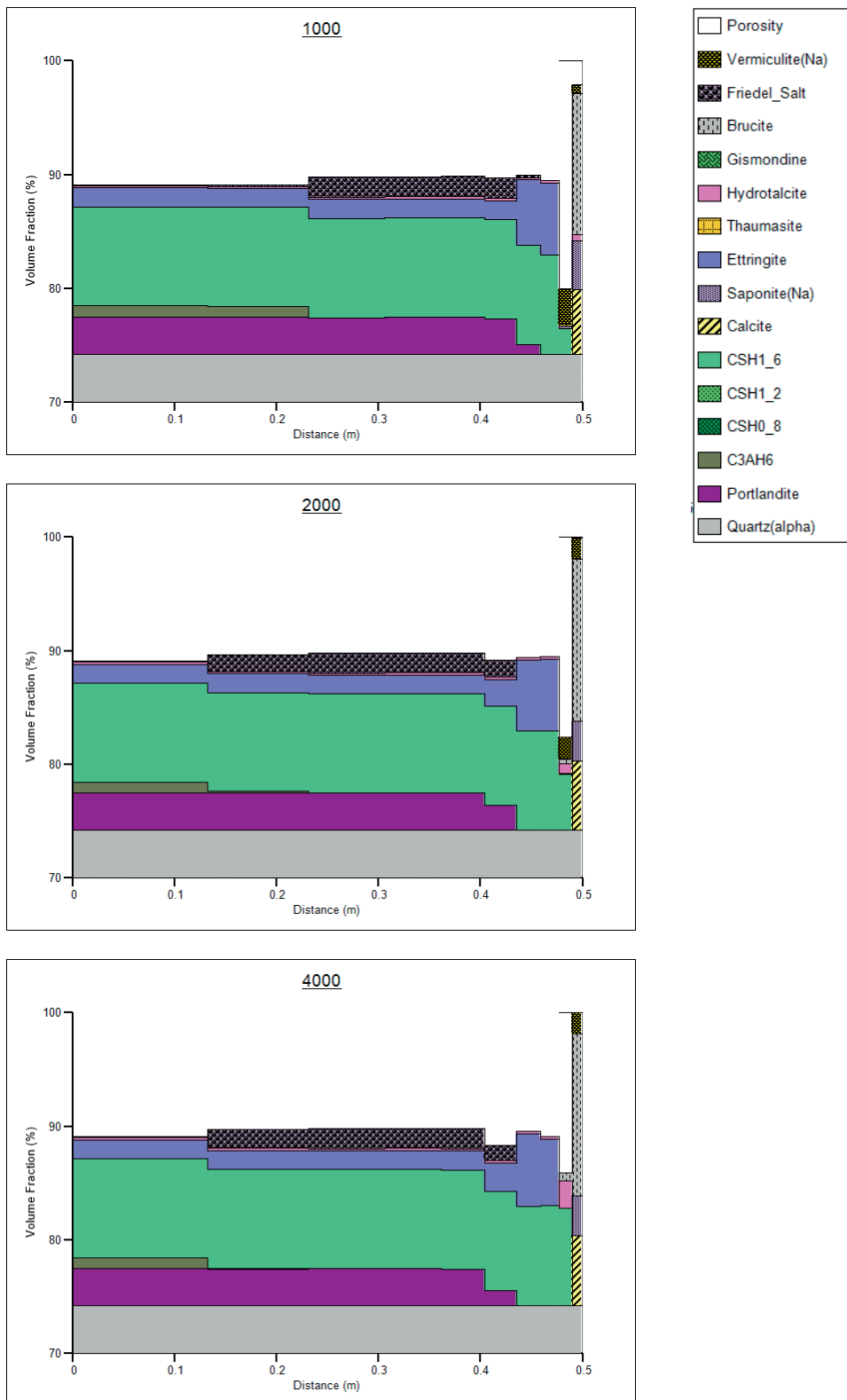
Figure 4-9 Volume fraction diagrams for preliminary 1D model at 1000, 2000 and 4000 years.
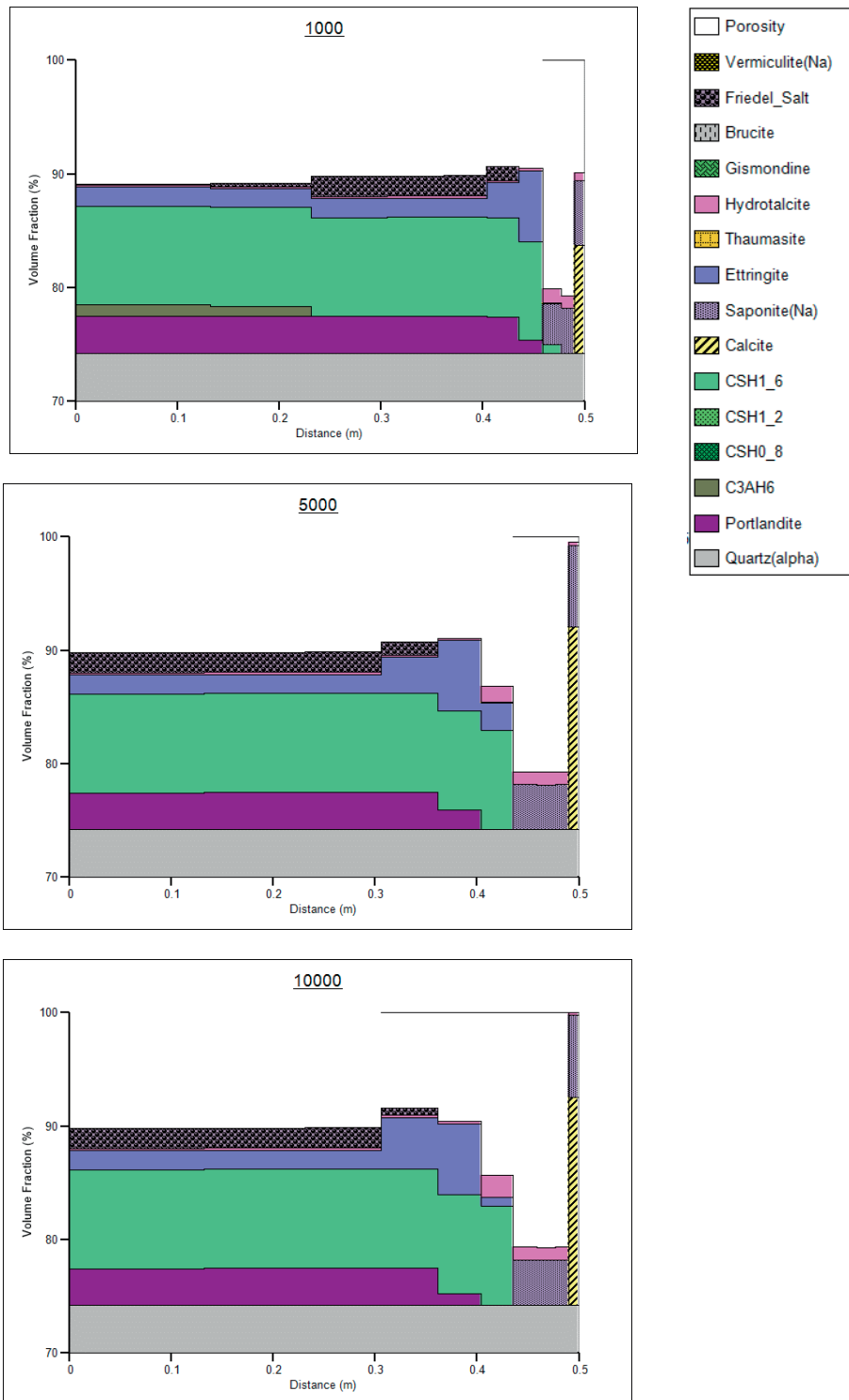
Figure 4-10 Volume fraction diagrams for preliminary 1D model at 1000, 5000 and 10 000 years, with brucite excluded as a potential cement alteration product.

By 2000 years (Figure 4-9), alteration of primary cement solids had continued and the proportion of Friedel's salt increased at a greater distance from the groundwater boundary. The model cell next to the groundwater boundary was almost completed clogged with alteration products (brucite > calcite > Na-saponite > Na-vermiculite)

by 2000 years. Between 2000 and 4000 years, there was continued alteration in the central region of the model, with re-precipitation of C-S-H gel in the second cell from the groundwater boundary, into which transport of solutes from the groundwater was inhibited due to pore clogging. The simulation continued until 4015 years by which time porosity in the outermost cell was zero and the model could not progress any further.

Given that brucite was mainly responsible for the pore clogging, the simulation was re-run with brucite excluded from the model. Brucite is actually under-saturated in both the groundwater and initial concrete pore water, but concrete pore water becomes saturated with respect to brucite as these two waters mix. The exclusion of brucite results in cement alteration being dominated by formation of Friedel's salt at greater depths into the concrete, with calcite, hydrotalcite and Na-saponite precipitating nearer to the concrete-groundwater interface (Figure 4-10), and pore clogging being almost complete after 10 000 years (the specified end-time, Figure 4-10). The implication of this, is that if a significant amount of dissolved Mg precipitated as brucite prior to water reaching a given fracture (for example if water has already reacted with cementitious materials), solids are still likely to precipitate in the fracture, but they are more likely to comprise carbonate minerals such as calcite, with some precipitation of secondary aluminosilicates (noting that rates of mineral growth of such minerals in cements are not well known).

4.9.2. Fracture model base case

Results from the base case are shown in Figure 4-11 to Figure 4-18.

Figure 4-11 shows the pH in the fracture-matrix system at 50 y. The plot highlights the difficulty of visualising results of porous media systems containing small fractures, since the small fracture regions are barely visible in the plot, even when zoomed.

The same data as Figure 4-11 are-plotted in Figure 4-12 (this time at 10^4 y) using the abstract compartmental view of the grid. Here, all grid cells are plotted with equal size, and connectivity between grid cells is indicated by arrows, so that in particular the 1-D nature of the matrix legs can be seen. From Figure 4-12 it is clear that there is a spatial dependence of the pH in the fracture at 10 000 y. Downstream (to the right of) of the first cell (at 0.005 m, from Table 4-8) the pH is almost identical to that in the matrix, suggesting that pH is buffered at cement values. Upstream (to the left of) of this point, a lower pH of around 11.4 is obtained. Hence the only location in the base case that pH differs significantly is in the fracture, immediately adjacent to the inlet.
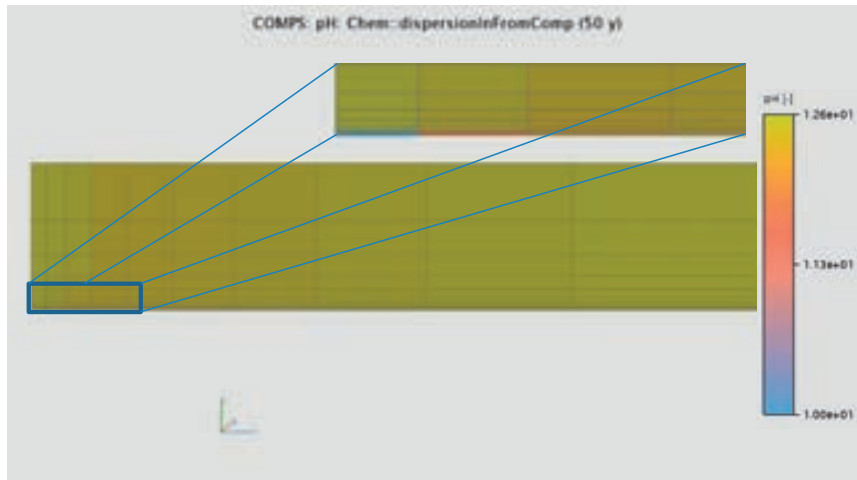
Figure 4-11: pH in base case at $t = 50$ y. Real geometry and zoomed.
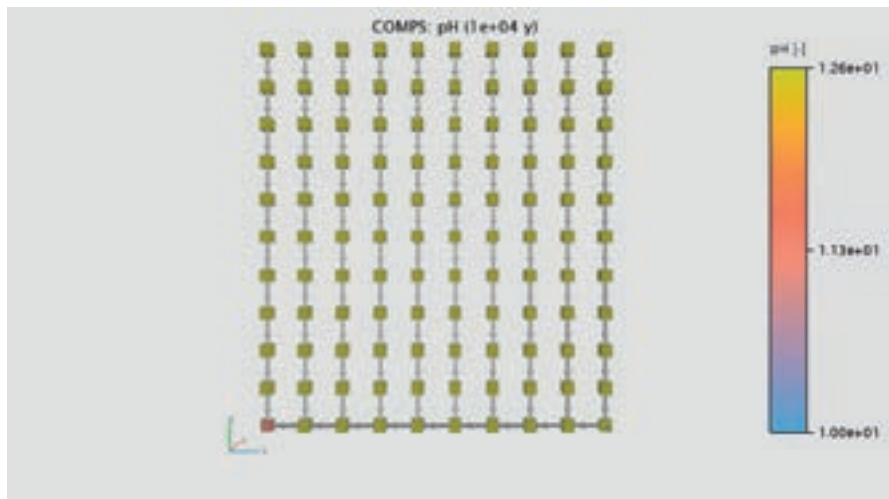
Figure 4-12: pH in base case at $t = 10^4$ y. Abstract geometry.

The porosity change in the model ($\theta(t)/\theta_0$) at $t = 10^4$ y is shown in Figure 4-13. Here it can be seen that porosity change is more spatially extensive than might be expected from the pH plot (Figure 4-12). Porosity in the fracture cell adjacent to the inlet is effectively reduced to zero, thus blocking the fracture pathway for advection, leaving slow diffusion through the clogging material as the only viable transport mechanism. The porosity in the second fracture cell (at 0.017 m) is also reduced, but further downstream in the fracture the porosity is largely unaltered.   In the matrix, near the clogged fracture region the porosity is also reduced, suggesting some partial clogging of the matrix porosity, however in the matrix immediately downstream of the clogged fracture region, the matrix porosity is increased by a factor of ~1.4, suggesting leaching of cement material from this location into the fracture.
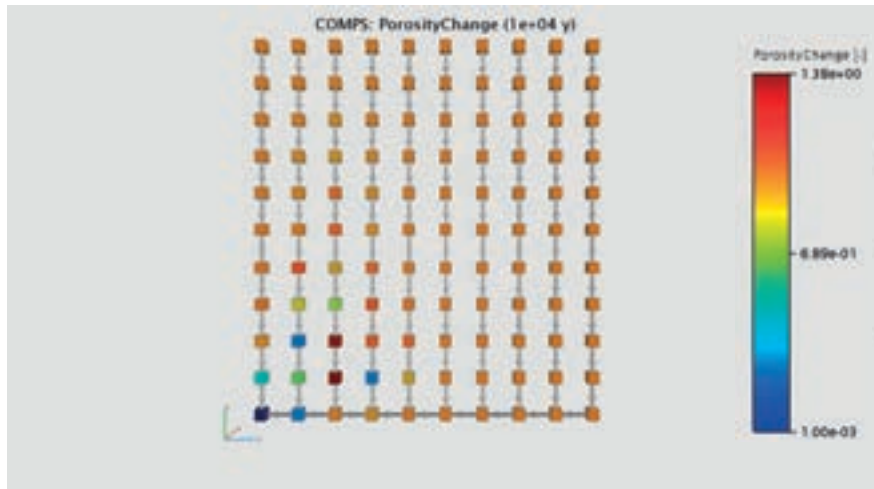
Figure 4-13: Porosity change ($\theta(t)/\theta_0$) in base case at $t = 10^4$ y. Abstract geometry.

The thickness of the armouring layer in the fracture is shown for each fracture cell as a function of time in Figure 4-14. The same result is shown in the armouring thickness profile plots in Figure 4-15. Armouring initially occurs in the first fracture cell, adjacent to the incoming water, which becomes fully clogged by around 70 y. A non-trivial amount of armouring also occurs in the second cell, but the rate of armouring here reduces once the first cell becomes fully armoured, when the flow rate is reduced and transport in the system becomes purely diffusive.
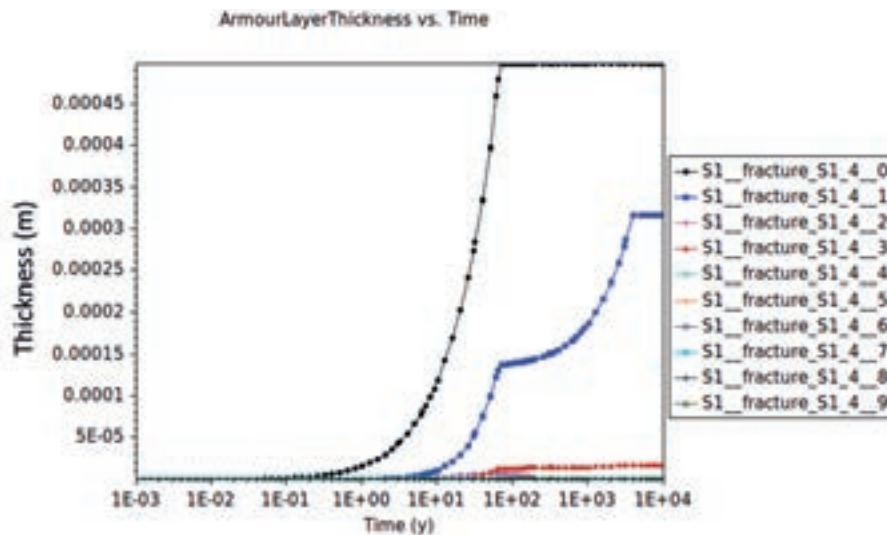
Figure 4-14: Evolution of armouring layer in fracture cells.
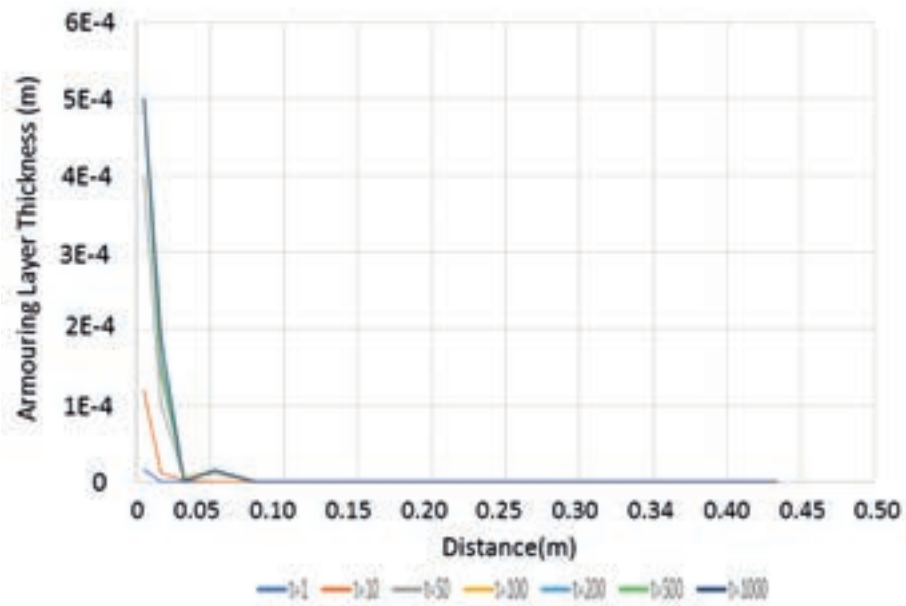
Figure 4-15: Profiles of armouring layer thickness across the system at $t = 1, 10, 50, 100, 200, 500, 1000$ y.

Profiles of the pH that arises in the fracture are shown in Figure 4-16. The greatest intrusion of low pH water into the fracture happens prior to clogging, when pH values fall to around 10 immediately adjacent to the fracture inlet. After clogging, the pH rises as the rate of advection falls due to the reduced fracture aperture, so that by 100 y, only the cells at the clogged location (which are assigned a trivial porosity to allow slow diffusion to continue) experience a pH that is below cementitious values, but even here the pH is not as low as the groundwater pH due to 'back-diffusion' of cement waters leached into the fracture downstream.
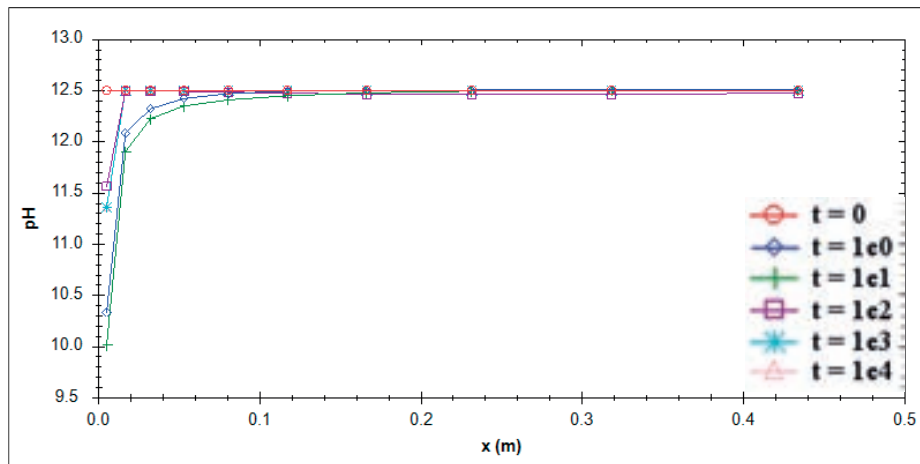
Figure 4-16: Profiles of pH across the system at $t = 0, 1, 10, 10^2, 10^3, 10^4$ y.

The reduction in Darcy velocity in the fracture, caused by the reduction in transmissivity due to the appearance of the armouring layer, is shown in Figure 4-17. This shows the fracture Darcy velocity as a function of time, where the flow rate clearly becomes zero at the onset of complete clogging. There are some small numerical fluctuations in the Darcy velocity after clogging, but these do not greatly affect the solution.

Figure 4-18 shows the composition of the armouring layer, being predominantly composed of brucite, calcite and a smaller amount of sepiolite (M-S-H gel proxy) at the clogged location. Brucite initially forms in the neighbouring location, but is transformed to hydrotalcite as the transport becomes diffusive-only. A thin ettringite armouring layer appears downstream.

Thus, in the base case, armouring does not lead to a situation where a low pH plume can penetrate along the entire fracture pathway, primarily due to the shut-down of advection after clogging has occurred. For a low-pH plume to develop, the fracture would require to become armoured to a depth exceeding the armouring diffusion-blocking thickness (which is set to 2.5×10^{-4} m in the model) while not becoming fully clogged anywhere. Possibilities for this to occur are investigated in the variant cases.
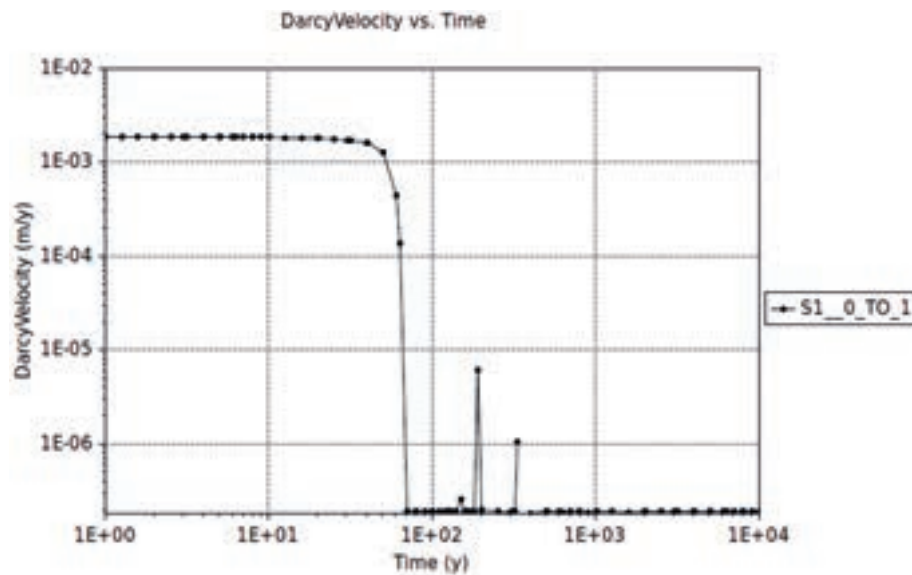
Figure 4-17: Evolution of Darcy velocity as the fracture clogs.
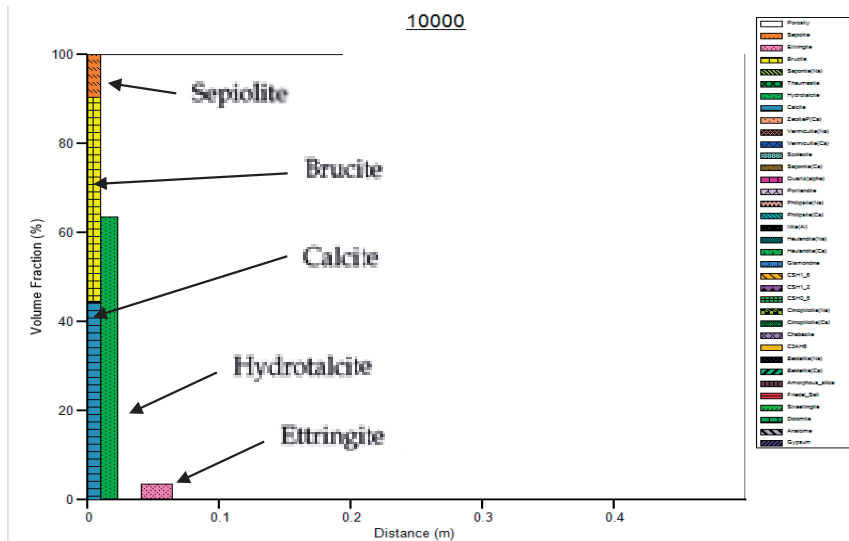
Figure 4-18: Composition of armouring layer along the fracture at $t = 10^4$ y.

4.9.3. Fracture model variant cases

Variant 1

In Variant 1 the porosity of the matrix decreases slightly throughout the modelled domain, compared to the base case (Figure 4-19). This change reflects the fact that in Variant 1 the armouring layer impedes movement of water and solutes between the matrix and fracture less effectively than in the base case. However, the general pattern of porosity variation in Variant 1 is like that seen in the base case (c.f. Figure 4-13 and Figure 4-19). The fracture becomes completely clogged in the fracture cell closest to the inlet (Figure 4-20), after which downstream mass transport within the fracture and cement matrix occurs only by diffusion.
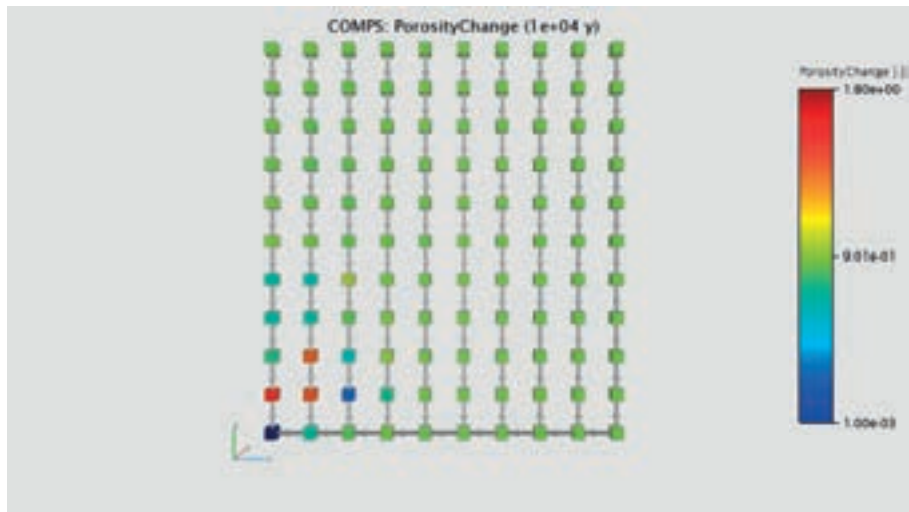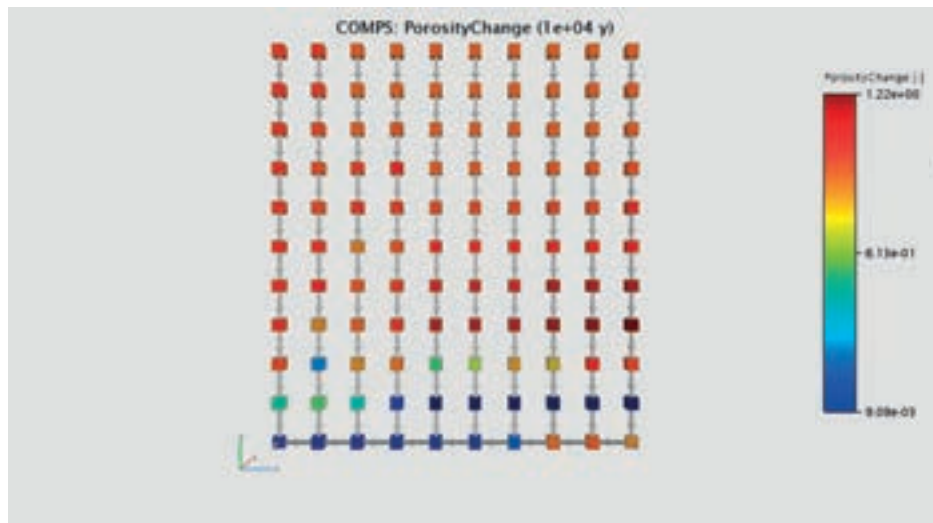
Figure 4-19: Variant 1 - Porosity change $(\theta(t)/\theta_0)$ at $t = 10^4$ y.
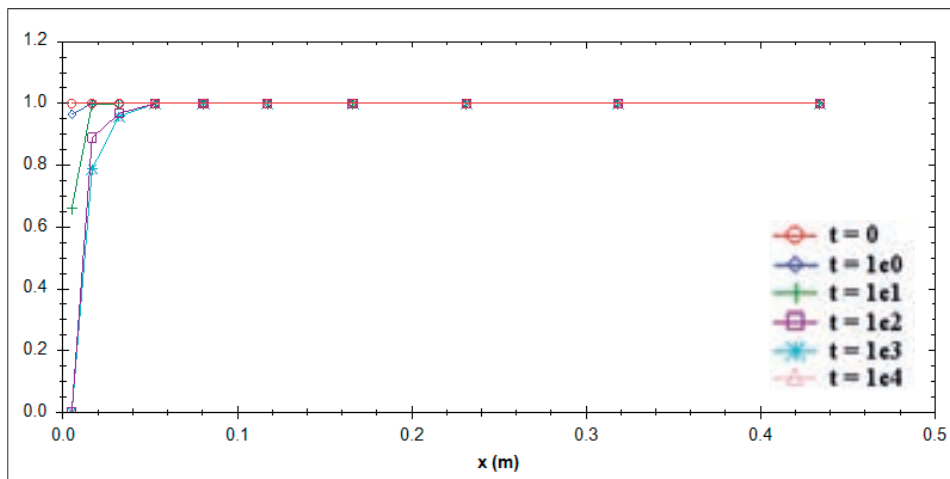
Figure 4-20: Variant 1 - Porosity profiles at $t = 0, 1, 10, 10^2, 10^3, 10^4$ y.

The temporal variations in porosity are reflected in temporal variations in pH (Figure 4-21). Initially at the inlet of the fracture, pH falls to reflect the inflow of relatively low-pH groundwater. However, the pH perturbation extends for a maximum of only c. 0.1 m along the length of the fracture. Once clogging of the fracture occurs adjacent to the inflow point, the pH along the length of the fracture returns to the high-pH cement-buffered value of c. 12.5. This situation occurs after c. 40 years, as is apparent from comparing the temporal variation in pH with the temporal variation in Darcy velocity (Figure 4-22).
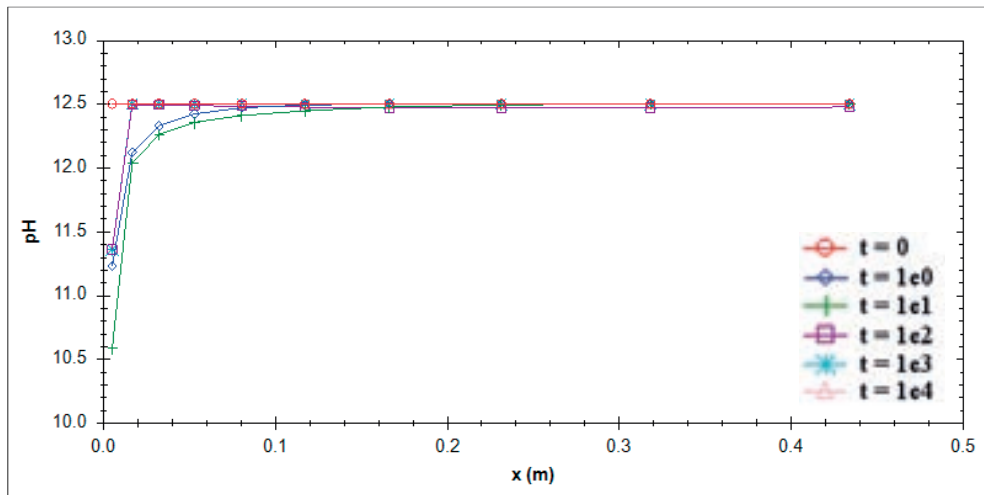
Figure 4-21: Variant 1 - pH profiles at $t = 0, 1, 10, 10^2, 10^3, 10^4$ y.
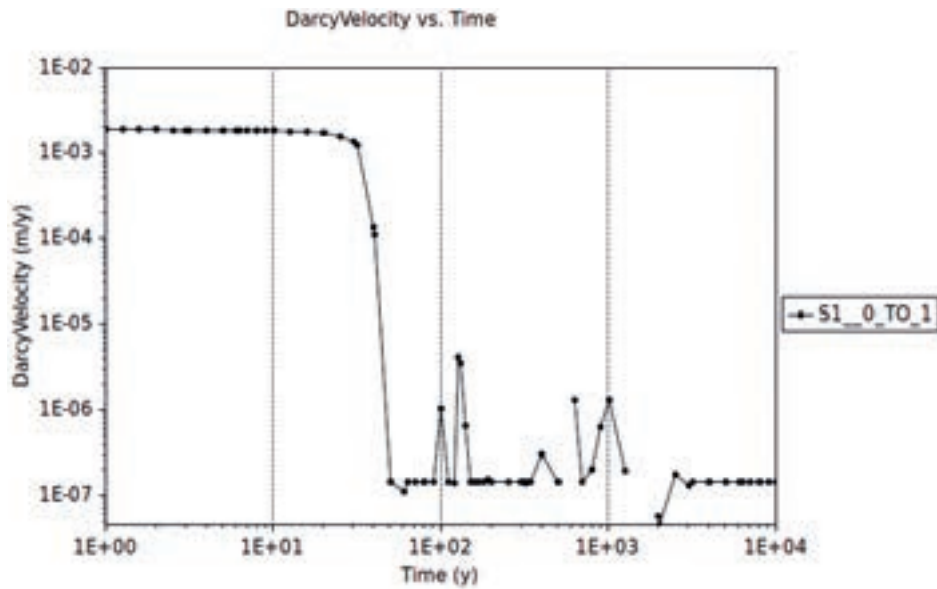
Figure 4-22: Variant 1 – Evolution of Darcy velocity in the fracture.

The armouring layer at the location of the cell adjacent to the inflow point is dominated by brucite, with lesser proportions of calcite and sepiolite (Figure 4-23). Further downstream, hydrotalcite and then ettringite become the dominant armouring phases.
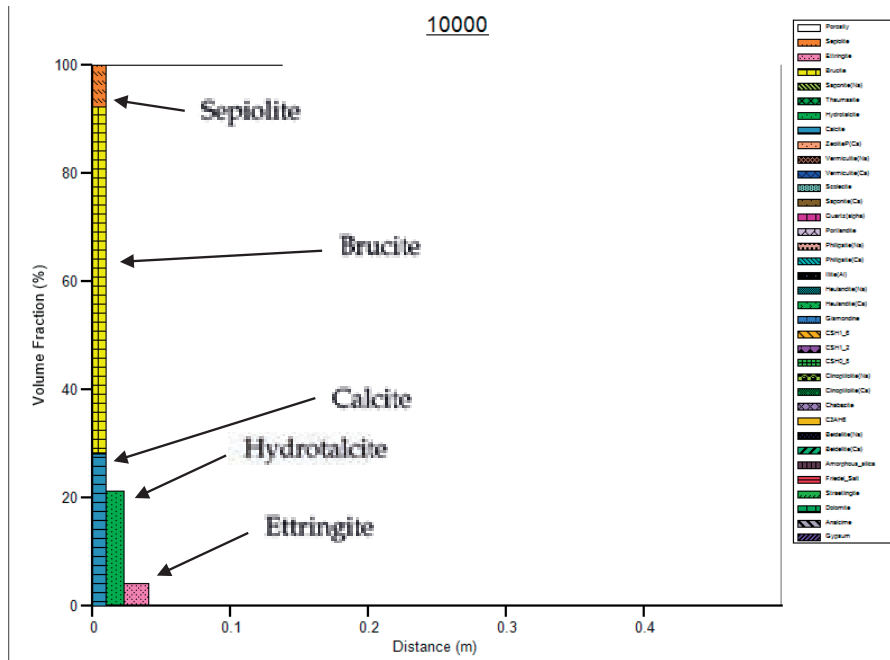
Figure 4-23: Variant 1 – Composition of armouring layer along the fracture at $t = 10^4$ y.

Variant 2

Compared to the results of the Base Case, those of Variant 2 show changes in porosity over a greater spatial scale (cf. Figure 4-13 and Figure 4-24). This difference reflects the fact that in Variant 2, water continues to flow by advection throughout the modelled time interval; complete clogging of the fracture is inhibited in this variant. A consequence is that armouring of the fracture walls due to interactions between the cement and the flowing groundwater continues for the full modelled time of 10,000 years. A marked decrease in porosity of the fracture and adjacent cement extends for a distance of c. 0.25 m along the fracture over this time (Figure 4-25). However, at a greater distance along the fracture than the zone in which porosity decreases there is a zone of porosity increase, caused by leaching of material from the cement. The greatest thickness of armouring layer upon the wallrock is seen in the second cell along the flowpath from the inflow point (Figure 4-24).

Near boundary where groundwater flows into the model, the decrease in porosity in Variant 2 occurs at a similar rate to the decreases seen in the Base Case (Figure 4-15) and Variant 1 (Figure 4-20). However, the minimum porosity allowed in Variant 2 is 0.1, which is attained near the inflow point after c. 400 years.

Figure 4-24: Variant 2 - Porosity change $(\theta(t)/\theta_0)$ at $t = 10^4$ y.
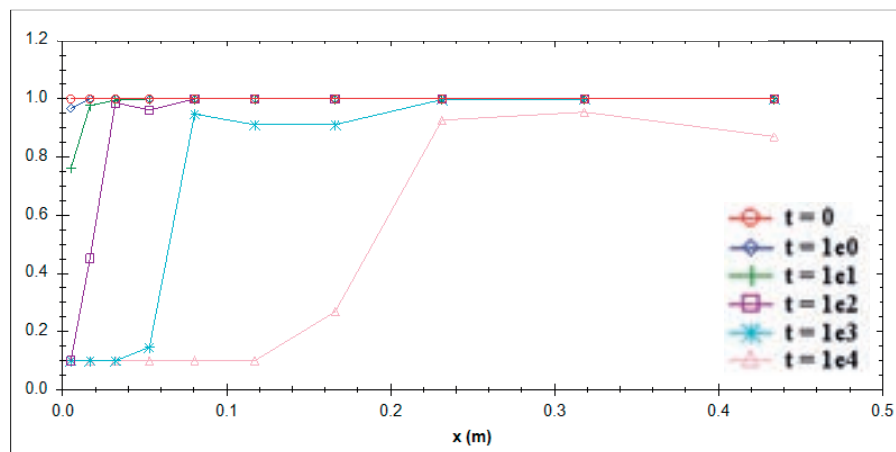
Figure 4-25: Variant 2 - Porosity profiles at $t = 0, 1, 10, 10^2, 10^3, 10^4$ y.

In Variant 2 the pH of the water in the fracture is perturbed throughout the modelled domain (Figure 4-26). However, once the fracture porosity near the inflow point has decreased to the minimum value permitted by the model (0.1), the water flowing downstream of the point attains a pH that is governed by mixing between cement pore water diffusing into the fracture and the groundwater flowing through the fracture by advection. In Variant 2, after 10,000 years of simulation time, this pH is c. 10.8, around 1.7 pH-units lower than the pH of the cement pore water. This variant demonstrates that, provided some open porosity remains open within the fracture, a plume of decreased-pH water could potentially penetrate through the cementitious barrier, given sufficient time. For the hydraulic parameters considered, this lowered pH is still substantially alkaline. However, in the interval to c. 0.25 m from the inflow point, where porosity is substantially reduced (Figure 4-25), there is a steep pH gradient in which the pH decreases from c. 10.8 (downstream end) to c.

7.2 (location of inflowing groundwater) (Figure 4-26). This gradient reflects the armouring of the fracture walls in this zone, which inhibits mixing between cementitious porewater and the inflowing groundwater (Figure 4-27).
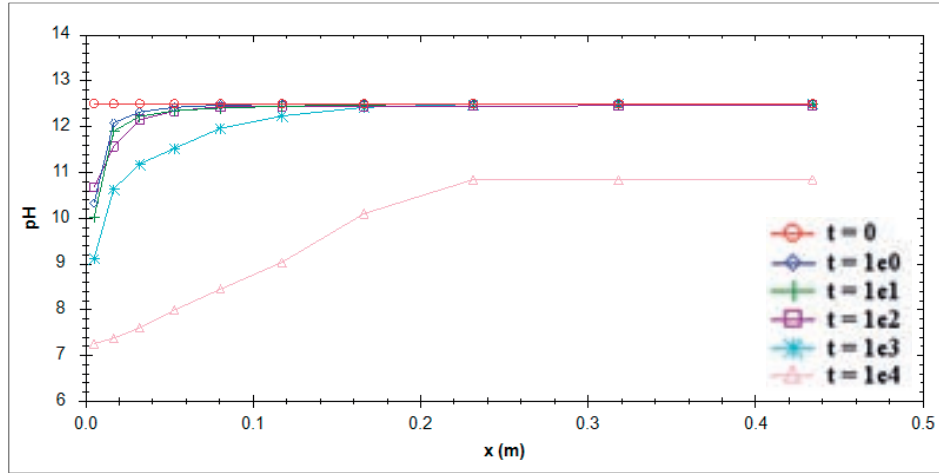
Figure 4-26: Variant 2 - pH profiles at $t = 0, 1, 10, 10^2, 10^3, 10^4$ y.
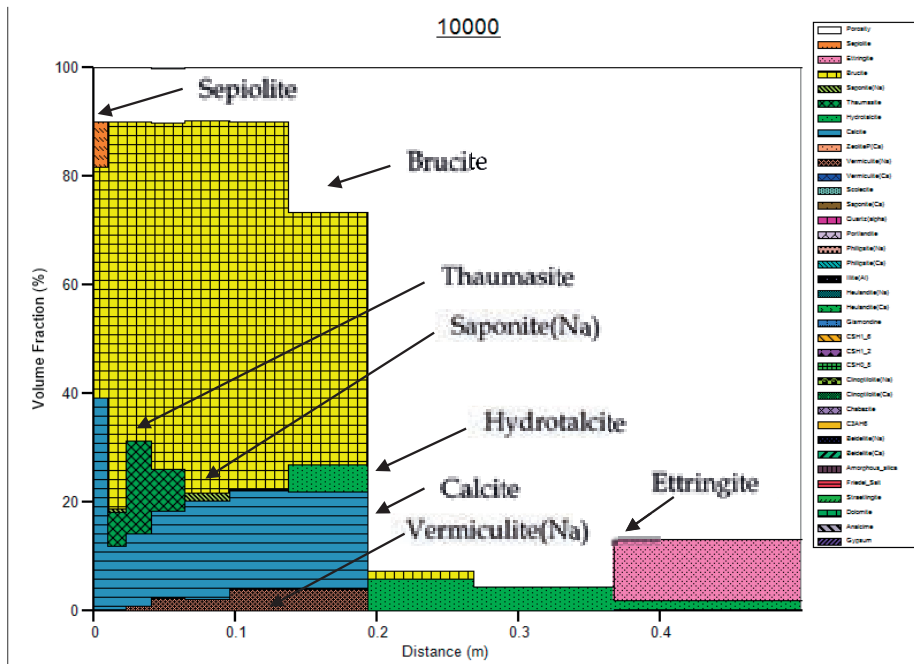
Figure 4-27: Variant 2 – Composition of armouring layer along the fracture at $t = 10^4$ y.

The fracture filling / armouring minerals (Figure 4-27) are similar to that produced by the Base Case (Figure 4-18) and Variant 1 (Figure 4-23). However, in Variant 2, the continuous flow of groundwater in the fracture by advection results in the armouring layer being developed throughout the length of the fracture. Additionally, continued supply of Na, Mg, SO₄ and CO₃ by the inflowing groundwater allowed formation of thaumasite (CaSiO₃CaSO₄CaCO₃:15H₂O) and Na-saponite (Na₀.₃₃Mg₃Al₀.₃₃Si₃.₆₇O₁₀(OH)₂) in the Variant 2 assemblage, which do not appear in the Base Case and Variant 1.

As in the Base Case and Variant 1, during the Variant 2 simulation there is a decrease in the Darcy velocity (Figure 4-28), which reflects the progressive filling of the fracture by mineral precipitates. However, in Variant 2, the Darcy velocity decreases much less, and over a much longer time interval, than in the Base Case and Variant 1. In Variant 2 the Darcy velocity decreases over only 1.5 orders of magnitude and over a time interval between c. 10 years and the end of the simulation period at 10,000 years (Figure 4-28). In contrast in the Base Case and Variant 1 the Darcy velocity decreases by 4 orders of magnitude over the time interval 20 years – 40 years (Figure 4-17 and Figure 4-22 respectively). In Variant 2, the decrease in Darcy velocity between c. 10 years and 10,000 years proceeds step-wise, reflecting the progressive decrease in porosity of each cell (Figure 4-28). As the porosity of a cell approaches the specified minimum value of 0.1, the velocity decreases rapidly and then reaches a plateau until the porosity of the next cell down the flow line approaches this minimum value, when there is another rapid decrease in Darcy velocity.
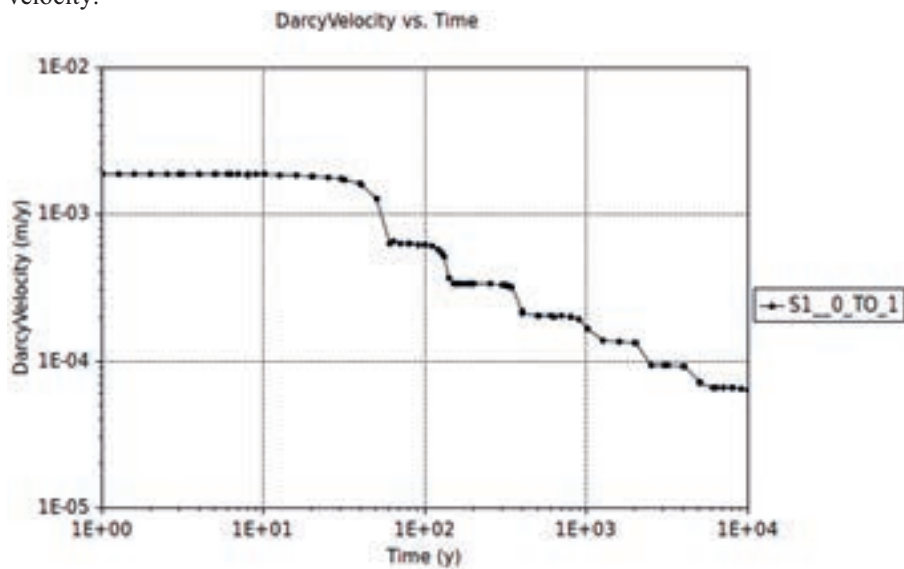
Figure 4-28: Variant 2 – Evolution of Darcy velocity in the fracture.

Variant 3

Variant 3 gives comparable results to Variant 2, but the variation in the porosity of the cement matrix extends further into the cement, reflecting greater exchange between cement porewater and groundwater flowing in the fracture (cf. Figure 4-24 and Figure 4-29). This greater exchange is a consequence of the higher relative diffusivity of the armouring layer in Variant 3 (10^{-1}) compared to Variant 2 (10^{-3}).
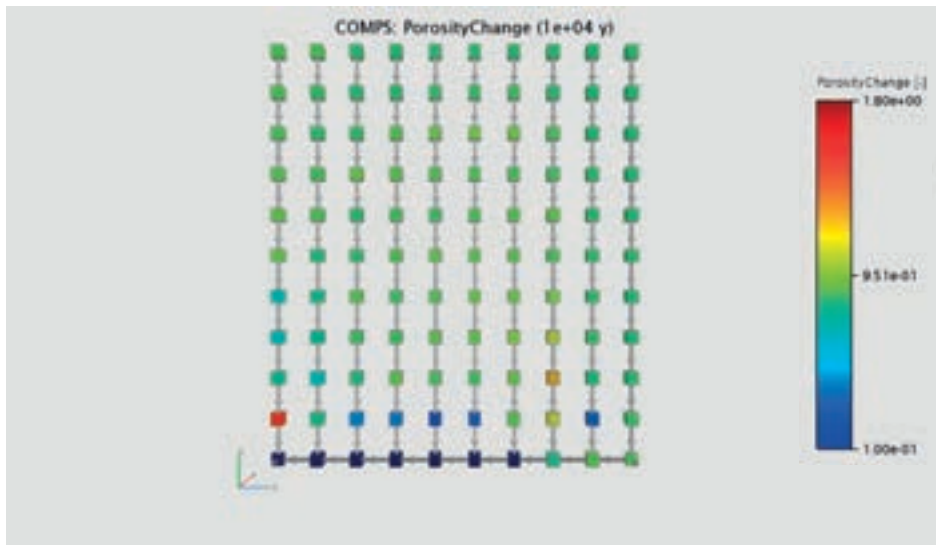
Figure 4-29: Variant 3 - Porosity change $(\theta(t)/\theta_0)$ at $t = 10^4$ y.

In Variant 3, even after 10,000 years, there is no decrease in porosity along the length of the fracture beyond 0.32 m from the inflow point (Figure 4-30). This unchanged porosity contrasts with Variant 2, where porosity decreases throughout the length of the fracture during this time (Figure 4-25). The reason for the difference is that in Variant 3, compared to Variant 2, the water chemistry in the fracture approaches the composition of the cement pore water closer to the inlet point. This more rapid change in Variant 3, compared to Variant 2, reflects the increased exchange rate between the cement pore water and flowing groundwater in the fracture in Variant 3.
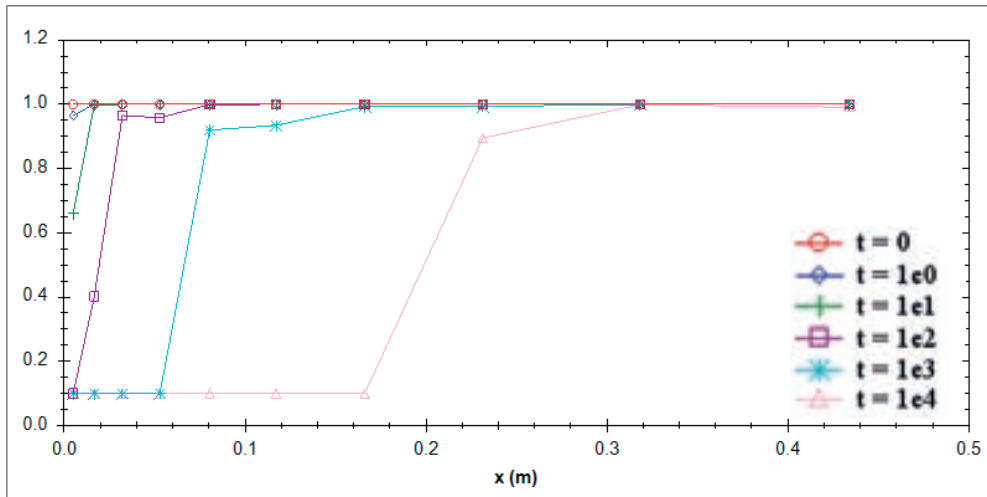
Figure 4-30: Variant 3 - Porosity profiles at $t = 0, 1, 10, 10^2, 10^3, 10^4$ y.

This increased interaction between the cement pore water and the groundwater is also apparent in the variations of pH versus time (Figure 4-31). At earlier times, the

variation in pH along the fracture is very similar in Variant 2 and Variant 3 (cf. Figure 4-26 and Figure 4-31). However, after 10,000 years the increase in pH with increasing distance from the inlet point is much steeper in Variant 3 than in Variant 2. Furthermore, in Variant 3 the maximum pH reached downstream from the inlet is 12.3 (Figure 4-31), which is about 0.2 pH units lower than the cement porewater and about 0.5 pH units greater than the highest value reached downstream from the inlet in Variant 2 (Figure 4-26).
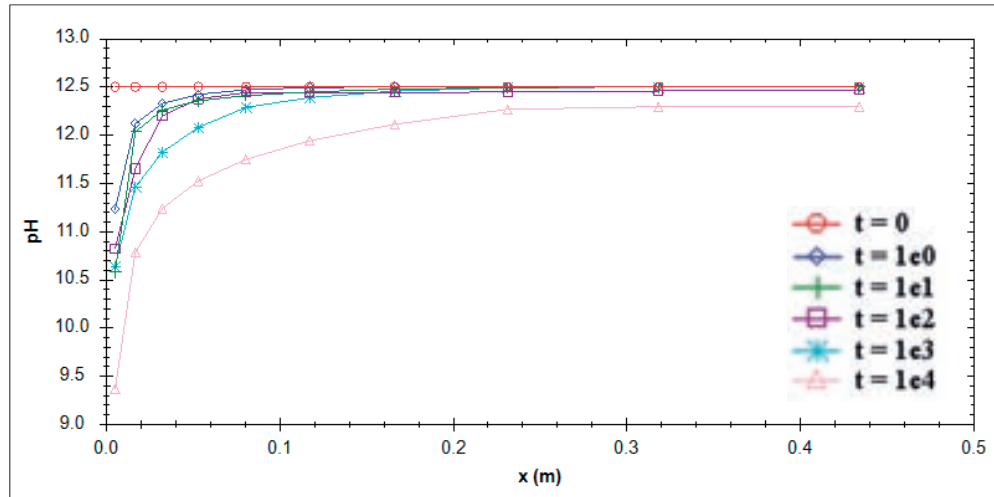
Figure 4-31: Variant 3 - pH profiles at $t = 0, 1, 10, 10^2, 10^3, 10^4$ y.

The variations in porosity and pH along the fracture are reflected in the mineral assemblage that forms the armouring layer (Figure 4-32). The minerals composing this layer after 10,000 years are similar to those that formed the armouring layer in Variant 2 after this time, but the maximum occlusion of porosity permitted by the model (0.9) extends to a greater length along the fracture in Variant 3 (c. 0.19 m; Figure 4-32) than in Variant 2 (c. 0.13 m; Figure 4-27).
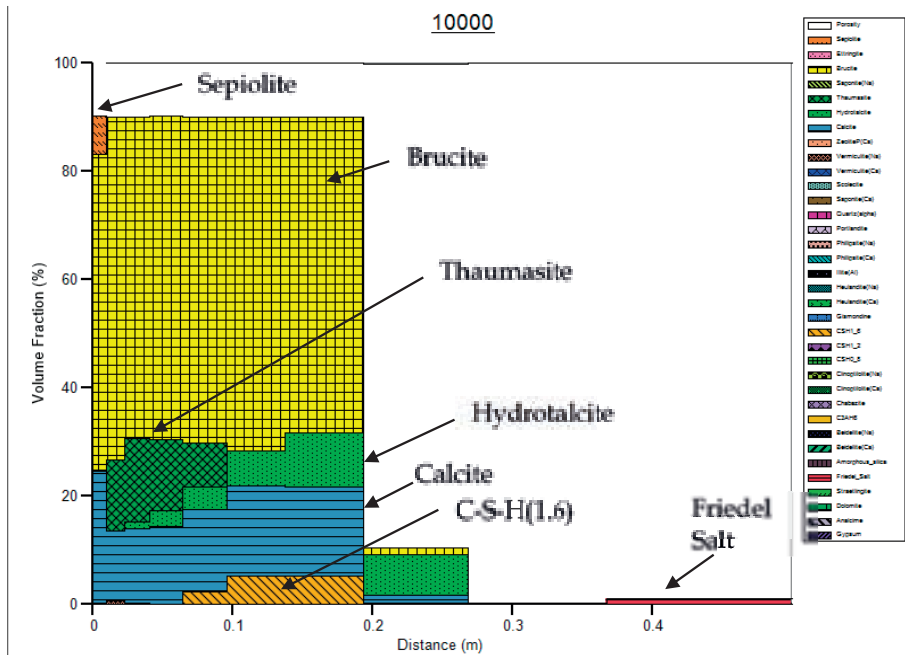
Figure 4-32: Variant 3 – Composition of armouring layer along the fracture at $t = 10^4$ y.

The increased interaction between cement pore water and groundwater in the fracture is also apparent in the mineral assemblage in Variant 3, with the appearance of C-S-H(1.6) occurring in the armouring layer. This cement solid is not predicted in Variant 2.

The increased rate of armouring in the upstream region of the fracture in Variant 3 compared to Variant 2 means that the rate of armouring in the downstream region is decreased in Variant 3 compared to Variant 2. Armouring occurs throughout the fracture in Variant 2 after 10,000 years (Figure 4-27), but in Variant 3 there is no significant armouring between 0.27 m and 0.38 m from the inflow after 10,000 years, and only a very thin layer of Friedel's salt between 0.38 m and the end of the modelled region (Figure 4-32).

The evolution of Darcy velocity in Variant 3 is very similar to the evolution in Variant 2, with step-wise decreases occurring as successive cells are occluded (Figure 4-33).
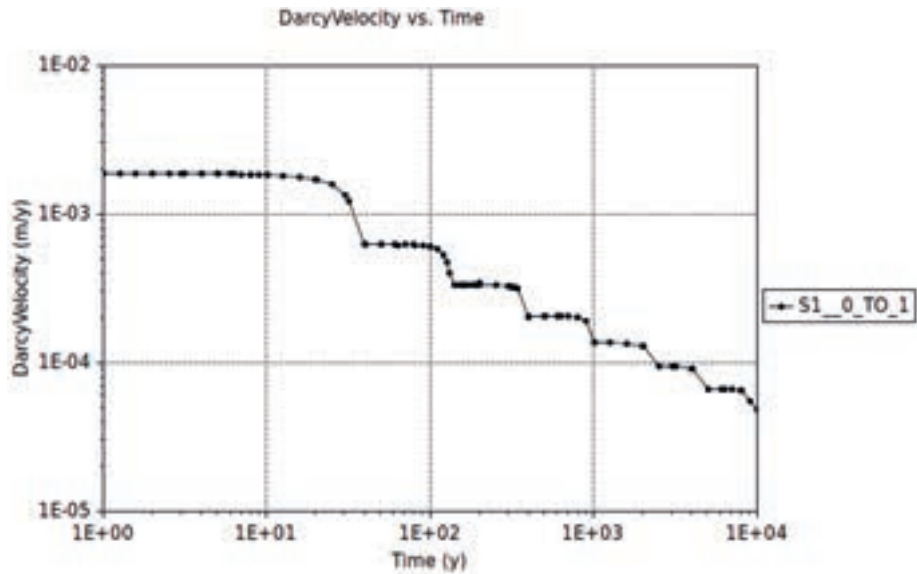
DarcyVelocity vs. Time

Figure 4-33: Variant 3 – Evolution of Darcy velocity in the fracture.

Variant 4

Variant 4 is the same as Variant 2 except for a much higher initial flow rate in the fracture (2.5×10^{-2} m/y in Variant 4, compared to 1.89×10^{-2} m/y in Variant 2). The results for Variant 4 are very similar to those for Variant 2, because as the fracture's porosity decreases to the minimum permitted value of 0.1, the two cases converge towards a similar state. In this state, diffusive mass transport from the cement's pores to the fracture is the dominant control on water chemistry in the fracture. Although the flow rate in the fracture at any given time is slightly more than an order of magnitude greater in Variant 4 than in Variant 2, once the porosity decreases to 0.1, there is little difference in the proportion of water in the fracture that is groundwater. Additionally, a greater flux of groundwater in the fracture tends to result in steeper solute concentration gradients between the groundwater and the cement porewater. These steeper solute gradients lead to greater solute fluxes between the fracture and matrix.

Because of this convergence of the systems states in Variant 4 and Variant 2, after 10,000 years the spatial variation in porosity within the modelled domain in Variant 4 is virtually identical to that in Variant 2 (cf. Figure 4-24 and Figure 4-34). Similarly, the temporal evolution of porosity in the fracture is very similar in each of these two variants (cf. Figure 4-25and Figure 4-35).
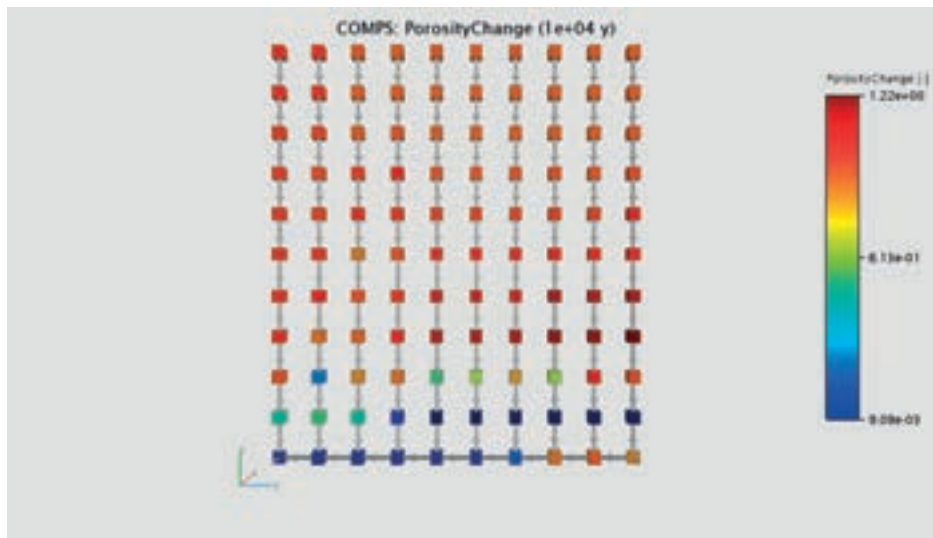
Figure 4-34: Variant 4 - Porosity change ($\theta(t)/\theta_0$) at $t = 10^4$ y.
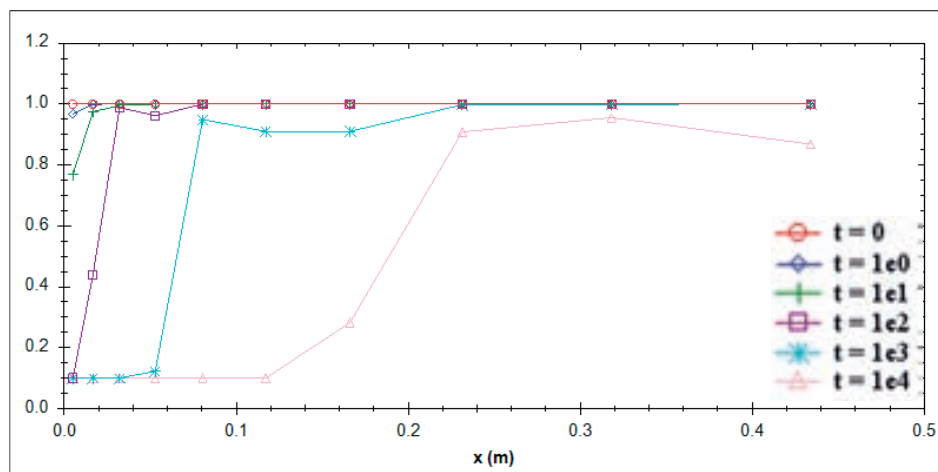

Figure 4-35: Variant 4 - Porosity profiles at $t = 0, 1, 10, 10^2, 10^3, 10^4$ y.

Mirroring the temporal variations in porosity, the variations in pH along the fracture are almost the same in Variant 4 as in Variant 2 (cf. Figure 4-36 and Figure 4-26). As in Variant 2, the pH of the water in the fracture is perturbed throughout the modelled domain (Figure 4-36). However, once the fracture porosity near the inflow point has decreased to the minimum value permitted by the model (0.1), the water flowing downstream of the point attains a pH that is governed by mixing between cement pore water diffusing into the fracture and the groundwater flowing through the fracture by advection. In Variant 4, after 10,000 years of simulation time, this pH is c. 11.0, around 1.5 pH-units lower than the pH of the cement pore water. This variant again demonstrates that, provided some porosity remains open within the fracture, a plume of decreased-pH water could potentially penetrate through the cementitious barrier, given sufficient time. For the hydraulic parameters considered, this lowered pH is still substantially alkaline. However, in the interval of c. 0.25 m from the inflow point, where porosity is substantially reduced (Figure 4-36), there is a steep pH gradient across which the pH decreased from c. 11 (downstream end) to c. 7.2 (location of inflowing groundwater) (Figure 4-26). This gradient reflects the

armouring of the fracture walls in this zone, which inhibits mixing between cementitious pore water and the inflowing groundwater (Figure 4-37).
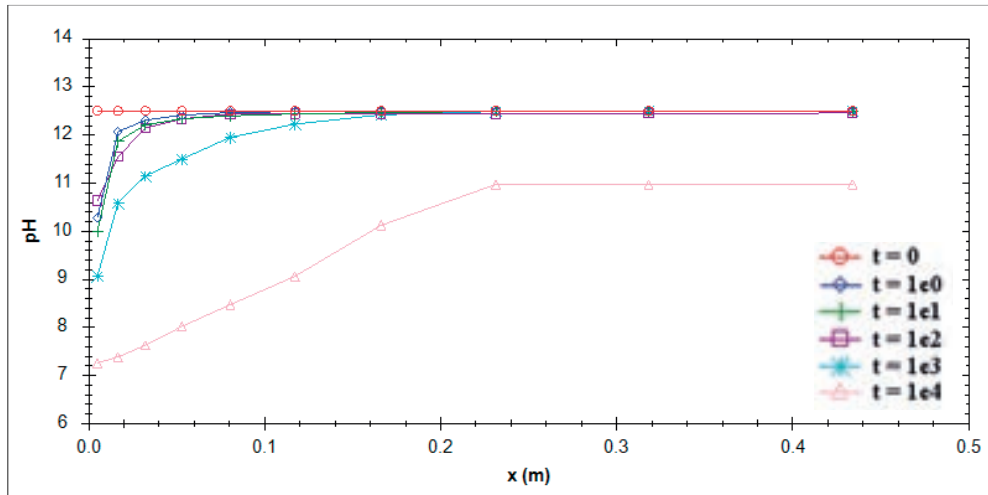

Figure 4-36: Variant 4 - pH profiles at $t = 0, 1, 10, 10^2, 10^3, 10^4$ y.

The spatial variation in the fracture-filling / armouring mineral assemblage developed in Variant 4 is very similar to that developed in Variant 2 (cf. Figure 4-37 and Figure 4-27). However, there are some subtle differences. In Variant 4, a slightly higher proportion of calcite is calculated to occur adjacent to the groundwater inflow point. Compared to Variant 2, in Variant 4 there is also slightly more brucite near the middle of the fracture (c. 0.19 m to 0.27 m from the inflow point). These variations can be explained by the greater rate at which solutes inflow in Variant 4, compared to Variant 2, but are small owing to the effective cement buffering once the porosity has decreased to the minimum permitted value.

The variation in Darcy velocity as a function of time is very similar in Variant 4 to that in Variant 2 (cf. Figure 4-38 and Figure 4-28). However, at any time the Darcy velocity in Variant 4 is slightly more than one order of magnitude greater than in Variant 2. Once again, step-wise decreases in Darcy velocity occur as successive cells are occluded (Figure 4-38).
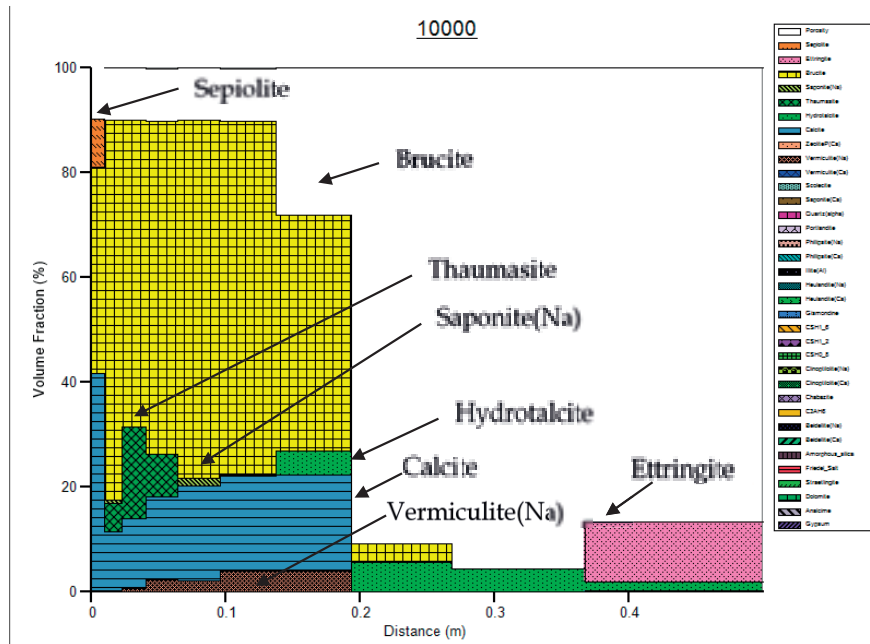
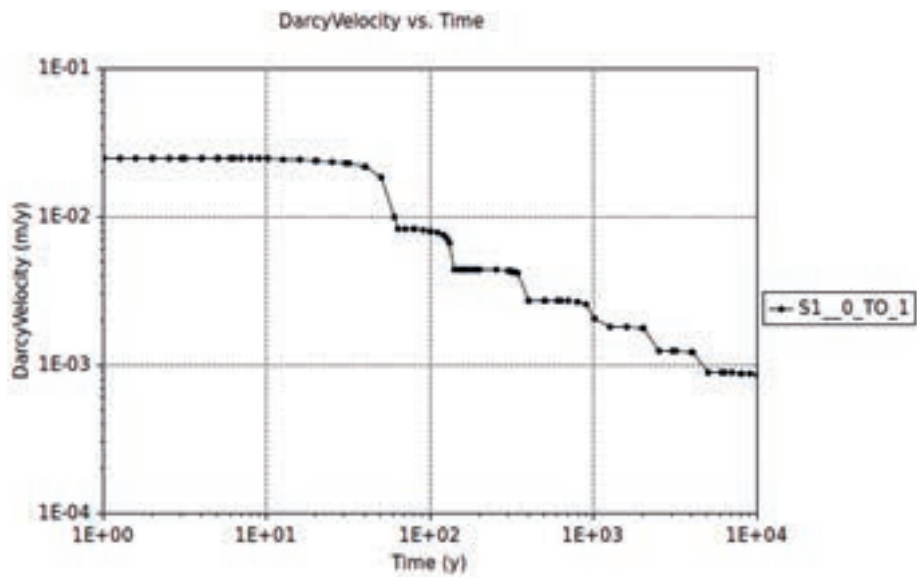**Figure 4-37:** Variant 4 – Composition of armouring layer along the fracture at $t = 10^4$ y.

Figure 4-38: Variant 4 – Evolution of Darcy velocity in the fracture.

Variant 5

Variant 5 is the same as Variant 3, except that the initial flow rate is slightly more than an order of magnitude greater (2.5×10^{-2} m/y compared to 1.89×10^{-3} m/y). That is, the relationship between Variant 5 and Variant 3 is the same as between Variant 4 and Variant 2. In the same way that there are only small differences between model outputs of Variants 4 and 2, there are also only very small differences between the outputs of Variants 5 and 3. Once again, these small

differences reflect that fact that, as the porosity of the fracture decreases towards the minimum specified value (0.1) the chemistry of the water in the fracture is buffered by diffusive mass transport between the fracture and the cement matrix.

Reflecting this buffering, the spatial variation in porosity after 10,000 years in Variant 5 is virtually identical to that in Variant 3 (cf. Figure 4-39 and Figure 4-29). Similarly, the temporal variations in porosity along the fracture are almost the same in Variant 5 and Variant 3 (cf. Figure 4-40 and Figure 4-30).
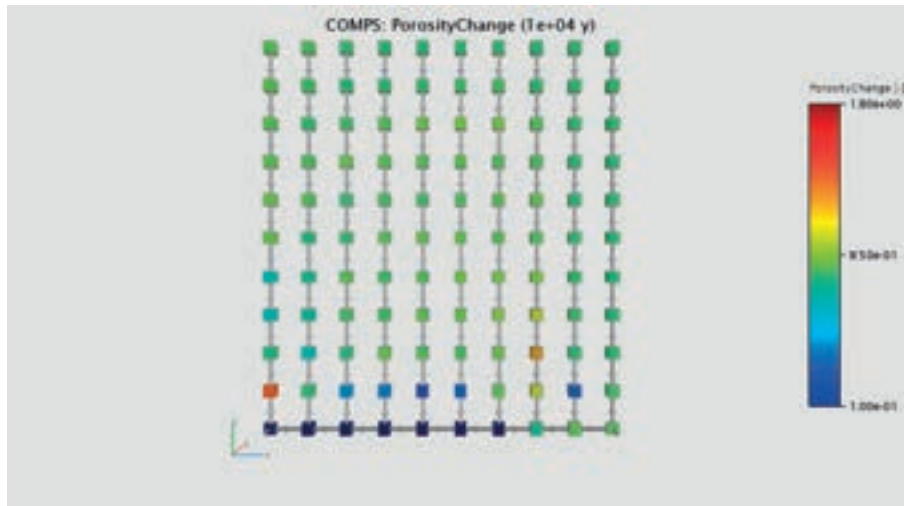

Figure 4-39: Variant 5 - Porosity change $(\theta(t)/\theta_0)$ at $t = 10^4$ y.

Variant 5 is also very similar to Variant 4, apart from having a higher relative diffusivity (10^{-1}) compared to Variant 5 (10^{-3}). This difference results in the porosity of the cement being affected over a greater distance in Variant 5 compared to Variant 4 (cf. Figure 4-39 and Figure 4-34). That is, the differences between results in Variant 5 and Variant 4 are similar to those seen between Variant 2 and Variant 3).

As in the other variants, in Variant 5 the temporal variation in porosity is closely mirrored by the variation in pH (cf. Figure 4-40 and Figure 4-41). At any time, the highest pH occurs downstream of the point where the minimum fracture porosity is attained. In this variant, after 10,000 years, the pH downstream of this point is c. 12.3, around 0.2 pH units lower than the value in the cement, identical to the result from Variant 3.
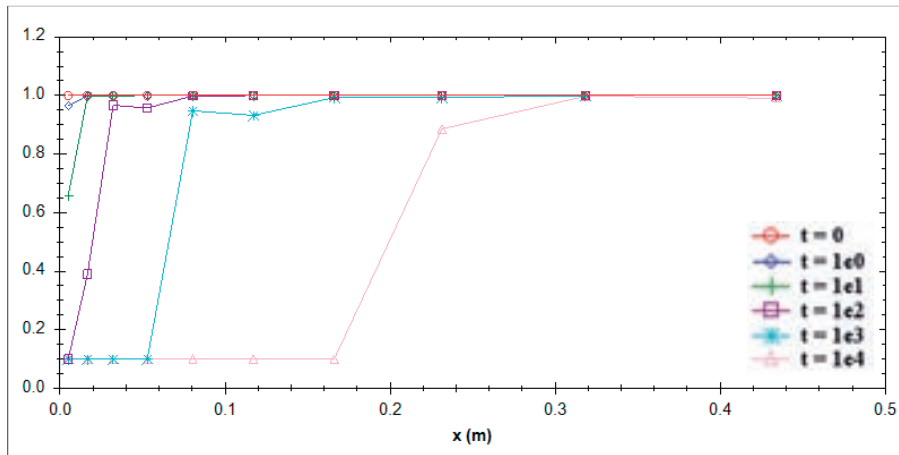
Figure 4-40: Variant 5 - Porosity profiles at $t = 0, 1, 10, 10^2, 10^3, 10^4$ y.
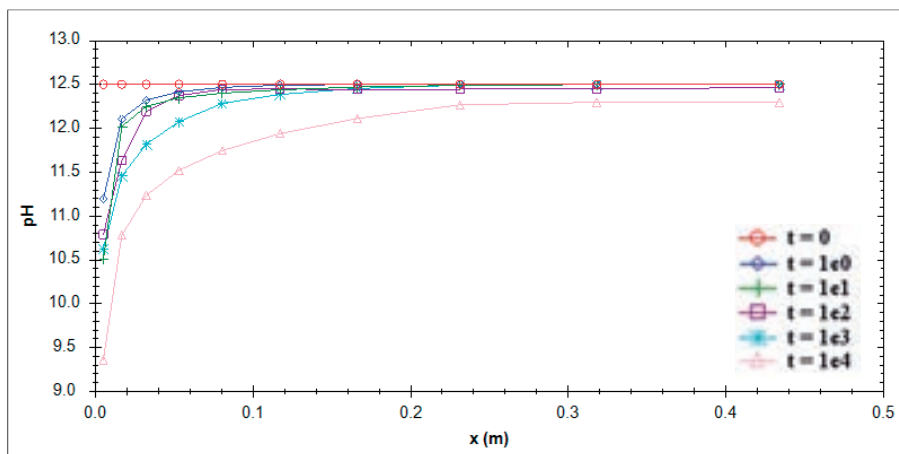

Figure 4-41: Variant 5 - pH profiles at $t = 0, 1, 10, 10^2, 10^3, 10^4$ y.

The mineralogy of the armouring developed in Variant 5 also differs very little from that produced in Variant 3 (cf. Figure 4-42 and Figure 4-32). Compared to Variant 3, in Variant 5 there is slightly more thaumasite between c. 0.75 and 0.9 m, and slightly more brucite near the middle of the fracture (c. 0.19 m to 0.27 m from the inflow point).
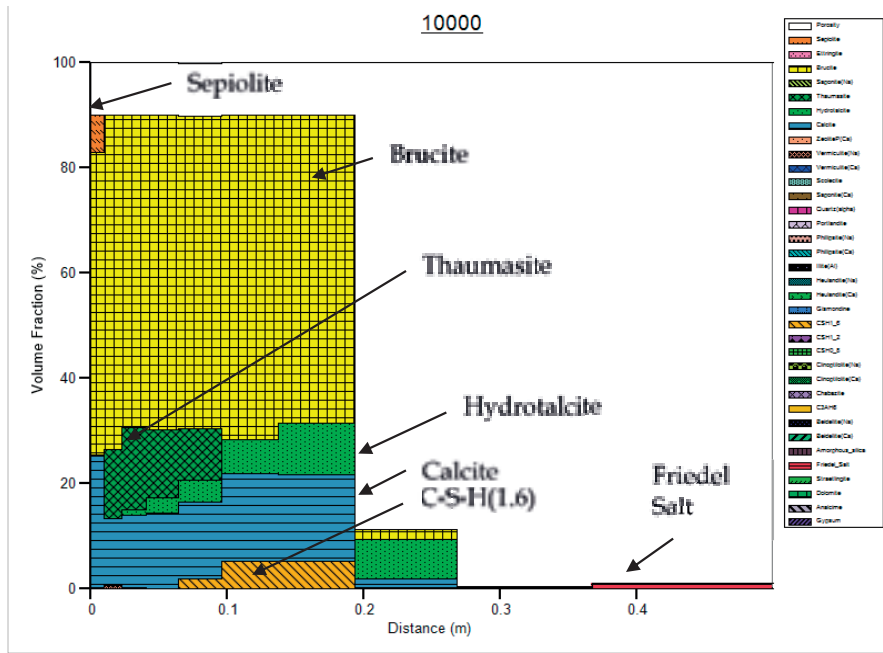
Figure 4-42: Variant 5 – Composition of armouring layer along the fracture at $t = 10^4$ y.

The variation in Darcy velocity as a function of time is very similar in Variant 5 to that in Variant 3 (cf. Figure 4-43 and Figure 4-33). However, at any time the Darcy velocity in Variant 5 is slightly more than one order of magnitude greater than in Variant 3. Once again, step-wise decreases in Darcy velocity occur as successive cells are occluded (Figure 4-43).

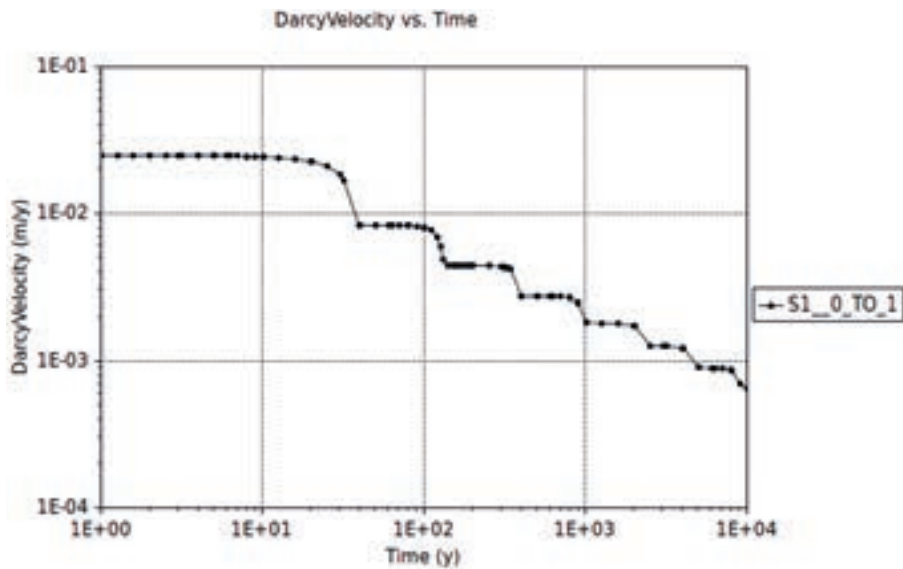**Figure 4-43:** Variant 5 – Evolution of Darcy velocity in the fracture.

4.10. Summary

The coupled simulations of advective-diffusive interactions between groundwater flowing through a fracture in the concrete vault wall and porewaters in the

neighbouring cementitious matrix of the concrete, indicate a strong tendency for the fracture to fill with secondary minerals. This filling is accompanied by a decrease in the flux of water through the fracture in the Base case and in all the variant cases.

For the range of parameters investigated the porosity evolution of the fracture and the corresponding pH profiles are much less sensitive to variations in Darcy velocity than to variations in the diffusivity of the armouring layer. This result reflects the fact that, as the fracture porosity decreases, the water chemistry becomes increasingly influenced by diffusive fluxes of solutes between the cement matrix and the groundwater. Thus, downstream from the last point along the flow path at which the minimum permitted porosity is attained, the relative diffusivity of the armouring layer is a much more important control on water chemistry than the advective flux.

The extent of buffering of groundwater pH by the cement as the groundwater flows through the fracture depends upon the degree to which the fracture fills with solids and the relative diffusivity of the armouring layer. The results show that the smaller the thickness of armouring and the smaller the diffusivity of the armouring layer compared to that of the cement matrix, the further along the fracture will relatively low-pH water penetrate; the smaller thickness is required to maintain a significant advective contribution to transport, the smaller diffusivity is required to limit buffering of fracture upstream porewaters by cement interactions. The greatest perturbation of pH from values in the cement matrix is given by Variants 2 and 4, in which there is both a small relative diffusivity of the armouring layer (10^{-3}) and an imposed continuously open fracture (the fracture porosity does not decrease below 0.1). However, even in these cases, after 10,000 years the pH remains alkaline (c. 11) at distances > 0.2 m from the point at which groundwater enters the cement. Were longer timeframes to be considered, then lower pH values could occur at greater distances from the inflow, but it seems unlikely that the low pH values would occur more than c. 2 m from the outer wall surface of the vault wall during the safety assessment time frame of 100,000 years. While such a distance is considerably greater than the thickness of the wall (0.4 m), it is still substantially less than the width of the vault (19.2 m). It is therefore to be expected that chemical, buffering by the grout present within the vault would ensure that water leaving the vault would continue to have high, cement-buffered, pH.

The modelling suggests that there would be no significant safety-relevant impacts on the chemical buffering capability of the cement in the SFR vaults over the assessment time frame of 10,000 years.

5. Potential for replacement of Ca- with Fe(II)-bearing minerals

5.1. Issues investigated

In general, the presence of high pH conditions due to cement leaching may be envisaged to result in a low potential for the development of significant concentrations of dissolved iron in a repository environment. However, large masses of iron compounds are present in many repository systems. In the SR-PSU, SKB has apparently given no consideration to the possibility that Fe may combine with solid phases present in cementitious barriers, thereby potentially altering the chemical buffering capability of these barriers and their longevity. Therefore, an assessment has been made of whether Fe-uptake could be significant and, if so, what implications there might be for the safety assessment.

It is expected that under anaerobic conditions steel will corrode to produce ferrous ions (Fe^{2+}) and hydrogen (partitioned between liquid and gaseous phases in accordance with Henry's law):

$$Fe(0) + 2H^+ = Fe^{2+} + H_2(aq). \tag{5-1}$$
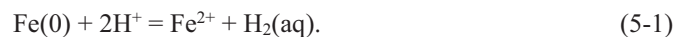
Depending on the composition of pore waters in contact with steel, several possible corrosion products could form, such as iron(II) hydroxide ($Fe(OH)_2$, possibly as a pre-cursor to magnetite, Fe_3O_4), iron carbonates, 'green rusts', iron sulphides, and Fe-rich clay minerals such as berthierine, cronstedtite or saponite (e.g. Wilson et al., 2015).

Portland cement contains a large amount of portlandite ($Ca(OH)_2$) which along with hydrated cement phases such as C-S-H (calcium-silicate-hydrate) gel, buffer cement porewater pH to values of ~12.5, after the leaching out of alkalis which initially give a pH of ~13. In low alkalinity cement blends, the addition of materials such as silica fume, (SF), blast furnace slag (BFS) or pulverised fly ash (PFA) inhibit the formation of portlandite, with most pH buffering being maintained by C-S-H gel at pH 11-12 (Codina, 2008).

Therefore, the ability for cement to maintain hyperalkaline conditions depends largely on the longevity of portlandite and C-S-H gel. In contrast to portlandite, $Fe(OH)_2$ tends to buffer pH at around ~9.5 (based on equilibration with pure water at 25 °C, using Geochemist's Workbench, Bethke, 2008). Lowering of pH due to extensive anaerobic metal corrosion and the replacement of Ca-bearing solids with Fe(II)-bearing solids could tend to inhibit ongoing passivation of corrosion reactions in the near-field.

The review and simple scoping calculations reported here aim to determine the feasibility of Fe(II)-bearing solids replacing Ca-bearing solids in the cementitious barriers of the SFR. Hence, it is aimed to judge whether pH could be lowered to values below those considered by the SR-PSU assessment, with implications for:

- decreased passivation of corrosion reactions, leading to more rapid degradation of metal components in the barrier system of the SFR, compared to those assumed by SKB in the SR-PSU; and
- consequent enhancement of concrete degradation rates in the near-field compared to those assumed by SKB in the SR-PSU.

5.2. Approach to investigating issues

To explore the potential for Fe(II) release from iron/steel corrosion to result in decreasing pH in cement porefluids, the following tasks were undertaken:

- steel corrosion processes were reviewed;
- iron compounds associated with cement were reviewed; and
- thermodynamic modelling was undertaken.

The thermodynamic modelling included: a review of the pH conditions associated with buffering by different cement solids and steel corrosion products; the aqueous solubility of iron/steel corrosion products; the potential for Fe-rich cement solids to form in cement and the effect of adding dissolved Fe(II) to cement pore fluid on pH.

5.3. Review of steel corrosion reactions

The corrosion of iron materials under anaerobic conditions may result in the formation of compounds such as $Fe(OH)_2$ or 'green rust' (double-layered hydroxyl salt compounds), and these have been considered metastable pre-cursors of magnetite (Fe_3O_4) (e.g. Genin et al., 2001; Tamaura et al., 1984).
The formation of $Fe(OH)_2$ as a corrosion product and generation of H_2 (distributed between gaseous and aqueous species depending on Henry's Law) can be represented by:

$$Fe + 2H_2O \rightarrow Fe(OH)_2 + H_2 \qquad (5-2)$$
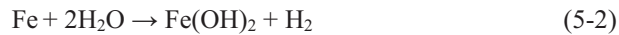
whereas magnetite formation from native iron can be represented by:

$$3Fe + 4H_2O \rightarrow Fe_3O_4 + 4H_2 \qquad (5-3)$$
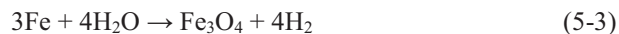
Magnetite may form from $Fe(OH)_2$ via the Schikkor reaction (e.g. El Hajj et al., 2013; King and Watson, 2010):

$$3Fe(OH)_2 \rightarrow Fe_3O_4 + H_2 + 2 H_2O \qquad (5-4)$$

Carbonate minerals may also form under relatively higher PCO_2 conditions (as associated with soils, sediments and sub-aerial environments), and if sufficient carbonate is available, minerals such as siderite ($FeCO_3$) or chukanovite ($Fe_2(OH)_2CO_3$) may also form (Rémazeilles and Refait, 2009; Schlegel et al., 2016). It has been suggested that chukanovite is metastable with respect to siderite (Azoulay et al., 2012).

The formation of siderite can be represented by:

$$Fe + CO_2(g) + H_2O \rightarrow FeCO_3 + H_2(g) \qquad (5-5)$$
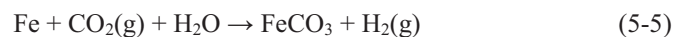
In the presence of sulphur, iron sulphide films may also form on steel; mackinawite and pyrrhotite are potential early-stage corrosion product in addition to pyrite (e.g. ASM 1987, 2005; El Mendili et al., 2013; El Mendili et al., 2014).

Under anaerobic conditions, initially trapped O_2 present in repository near-field environments will be consumed, and Fe(III) corrosion products initially formed will be transformed to magnetite, either by reaction with dissolved Fe(II) (King and Watson, 2010) (Figure 5-1):
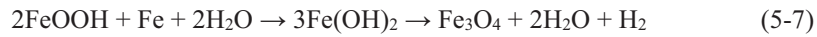
$$2FeOOH + Fe(II) \rightarrow Fe_3O_4 + {_2}H+ \qquad (5\text{-}6)$$
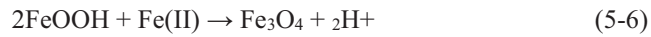
or by reductive dissolution coupled to C-steel dissolution (King and Watson, 2014):

$$2FeOOH + Fe + 2H_2O \rightarrow 3Fe(OH)_2 \rightarrow Fe_3O_4 + 2H_2O + H_2 \qquad (5\text{-}7)$$

Under aerobic conditions, corrosion may occur such that Fe(III)(oxy)hydroxides such as ferrihydrite, lepidocrocite (γ-FeO(OH)) and goethite (α-FeOOH) are produced (e.g. Ishikawa et al., 2001; Antunes et al., 2003), for example:

$$4Fe + 3O_2(g) + 2H_2O \rightarrow 4\ FeOOH \qquad (5\text{-}8)$$

Minerals such as ferrihydrite ($Fe_2O_3:0.5H_2O$) are likely to be present as small disordered crystals which may recrystallise to higher stability goethite and/or hematite (Fe_2O_3), and green rust (if present as an earlier produce of corrosion) and may also undergo recrystallisation (e.g. Schwertmann and Murad, 1983; Schwertmann and Fechter, 1994; Refait et al., 2003b). Maghemite, which has a spinel structure like magnetite, but a lower Fe(II) content, has also been identified as a steel corrosion product (e.g. Daub et al., 2011).

The presence of clay minerals near anaerobically corroding steel could also lead to the formation of several different iron-rich clay minerals depending on prevailing chemical conditions (see reviews by Wersin et al., 2008; Wilson et al., 2015).

The rate of carbon-steel dissolution depends on pH and increasing pH promotes the passivation of C-steel (King and Watson, 2010). The effect of passivity is most evident from the rates of anaerobic general corrosion, which are of the order of 1 µm/y at near-neutral pH and < 0.1 µm/y in alkaline solution (King and Watson, 2010). However, along with this passivity comes a higher probability of the initiation of localised corrosion (King and Watson, 2010).
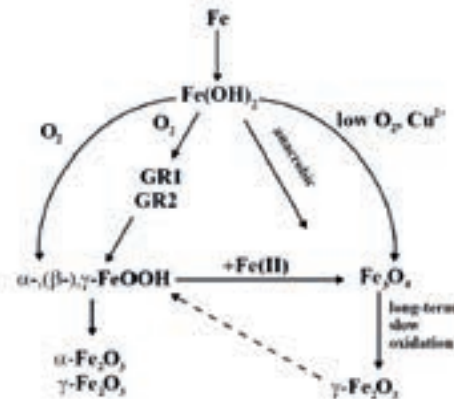

Figure 5-1: Schematic showing formation and alteration of ferrous and ferric compounds as a result of carbon steel corrosion processes (King and Stroes-Gascoyne, 2000).

5.4. Iron compounds in cement

In ordinary Portland cement, only two-thirds of the Fe(III) occurs in ferrite (C$_4$AF in cement notation, composition of 2Ca$_2$(Al,Fe)$_2$O$_5$). The rest of the Fe(III) being associated with alite (C$_3$S, or Ca$_3$SiO$_5$) and aluminate (C$_3$A or Ca$_3$Al$_2$O$_6$) (Taylor, 1990). Most of the iron present in Portland cements is as Fe(III), but calcium aluminate cements (e.g. ciment fondue) may also contain Fe(II) (3-6 wt.% Fe(II) as FeO in 'ciment fondue', Taylor, 1990) and wüstite (FeO) has been reported (Taylor, 1990).

The hydration of C$_4$AF resulted in the formation of AFm, AFt or hydrogarnet, with Fe(III) hydroxide gel (Taylor, 1990). Fe(III) can substitute for Al to form solid solutions in cement phases (Taylor, 1990), with Fe(III)-bearing forms of several cement solids being reported, including: ettringite (e.g. Möschner et al., 2009); siliceous hydrogarnet (e.g. Dilnesa et al., 2014; Vespa et al., 2015); calcium sulfoaluminate/monosulfate (Idrissi et al., 2010; Dilnesa et al., 2012); and iron-monocarbonate/iron-hemicarbonate (Dilnesa et al., 2011). In 'type V' (sulphate resistant) Portland cement, calcium ferrite (C$_2$F) can occasionally occur, and upon hydration this produces C$_4$FH$_{13}$ which breaks down into C$_3$FH$_6$, which in turn rapidly breaks down to portlandite and hematite (Gartner et al., 2002).

A recent study of FeO-SiO$_2$ slag reacting with portlandite suggested that the major mineral of FeO-SiO$_2$ slag was fayalite (Fe$_2$SiO$_4$) and that the pozzolanic productions of FeO-SiO$_2$ slag were mainly hydrated calcium silicate (C-S-H) and a small amount of Fe(OH)$_2$ gel. It was also suggested that 'a few Fe^{2+} ions' entered the structure of C-S-H by replacing Ca^{2+} with Fe^{2+} (Sheng et al., 2016). However, based on literature searches using Science Direct, Google Scholar, and Research Gate, very few studies have appeared to consider the possibility of Fe^{2+} substituting for Ca^{2+} in silica-hydrate gels or for the formation of Fe(II)-rich hydration products other than Fe(OH)$_2$.

5.5. Thermodynamic modelling of potential Fe(II)-cement interactions

The hydration of Portland cement clinker results in the formation of portlandite, which in pure water, buffers pH to a value of ~12.5 and a concentration of Ca^{2+} of ~10^{-2} molal at 25 °C (this is typical of Portland cement porewater after alkalis such as K and Na have flushed out, these can result in pH ~13). Low pH cements (generated by the addition of silica fume, silica flour, blast furnish slag or fly ash) typically result in pH ~11-12 (Codina, 2008). If cement leaching proceeds such that portlandite is lost and low Ca/Si ratio C-S-H gel and amorphous silica remain (but there is no carbonation), a pH of ~10 could be expected to evolve. Assuming a low Ca/Si C-S-H gel (Ca$_{0.8}$SiO$_{2.8}$1.54H$_2$O) and amorphous silica are in equilibrium with pure at 25 °C, a value of 10.03 is predicted using PHREEQC (Parkhurst and Appelo, 2013) and v1.01 of the thermoddem database, BRGM, 2017). If cement reacts with a groundwater rich in Mg, brucite (Mg(OH)$_2$) may form (Taylor, 1990), which tends to buffer water to a pH of ~10 (pH 10.5 calculated using the thermoddem database, version 1.01; pH 10.21 using the llnl.dat database). The carbonation of cement will tend to result in a significant reduction in pH, depending on intruding water chemistry, in particular the prevailing PCO$_2$. However, a pH of ~8 is likely where there is calcite equilibrium (a pH of 8.3 is calculated using both the thermoddem and llnl databases when PCO$_2$ is set at atmospheric conditions, i.e. 10-3.5 bar).

The maximum concentration of dissolved Fe in solution from corroding steel will depend on prevailing pH, the solubility of the corrosion products and the rate of steel corrosion (which is suppressed under very alkaline conditions). An indication of potential variation in the solubility of steel corrosion products as a function of pH is given in the solubility diagrams given in Figure 5-2, which were produced assuming a very low $fO_2(g)$ (a value just slightly higher than that associated with $H_2(g)$-$H_2O(l)$ equilibrium, noting that anaerobic steel corrosion generates $H_2(g)$).
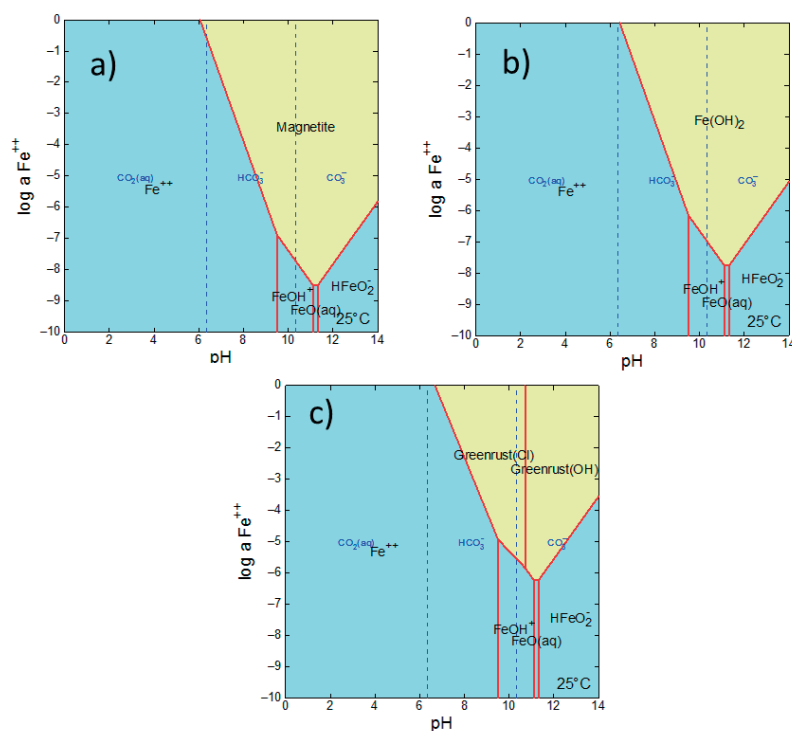

Figure 5-2: Solubility diagrams for iron with Na^+ and Cl^- activities as in reference 'brackish/saline' groundwater (Auqué et al., 2013) groundwater, log f $O_2(g)$ = -83 (0.1 log units above $H_2(g)$-$H_2O(l)$ equilibrium) , log f $CO_2(g)$ = -13 (cement equilibration). (a): magnetite as main iron mineral; (b) magnetite (Fe_3O_4) suppressed; (c): $Fe(OH)_2$ suppressed. All activity diagrams were generated using the 'Act2' module of Geochemist's Workbench (Bethke, 2008) and thermmodem database (BRGM, 2017), unless stated otherwise. Greenrust(Cl) and greenrust(OH) have the compositions $Fe_4(OH)_8Cl$ and $Fe_3O_2(OH)_4$, respectively.

The diagrams show that magnetite is the most stable compound in the system Fe(II)-Fe(III)-H-Cl-O, followed by metastable $Fe(OH)_2$, then Cl or OH-green rust. The solubility of the solids varies in similar trends depending on pH, which reflects the dominant predicted dissolved Fe species. The diagrams all show the tendency for minimum Fe^{2+} activities at pH ~11, with values being broadly similar at pH 10 and pH 12 to 12.5. Therefore, the solubility of steel corrosion products is unlikely to become enhanced until pH is <10, with a sharp increase occurring between pH 8 and 6. Interestingly, the equilibration of pure water with $Fe(OH)_2$ results in a pH of 9.08 calculated using the thermoddem, version 1.01, database and PHREEQC; and a pH of 9.46 calculated using 'llnl.dat'. The 'llnl.dat' database uses the same parent thermodynamic data as the default Geochemist's Workbench database 'thermo.com.v8.r6+'. A solubility diagram showing magnetite calculated using these data is compared to that given using the thermoddem, version 1.01, database in Figure 5-3. There are some differences in the identity of iron species at high pH, but the overall trends in Fe^{2+} activity as a function of pH are similar.
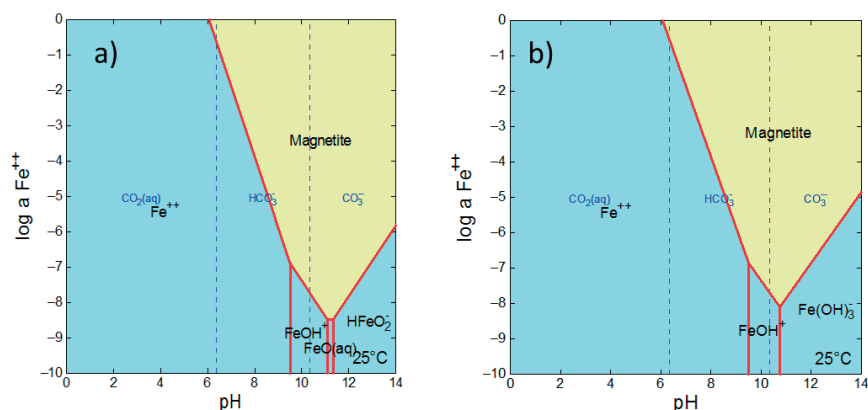
Figure 5-3: Solubility diagrams for iron with Na$^+$ and Cl$^-$ activities as in 'brackish/saline' groundwater, log f O$_{2(g)}$ = -83 (0.1 log units above H$_{2(g)}$-H$_2$O$_{(l)}$ equilibrium) , log f CO$_{2(g)}$ = -13 (cement-equilibrated). (a) thermoddem, version 1.01, database; (b) thermo.com.v8.r6+ database.

In a system where sulphide is present (assuming sulphate present in cement porewater can be reduced, a process which tends to be kinetically inhibited) and equilibrium with pyrite (FeS$_2$), Fe$_{11}$S$_{12}$ is predicted to buffer dissolved Fe^{2+} activities to very low values (<10-7.5 at pH > 8; Figure 5-4). Siderite (FeCO$_3$) is only likely to form as a steel corrosion product where there is significant dissolved carbonate and pH ~6 – 9 (Figure 5-5) i.e. there has been significant leaching and carbonation of the cement.

Figure 5-4: Solubility diagram for iron with Na$^+$ and Cl$^-$ activities as in 'brackish/saline' groundwater and sulphate buffered by pyrite (log f O$_{2(g)}$ = -83, i.e. 0.1 log units above H$_{2(g)}$-H$_2$O$_{(l)}$ equilibrium), log f CO$_{2(g)}$ = -13 (cement-equilibrated).
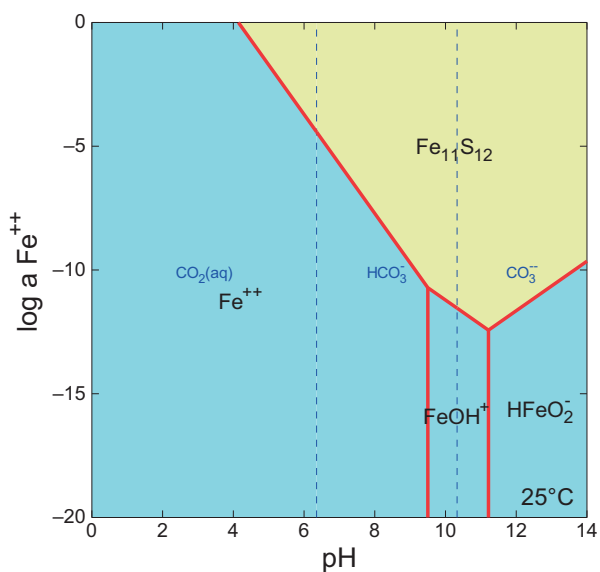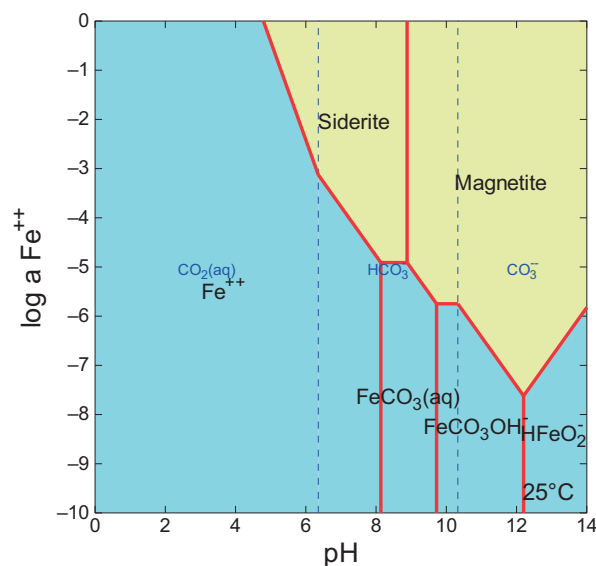
Figure 5-5: Solubility diagram for iron with Na+ and Cl- activities as in 'brackish/saline' groundwater with sulphate buffered by pyrite (log f O_2(g) = -83, i.e. 0.1 log units above H_2(g)-H_2O(l) equilibrium), log f CO_2(g) = -3.5 (atmospheric).

As previously noted, very little work appears to have been carried on the potential for Fe(II) substitution into cement, especially the incorporation of Fe(II) into C-S-H gel. However, some indication of the potential effect of Fe(II) substitution into portlandite can be ascertained by assuming that $Fe(OH)_2$ and $Ca(OH)_2$ form an ideal solid-solution. Reaction between an ideal solid-solution comprising 1 mole of $(Ca,Fe)(OH)_2$ and 1 litre of pure water may be simulated using PHREEQC with different initial proportions of Ca and Fe(II) end members to determine resulting pH and solute concentrations/activities. The results of such calculations are given in Table 5-1. For a solid solution comprising mole fractions (X) of 0.5 of for both end-members results in the equilibrium pH being ~0.1 units less than that of pure portlandite. With $XCa(OH)_2$ = 0.1 and $XFe(OH)_2$ = 0.9, a pH of 12.09 is calculated, and if only 1% of the solid solution is comprised of the Ca end-member, the calculated pH is 11.7. This value is substantially higher than the value of 9.08 that is obtained by equilibration of pure water with pure $Fe(OH)_2$. Therefore, even assuming significant replacement of Ca with Fe(II) in a theoretical ideal solid-solution, the equilibrium pH is affected to only a small degree (reflecting the greater aqueous solubility of $Ca(OH)_2$ compared to $Fe(OH)_2$).

Table 5-1: pH and total dissolved Fe and Ca concentrations calculated for pure water equilibrated with 1 mol/kg of an ideal solid solution with different mol fractions (X) of $Ca(OH)_2$ and $Fe(OH)_2$ end members.

Initial X $Ca(OH)_2$	Initial X $Fe(OH)_2$	pH	Total Ca (mol/kg)	Total Fe (mol/kg)	Final $Ca(OH)_{2(s)}$ (mol/L)	Final $Fe(OH)_{2(s)}$ (mol/L)
0.5	0.5	12.36	1.49E-02	1.70E-07	0.485	0.5
0.25	0.75	12.24	1.11E-02	1.95E-07	0.24	0.75
0.1	0.9	12.09	7.58E-03	1.70E-07	0.092	0.9
0.05	0.95	11.98	5.67E-03	1.43E-07	0.044	0.95
0.01	0.99	11.7	2.83E-03	9.29E-08	0.0072	0.99

In addition to considering the release of Fe(II) from classic steel corrosion products, the stability of known Fe-rich cement solids and minerals can be considered using activity diagrams, as in Figure 5-6. The diagrams show that the Fe(III)-bearing solids C_4FH_{13} ($Ca_4Fe_2O_7$ $13H_2O$) and C_3FH_6 ($Ca_3Fe_2(OH)_{12}$) appear with very low fO_2 values (close to $H_2(g)$-$H_2O(l)$ equilibrium). However, these solids only occur under very high values of log a Fe^{2+}/ a $(H^+)^2$ activity, noting that $Fe(OH)_2$ equilibrium corresponds to a value of 12.9 log units. Fe(II)-bearing saponite (a smectite clay mineral with composition $Ca_{0.17}Mg_2FeAl_{0.34}Si_{3.66}O_{10}(OH)_2$) occurs under similarly high ratios, but at higher dissolved silica activities (as would be expected, see Wilson et al., 2015). Note that other Fe(III)-bearing cement minerals included in the thermoddem, version 1.01, database are Fe-monosulfate ($Ca_4Fe_2SO_{10}12H_2O$) and Fe-ettringite ($Ca_6Fe_2(SO_4)_3(OH)_{12}26H_2O$).

Figure 5-6: Activity diagram showing stability of cement solids and silicate minerals as a function of log a $Fe^{2+}/(H^+)^2$ and a $H_4SiO_4(aq)$. Ca^{2+} is buffered by Portlandite, Al^{3+} is buffered C_3AH_6, Mg^{2+} is buffered by hydrotalcite, SO_4^{2-} is buffered by ettringite. Na and Cl activities are as in reference SFR 'brackish/saline' groundwater (Auqué et al., 2013). (a) log f $O_2(g)$ = -83 bar (near to $H_2(g)$-$H_2O(l)$ equilibrium; (b) log f $O_2(g)$ = -72.77 bar (magnetite-hematite, i.e. Fe_3O_4-Fe_2O_3, equilibrium). Vermiculite is a layer silicate mineral ('SO' composition is $Ca_{0.445}(Si_{2.778}Al_{1.222})(Al_{0.216}Mg_{2.475}Fe_{0.254})O_{10}(OH)_2$; 'Ca' composition is $Ca_{0.43}Mg_{3.00}Si_{3.14}Al_{0.86}O_{10}(OH)_2$.

If Fe-ettringite is assumed to buffer SO_4^{2-}, then C_4FH_{13} and C_3FH_6 are replaced with Fe-monosulphate (Figure 5-7).
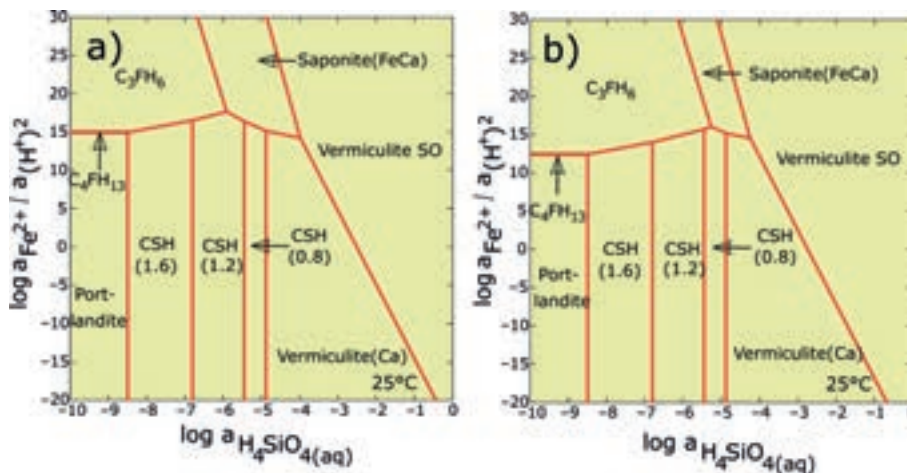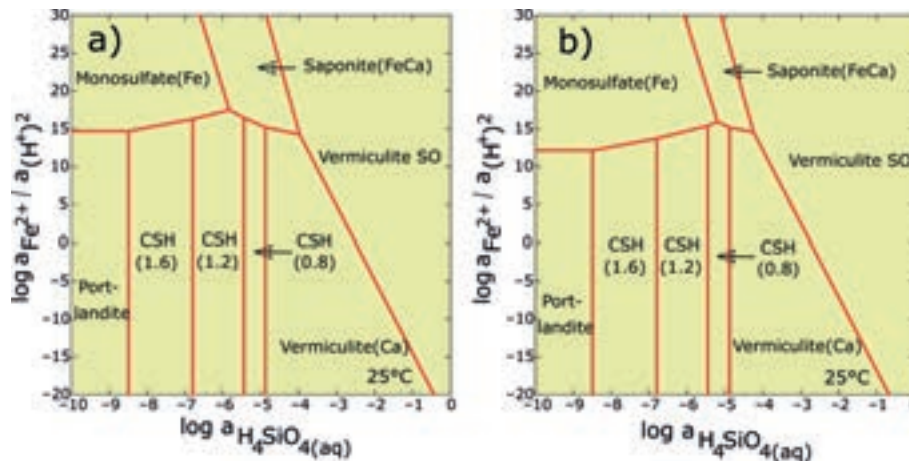
Figure 5-7: Activity diagram showing stability of cement solids and silicate minerals as a function of log a $Fe^{2+}/(H^+)^2$ and a $H_4SiO_4(aq)$. Ca^{2+} is buffered by Portlandite, Al^{3+} is buffered C_3AH_6, Mg^{2+} is buffered by hydrotalcite, SO_4^{2-} is buffered by Fe-ettringite, Na and Cl activity as in reference SFR 'brackish/saline' groundwater (Auqué et al., 2013). (a) log f $O_2(g)$ = -83 bar (near to $H_2(g)$-$H_2O(l)$ equilibrium; (b) log f $O_2(g)$ = -72.77 bar (magnetite-hematite, i.e. Fe_3O_4-Fe_2O_3, equilibrium).

In addition to considering the stability of different iron-rich solids that may form as steel corrodes in the presence of cement using activity diagrams, two simple titration models were developed using the 'React' module of Geochemist's Workbench (Bethke, 2008). In Model 1, the following mineral buffers were specified: portlandite (Ca^{2+}), hydrotalcite (Mg^{2+}), magnetite (Fe^{2+}), C_3AH_6 (Al^{3+}), with a water containing 0.065 molal Na^+, 0.0978 molal Cl^- with redox specified by setting log f $O_2(g)$ at -83 bar. The initial concentration of dissolved Fe^{2+} was set at 1e-12 mol/L. The number of moles of solids present were assumed to be the same as those in the cement composition by Cronstrand (2014), given a total porosity of 30% and the presence of 1 kg of water. Into this, FeO(aq) was titrated in a series of 100 steps until the number of moles added was twice that of portlandite. Sulphate was excluded to simply the model. Several minerals were excluded as potential secondary minerals, especially aluminosilicates that tend to form under high T/P conditions (such as those associated with metamorphic or igneous rocks). Crystalline CSH minerals were also excluded, as were magnetite and Fe(III)(hydr)oxides to maximise the potential dissolved Fe concentrations that could evolve as $Fe(OH)_2$ precipitated. The models show that as FeO(aq) was titrated into the system (with distribution of Fe between different solid and liquid species being determine by apparent thermodynamic equilibrium), $Fe(OH)_2$ precipitated (Figure 5-8), such as that very early in the titration the dissolved Fe^{2+} concentration increased to 1.2e-7 molal (Figure 5-9). The continued precipitation of $Fe(OH)_2$ was associated with a reduction in the mass of water present (Figure 5-8) and a small reduction in pH (Figure 5-9).

Figure 5-8: Graphs showing mass of water (a) and moles of minerals (b) calculated in Fe titration model 1.

Figure 5-9: Graphs showing concentrations of solutes (a) and pH (b) calculated in Fe titration model 1.

In the second titration model, an illustrative 'significantly degraded' cement was simulated, by specifying CSH (0.8) ($Ca_{0.8}SiO_{2.8} \cdot 1.54H_2O$) buffering the initial Ca^{2+} concentration, with amorphous silica buffering H_4SiO_4(aq) and gismondine buffering Al^{3+}. In this model iron-rich silicates were excluded along with silica polymorphs and Mg-bearing minerals. The initial amounts of C-S-H, and amorphous silica were set at 10 moles (assuming loss of portlandite and depletion in Ca/Si ratio in C-S-H) and the initial amount of gismondine (included as a representative aluminosilicate) was set at 1 mole. In this model, heulandite and Na-phillipsite were found to be more stable than gismondine, $Fe(OH)_2$ precipitated (Figure 5-10), with negligible effect on pH (Figure 5-11), other than that occurring due to loss of water as $Fe(OH)_2$ formed. In this model, the low Ca/Si C-S-H and amorphous silica resulted in an initial pH of 9.75. As in Model 1, the concentration of Fe^{2+} rapidly increased (but to a higher value of 1e-6 molal) with negligible effect on pH, other than pH decreasing as the mass of water decreased (Figure 5-10 and Figure 5-11).
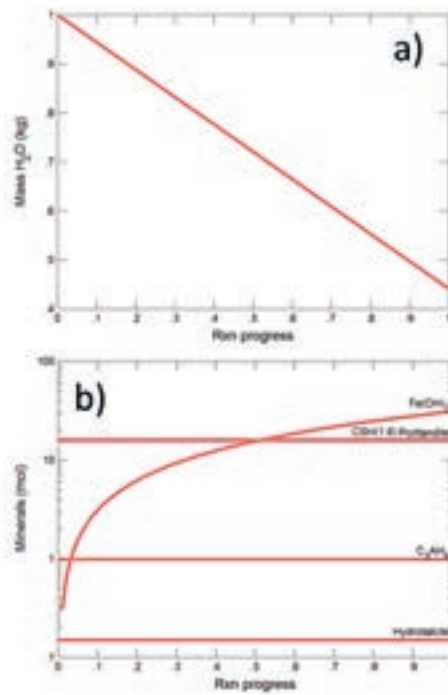

Figure 5-10: Graphs showing mas of water (a) and moles of minerals (b) calculated in Fe titration model 2.

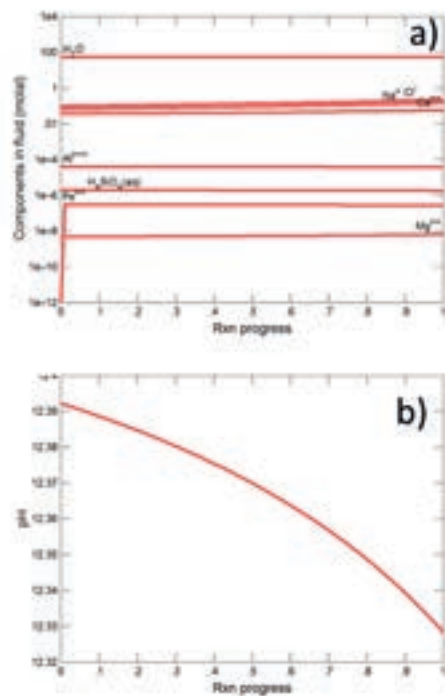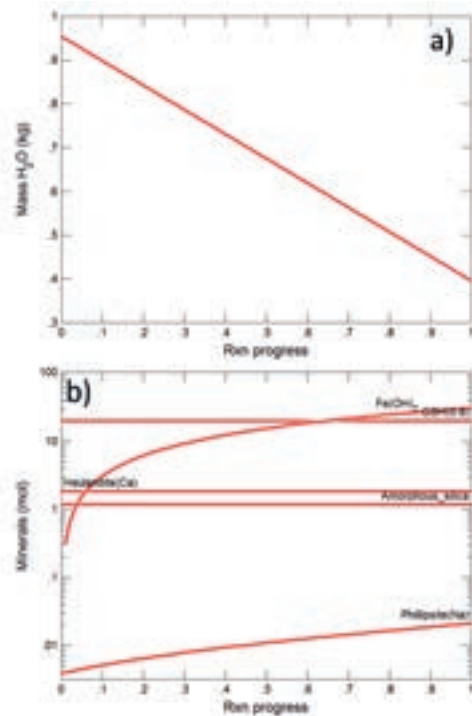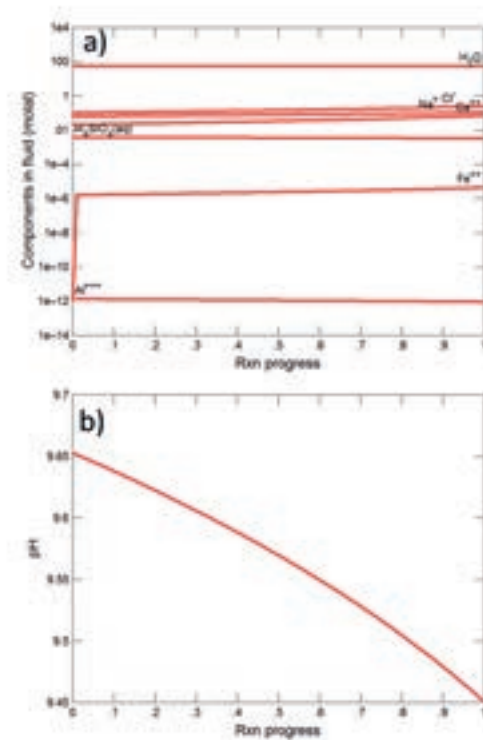**Figure 5-11:** Graphs showing concentrations of solutes and pH calculated in Fe titration model 2.

5.6. Summary

Under anaerobic conditions, steel corrosion is likely to result in the formation of metastable $Fe(OH)_2$ or green rust which can convert to magnetite. Relatively high carbonate activities are required, i.e. $f\,CO_2(g)$ conditions lower than those associated with cement in order to form green rust. In the presence of silicate minerals, iron(II)-rich clay minerals can form, but this is generally observed in iron-bentonite systems, in which cement is not included. Fe(II)-sulphides may also form, if sulphate reduction can occur.

There is little information on Fe(II) in cement, where Fe is mostly present as Fe(III) which can substitute for Al^{3+}. There is a very limited amount of evidence, but it appears as if $Fe(OH)_2$ can be present. Steel corrosion products such as magnetite, $Fe(OH)_2$ and green rust have similar solubilities (in terms of order of magnitude) at pH values of ~10 and ~12.5, with minimum values tending to occur at pH ~11. The solubility of such solids is only likely to significantly increase once C-S-H gel is lost from the cement and pH is buffered by calcite (i.e. the cement is severely degraded).

The formation of $Mg(OH)_2$ due to the replacement of Ca^{2+} in cement by Mg^{2+} from groundwater will tend to result in cement porewater pH values of ~10. Therefore, in addition to steel corrosion rates being very low under hyperalkaline conditions associated with cement, the solubilities of iron-rich corrosion products are also very low, with thermodynamic modelling suggesting maximum dissolved Fe(II) concentrations of ~10^{-7} molal under anaerobic conditions, whilst dissolved Ca concentrations tend to be ~10^{-2} molal. Therefore, the concentrations of dissolved Ca

are likely to remain several orders of magnitude greater than Fe(II) species, even assuming that corrosion is not kinetically inhibited.

$Ca(OH)_2$ is much more soluble than $Fe(OH)_2$, a theoretical ideal solid-solution model including these two solid phases as end-members suggests that a very large amount of replacement of Ca by Fe(II) would be required for any significant effect on pH, assuming the solubility of such a solid solution was the main control on pore water pH. Therefore, substitution of Ca by Fe(II) is unlikely to result in pH decrease, even if Fe(II) is available to take part in reactions. Titration calculations also suggest that the addition of Fe(II) to cement-water systems results in equilibrium solubility of $Fe(OH)_2$ being rapidly attained, with negligible effect on pH.

Thermodynamic modelling suggests that Fe(III) solids such as C_4FH_{13} and C_3FH_6 could potentially be stable even under very low f $O_2(g)$ conditions (approaching the lower limit of water stability), but that the corresponding log a $Fe^{2+}/(aH^+)^2$ required for this is greater than that associated with $Fe(OH)_2$ equilibrium. Overall, it seems unlikely that Fe(III)-rich cement solids would form due to release of Fe from corrosion.

Overall, although there is a lack of data on Fe(II) behaviour in cement, thermodynamic modelling suggests that there is little potential for Fe(II) to replace Ca in cement to any significant extent such that hyperalkaline conditions are suppressed.

6. K$_d$ values and representation of retardation in the SR-PSU assessment

6.1. Issues investigated

The SR-PSU assessment considered the following transport- and retardation-related processes in the geosphere (SKB, 2015a,b):

- radioactive decay and ingrowth;
- advection;
- dispersion;
- rock matrix diffusion; and
- sorption.

Decay rates and ingrowth rates were specified to be proportional to each radionuclide's inventory or to the parent radionuclide's inventory, respectively. The model was parameterised by appropriate decay constants and branching ratios.

Advective fluxes of radionuclides were determined using the calculated groundwater fluxes in fractures, which were derived from hydrogeological data obtained from the site (Odén et al., 2014). For each flowpath, a Peclet number (dimensionless) that represents the ratio between advective and dispersive transport was specified. This parameter enabled dispersion due to groundwater velocity variations to be specified.

Rock matrix diffusion was modelled using Fick's laws. The effective diffusivity of each radionuclide was estimated from the geometric formation factor and the diffusivity of the radionuclide water at infinite dilution.

SKB assume that diffusing radionuclides can access all the rock between water-conducting fractures. That is, the maximum matrix penetration depth of a radionuclide from any fracture is equal to half the spacing between fractures. Fracture frequencies range from 0.02 m^{-1} to 0.36 m^{-1} (SKB, 2015a). SKB used this latter value to conservatively estimate a penetration depth of 1.4 m (i.e. the smallest maximum penetration depth consistent with the fracture spacing). Over this distance, all the pores in the rock's matrix were assumed to be interconnected.

SKB represent sorption by the common K$_d$ approach:

$$K_d = \frac{S}{C} \qquad\qquad (6\text{-}1)$$

where: K$_d$ is a sorption coefficient (m^3/kg), S is the concentration of the element sorbed on the sorbate of interest in mol / kg; and C is the aqueous concentration of the sorbate in mol / m^3.

Element-specific K$_d$ values were used to model sorption in the rock matrix. As in the SR-Site assessment the model included only sorption in the rock matrix. Again, SKB considered that omitting sorption on fracture filling and lining minerals is conservative.

Two key questions arise:

- Has SKB sufficiently justified the use of K_d data obtained for the SR-Site assessment in the SR-PSU assessment, given that there are differences between chemical conditions at depth at the site of the proposed KBS-3 repository and in the environs of the SFR?
- Is it truly conservative to neglect sorption on fracture filling / lining minerals (taking into account that sorption on such minerals would tend to minimise radionuclides involving rock matrix diffusion)?

6.2. Previous reviews of retardation

6.2.1. Previous reviews of rock matrix diffusion

Haggerty (2012) has previously reviewed SKB's treatment of rock matrix diffusion in the SR-Site assessment for the SF repository at Forsmark. He concluded SKB's research into rock matrix diffusion to be of generally excellent quality and based on a sound understanding of the fundamental rock matrix diffusion process. He also considered SKB's use of mean values for parameters used to represent rock matrix diffusion in the SR-Site assessment to be justified. These mean values are based on thousands of measurements made by SKB. However, two important findings of Haggerty (2012) are:

- '*SKB has not conclusively demonstrated that the penetration depth is large (meters). The largest distance over which diffusion has been directly measured in situ is 0.40 m (Birgersson and Neretnieks, 1990) at the Stripa mine. For Forsmark, the largest distance is 0.05 m, in lab samples (destressed). There is indication from through electromigration (TEM) and electrical resistivity measurements that diffusion can penetrate further. However, these measurements are indirect.*'
- '*In general, I believe that SKB has not sufficiently characterised the effects of fracture coatings and heterogeneity on transport at Forsmark. Crawford et al. (2008) indicates that the effects of variability in diffusivity and sorption properties within the fracture coatings are probably not important for safety assessment. However, results in the same report suggest that early breakthrough could be significantly affected by changes in the materials property group (diffusivity and sorption).*'

Nevertheless, Haggerty (2012) was of the opinion that these limitations would not adversely affect the outcomes of the safety assessment.

6.2.2. Previous reviews of sorption

Details of the processes that may affect sorption are found in previous reviews (Randall, 2012; Bertetti, 2014) and in supporting documents for the SR-PSU safety analysis (Crawford, 2010, 2013; SKB, 2014f,g,b).

On behalf of SSM, Bertetti (2016) has previously reviewed handling of K_d-values used in radionuclide transport calculations in the safety assessment SR-PSU. The

main focus of this review was sorption in the near-field, although it also gave some consideration to far-field sorption.

The review of Bertetti (2016):

1. covered the experimental justification and theoretical understanding underpinning the selection and justification of K_d values;
2. identified those radionuclides for which it is most important to determine K_d values, and assessed the validity of these K_d values obtained by SKB;
3. considered the treatment of uncertainties in K_d values by SKB, and related sensitivity analyses carried out by SKB.

In the SR-PSU assessment, SKB used very similar approaches to define K_d value ranges for near- and far-field sorption to those approaches that have been applied commonly in other assessments. The K_d value ranges and methods used to define them are almost identical to those in the earlier SFR 1 and SR-Site performance assessments (SKB, 2010b, 2014f,b; Ochs and Talerico, 2004).

Bertetti (2016) considered the approach used by SKB to adjust laboratory K_d measurements to in-situ values is reasonable. This approach, which is reported in Ochs and Talerico (2004) and Crawford (2010, 2013) involves correcting for the perturbations to the conditions of rock samples that occur between their undisturbed in-situ states and their analyses in the laboratory. Specifically, 'transfer factors' are applied to correct for:

- changes in accessible surface area;
- mechanical damage;
- changes in cation exchange capacity; and
- groundwater chemical variations.

Bertetti (2016) judged that although there are often large uncertainties, generally acceptable methods were employed to derive the K_d values used in the assessment. In his opinion, SKB's expected geochemical conditions in the near- and far-field of the SFR are defensible. He concluded that the far-field K_d values are appropriately biased towards low values because of the applied surface area corrections.

6.3. Retardation in SR-PSU

6.3.1. Sources of transport and retardation parameter values

The effective matrix diffusivities used in the SR-PSU assessment are given in SKB, (2014g). The values were recommended by Löfgren (2014)[1], based on formation factor logging *in situ* by electrical methods in boreholes KFR102B and KFR105. However, additionally, for the SR-PSU, diffusivities were estimated from in-situ

---

[1] According to page 71 of SKB (2014g) the data were taken from Löfgren and Sidborn (2010), SKB report R-09-31. However, this report concerns statistical analysis of results from fracture mapping. It is therefore concluded that the reference is erroneous and that Löfgren (2014), which recommends diffusivities for the SR-PSU is the correct one.

formation factors measured on rock around boreholes KFR105 and KFR102B. These data extended to the near-surface, unlike the diffusivities obtained for the SR-Site assessment.

Löfgren (2014) notes that compared to the host rock for the planned SF repository at Forsmark, average formation factors are four to five times larger at the SFR site. He attributed the difference to the shallower depth of the SFR, which results in less stress being exerted by overburden, such that pore space tends to be better connected than at greater depth.

No porosity measurements were made on rock from the SFR site. Therefore, the rock porosity measurements provided for SR-Site, based on the Forsmark site investigations, were used (SKB 2010b).

The K_d data used in the SR-PSU assessment were based on those used for the SR-Site assessment (Crawford, 2010; Crawford, 2013). This approach is justified by SKB by stating that the rock surrounding the SFR is geochemically similar to the geosphere around the proposed SF repository (SKB, 2014f).

To adjust laboratory measurements of K_d to in-situ values, the SR-PSU assessment used the same 'transfer factors' as for the SR-Site assessment, except for the chemical transfer factor f_{chem}:

$$f_{chem} = \frac{K_{d(calc)}}{K^0_{d(calc)}} \qquad (6\text{-}2)$$

where: $K_{d(calc)}$ is the K_d calculated for in-situ conditions, and $K^0_{d(calc)}$ is the K_d calculated for reference (laboratory) conditions.

Different f_{chem} values were specified in the SR-PSU assessment because the groundwater chemistry around the SFR repository is different to that in the deeper proposed SF repository site. Specifically, compared to the region immediately around the proposed SF repository, at the SFR:

- The groundwater is less saline.
- There is a higher component of meteoric water.
- The groundwater has a lower concentration of Ca, higher Na/Ca and a higher carbonate concentration.

The values of f_{chem} chosen by SKB to derive K_d values for use in the SR-PSU therefore take account of:

- The expected enhanced sorption of cation-exchanging solutes compared to near the proposed SF repository.
- The expected decreased sorption of cations that form surface complexes and complexes with dissolved carbonate, compared to near the proposed SF repository.

For the radionuclide transport calculations done as part of the SR-PSU assessment, rock matrix K_d values were selected from log-normal distributions (SKB, 2014f). For the main scenario, which represents the most likely changes in the repository and its environment, this selection was made as follows (Crawford, 2013):

- The lowest K_d value was selected for each element for the whole assessment period, for each of three groundwater types, except for radionuclides that show pH-sensitive and redox-sensitive speciation. The three groundwater types for which pdfs were specified are:
  - temperate saline/brackish water;
  - early temperate/periglacial water; and
  - late temperate/periglacial water.
- For Np(IV), Pu(III/IV), Sn(IV) and U(IV) K_d values for environments with pH < 10 were then selected.
- For radionuclides that show redox-dependent sorption (e.g. Np(IV) and Tc(IV)), Kd values for reducing conditions were used in the main scenario, because conditions are expected to remain reducing.
- Po-210 was assigned the same K_d as its parent Pb-210.

K_d values specified for groundwater during glacial conditions were not used. Instead, calculations of radionuclide transport during glacial periods transported radionuclides directly from the near-field to the biosphere.

6.3.2. Transport and retardation in scenarios

The importance of transport and retardation were investigated via analysis of several scenarios (SKB, 2014a,g):

- the 'main scenario', which represents the most probable evolution of external conditions, and realistic, or justifiable pessimistic assumptions with respect to the internal conditions;
- a set of 'less probable' scenarios, each of which represents the failure of a safety function; and
- a set of 'residual' scenarios, chosen to illustrate the significance of individual barrier functions, exposure due to human intrusion or consequences of an unsealed repository, and consequences of external conditions within the range defined by the SR-PSU climate scenario, but not considered by the main scenario.

In all these scenarios except one, retardation by sorption in the rock matrix (following rock matrix diffusion) is included. The exception is the residual scenario 'Loss of barrier function – no sorption in bedrock', in which K_d values in the rock matrix are set to zero. In other respects, this scenario is identical to a global warming variant of the main scenario (the base case).

Comparison between analyses of the 'Loss of barrier function – no sorption in bedrock' scenario (calculation case CCR_B2) and the other scenarios reveal that far-field sorption influences doses in the biosphere to a much smaller extent than near-field sorption. The peak dose calculated in by CCR_B2 is 10.4 µSv, slightly higher than the estimate for the global warming variant of the main scenario, which is 8.2 µSv, but still below the risk criterion of 14 µSv. The peak dose occurs 400 years earlier than in the global warming calculation case.

In CCR_B2, U-235 and U-238 are relatively high contributors to doses. The cause is mainly releases from the1BLA vault, which contains LLW in ISO containers and is not concrete lined or backfilled. The geosphere is therefore clearly relatively important for a waste vault lacking engineered barriers.

SKB also investigated the significance of a loss of barrier function in the repository, in a scenario entitled 'Loss of barrier function – no sorption in the repository'. This scenario was analysed in calculation case CCR_B1. In this case, K_d values in the repository are set to zero, but all other parameter values were kept the same as those in the global warming variant of the main scenario. That is, in CCR_B1 sorption is allowed to occur in the bedrock.

In CCR_B1, the peak dose was calculated to be 41.4 μSv, which is greater than the peak dose for the global warming calculation case by a factor of about 5. In CCR_B1, the peak dose also occurs almost 20,000 years later than in the main scenario. Thus, sorption in the rock matrix would not be sufficient to compensate for a loss of sorption in the repository.

SKB used the Ecolego compartment modelling software to undertake the radionuclide transport calculations. In this modelling, rock matrix diffusion was simulated by specifying a series of 20 rock matrix compartments adjacent to each of 20 flowing fracture compartments. Thus, there are 420 compartments in total. The widths of the matrix compartments increase with increasing distance from the fracture. The first matrix compartment (the one closest to the compartment) has a width of 0.0001 m. The width of each subsequent matrix compartment is then 1.5667 times greater than the width of the previous matrix compartment, which is closer to the fracture. By applying this factor the total width of the 20 compartments is 1.4 m.

The compartment representation used in the assessment is illustrated in Figure 6-1.
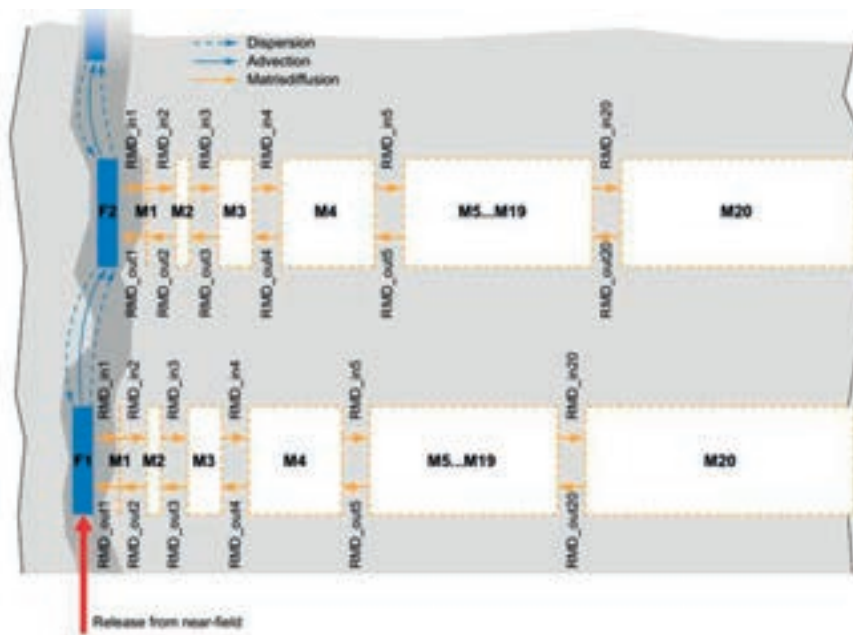
Figure 6-1: Schematic illustration of the geosphere model showing compartments representing a fracture (blue boxes, F) and confining rock matrix (white, M). Advective transport between the fracture compartments and diffusive transport from these compartments into the matrix is represented. Solid blue arrows represent advective transport, dashed blue arrows represent dispersion, and yellow arrows represent diffusion (after SKB, 2015b).

In this model, diffusion cannot occur in the rock matrix parallel to the fracture.

In the SR-PSU assessment SKB considered that presently-observed groundwater chemistry profiles at the SFR and in nearby inland areas represent the hydrochemical profiles likely to exist in future. These observed profiles were used to predict a series of groundwater compositional ranges for the different time intervals in the reference glacial cycle of the safety assessment.

6.4. Implications for safety

The main safety assessment report for the SR-PSU (SKB, 2015b) states that (Section S2.1, Safety Principles, on page 14):

'*Retention of radionuclides is achieved by the performance of the engineered barriers and the repository environs. The properties of the wastes, together with the properties of the waste containers and of the engineered barriers in the waste vaults, contribute to safety by providing low water flow and a suitable chemical environment to reduce the mobility of the radionuclides. The host rock provides stable chemical and physical conditions and favourable low groundwater flow conditions.*'.

The main safety function of the geosphere that influences retention is stated to be low groundwater flow in the bedrock (SKB (2015b), page 18, Section 5). Thus, the retention properties of the geosphere are considered by SKB to be of secondary importance. The results of the calculation cases presented by SKB (SKB, 2015a,b) are consistent with this conclusion. They imply that uncertainties in sorption in the geosphere do not call into question the safety of the facility. In the opinion of the review, this conclusion is justified.

However, SKB's analysis of the bedrock's barrier function considers only uncertainties in sorption, by comparing case CCR_B2, which neglects sorption in the rock matrix, with other calculation cases, which include such sorption. Within the set of analysed scenarios, there is apparently no consideration of the impact of uncertainties in rock matrix diffusion. Presumably in case CCR_B2, the absence of sorption causes diffusing radionuclides to penetrate more rapidly and / or to greater depth within the rock matrix than in the other scenarios. The retardation provided by rock matrix diffusion is therefore enhanced in CCR_B2 compared to the other scenarios in which sorption in the matrix occurs. This raises the question as to the relative importance of rock matrix diffusion and sorption in the rock matrix as retardation mechanism. Specific questions are:

- If rock matrix diffusion and sorption are both neglected, then would the dose criterion be exceeded?
- If the answer is yes, then how much would rock matrix diffusion need to be diminished from that attained in the main scenario, for the dose criterion to be exceeded?

None of the reviewed documents provide details of the matrix diffusion depth attained in any of the scenarios, or of the rate of radionuclide uptake by this mechanism. It therefore cannot be judged how important this effect may be. It would be helpful for SKB to present additional cases in which rock matrix diffusion is diminished in order to answer these questions.

6.5. Summary

In the SR-PSU assessment, retardation of migrating radionuclides occurs by:

- Rock matrix diffusion, modelled using Fick's laws; and
- Sorption, modelled using equilibrium distribution coefficients, K_d.

SKB assume that diffusing radionuclides can access all the rock between water-conducting fractures.

The K_d data used in the SR-PSU assessment were based on those used for the SR-Site assessment. However, an adjustment was made to the SR-site data to allow for the different groundwater chemistry in the host rock of the proposed SF repository and in the host rock of the SFR.

Diffusivities were estimated from *in-situ* formation factors of the rock around boreholes KFR105 and KFR102B at the location of the SFR, as determined by electrical methods.

Rock porosity measurements used in the SR-PSU assessment were the same as used in the SR-Site assessment.

From the perspective of safety, SKB consider the retention properties of the geosphere to be of secondary importance compared to low groundwater flow in the bedrock. They imply that uncertainties in sorption in the geosphere do not call into question the safety of the facility. This conclusion seems justified.

However, there are uncertainties concerning the relative importance of rock matrix diffusion and sorption in the rock matrix as retardation mechanism. It is unclear whether the dose criterion would be exceeded if rock matrix diffusion and sorption are both neglected. If the dose criterion could be exceeded in this case, then it would be instructive to determine whether diminishing matrix diffusion on its own could cause the dose criterion to be exceeded. It would be helpful for SKB to present additional cases in which rock matrix diffusion is diminished in order to answer these questions.

7. Summary and conclusions

The following issues were reviewed:

- the potential for fracture armouring in concrete components of the SFR's engineered barrier system (EBS), by secondary minerals produced as inflowing groundwater interacts with porewater in the cementitious concrete matrix;
- the potential for Ca-bearing minerals in cement within the EBS to be replaced by Fe(II)-bearing minerals, with consequent implications for the cement's chemical buffering capability and longevity; and
- conservatism in the radionuclide retardation model in the SR-PSU assessment, accounting for the fact that retardation involves a combination of sorption and rock matrix diffusion.

Were it to occur along fractures in concrete that remain pathways for groundwater flow, potentially armouring could cause relatively low-pH water to contact the wastes. Consequently, corrosion of metallic barrier system components might not be passivated to the extent expected by SKB and certain radionuclides might be more soluble in the groundwater than SKB anticipate. Each of these processes might cause a higher flux of radionuclides from the SFR than assessed in the SR-PSU.

Several coupled models were developed to investigate the effects of armouring. Groundwater inflow to a vault, via a fracture in a concrete wall, was simulated for different assumed conditions. The simulations all revealed a tendency for the fracture to self-seal by the precipitation of Mg-rich secondary minerals.

If brucite ($Mg(OH)_2$) were to precipitate in the backfill, 'upstream' of the cement, it would remove some of the Mg from the groundwater entering fractures in the concrete. Such Mg removal could potentially reduce the expected amount of fracture clogging, brucite being a major predicted clogging phase. However, the modelling demonstrates that even in this case carbonate minerals such as calcite, and secondary aluminosilicates, are still likely to precipitated and clog the fracture

The extent to which groundwater pH is buffered by the cement in the walls of a fracture depends upon the degree to which newly precipitated minerals fill the fracture, and the diffusivity of the armouring layer. The model results show that the thinner an armouring layer and the smaller its diffusivity compared to that of the cement matrix, the further along the fracture will relatively low-pH water penetrate. The smaller thickness maintains a significant advective contribution to transport, while the smaller diffusivity is required to limit buffering of fracture upstream porewaters by cement interactions. The greatest pH perturbation from values in the cement matrix is given by model variant cases (Variants 2 and 4), in which the relative diffusivity of the armouring layer is relatively small (10^{-3}), and the fracture is assumed to be continuously open (the fracture porosity is limited to 0.1). In these cases, pore waters with pH ~11 could potentially enter the vault. However, the decreased pH at downstream locations only reduces to c.10.8 after 10,000 years.

The modelling suggests that there would be no significant safety-relevant impacts on the chemical buffering capability of the cement in the SFR vaults over the assessment time frame considered here of 10,000 years.

In the SR-PSU, SKB has apparently given no consideration to the possibility that Fe may combine with solid phases present in cementitious barriers, thereby potentially

altering the chemical buffering capability of these barriers and their longevity. To explore the potential for Fe(II) release from iron/steel corrosion to result in decreasing pH in cement pore fluids, the following tasks were undertaken:

- steel corrosion processes were reviewed;
- iron compounds associated with cement were reviewed; and
- thermodynamic modelling was undertaken.

Overall, although there is a lack of data on Fe(II) behaviour in cement, thermodynamic modelling suggests that there is little potential for Fe(II) to replace Ca in cement to any significant extent, such that hyperalkaline conditions are suppressed.

SKB has modelled retardation of radionuclides in the geosphere by a combination of:

- rock matrix diffusion; and
- sorption on minerals within the rock matrix, which contact the radionuclides because of rock matrix diffusion.

SKB use linear distribution coefficients (K_d values) to represent sorption. The K_d values used are based on the data acquired by SKB to support its SR-Site safety assessment for the proposed Spent Fuel (SF) repository at nearby Forsmark. In the SR-Site assessment 'transfer factors' were used by SKB to adjust laboratory sorption data to in-situ conditions. A similar approach was used for the SR-PSU assessment. SKB assumed that all the transfer factors used in the SR-Site assessment, except for the chemical transfer factor, f_{chem}, are also valid for the sub-surface conditions around the SFR. However, SKB specified different f_{chem} values because the groundwater chemistry around the SFR repository is different to that in the deeper proposed SF repository site.

The K_d approach does not accurately represent actual sorption mechanisms and uncertainties associated with applying the approach are large. However, for the far-field, SKB's analysis provides confidence that the limitations of the K_d approach does not have adverse consequences for the demonstration of safety; overall safety is much more influenced by sorption in the near-field than in the far-field.

However, SKB has not demonstrated that its treatment of radionuclide retardation in the geosphere is truly conservative. In particular, neglecting sorption on fracture-filling minerals is not conservative with respect to retardation by rock matrix diffusion, because radionuclides are permitted to enter the rock matrix more readily than if sorption on fracture-filling minerals does occur.

SKB's analysis of the bedrock's barrier function considers only uncertainties in sorption. Within the set of analysed scenarios, there is apparently no consideration of the impact of uncertainties in rock matrix diffusion. The absence of sorption in the 'Loss of barrier function – no sorption in bedrock' scenario' presumably causes diffusing radionuclides to penetrate more rapidly and / or to greater depth within the rock matrix than in the other scenarios. The retardation provided by rock matrix diffusion is therefore enhanced compared to the other scenarios in which sorption in the matrix occurs. This raises the question as to the relative importance of rock matrix diffusion and sorption in the rock matrix as retardation mechanisms. Specific questions are:

- If rock matrix diffusion and sorption are both neglected, then would the dose criterion be exceeded?
- If the answer is yes, then how much would rock matrix diffusion need to be diminished from that attained in the main scenario, for the dose criterion to be exceeded?

It would be helpful for SKB to present additional cases in which rock matrix diffusion is diminished in order to answer these questions.

8. References

Andrews, J. E., Brimblecombe, P., Jickells, T. D., and Liss, P. S. 1996. An Introduction to Environmental Chemistry, Blackwell Science, Oxford, UK.

Antunes, R.A., Costa, I., and de Faria, D.L.A. 2003. Characterisation of corrosion products formed on steels in the first months of atmospheric exposure. Materials Research 6, 403–408.

Arthur, R., Sasamoto, H., Walker, C., and Yui, M. 2011. Polymer model of zeolite thermochemical stability. Clays and Clay Minerals. 59, 626-639.

Auqué, L. F., Gimeno, M., Acero, P., and Gómez, J. 2013. Composition of groundwater for SFR and its extension, during different climatic cases, SR-PSU, SKB Report R-13-16, Swedish Nuclear Fuel and Waste Management Company, Stockholm, Sweden.

ASM. 1987. Metals Handbook, Ninth edition, Volume 13, Corrosion. American Society for Metals International, Metals Park, OH.

ASM. 2005. ASM Handbook, Volume 13B, Corrosion: Materials. American Society for Metals International, Metals Park, OH.

Azoulay, I., Rémazeilles, C., and Refait, Ph. 2012. Determination of standard Gibbs free energy of formation of chukanovite and Pourbaix diagrams of iron in carbonation media. Corrosion Science 58, 229-236.

Balonis, M. Lothenbach, B., Le Saout G., and Glasser, F.P. 2010. Impact of chloride on the mineralogy of hydrated Portland cement systems. Cement and Concrete Research, 40, 1009-1022.

Baur, I., Keller, P., Mavrocordatos, D., Wehrli, B., and Johnson, C.A. 2004. Dissolution– precipitation behaviour of ettringite, monosulfate, and calcium silicate hydrate. Cement and Concrete Research, 34, 341–348.

Bertetti, F.P. 2014. Detailed assessment of radionuclide Kd values for the geosphere: Main Phase Review. SSM Technical Note 60, 2014-38.

Bertetti, F.P. 2016. Review of handling of Kd-values used in radionuclide transport for near- and farfield in the safety assessment SR-PSU. SSM Technical Note (unpublished at time of writing)

Bethke, C.M. 2008. Geochemical and Biogeochemical Reaction Modeling. Cambridge University Press.

Birgersson, L.I., and Neretnieks I. 1990. Diffusion in the matrix of granitic rock: field test in the Stripa mine. Water Resources Research, 26, 2833–2842.

Blanc, P., Lassin, A., Piantone, P., Azaroual, M., Jacquemet, N., Fabbri, A., and Gaucher, E.C. 2012. Thermoddem: a geochemical database focused on low temperature water/rock interactions and waste materials. Applied Geochemistry. 27, 2107–2116.

Brew, D.R.M., and Glasser, F.P. 2005. Synthesis and characterisation of magnesium silicate hydrate gels. Cement and Concrete Research, 35, 85-98.

BRGM. 2017. Thermoddem database: http://thermoddem.brgm.fr/

Buenfeld, N.R., and Newman, J.B. 1986. The development and stability of surface layers on concrete exposed to sea-water. Cement and Concrete Research, 16, 721-732.

Byegård, J., Selnert, E., and Tullborg, E-L. 2008. Bedrock transport properties. Data evaluation and retardation model. Site descriptive modelling, SDM-Site Forsmark. SKB Report R-08-98.

Chipera, S.J., and Apps, J.A. 2001. Geochemical stability of natural zeolites in: Natural Zeolites: Occurrence, Properties, Applications (D.L. Bish and D.W. Ming, editors). Reviews in Mineralogy and Geochemistry, 45. Mineralogical Society of America, Washington D.C. and the Geochemical Society, St. Louis, Missouri, USA.

Codina, M., Cau-dit-Coumes, C., Le Bescop, P., Verdier, J., and Ollivier, J.P. 2008. Design and characterisation of low-heat and low-alkalinity cements. Concrete and Cement Research 38, 437-448.

Crammond, N. 2002. The occurrence of thaumasite in modern construction – a review. Cement and Concrete Composites, 24, 393–402.

Crawford, J. 2008. Bedrock transport properties Forsmark Site descriptive modelling SDM-Site Forsmark. SKB Report R-08-48.

Crawford, J. 2010. Bedrock Kd data and uncertainty assessment for application in SR-Site geosphere transport calculations. SKB Report R-10-48.

Crawford, J. 2013. Quantification of rock matrix Kd data and uncertainties for SR-PSU. SKB Report R-13-38.

Cronstrand, P. 2007. Modelling the long-time stability of the engineered barriers of SFR with respect to climate changes, SKB Report R-07-51.

Cronstrand, P. 2014. Evolution of pH in SFR 1, SKB Report R-14-01.

Curtis, P., Markström, I., Petersson, J., Triumf, C-A., Isaksson, H., and Mattsson, H., 2011. Site investigation SFR. Bedrock geology. SKB Report R-10-49.

Daub, K., Zhang, X., Wang, L., Qin, Z., Noël, J.J., and Wren, J.C. 2011. Oxide growth and conversion on carbon steel as a function of temperature over 25 and 80 °C under ambient pressure. Electrochimica Acta, 56, 6661-6672.

Dilnesa, B.Z., Lothenbach, B., Le Saout, G., Renaudin, G., Mesbah, A., Filinchuk, Y., Wichser, A., and Wieland, E. 2011. Iron in carbonate containing AFm phases. Cement and Concrete Research, 41, 311-323.

Dilnesa, B.Z., Lothenbach, L., and Renaudin, G. 2012. Satbility of monosulfate in the presence of iron. Journal of the American Ceramic Society, 95, 3305-3316.

Dilnesa, B.Z., Wieland, E., Lothenbach, B., Dähn, R., and Scrivener, K.L. 2014. Fe-containing in hydrated cements. Cement and Concrete Research, 58, 45-55.

Duro, L., Domènech, C., Grivé, M., Roman-Ross, G., Bruno, J., and Källström, K.(2014). Assessment of the evolution of the redox conditions in a low and intermediate level nuclear waste repository (SFR1, Sweden). Applied Geochemistry, 49, 192-205.

El Hajj, H., Abdelouas, A., El Mendili, Y., Karakurt, G., Grambow, B., and Martin, C. 2013. Corrosion Science, 76, 432-440.

El Mendili, Y., Abdelouas, A., and Bardeau, J.-F. 2013. Insight to the mechanism of carbon steel corrosion under aerobic and anaerobic conditions. Physical Chemistry Chemical Physics, 15, 9197-9204.

El Mendili, Y., Abdelouas, A., Karakurt, G., Aït Chaou, A., Eddehli, R., Bardeau, J.-F., and Grenèche, J.-M. 2014. Applied Geochemistry, 52, 76-85.

Idrissi, M., Diouri, A., Damidot, D., Greneche, J.M., Alami Talbi, M., and Taibi, M. 2010. Characterisation of iron inclusion during the formation of calcium sulfoaluminate phase. Cement and Concrete Research, 40, 1314-1319.

Ishikawa, T., Katoh, R., Yasukawa, A., Kandori, K., Nakayama, T., and Yuse, F. 2001. Influences of metal ions on the formation of b-FeOOH particles, Corrosion Science, 43, 1727–1738.

Gartner, E.M., Young, J.F., Damidot, D.A., and Jawed, I. 2002. Hydration of Portland cements, in: Structure and Performance of Cements (2nd Ed), J. Bensted and P. Barnes (eds.), Spon Press, London.

Gaucher, E.C., Tournassat, C., and Nowak, C. 2005. Modelling the geochemical evolution of the multi-barrier system of the Silo of the SFR repository, SKB Report R-05-80.

Génin, J.-M.R., Refait, P., Bourrié, G., Abdelmoula, M., and Trolard, F. 2001. Structure and stability of the Fe(II)–Fe(III) green-rust ''fougerite'' mineral and its potential for reducing pollutants in soil solutions. Applied Geochemisty, 16, 559–570.

Gimeno, M. J., Auqué, L. F., Gomez, J. B., and Acero, P. 2011. Site investigation SFR Water-rock interaction and mixing modelling in the SFR, SKB Report P-11-25.

Haggerty, R. 2012. Review of Matrix Diffusion and related properties of intact rock in SKB's Licence Application for a Spent Nuclear Fuel Repository in Forsmark, Sweden. SSM Technical Note 23, 2012:44.

Höglund, L. 1992. Some notes on ettringite formation in cementitious materials; Influence of hydration and thermodynamic constraints for durability. Cement and Concrete Research 22: 217-228.

Höglund, L.O. 2001. Project SAFE. Modelling of long-term concrete degradation processes in the Swedish SFR repository. SKB Report R-01-08.

Höglund, L.O. 2014. The impact of concrete degradation on the BMA barrier functions. SKB Report R-13-40, Swedish Nuclear Fuel and Waste Management Company, Stockholm, Sweden.

King, F. and Watson, S. 2010. Review of the Performance of Selected Metals as Canister Materials for UK Spent Fuel and/or HLW. Quintessa Report QRS-1384J-1 for Radioactive Waste Management Directorate, Nuclear Decommissioning Authority, Harwell, UK.

King, F. and Stroes-Gascoyne, S. 2000. An assessment of the long-term corrosion behaviour of C-steel and the impact on the redox conditions inside a nuclear fuel waste disposal container. Ontario Power Generation Nuclear Waste Management Division Report No: 06819-REP-01200-10028.

Kohler, S.J., Defaud, D., and Oelkers, E. 2003. An experimental study of illite dissolution kinetics as a function of pH from 1.4 to 12.4 and temperature from 5 to 50 °C. Geochimica et Cosmochimica Acta, 67, 3583–3594.

Löfgren, M. 2014. Recommendation of rock matrix effective diffusivities for SR-PSU Based on formation factor logging in situ by electrical methods in KFR102B and KFR105. SKB Technical Report R-13-39.

MacPhee, D.E., and Barnett, S.J. 2004. Solid solution properties in the ettringite-thaumasite solid solution series, . Cement and Concrete Research, 34, 1591-1598.

Möschner, G. Lothenbach B., Winnefeld, F., Ulrich A.,. Figi, R., and Kretzschmar, R. 2009. Solid solution between Al-ettringite and Fe-ettringite (Ca6[Al1-xFex(OH)6]2(SO4)3 .26H2O), Cement and Concrete Research, 39, 482-489.

Moranville, M., Kamali, S., and Guillon, E. 2004. Physicochemical equilibria of cement-based materials in aggressive environments – experiment and modelling. Cement and Concrete Research 34: 1569-1578.

Murphy, W.M., Pabalan, R.T., Prikryl, J.D., and Goulet, C. 1996. Reaction kinetics and thermodynamics of aqueous dissolution and growth of analcime and clinoptilolite at 25°C. American Journal of Science, 296, 128-186.

Nilsson, A.-C., Tullborg, E.-L., Smellie, J. A. T., Gimeno, M., Gomez, J., Auqué, L. F., Sandström, B., and Pedersen, A. K. 2011. SFR site investigation Bedrock Hydrogeochemistry, SKB Report R-11-06.

Ochs, M., and Talerico, C. 2004. SR-Can. Data and uncertainty assessment. Migration parameters for the bentonite buffer in the KBS-3 concept. SKB Technical Report TR-04-18.

Odén, M., Follin, S., Öhman, J., and Vidstrand, P. 2014. SR-PSU Bedrock hydrogeology. Groundwater flow modelling methodology, setup and results. SKB Report R-13-25.

Palandri, J.L., and Kharaka, Y.K. 2004. A compilation of rate parameters of mineral-water interaction kinetics for application to geochemical modelling. US Geological Survey Open File Report 2004-1068. USA.

Parkhurst, D.L., and Appelo, C.A.J. 2013, Description of input and examples for PHREEQC version 3—A computer program for speciation, batch-reaction, one-dimensional transport, and inverse geochemical calculations: U.S. Geological Survey Techniques and Methods, book 6, chap. A43, 497 p., available only at http://pubs.usgs.gov/tm/06/a43.

Phillips, D. H., Gu, B., Watson, D. B., Roh, Y., Liang, L., and Lee, S. Y. 2000. Performance evaluation of a zerovalent iron reactive barrier: mineralogical characterisitics. Environmental Science and Technology, 34, 4169-4176.

Purser, G., Milodowski, A.E., Harrington, J.F., Rochelle, C.A., Butcher, A., and Wagner, D. 2013. Modification to the flow properties of repository cement as a result of carbonation. Proceedings of Earth and Planetary Sciences, 7, 701-704.

Quintessa Limited (2013). QPAC: Quintessa's General-Purpose Modelling Software. QRS-QPAC-11.

Randall, M. 2012. Review of radionuclide sorption on bentonite and Forsmark bedrock material. Technical Note 2012:63, Stockholm, Sweden: Swedish Radiation Safety Authority (SSM).

Reardon, E. J. 1995.Anaerobic corrosion of granular iron: measurement and interpretation of hydrogen evolution rates. Environmental Science and Technology, 29, 2936-2945.

Refait, P., Memet, J.B., Bon, C., Sabot, R., and Genin, J.M.R. 2003a. Formation of the Fe,II–Fe,IIIÆhydroxysulphate green rust during marine corrosion. Corrosion Science, 45, 833–845.

Refait, P., Benali, O., Abdelmoula, M., and Genin, J.M.R. 2003b. Formation of ''ferric green rust'' and/or ferrihydrite by fast oxidation of iron, II–III hydroxychloride green rust. Corrosion Science, 45, 2435–2449.

Rémazeilles, C., and Refait, Ph. 2009. Fe(II) hydroxycarbonate Fe2(OH)2CO3 (chukanovite) as iron corrosion product: Synthesis and study by Fourier Transform Infrared Spectroscopy. Polyhedron, 28, 749-756.

Rozalén, M., Huertas, F.J., Brady, P.V., Cama, J., García-Palma, S., and Linares, J. 2008. Experimental study of the effect of pH on the kinetics of montmorillonite dissolution at 25°C. Geochimica et Cosmochimica Acta, 72, 4224-4253.

Sandström, B., and Stephens, M B. 2009. Mineralogy, geochemistry, porosity and redox properties of rocks from Forsmark. Compilation of data from the regional model volume for SR-Site. SKB Report R-09-51.

Sandström, B., and Tullborg, E.-L. 2011. Site investigation. SFR Fracture mineralogy and geochemistry of borehole sections sampled for groundwater chemistry and Eh. Results from boreholes KFR01, KFR08, KFR10, KFR19, KFR7A and KFR105. SKB Report P-11-01.

Sandström, B., Nilsson, K., and Tullborg, E.-L. 2011. Site Investigation SFR. Fracture mineralogy including identification of uranium phases and hydrochemical characterisation of groundwater in borehole KFR106, SKB Report P-11-41.

Santhanam, M., Cohen, M.D., and Olek, J. 2002. Mechanism of sulfate attack: a fresh look part I: summary of experimental results. Cement and Concrete Research, 32, 915–921.

Savage, D., 2011. A review of analogues of alkaline alteration with regard to long-term barrier performance. Mineralolgical Magazine, 75, 2401–2418.

Savage, D., Arthur, R. C., and Saito, S., 1999a. Geochemical factors in the selection and assessment of sites for the deep disposal of radioactive wastes. *In* Chemical Containment of Wastes, Geological Society of London Special Publication 157, pp. 27-45.

Savage, D., Arthur, R. C., Saito, S., and Morooka, K. 1999b. Water-rock buffering of pH and redox and consequences for the performance of the far-field barrier. *In* Radioactive Waste Management and Environmental Radiation,(ICEM), Nagoya, Japan.

Savage, D., Noy, D., Mihara, M. 2002. Modelling the interaction of bentonite with hyperalkaline fluids. Applied Geochemistry, 17, 207-223.

Savage, D., Benbow, S., Watson, C., Takase, H., Ono, K., Oda, C., and Honda, A. 2010. Natural systems evidence for the alteration of clay under alkaline conditions: an example from Searles Lake California. Applied Clay Science, 47, 72-81.

Savage, D., Soler, J.M., Yamaguchi, K., Walker, C., Honda, A., Inagaki, M., Watson, C., Wilson, J., Benbow, S., Gaus, I., and Rueedi, J. 2011. A comparative study of the modelling of cement hydration and cement-rock laboratory experiments. Applied Geochemistry, 26, 1138-1152.

Schwertmann, U., and Murad, E. 1983. Effect of pH on the formation of goethite and hematite from ferrihydrite. Clays and Clay Minerals, 31, 277–284.

Schwertmann, U., and Fechter, H. 1994. The formation of green rust and its transformation to lepidocrocite. Clay Minerals, 29, 87–92.

Sheng, G., Wang, B., Wang, S., and Wang, Z. 2016. Pozzolanic reaction of FeO-SiO2 slag with Portlandite. Journal of Solid Waste Technology and Management 42(1), 51-57.

Sidborn, M., Sandström, B., Tullborg, E-L., Delos, A., Molinero, J., Hallbeck, L., and Pedersen, K. 2010. SR-Site: Oxygen ingress in the rock at Forsmark during a glacial cycle. SKBTechnical Report TR-10-57.

SKB, 2010a. Radionuclide transport report for the safety assessment SR-Site, SKB Techincal Report TR-10-50.

SKB, 2010b. Data report for the safety assessment SR-Site. SKB Technical Report TR-10-52.

SKB, 2011. Site description of the SFR area at Forsmark at completion of the site investigation phase SDM-PSU Forsmark. SKB Technical Report TR-14-01.

SKB. 2014b. Geosphere process report for the safety assessment SR-PSU. SKB Technical Report TR-14-05.

SKB, 2014c. Waste form and packaging process report for the safety assessment SR-PSU, SKB Technical Report TR-14-03.

SKB, 2014d. Engineered barrier process report for the safety assessment SR-PSU, SKB Technical Report TR-14-04.

SKB, 2014e. FEP report for the safety assessment SR-PSU, SKB Technical Report TR-14-07.

SKB. 2014f. Data report for the safety assessment SR-PSU. SKB Technical Report TR-14-10.

SKB. 2014g. Input data report for the safety assessment SR-PSU. SKB Technical Report TR-14-12.

SKB. 2015a. Radionuclide transport and dose calculations for the safety assessment SR-PSU. SKB Technical Report TR-14-09.

SKB. 2015b. Safety analysis for SFR Long-term safety Main report for the safety assessment SR-PSU. SKBTechical Report TR-14-01.

SSM. 2016. SSM's external experts' reviews of SKB's safety assessment SR-PSU – hydrogeological and chemical aspects Initial review phase. Technical Note 2016:08, Stockholm, Sweden: Swedish Radiation Safety Authority (SSM).

Tamaura, Y., Yoshida, T., and Katsura, T. 1984. The synthesis of green rust II, (FeIII–FeII) and its spontaneous transformation to Fe3O4. Bulletin of the Chemical Society of Japan, 57, 2411–2416.

Taylor, H.F.W. 1990. Cement chemistry. Academic Press, London.
Vespa, M., Wieland, R., Dähn, R., Lothenbach, B. (2015) Identification of the Thermodynamically Stable Fe-Containing Phase in Aged Cement Pastes. Journal of the American Ceramics Society, 1-9.

Thaumasite Expert Group. 1999. The thaumasite form of sulphate attack: risks, diagnosis, remedial works and guidance on new constructions. Department of the Environment, Transport and the Regions (DETR). London, UK.

Wersin, P., Birgersson, M., Olsson, S., Karnland, O., and Snellman, M. 2008. Impact of corrosion-derived iron on the bentonite buffer within the KBS-3H disposal concept. The Olkiluoto site as case study. SKB Report R-08-34.

Wilkin, R. T., Puls, R. W., and Sewell, G. W. 2003. Long-term performance of permeable reactive barriers using zero-valent iron: geochemical and microbiological effects. Groundwater, 41, 493-503.

Wilson, J., Savage, D., Cuadros, J., Ragnarsdottir, K.V. and Shibata, M. 2006. The effect of iron on montmorillonite stability. (I) Background and thermodynamic modelling. Geochimica et Cosmochimica Acta, 70 (2), 306-322.

Wilson, J.C., Benbow, S., Watson, C., Sasamoto, H., and Savage D. 2015. Fully-coupled reactive transport models of the iron-bentonite interface. Applied Geochemistry, 61, 10-28.

Wilson, J.C., Benbow, S., Metcalfe, R., and Lueng, H. 2017. Reactive transport modelling of a shale-bentonite interface in a hypersaline system. Applied Geochemistry, 76, 60-73.

<div align="center">

APPENDIX 1

Coverage of SKB reports

</div>

Following reports have been covered in the review.

Table A:1

Reviewed report	Reviewed sections	Comments
[*insert SKB report number and title*]	[*insert reviewed sections*]	[*insert comments, if any*]
R-08-34, Impact of corrosion-derived iron on the bentonite buffer within the KBS-3H disposal concept. The Olkiluoto site as case study		
TR-14-09, Radionuclide transport and dose calculations for the safety assessment SR-PSU		
TR-14-10, Data report for the safety assessment SR-PSU		
TR-14-15, Geosphere process report for the safety assessment SR-PSU. SKB Technical Report		
R-10-48, Bedrock Kd data and uncertainty assessment for application in SR-Site geosphere transport calculations		
R-13-16, Composition of groundwater for SFR and its extension, during different climatic cases		
R-13-38, Quantification of rock matrix Kd data and uncertainties for SR-PSU.		

R-13-40, The impact of
concrete degradation on the
BMA barrier functions

R-14-01, Evolution of pH in
SFR 1

Author: G. Sällfors[1]
            [1] GeoForce AB, Billdal

4

Review of physical and mechanical properties of bentonite – Main review phase

Contents

1. Introduction

1.1. Background

The Swedish Radiation Safety Authority (SSM), at the end of 2014 received an application from Svensk Kärnbränslehantering AB (SKB) for the expansion of the repository at Forsmark for the disposal of low- and intermediate-level radioactive waste. Ultimately the Swedish Government will decide on the matter and SSM has the task of reviewing the application and giving an advisory statement.

An important part of the application is SKB's assessment of the long-term safety of the repository, which is documented in the safety analysis named SR-PSU.

SSM's review of the application has been divided into an initial review phase and a main review phase. The initial review phase has been completed and this Technical Report is part of the main review.

1.1.1. The initial review phase

The objectives of the initial review phase were:
- To develop a broad understanding of the application.
- To determine whether SKB's documentation was understandable and complete with regard to the information needed to be able to make a proper assessment of the application. SSM asked SKB to provide complementary information on certain issues at the end of the initial review phase.
- To identify key review topics for the main review phase. These were topics that have a potentially significant impact on the assessment of whether the application fulfils relevant requirements. Furthermore, these are topics on which it tends to be difficult to make judgments.

1.1.2. The main review phase

This main review phase has involved more detailed analysis of specific issues. The specific review tasks for the main review were identified during the initial review phase. These tasks have been reviewed and considered with SSM as seen below.

1.2. Scope and objectives

This report has been developed as part of the main review phase. It focuses on the physical and mechanical properties of the bentonite components of the SFR and their contribution to the performance and safety of the repository.

The general objectives and considerations of the main review were defined by SSM as follows:

- The consultant(s) shall review in relative detail SKB's reporting concerning the physical and mechanical properties and processes of bentonite, covering the issues identified during the initial review phase, as well as issues newly identified during this main review phase.

- The consultant(s) shall give clear comment on SKB's reporting of different properties and processes regarding scientific soundness, technical reliability, as well as pedagogical quality.
- The consultant(s) shall give their judgement on whether SKB has given clear reporting on bentonite's safety function and the evolution of such functions with time. The consultant(s) need to comment on whether the safety function indicators related to bentonite (given in, among others, Table 5-3 of the SR-PSU main report, SKB TR-14-01) are trustworthy.
- If applicable, the adequacy of relevant models, data and underlying assumptions should be assessed as well as the handling of uncertainties. Merits and weaknesses of SKB's work should be stated.

The specific description of the review assignment for the main phase was given as:

The consultant(s) are expected:

- To review the initial state of the various components that contain bentonite in different parts of the repository, focusing on the initial state and the physical and mechanical properties of the bentonite (SKB TR-14-02 and references therein). Examples of such components are, among others, bentonite at the bottom of the silo; bentonite around the periphery of the silo; bentonite at the top of the silo; bentonite in the plugs and transition zones; bentonite in the access tunnels; and bentonite in sealing of boreholes. These components were identified and considered during the initial review phase (SSM Report 2016:12, Part 1, Section 3.2). The focus of the review should be on the initial material composition and density, the forms of installation (compacted blocks or direct filling), as well as their connections with safety function parameters, such as swelling pressure, and hydraulic conductivity.
- To review SKB's reporting on the process of hydraulic saturation (SKB TR-14-04 and references therein). The issues that need to be focused on could be the thermodynamic, osmotic as well as multiphase fluid mechanical approaches for predicting the saturation. Connections with water supply from the hydrological modelling should also be reviewed.
- To review SKB's reporting on the process of piping erosion (SKB TR-14-04 and references therein). The focus should be on whether SKB's quantification of mass loss through piping erosion is scientifically and technically reasonable, and whether SKB's handling of the impact of piping erosion on the long-term safety of repository is sufficiently conservative.
- To review SKB's reporting on gas transport through bentonite components. The review should focus on the scientific soundness of the modelling and experimental results on the break-through pressure for gas release through bentonite materials.

1.3. This report

The structure of this report is as follows:

- Section 2 provides a brief introduction to the design of the SFR and describes where and how bentonite and bentonite-based materials are used. A short summary of their main functions are also given.
- Section 3 identifies and briefly describes the structure of the SKB documentation which has been reviewed and SKB's approach to reporting on bentonite-related topics.
- Section 4 deals with the initial state of the bentonite and bentonite related materials used to form barriers in the repository system.
- Section 5 treats the saturation process and how it develops with time.
- Section 6 the phenomenon of piping and erosion is evaluated
- Section 7 scrutinises the problem of gas transport
- Section 8 deals with possible freezing of the bentonite
- Section 9 summarises the conclusions from this review task.

2. Description of the SFR Disposal Facility

In the Initial Review a fairly detailed description of the SFR Disposal Facility was given. Only a brief summary of the description is included here. For the reader, who is interested in a more detailed description, the initial review document is recommended (SSM, Report 2016:12).

2.1. Overview of the SFR disposal facility

Sections 1.2 and 4.3 of SKB 2014a (TR-14-01) describe the SFR broadly as follows. The SFR is designed as a sub-sea disposal facility excavated in hard-rock that is accessed via tunnels from an associated surface facility.

The existing part, 'SFR 1', comprises a silo and four waste vaults for different waste categories. The waste vaults are located about 60 m beneath the surface of the sea. The bottom of the silo is located deeper, however, at ~130 m beneath sea level.

The proposed extension, 'SFR 3', would comprise six waste vaults. The waste vaults in the new part of the facility would be located ~120 m beneath sea level, which means that they will be close to the level of the bottom of the silo, see Figure 2.1.

Figure 2.1 The existing SFR 1 (light grey) and the proposed extension SFR 3 (blue) with access tunnels. The waste vaults in the figure are the silo for intermediate-level waste, vault 1 and vault 2BMA for intermediate-level waste, vaults 1–2BTF for concrete tanks with intermediate-level waste with low activity levels, vaults 1BLA and 2–5BLA for low-level waste and the vault 1BRT for reactor pressure vessels.
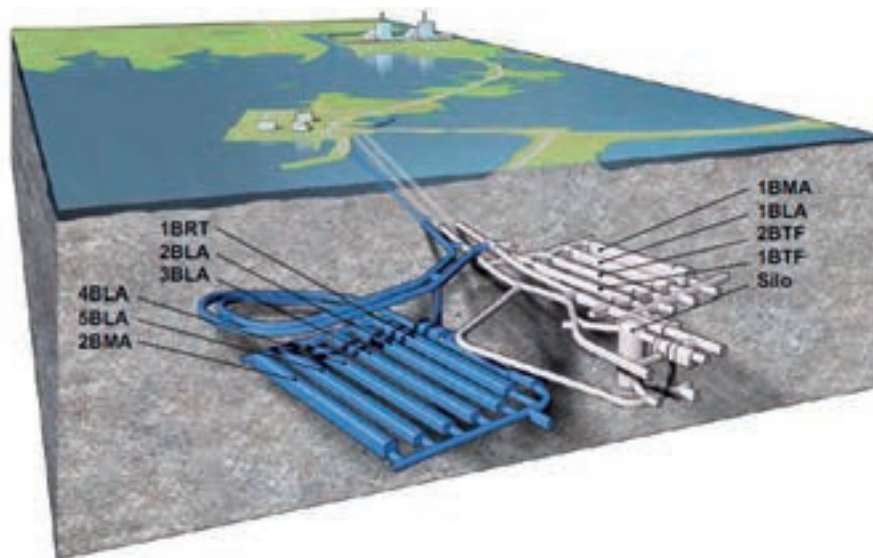
Currently, there are two access tunnels. In order that whole reactor pressure vessels can be emplaced in the repository, a third access tunnel is planned.

The SFR facility will eventually be decommissioned when all of the waste has been disposed of. When the decision for final closure is taken, decommissioning of the facility will begin and will continue until the repository has been closed and sealed.

Closure will include installation of backfill material and plugs at selected locations in the underground facility. The primary purpose of these engineered barriers is to reduce the flow of water through the waste and impede human intrusion into the repository. Plugs are to be installed in access tunnels and connecting shafts, and all tunnels are to be backfilled with macadam. The upper part of the access tunnels is to be filled with stone blocks and sealed with concrete plugs. Finally, the ground surface will be restored so that it blends in with the surrounding landscape. In addition, all boreholes at SFR will be sealed so that the water flow in the surrounding rock is not affected by their presence.

The closed repository is illustrated in Figure 2.2. The plug sections comprise hydraulically tight sections filled with bentonite that is held in place by mechanical constraints.

Figure 2.2 Schematic plan of SFR 1 and SFR 3, with a detailed view of the silo. Key to numbering: 1) Plugs in access tunnels, 2) Transition material, 3) Mechanical plug of concrete, 4) Backfill material of macadam, 5) Hydraulically tight section of bentonite, 6) Backfill material in access tunnels and the central area of the tunnel system, 7) Non-backfilled openings. Note that the figure shows Layout 2.0 but that Layout 1.5 was used in SR-PSU modelling.
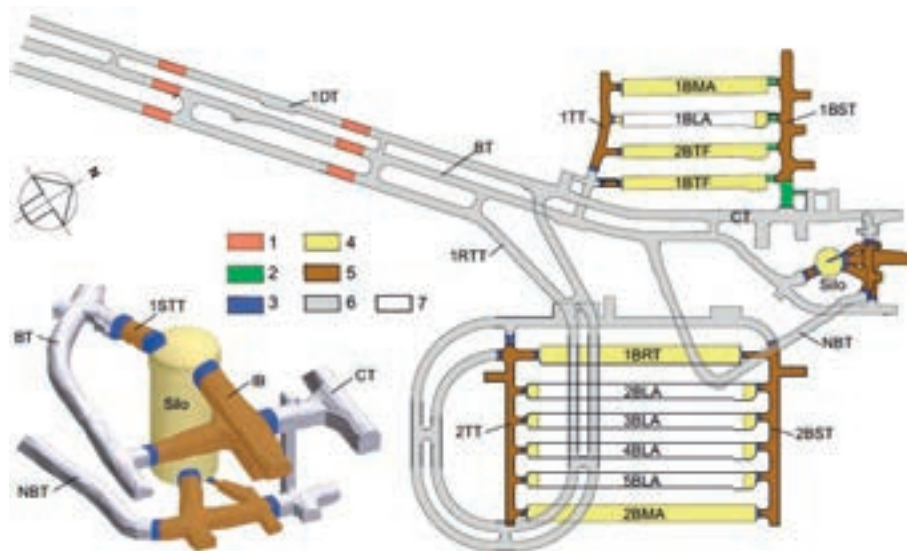
2.2. Uses and functions of bentonite barriers at SFR

Bentonite blocks, bentonite pellets and mixtures of bentonite and sand, or bentonite and crushed bedrock material are used in a number of applications for the SFR repository. The main function of the bentonite-based components is to provide a hydraulic barrier and prevent or limit water flow through the repository, which could lead to migration of radionuclides. Another important property of the bentonite-based components is the development of a swelling pressure as the material gradually becomes saturated. The swelling pressure is, in certain cases important as part of the mechanical stability of the system. The different applications of bentonite or bentonite mixtures in the SFR are briefly described in the following paragraphs.

2.2.1. The silo

The silo is built in a huge cylindrical rock cavern, which is 35 m in diameter and 70 m high, and which is located between 65 m and ~130 m below the surface. The silo itself has a diameter of 25 m and is 50 m high. Bentonite or bentonite mixed with sand or crushed rock surrounds the silo at the bottom, along the periphery and at the top. The bentonite is from Milos in Greece, but has been converted from its original Ca-form to the Na-state by soda treatment.

Bentonite at the bottom of the silo

Above the base of the rock cavern, a 1.5 m thick layer of a sand/bentonite mixture is placed. The proportions of sand to bentonite are 90/10 and it is compacted in a number of layers, resulting in a very stiff foundation. The purpose of this sand/bentonite mixture is twofold, it shall act as a hydraulic barrier and it should also constitute a firm base for the foundation of the silo and allow very little settlement. SKB's target value for the constraint modulus of the mixture was 100 to 150 MPa. Settlement during filling of the silo has been monitored (Pusch 2003) and it seems that up until 2002 (the date of the last reported observations), the target value for the constraint modulus was reached with a good margin. However, no results from measurements made after 2002 have been found during this review.

The bentonite/sand bottom bed should also have a hydraulic conductivity less than $^1/_{10}$ of the host rock, which is believed to be 10^{-8} m/s. Laboratory testing of bentonite/sand mixtures with densities similar to the bottom bed revealed values on the order of 10^{-10} m/s, which are well below the required values.
The swelling pressure of the bottom bed has been estimated through laboratory tests and found to be on the order of 50 to 100 kPa, which means that it will have very little impact on the movement of the silo.

Bentonite around the periphery of the silo

The bedrock walls are covered with shotcrete, which also contains a system of drains. The space between the shotcrete and the silo is filled with bentonite pellets, which are not compacted. The purpose of the bentonite pellets is to act as a hydraulic barrier and, in the longer term, to support the silo and the surrounding rock mass with a swelling pressure. The recommended minimum value of the hydraulic conductivity here is also $^1/_{10}$ of that of the surrounding rock mass and, thus, it should be less than 10^{-9} m/s. Testing of the bentonite at the densities expected has shown that the hydraulic conductivity in all parts of the bentonite is expected to be equal to, or less than, 10^{-10} m/s.

Bentonite swelling pressures and densities have been measured a number of times since emplacement and are reported in Pusch (2003). The bentonite pellets are far from saturated, and so far the swelling pressures have been well below the maximum values of 500 kPa. The swelling pressures also appear to be far more uniform than assumed in the design. However, no results from measurements after 2002 have been found, either for the degree of saturation, or for swelling pressure.

Bentonite at the top of the silo

The silo is closed with a number of concrete lids on top of which 1.5 m of a sand/bentonite mixture will eventually be compacted. The purpose of this bentonite/sand mixture is mainly to act as a hydraulic barrier, but it is also intended to support the frictional material filling the void above the silo. No information on the criteria for this sand/bentonite mixture material has been found.

2.2.2. The plugs and transition zones

With the exception of the silo, each of the different parts of the SFR, that is all the BLAs, both BMAs, both the BTFs and the BRT (see Figures 2.1 and 2.2), are to be closed off by a concrete plug at one end and transition material, consisting of a 30/70 mixture of bentonite/crushed rock, at the other end. The silo is closed off by a number of plugs incorporating a bentonite section between two concrete plugs.

The concrete plugs constitute a mechanical boundary for the vault, and the bentonite/crushed rock constitutes a first hydraulic barrier and also, in some cases, a transition to the bentonite in the tunnels.

The transition zones are supposed to have a hydraulic conductivity of 10^{-9} m/s to 10^{-11} m/s, depending on the density of the mixture. These hydraulic conductivities are based on laboratory test results, but the possibility of achieving these values in full scale testing is yet to be demonstrated.

The tight sections, which are constituted from bentonite blocks, have a target hydraulic conductivity value of 10^{-12} m/s to 10^{-13} m/s for an average emplaced dry density of 1,400 kg/m^3. It should be possible to achieve these hydraulic conductivity values, but it needs to be demonstrated that the densities can be achieved not only in a dry tunnel, but also if some water leaks in to the tunnel during operations. Another important question is how the Excavation Disturbed or Damaged Zone (EDZ) is to be dealt with during plug design and construction, both conceptually and in practice.

2.2.3. The access tunnels

The access tunnels immediately outside the different repository tunnels are to be filled with bentonite. The bentonite will be emplaced in the form of compressed blocks, and the space between the blocks and the bedrock wall will be filled with bentonite pellets. These parts of the tunnels shall function as hydraulically tight sections. In the access tunnels, between each part of the repository there will be one area where according to SKB the EDZ will '*be removed*' in order to stop parallel flow of water in the EDZ. Again, more detail is needed on how this will be done in practice.

2.2.4. Sealing of boreholes

A number of boreholes intersect the repository area and these need to be sealed and closed off. SKB has suggested two different methods and both are supposed to function, even for rather deep boreholes. Highly-compacted bentonite is used where tight seals are needed and cement-stabilized plugs are cast where the boreholes pass through fracture zones. Based on this review, there should not be any real difficulty

in sealing intact boreholes, but there could be more problems for anomalous or 'failed' boreholes, and alternative methods might be needed.

3. SKB's documentation

3.1. Structure

Figure 3.1. illustrates the structure of SKB's documentation including the SR-PSU safety assessment.

Figure 3.1 SKB's documentation of the safety assessment for the SFR. The main reports reviewed in this review task are highlighted in red.
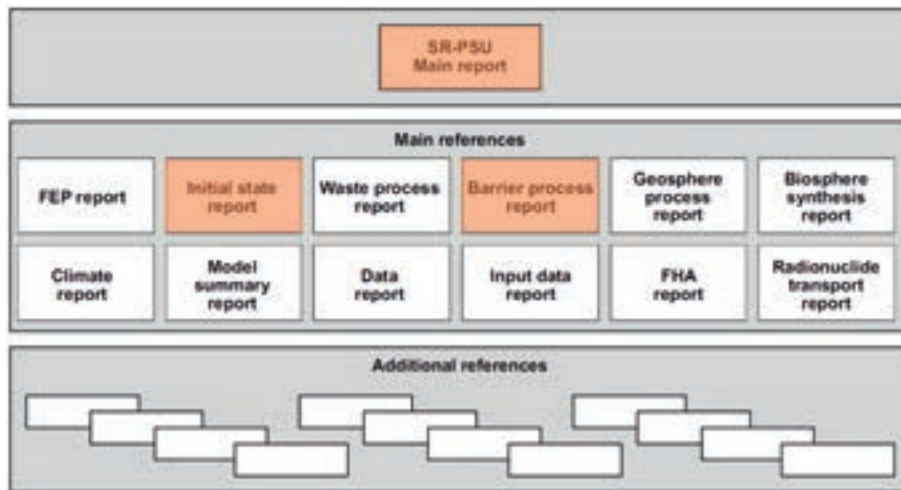
3.2. Content

The Main Report for the SR-PSU safety assessment (SKB 2014a, TR-14-01) is an approximately 500 page long document that addresses the following topics:

- Introductions, including a summary of SKB's system for waste disposal, background on the SFR repository, a description of the wastes to be disposed of, a summary of the applicable regulations, and an introduction to safety assessment.
- A detailed description of SKB's safety assessment methodology, introducing the safety principles and regulatory requirements, setting out SKB's ten step methodology and discussing its application over certain timescales and how uncertainties are addressed. Brief information is also given on quality assurance of the safety assessment.
- SKB's approach to the handling of FEPs (Feature, Events and Processes) and a description of how FEPs are addressed in the following areas; initial state FEPs, internal processes, external conditions.
- A description of the initial state of the repository and its surroundings, including the wastes, the repository itself, the climate, 'surface systems' (such as topography, near-surface hydrology, ecosystems, human populations and water and land uses), the bedrock, hydrogeology and groundwater chemistry.
- Safety functions.

- The 'reference evolution' envisaged for the repository (the climate and expected changes over the assessment period, including periods of temperate and periglacial conditions).
- SKB's approach to the selection of scenarios for the SR-PSU safety assessment, including a 'main scenario', less probable scenarios, residual scenarios and scenario combinations.
- A description of the calculation cases undertaken in the SR-PSU safety assessment, including descriptions of the models and data used, and identifying the safety relevant radionuclides.
    - Within the main scenario different calculations are taken for:
        - A global warming case.
        - An early periglacial case.
        - Collective dose.
    - Calculations are undertaken for the following less probable scenarios:
        - A high inventory case.
        - A high groundwater flow case.
        - An accelerated concrete degradation case.
        - An accelerated bentonite degradation case.
        - An earthquake case.
        - A case with high concentrations of complexing agents.
        - A case with a water well downstream of the facility.
        - A human intrusion case in which a well is drilled into the facility.
    - Calculations are undertaken for the following 'residual' scenarios:
        - No sorption in the repository.
        - No sorption in the bedrock.
        - High water flow in the repository.
        - Alternative redox conditions in the repository.
        - Extended global warming conditions.
        - Unclosed repository.
        - Future human actions.
        - Glaciation and post-glacial conditions.
- Safety assessment results in terms of calculated results for radionuclide transport and assessed doses.
- A discussion of risk in terms of protection of human health and environmental protection.
- Conclusions, including an assessment of the need for further research and further developments in terms of waste characterisation and facility design and operation.

The Initial State Report (SKB 2014b, TR-14-02), comprises some 120 pages. It was produced as a part of the second step in SKB's ten-step assessment methodology (i.e. 'description of initial state') and it details the initial state of the repository at the time of its closure. The report also describes waste acceptance criteria, the reference waste inventory, the repository reference design, and control and inspection processes that will be used to secure an appropriate initial state of SFR. Conclusions are drawn on the expected state of the repository and its environs immediately after closure for each of the eight repository vaults and for the repository plugs and closure components (see below). For example for the silo, one conclusion of the report is that '*the bentonite wall filling is stable and only small movements have been detected in the top filling, which indicates that the water absorption in the bentonite is insignificant*'. An appendix to the report contains detailed information on the waste packages and repository vaults.

The Engineered Barrier Process Report (SKB 2014c, TR-14-04), comprises some 340 pages. It was produced as a part of the fourth step in SKB's ten-step assessment methodology (i.e. '*description of internal processes*') and it documents available scientific knowledge on, and SKB's handling of, processes that may occur in the repository engineered barriers. The processes considered were identified by SKB as being of relevance to the long term safety of the SFR based on the findings from a previous safety assessment. The Engineered Barrier Process Report (SKB 2014c, TR-14-04) describes the repository components and their safety functions, and then uses a defined template to discuss systematically each of the thermal, hydraulic, mechanical, chemical and radionuclide transport processes that might occur in each part of the SFR. The range of processes considered is not exhaustive, but is quite broad and appears to include the most important factors that are, or could be, relevant to safety.

4. Initial State of the Bentonite

Safety functions are defined in order to illustrate the way in which a repository component contributes to safety, and safety function indicators provide a measureable or calculable property of a repository component that is used to indicate the extent to which a safety function is fulfilled.

4.1. The Silo

4.1.1. Base of the Silo

The silo, which is cast in concrete, rests upon a base of a mixture of sand and bentonite, with 10 % bentonite and 90 % sand. The layer is 1.5 m thick and its main purpose is to form a rigid foundation for the silo. The bed was compacted in several layers and obtained the required density and homogeneity, according to the procedures used during construction.

The settlement of the silo has been monitored and is very limited. Modelling of the settlements has been compared with the actual settlements reported by SKB. The deviation between prediction and performance has been very small so far. Further settlement will also be very small, as the sand bentonite mixture is strain hardening and, thus, the compression modulus will increase with increasing strain.
The modelling and performance is very satisfactory.

4.1.2. Periphery of the Silo

The bedrock cavern, in which the silo is constructed, is covered with a shotcrete layer, in which a draining system is incorporated in order to limit water inflow to the bentonite. The rest of the volume is filled with bentonite buffer, which is not compacted.

The bentonite surrounding the silo, in combination with the draining system adjacent to the bedrock, shall prevent water to flow into the silo. Pressure cells were installed to measure the pressure build up, and an increasing pressure with time would be an indicator of water uptake of the bentonite. So far, the pressures measured have been very small, and well below the acceptable pressures, thus indicating that the drainage system around the silo is working well.

4.1.3. Top of the Silo

Above the top lid of the silo and the adjacent thin layer of sand, a sand/bentonite mixture will be placed and compacted. The proportions of the sand/bentonite mix are 90 % sand and 10 % bentonite - the same proportions as at the bottom of the silo. This compacted sand/bentonite mixture will not be emplaced until closure of the silo, but careful restrictions for mixing and compaction are given and, thus, this layer will be intact and should provide a good support for the thin concrete top and the overlying fill of friction material. No specific safety functions are given for this material however and, thus, there are no safety functions indicators either.

4.2. Plugs and Transition Zones

There will be two sets of plugs in the access tunnels, consisting of concrete plugs with up to 10 m of bentonite in between. These will be the last part of the plant to be installed, apart from the backfilling of the rest of the access tunnels. A number of mechanical plugs of concrete will be installed to:

- Completely seal off the silo.
- Completely seal off 1BRT, 2BLA – 5BLA and 2BMA.
- Partly seal off 1BMA, 1BLA and 1BTF and 2BTF.

All of these plugs will be accompanied with an outer zone of a hydraulically tight section of bentonite. Furthermore, between the concrete plug and the waste there will be a zone filled with backfill of macadam.

The concrete plugs are designed to function as a mechanical constraint and the main function of the bentonite adjacent to the plug is to act as a hydraulic barrier. All areas around the bentonite and the transition material shall be treated so that the damage zone is removed by controlled methods, in order to close off all bypass flow of water. The most relevant safety function for the bentonite thus is hydraulic conductivity.

4.3. Access Tunnels

The access tunnels at repository level, outside the plugged sections, will be backfilled with macadam. The rest of the access tunnels will also be filled with macadam. Adjacent to the connection between the access tunnels, a plug consisting of a 10 m long section of bentonite, surrounded by concrete plugs, will be installed in each tunnel, see Section 4.2.

4.4. Boreholes

Boreholes in the vicinity of the repository will be sealed. In areas where the hydraulic conductivity of the bedrock is high, the boreholes will be stabilized in order to maintain structural stability. Here the material used for the plugging will be quartz sand/cement. In areas where a hydraulic conductivity will be maintained, the boreholes will be sealed with highly-compacted bentonite. Two different methods are available.

4.5. Relevant Safety Function Parameters

4.5.1. Swelling pressure

The achievement of suitable bentonite swelling pressures is crucial, particularly for the proper functioning of the bentonite pellets surrounding the silo. The swelling pressure needs to be larger than 100 kPa, but not larger than 500 kPa. So far, as reported by Pusch (2003), no pressures outside the admissible pressure range have developed. Once the volume of bentonite pellets has saturated, the swelling pressures should be rather uniform, as long as only limited piping and erosion have taken place. Full saturation should occur long before the concrete silo deteriorates

and, thus, the structure of the whole design should remain intact. However, some 13 years have elapsed since the last swelling pressure measurements were reported and it is extremely important to ensure that the swelling pressures have not changed radically during this period. Thus, more recent monitoring data ought to be gathered and reviewed.

4.5.2. Hydraulic conductivity

As part of the repository design process, target values are given for the hydraulic conductivities of each of the different applications of bentonite-based materials in the SFR (e.g. the tight sections, the transition material, the filling around the silo, the beds below and above the silo, the access tunnels and the borehole seals). The material densities specified do correspond to, and should provide, the desired hydraulic conductivities, but it remains to be shown that these densities can be obtained under practical working conditions.

5. Saturation of Bentonite

The saturation and resulting hydraulic conductivity of the bentonite-based barriers are considered in the safety assessment. The safety function indicator attributed to the bentonite-based materials of the silo and plugs is, however, defined in terms of providing low hydraulic conductivity, which contributes to the safety function 'low flow in the waste vaults' and the safety principle 'retention of radionuclides' (SKB 2014a, TR-14-01, Table 5-3).

In terms of the assumed/assessed importance to safety of the engineered barriers, it is notable that according to SKB, the bentonite components are only really considered important for the silo (SKB 2014a, TR-14-01, Table 11-1).

5.1. The Silo

In detail the saturation process for the complete silo and its waste is complicated, as the structure has several different components. Very slowly the bentonite surrounding the silo will take up water and swell. Eventually this bentonite will become saturated and as the gradient builds up, which is a very slow process, the concrete silo will start its saturation process. Not until large parts of the silo are saturated, will water start slowly flowing into the waste compartment and eventually reach the waste. Then when all the material is basically saturated, water might start to flow through and out from the silo. This flow will be extremely limited, as the gradients will be very small and the water must pass the saturated bentonite with its very low hydraulic conductivity. The saturation process will also be constrained by the presence of air in the bentonite, the compartments as well as in the waste itself.

Uncertainties in the rate and pattern of silo saturation are mainly associated with the hydraulic conductivity of the surrounding bedrock and also with the number and sizes of cracks in the silo. It is beyond the scope of this review task to consider these uncertainties in any detail for this report, but most important, the flow of water through the silo will be very limited.

5.2. Plugs and Transition Zones

The scenarios for the plug and the transition zones are similar to that of the silo and the same conclusions are valid also for these components.

5.3. Access Tunnels

The bentonite between the concrete plugs in the three access tunnels will slowly saturate, primarily from water flowing in through cracks in the bedrock. The bentonite will probably swell irregularly, but the concrete plugs will keep it intact. After full saturation, the bentonite will be fairly homogenous and will provide a hydraulic barrier against further flow of water and due to their very low hydraulic conductivity.

The access tunnels immediately outside and adjacent to the silo, and the BLA, BMA, BRT and BTF vaults are also to be filled with bentonite blocks and bentonite pellets and will gradually be saturated. Uneven saturation will most likely occur, but

also here the bentonite will eventually become rather homogenous, due to the development of the swelling pressure.

There could be the possibility that SKB will in future encounter zones of the bedrock in the new excavations where there are relatively higher rates of water flow, and so they should have contingency plans for how to cope with such situations during tunnel construction and emplacement of the bentonite components, and for assessing the possible consequences of such flows on bentonite saturation. These plans and assessments will need to take account of the particular compositions of the bentonite and of the proportions of bentonite and other materials (crushed rock etc.) to be used in barrier construction.

5.4. Boreholes

The boreholes in the vicinity of the repository will be sealed with highly compacted bentonite rings or circular discs. The saturation will also here originally be heterogeneous and cause some movements of the yet dry parts. As the modulus of also the dry compacted bentonite is rather high, wetting and swelling of parts of the bentonite will not cause any larger displacement of adjacent rings. Once the bentonite in the complete borehole is saturated, the density of the bentonite will most probably vary within a rather narrow range, well above what is required.

5.5. Modelling of saturation

It is obvious that the time required to achieve full saturation of the bentonite in the different applications will vary considerably, depending in particular on the percentage of bentonite in the material and on the hydraulic conductivity of the materials and also to a great extent on the frequency and sizes of the fractures in the surrounding rocks. SKB has not presented detailed modelling of the saturation process for most of these applications.

It would be sensible, therefore, for SSM to ask SKB to provide a more complete set of modelling analyses that examines the properties, behaviour and evolution of each of the bentonite-based barriers in the SFR in order to allow more in depth reviews to be undertaken. However, given that there will always be uncertainties e.g., in the local structure and hydraulic properties of the rocks, advanced modelling has its limitations and must be accompanied by sound engineering judgement. In this case, the reviewer is convinced that, if the production plan is followed and carefully monitored, the bentonite in all the applications discussed here will fulfil the criteria given.

6. Piping and Erosion of Bentonite

6.1. The Silo

As the bentonite surrounding the silo has a comparatively low density and low swelling pressure, some sort of piping and erosion might take place, if water flows in through a crack in the bedrock and the shotcrete at a pace larger than the bentonite can absorb.

The uncertainty related to piping and erosion cannot be neglected. It is highly dependent on the hydraulic characteristics of the bedrock. If considerable erosion takes place, it is difficult to be certain that the so formed channels will heal, even once the gradients are lowered again when the bentonite becomes saturated and the erosion stops. However, once all the bentonite is saturated, the effective stresses in the bentonite will be comparatively small, the hydraulic gradients will be low, and it is very likely that the swelling pressure will be large enough then to heal and close the channel.

Some investigations have been reported, but more understanding of the piping and erosion phenomenon is needed, especially as most modelling is based on empirical data. No analytical model is yet available. It is therefore fair to say that the uncertainties are rather large.

The sand/bentonite mixture below and above the silo is less likely to be harmed by piping and erosion, partly due to low gradients and partly because the percentage of bentonite in these regions (10 %) is well above the critical percentage (6 %).

6.2. Plugs and Transition Zones

Many of the plugs and transition zones in contact with the bedrock consist of either bentonite pellets at a low density, or a 30/70 mixture of bentonite and crushed rock. These materials might not be able to resist erosion of bentonite, and channels might be formed where erosion might continue and result in loss or relocation of bentonite.

Again, as the material becomes saturated, the gradients will become small, the effective stresses low and the bentonite will start to swell again. Most likely the channels which might have been formed will close again. However, piping and erosion is a complicated process to model and the uncertainties are comparatively large. Further investigations are needed and are also in progress.

6.3. Access Tunnels

For the access tunnels, the issues are approximately the same as have been described for the plugs and transition zones in Section 6.2.

6.4. Sealing Boreholes

If a borehole is intersected by a crack in the bedrock with substantial flow of water, piping and erosion will most likely occur. The adjacent bentonite will swell and move towards the area where the crack is and, thus, substantial loss of bentonite might occur. However, eventually the bentonite on each side of the crack will most likely develop a swelling pressure against the borehole wall to stop any further movement of the bentonite towards where the flow of water takes place. Thereby no further loss of bentonite will occur. Whether the borehole is open where the crack intersects the borehole is of no importance as long as no flow occurs along the borehole.

Therefore, the critical phase during which piping and erosion of bentonite around the silo might occur is the transient period after the silo has been filled and closed and the pumping has just been stopped. If the water flow from the bedrock is substantial, the drains will fill up rather quickly, and a large hydraulic gradient might develop across the compacted sand/bentonite foundation bed. As the bentonite content in the foundation bed is only 10%, it is prone to internal erosion and piping. The bentonite pellets could also be harmed by piping and erosion, and here also large hydraulic gradients might develop in the early phase after pumping is stopped. It will be important, therefore, to carefully manage the process of stopping the pumping and, thereby, control the gradual filling of the drainage system around the silo in order not to allow too large hydraulic gradients.

SSM should, therefore, consider requiring SKB to provide further information and conduct more detailed analyses of the likely water inflows to the repository. SKB should also report on its plans for the cessation of pumping and managing the transition from operating conditions to long-term post-closure conditions.

7. Gas Transport in the Bentonite

Gas (air) will initially be trapped in the repository and the pressure of these gases will increase as the saturation process proceeds. Some chemical reactions such as the consumption of oxygen and the production of hydrogen during corrosion may also affect gas pressures. With increasing pressure, some gas will gradually dissolve in the water. However, the pore pressure and gas solubilities may not be high enough that all of the gas can be dissolved and so some may remain in the pores of the bentonite. Eventually the gas pressure might be so high locally that it exceeds the pore entry pressure for the bulk of the bentonite and it may penetrate and flow through fractures in the clay and bedrock. Locally the presence of a discrete gas phase might limit water transport; this might be unfavourable for the saturation and sealing of the bentonite, but favourable in the sense that it decreases the flow area for the water and could result in a smaller hydraulic gradient compared to the fully saturated bentonite. It can be understood, therefore, that the issue of the presence of a separate gas phase and the occurrence any discrete gas transport is a complex, coupled hydro-mechanical-chemical process which is likely also to be spatially heterogeneous. In conclusion, any presence of gas or gas transport in the bentonite surrounding the silo, in the plugs and transition zones, access tunnels or trapped in the boreholes can be considered a hazard or a violation of the safety functions. Based on this review it is an issue that for the SFR has not yet entirely been resolved.

8. Freezing of the Bentonite

It has been pointed out by SKB, that freezing of the bentonite in the different applications might be a potential hazard and the consequences at the SFR are treated in several SKB references.

The following was concluded in the Initial review phase
SKB (2014f, R-14-29) notes that:

- The influence and extent of possible frost-heave in the silo has been quantified under the assumption that the material is frost susceptible and that no density redistribution occur as a consequence of freezing. The results suggest that no damaging pressures will develop in the silo due to ice-lens build up, but that the extent to which the silo bentonite will self-heal after ice lenses thaw remains an open question. Page 380 of SKB 2014a (TR-14-01) indicates that, '*A finite element calculation of the self-healing (after an ice-lens formation) of a spherical void with the radius 0.5 m, which would represent severe damage to the bentonite caused by piping and erosion, has been done (Cronstrand 2014). Although the results cannot be used without reservations, they indicate that the bentonite would be fairly unaffected close to the concrete silo, which means that the sealing function would remain effective. This process should however be given further attention, since the self-sealing ability is crucial and both model capabilities and material data relevant to the silo bentonite are somewhat lacking.*' It has not been possible to review and evaluate the cited reference (Cronstrand 2014) in any detail during this initial review task.
- The redistribution of silo bentonite density as a consequence of freezing has been quantified based on the expected osmotic response and the assumption of having a frictionless system. This analysis shows that, instead of forming ice in the bentonite, it may be possible for substantial density redistribution to occur.
- The effect of frost weathering (i.e. the effect of "trapping" unfrozen bentonite water within frozen surroundings, which then transforms into ice as temperature is lowered further) may give rise to possible pressure peaks. An estimation of maximum pressure has been made based on considering mechanical and chemical equilibrium between bentonite and ice, and assuming a simple elastic mechanical response. The results suggest that pressure peaks on the order of several tens of MPa cannot be ruled out.

It is rather obvious that freezing of bentonite at SFR may result in several complex effects, including transient pressure increases, a certain amount of redistribution of bentonite mass and, in the longer term, possibly in increased hydraulic conductivities.

No further information or modelling of freezing have been supplied since the initial review and, therefore, the need for further research and modelling remains. In the initial review all of the detailed quantifications and arguments around these processes suggested that bentonite freezing and its effects could form the subject of a more detailed review.

9. Representation of Bentonite Barriers in Safety Assessment

9.1. Initial state and evolution

After closure, the engineered structures, including the barriers composed of bentonite-based materials will slowly become hydraulically saturated. In the safety assessment, the saturation process is assumed to be instantaneous following closure (SKB 2014a, TR-14-01, page 144). This is not a fully realistic assumption and the implications of slow re-saturation should perhaps be considered by more detailed modelling studies.

Page 151 of SKB 2014a (TR-14-01) indicates that during the first thousand years after closure water flows through the repository vaults increase by approximately two orders of magnitude on going from submerged conditions to on-shore conditions. According to SKB, this is the most important process affecting the flow through the repository during this period. During the first thousand years after closure, degradation processes start to influence the hydraulic properties of concrete structures and materials in the repository (SKB 2014a, TR-14-01, section 6.3.8). SKB's analyses suggest that the resulting effect on groundwater flow through the repository is small, however, compared with the increase in flow due to the retreating shoreline. The hydraulic properties of the bentonite barriers in the repository are assumed not to change during the first thousand years after closure (SKB 2014a, TR-14-01, page 151).

In the longer-term (i.e. more than 1,000 years after closure) SKB's assessment assumes that the hydraulic conductivity of cementitious repository components increases until a 'completely degraded' state is reached when the concrete no longer provides a barrier to water flow. A similar approach has been taken for representing the effects of degradation of bentonite seals in tunnels at the ends of the vaults, and 'complete' degradation is estimated to lead to an order of magnitude increase in flow in the 1BMA and BTF vaults. In contrast, water flows through the silo are assumed to remain more or less constant because the silo is assumed to remain protected by its surrounding bentonite barrier (SKB 2014a, TR-14-01, section 6.4.5), which emphasises the importance attached to the bentonite barrier around the silo.

SKB (2014a, TR-14-01, section 6.5.2) notes that during periods of periglacial conditions, it is possible for temperatures to be low enough for the entire repository to freeze. A ground temperature below 0°C at repository depth cannot be ruled out during the first possible occurrence of permafrost between 17,500 AD and 20,500 AD in the early periglacial climate case ground temperature of –3°C or less at repository depth cannot be ruled out during the occurrence of permafrost around 52,000 AD both in the early periglacial climate case and the global warming climate case. Under periglacial climate conditions, the most relevant scenarios for the SFR area predict significantly lower total flow through the waste vaults, longer path lengths and travel times, and higher flow-related transport resistance values compared with the values under temperate conditions. However, the results are dependent on the extent and number of taliks in the flow domain, and some of the waste vaults may experience small increases in total flows under periglacial relative to temperate conditions. The possible consequences of bentonite freezing have been briefly mentioned above in Section 8.

9.2. Bentonite degradation scenario

Section 7.6.4 of SKB 2014a (TR-14-01) describes a bentonite degradation scenario. The bentonite degradation scenario is based on an assumption that the safety function '*low flow in waste vaults*' deviates from the main scenario due to uncertainties in the consequences of extensive periglacial conditions in combination with uncertainties in the sealing properties of the bentonite. SKB assesses the probability of this scenario to be low, considerably less than 10%.

In the bentonite degradation scenario, the effects of the ice-lens formation are assumed to be so large that the bentonite surrounding the silo will have a permanently increased hydraulic conductivity, which results in an increase in water flow. It is further assumed that ice-lens formation occurs during the first permafrost period in the early periglacial climate case (i.e. in the period from 17,500 to 20,500 AD).

SKB argues that the concrete will not freeze as the temperature needed for concrete to freeze is lower than the temperature needed for bentonite to freeze. SKB also argues that the size of the plugs implies that harmful ice-lens formation could not occur and hence treats the plugs in the same way as in the main scenario. No more detailed justifications for these assumptions have been seen however.

A calculation case was set up to evaluate the influence of an ice-lens on the flow in the silo (Abarca et al. 2013). In the model, the affected bentonite barrier was simulated by defining a ring of high permeability material, surrounding the silo concrete structure at mid-height. The results suggested an order of magnitude increase in flow in the degraded volume, whereas the flow increase in the rest of the silo was moderate. The silo concrete structure limited the amount of water that could penetrate the waste.

SKB argues that this scenario can also be seen as representative for other bentonite degradation processes, for example montmorillonite alteration due to interactions with cementitious materials. However, this latter argument in particular does not at first sight seem particularly sound.

Section 9 of SKB 2014a (TR-14-01) summarises the many results from the safety assessment calculations. The results are presented in terms of assessed potential annual dose and the contributions of different radionuclides to peak dose are tabulated.

Results for the bentonite degradation scenario (peak potential annual dose of 5.9 µSv at 6,250 AD, dominated by releases from the silo and by Mo-93 and C-14) (SKB 2014a, TR-14-01, Table 9-6) are broadly similar to those for the global warming variant – having a slightly earlier and higher peak and a very slightly lower tail in the long-term.

Results for the residual high flow in the repository scenario, in which both the concrete and bentonite barriers of the repository were assumed to have degraded properties from the start of the assessment, are almost one order of magnitude higher than those for the global warming variant (peak potential annual dose of 46.9 µSv at 5,000 AD, dominated by releases from the silo and by Mo-93, C-14 and Ni-59) (SKB 2014a, TR-14-01, Table 9-13).

Tables 9-20 and 9-21 of SKB 2014a (TR-14-01) together provide a useful summary of the assessment results for all of the scenarios considered. These tables help to put

the results for the bentonite degradation and engineered barrier related scenarios into a wider context. For example, they show that higher peak potential annual doses are calculated for several of the intrusion wells scenarios, although these scenarios are attributed very low probabilities and, hence, lower risks (SKB 2014a, TR-14-01, Tables 10-1 and 10-2).

After 50,000 years, freezing of the concrete barriers in the repository may occur. Further, ice-sheet development cannot be excluded. At that time, the activity of radionuclides in the repository is completely dominated by the limited amount of long-lived radionuclides with a half-life so long that they will not decay substantially during the assessment period.

At the end of the assessment period (i.e. 100,000 years), the levels of all of the disposed radionuclides are close to, if not below, clearance levels.

Given this discussion, it would appear that key assumptions include:
- The period for which the repository is assumed to remain undisturbed (i.e. the 1,000 or 3,000 year period depending on the scenario in which there is assumed to be no human intrusion), and
- The time after which the repository might suffer damage due to ice sheet development.
- The probabilities assigned to the scenarios.

Even so, an important point to note is that according the SKB 2014a (TR-14-01, page 369), '*The contribution from uranium progeny to the total risk is not projected to increase significantly beyond 100,000 years*'. Thus, although SKB cannot exclude the possibility that permafrost may reach repository depth, or that future ice-sheet development may have a severe impact on the protective capability of the repository, limitation of the amount of long-lived radionuclides that are disposed of (i.e. Waste Acceptance Criteria) ensures that regulatory requirements for the protection of human health and environment are met even after such events. This limitation of the inventory of long-lived radionuclides is also used by SKB to justify the depth of the proposed repository extension (SKB 2014a, TR-14-01, page 369).

10. Conclusions

During this review it has become clear that SKB has undertaken and documented a highly competent and systematic safety assessment for the SFR. The documentation and safety assessment that SKB has provided and undertaken are well structured and well written, and cover the necessary areas.

The documentation is generally transparent and traceable to underlying references. The scientific soundness of most of the many and various studies that underlie the safety assessment appears to be satisfactory. There is however a need for ongoing monitoring of the SFR and updating of the safety assessment and documentation to take account of new information and fill some minor gaps in the scientific basis.

The technical solutions for the disposal of the wastes that SKB has presented are mature in the sense that SFR already exists and has been operating safely for a number of years. SKB has not yet, however, fully demonstrated that the engineered barriers can be installed as designed under realistic conditions underground and they will need to continue work to fully develop the necessary techniques and plans.

References

Abarca, E., Idiart, A., de Vries, L.M., Silva, O., Molinero, J. and von Schenk, H., 2013. *Flow modelling on the repository scale for the safety assessment SR-PSU.* SKB TR-13-08, Svensk Kärnbränslehantering AB.

CEA, 2009. N*uclear waste conditioning: A Nuclear Energy Division monograph.* Paris: CEA.

Cronstrand, P., 2014. *Evolution of pH in SFR 1*. SKB R-14-01, Svensk Kärnbränslehantering AB.

Emborg, M., Jonasson, J.-E. and Knutsson, S., 2007. *Långtidsstabilitet till följd av frysning och tining av betong och bentonit vid förvaring av låg- och medelaktivt kärnavfall i SFR 1*. SKB R-07-60, Svensk Kärnbränslehantering AB. (In Swedish.)

Gaucher, E.C. and Blanc, P., 2006. *Cement/clay interactions - A review: Experiments, natural analogues, and modeling*. Waste Management, Elsevier, Vol. 26, pp.776-788.

Pusch, R., 2003. *Design, construction and performance of the clay-based isolation of the SFR silo*. SKB R-03-30, Svensk Kärnbränslehantering AB.

Savage, D., Noy, D. and Mihara, M., 2002. *Modelling the interaction of bentonite with hyperalkaline fluids*, Applied Geochemistry Vol. 17, pp. 207-223.

SKB, 2010. *Long-term safety for the final repository for spent nuclear fuel at Forsmark. Main report of the SR-Site Project,* SKB Report TR-11-01, Svensk Kärnbränslehantering AB.

SKB, 2014a. *Safety analysis for SFR. Long-term safety. Main report for the safety assessment SR-PSU*, SKB TR-14-01, Svensk Kärnbränslehantering AB.

SKB, 2014b. *Initial state report for the safety assessment SR-PSU*, SKB TR-14-02, Svensk Kärnbränslehantering AB.

SKB, 2014c. *Engineered barrier process report for the safety assessment SR-PSU*, SKB TR-14-04, Svensk Kärnbränslehantering AB.

SKB, 2014d. *Miljökonsekvensbeskrivning. Utbyggnad och fortsatt drift av SFR*. Svensk Kärnbränslehantering AB. (in Swedish)

SKB, 2014e. *Waste process report for the safety assessment SR-PSU.* SKB TR-14-03, Svensk Kärnbränslehantering AB.

SKB, 2014f. *Freezing of bentonite components in SFR. Modeling and laboratory testing*. SKB R-14-29, Svensk Kärnbränslehantering AB

Authors: M. Apted and R. Arthur[1]
           [1]INTERA Incorporated, Austin, Texas, U.S.A.

5

Review of chemical properties of bentonite – Main review phase

Abstract

This review addresses chemical properties, together with processes that involve or impact such properties, of bentonite-containing barriers for the planned expansion of the Swedish Nuclear Fuel and Waste Management Company's (SKB's) low- and intermediate-level waste SFR facility. Relevant reports that are part of SKB's overall SR-PSU safety analysis are the basis of this review (SKB, 2014a-h).

Bentonite is used in different parts of the SFR, due to its unique physical and mechanical properties, as well as its relative stable chemical properties in the disposal environment. Bentonite is dominantly composed of montmorillonite, which displays a high swelling pressure, low hydraulic conductivity and low solute diffusivity, which makes it a good retardation material for potential radionuclide release from the repository. In particular, the Silo portion of the SFR uses bentonite as a fill between the concrete "waste-vault" and the wall of the bedrock. The Silo may be suitable for accommodating more than 70% of the total radioactivity-inventory of the entire SFR facility. In addition, either bentonite or 10% bentonite/90 % sand mixture are used as floor material, or in plugs, or backfill of access tunnels. This report reviews chemically based isolation-properties of bentonite/montmorillonite, and possible chemical and mineralogical changes that might arises to change such retardation safety-functions.

The review has been evaluated with regard to:

- Completeness,
- Scientific soundness and quality,
- Adequacy of relevant models, data and safety functions,
- Handling of uncertainties,
- Safety significance,
- Quality in terms of transparency and traceability of information, and
- Feasibility of manufacturing, construction, testing, implementation and operation.

The scope of this review is directed at *chemical* processes and properties of bentonite as they affect assigned safety functions. The SR-PSU scenario analyses on "bentonite degradation," also considers events such as future glacial-conditions of freeze/thaw and potential development of ice-lens within bentonite. These are *physical* processes, however, leading to degradation of *physical* properties of hydrological and mechanical safety functions of bentonite, and are therefore beyond the specific scope of this review.

A primary chemical process that can affect chemical properties upon which safety functions of bentonite-containing barriers are based is *mineralogical transformation and/or dissolution of the montmorillonite/ smectite in bentonite*. There are two resulting impacts on identified safety functions for bentonite-containing barriers in the SFR. First, such transformation reduces the effective swelling pressure of bentonite, which is correlated to sustaining a low hydraulic conductivity safety function. The second impact is in degrading the sorptive safety function of bentonite-bearing barriers. It is noted, however, that the SR-PSU safety assessments for radionuclide transport, while including sorptive characteristic for bentonite, instead primarily rely on sorption by cement/ cement-degradation products and the far-field host rock.

2

Another chemical-related process possibly affecting long-term safety functions of bentonite-containing barriers is so-called 'chemical erosion'. In this process, as modeled by SKB, the necessary chemical environment for formation of bentonite colloids is considered, then linked to a force-balance analysis of the rate of removal of such colloids at the intersection of the bentonite with fluid-carrying fractures in the host rock. Sustained removal of bentonite would eventually lower density and swelling pressure of the bentonite, degrading the low hydraulic conductivity safety function.

It is concluded from this initial review that (1) the SKB reports and analyses regarding reported chemical properties of bentonite-containing barriers, and processes that involve or impact such properties, within the planned SFR expansion are of good scientific quality, with reasonable, transparent and traceable treatment of uncertainties for the models and data that are reported; (2) with respect to completeness, however, there is under-representation and lack of appropriate attention for certain chemical processes and biologically mediated montmorillonite transformation that might impact the long-term chemical/ mineralogical properties, hence safety functions, of bentonite-containing barriers in the SFR. Based on published SR-PSU safety analyses, for example, degradation in the sorption safety-function of bentonite-containing barriers is likely to be of minor safety significance. This is because of the relatively short path lengths of such bentonite-containing barriers compared to sorption safety-functions arising from spatially larger cement and host-rock barriers. As a further caution, it also noted that the time-scales over which such potential additional chemical and bio-chemical processes might occur could be relatively long with respect to the expected duration of the safety functions for bentonite-bearing barriers. Thus, in the absence of such data, it is not possible to state the degree to which such additional impacts might, or might not, be safety significant over relevant regulatory timescales.

Based on this review, the following chemical processes/ properties affecting bentonite-containing barriers in the SFR should be considered for further confirmation to enhance regulatory confidence in SKB's safety assessment:

- Processes affecting dissolution and/or transformation of montmorillonite/ smectite (the key swelling clay that is in bentonite) at relevant SFR conditions, especially the (1) role of microbially catalyzed reactions, (2) role of reducing conditions on Fe(III) reduction to Fe(II) in octahedral sites of montmorillonite, and (3) role of cement-derive high pH pore water, with possible resulting impacts on swelling pressure and sorption properties.
- SKB's thermodynamic and structural model for water in bentonite (e.g., Birgersson et al., 2008; 2010), in which montmorillonite and the associated water are considered as a homogeneous-mixture model (HMM), differs from the views of other repository programs that are also evaluating bentonite-containing barriers (e.g., Nagra, 2014). Further independent evaluations by SSM to compare and identify possible, different long-term performance impacts among credible alternative models may be warranted.

Contents

1. Introduction

The Swedish Radiation Safety Authority (SSM) received an application for the expansion of the Swedish Nuclear Fuel and Waste Management Company's (SKB's) final repository for low and intermediate level waste at Forsmark (SFR) on the 19 December 2014 (SKB, 2014a-h). SSM is tasked with the review of the application and will issue a statement to the government for its consideration in due course. An important part of the application is SKB's assessment of the long-term safety of the repository, which is documented in the safety analysis named SR-PSU.

SSM's review is divided into an initial review phase and a main review phase. The previous initial phase of the review had a number of general objectives, including:

- A broad understanding of the application should be achieved.
- Assess if SKB's documentation is understandable and complete with regard to the information that is needed to be able to make an assessment of the application.

The key review topics for the main review phase shall be identified. These are topics that will have a significant impact on the assessment if the application fulfills relevant requirements. This assignment concerns the chemical conditions in the SFR repository and its surroundings in the main phase review. The two important aspects covered here are:

- The characterization of the present natural hydrochemical conditions at the site and;
- An assessment of how repository construction may affect the above conditions.

Previous reviews (e.g., Savage, 2016) have been published by SSM regarding how the engineered barrier systems, mainly the concrete components but also including bentonite-containing barriers, and the various SFR waste forms are expected to exert an appreciable influence on the chemical conditions within and around the repository construction. The chemical conditions are expected to gradually change over the time-scale addressed by SR-PSU, which depends both on internal transformations such of solid phases (e.g., concrete, metal, minerals), and on the external gradual dissolution and/or transformation of groundwater conditions, changes in sea level and recharge/ infiltration. As noted in Savage (2016), chemical conditions within and around the repository are important since they exert an influence on:

- The release of radionuclides from the different waste forms;
- Retardation and transport of radionuclides within the repository vaults and the surrounding bedrock;
- Interactions, alterations and degradation in safety functions of waste and engineered components in the repository.

SKB has addressed these aspects within the main scenario of SR-PSU, but also within some of the less likely scenarios and some of the residual scenarios. The following general points have been included:

- Familiarization with SKB's documentation, giving a brief account of the structure and most relevant parts as well as the safety relevance of the review.

- Suggestion of important review topics for the main review phase and a description of their importance in view of the safety assessment results.
- Where applicable, the adequacy of relevant models, data and safety functions have been assessed as well as the handling of uncertainties.
- Assessment of the need for additional information or clarifications that are deemed necessary to effectively assess the license application in depth.
- Assessment and brief evaluation of the overall quality of SKB's documentation, including a brief assessment of the structure, transparency, traceability, scientific soundness, as well as maturity of SKB's technical solutions and of SKB's methodology.

6

2. Review Document for SR-PSU

The scope of this review[1] addresses the following four areas:

- Section 3: review of the initial state of different components that contain bentonite in different parts of SKB LILW SFR repository, focusing on the initial state that are related to chemical properties of bentonite and how mineralogical and chemical properties are related to safety function parameters such as swelling pressure and hydraulic conductivity, as documented in SKB TR-14-02 and references therein;
- Section 4: review bentonite-interactions with cementitious materials and possible degradation of bentonite, as documented in SKB (2014d) and references therein;
- Section 5: review the process of phase changes/ freezing, including thermodynamic approach to assess freezing-point temperature and consequence of ice-lens formation, as documented in SKB (2014d) and references therein;
- Section 6: review the formation of, stability of, and possible enhancement of radionuclide transport by bentonite colloids as envisioned by SKB's colloid-chemistry approach, as documented in SKB (2014d) and references therein.
- Section 7 presents a brief summary of key observations and conclusions from these four review sections.

A number of reports and papers have been read and evaluated for this review and are briefly described below.

SKB (2014a) is the main report for the SR-PSU safety assessment. Initial groundwater chemistry is presented Section 4.8 (page 122-128), while Section 6 documents the reference repository evolution for the first 1 ka (kilo annum) after closure, and Sections 6.3.6, 6.3.7, and 6.3.8 describe geochemical evolution, chemical evolution of the waste domain and evolution of the engineered barriers, respectively. A comparable arrangement of descriptions for the temperate climate domain after 1 ka and periods of periglacial climate domain after 1 ka are described in Sections 6.4 and 6.5, respectively. Following the lead of Savage (2016), important quotes from the Conclusions Section of SKB (2014a, page 364 and following) are noted here regarding the safety functions and geochemical requirements of the natural and engineered barriers, including bentonite-containing barriers:

- "…the rock also provides a stable chemical environment, including anaerobic conditions which contribute to protecting reducing conditions at repository depth. Reducing conditions imply that iron corrodes only slowly

---

[1] SKB's report "Safety analysis for SFR Long-term safety: Main report" (SKB, 2014a) that is available for download from SKB's web site is marked "Revised Edition." SKB (2014d), the main source directed for review, is replete with unpublished references (page 344), unfinished sentences ("*although*", Section 3.2.5), and incomplete tables (e.g., Table 4-1). Furthermore, many of the other supporting reports also show an "update" subsequent to their initial publication. All of these deficiencies raises a quality assurance concern for this review, especially the possibility that SKB may issue future revisions of the contents of reports on which this review is based. As a matter of quality management and control, these facts must be noted and it must be stated that the reviews conducted here are valid only for versions of reports downloaded from SKB's web site as of October 31, 2016. Nor will INTERA be responsible for providing any revised comments on possible later versions of these reports.

and that the mobility of certain safety critical radionuclides (particularly radioisotopes of uranium) is low." (page 370)

- "For the Silo, the pH-buffering function of the concrete and the grout keeps gas production due to microbial activity and iron corrosion low. The choice of concrete as an engineering material also ensures good sorption properties." (page 371)
- "Sorption of radionuclides has been shown to be the main mechanisms controlling retardation in the repository. Sorption occurs mainly on the cementitious materials in barriers and waste packages. The sorption depends on the amount of available concrete surfaces, but also on the chemical composition of the water in the repository. The importance of sorption is strongly related to the chemical characteristics of individual radionuclides, including their redox state." (page 373)

Geochemical aspects of the evolution of the Forsmark site is described in SKB (2014e, Chapter 5). Regarding completeness of chemical properties and processes affecting bentonite-containing barriers, the following topics are described: rock-water interactions in the rock matrix; microbial processes; and degradation of grout. An overview of each process is provided, as well as dependence between processes and other, relevant variables. Modeling, including definition of boundary conditions, and data from experimental studies and other sources are also noted (SKB, 2014e). Safety significance within the context of the time scale of the safety assessment, as well as treatment of uncertainties are also referenced.

As a potential impact on the chemical properties and processes of bentonite-containing barriers, the chemical processes in cementitious waste and waste packaging are assessed in Sections 3.5 and 4.4 of SKB (2014c). In particular, the Höglund (2013) report on degradation of concrete and generation of high pH water is also reviewed because high-pH water might adversely impact the chemical properties of bentonite material. Höglund (2013) presents modelling of both physical and chemical processes in much greater detail than previous SKB studies (e.g., Gaucher et al., 2005; Cronstrand, 2007). As such, Höglund (2013) is extensively used in evaluating concrete degradation in SKB (2014d).

3. Initial State of Different Components that Contain Bentonite

3.1. Overview to Safety Functions/ Potential Aspects of Bentonite-based Materials in SFR

There are different bentonite-bearing components within the planned SFR (SKB, 2014a):

- Bentonite at the bottom of the Silo;
- Bentonite in plugs and transition zones;
- Bentonite in access tunnels;
- Bentonite in sealing of boreholes.

SKB (2014d, Sections 3.2.5 and 3.2.6) groups these bentonite-containing barriers into "Silo" and "Plugs and other closure components." The same grouping is adopted here.

Figure 3-1 (Figure 1-4 with caption, from SKB, 2014b) shows the approximate locations of these various bentonite-bearing components in SFR.
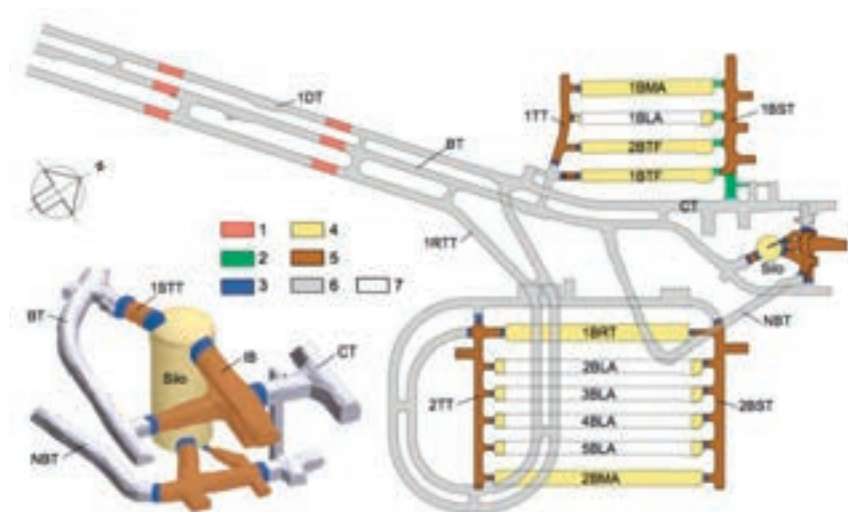
Figure 1-4. Overview of SFR after closure with detailed view of the silo. Key to numbering: 1) Plugs in access tunnels 2) Transition material 3) Mechanical plug of concrete 4) Backfill material of macadam 5) Hydraulically tight section of bentonite 6) Backfill material in access tunnels and tunnel system 7) Non-backfilled openings. Note that the figure shows Layout 2.0; Layout 1.5 is used in SR-PSU modelling. The difference that can be seen in the figure is that BRT is longer than in Layout 1.5.

Figure 3-1   Overview of Barriers, including Bentonite-bearing Components, in SFR Planned Expansion.

The initial states of these components as related to chemical properties of bentonite and associated safety functions parameters from such properties are reviewed in the

9

sub-sections below. As noted in Table 2-1 of SKB (2014b), the basic safety functions (termed "potential aspects") for bentonite-bearing components of SFR, particularly the Silo, are related to:

- Limiting advective groundwater-flow through waste-containing vaults (including hydraulic sealing);
- Mechanical stability of waste vaults;
- Sorption of radionuclides possibly released from waste vaults (especially ILW Silo).

With respect to the safety function of limiting advective flow via low hydraulic conductivity, SKB (2014a, Section 5.4.2) states:

> "The bentonite buffer surrounding the silo has a low hydraulic conductivity and will limit the water flow through the silo. However, there is a slight possibility that gas formed inside the silo will create an over-pressure that can violate this principle and expel water."

With respect to mechanical stability aspects of engineered barriers including bentonite-based materials, SKB (2014a, Section 5.4.2) also states:

> "No specific safety function for long-term safety is linked directly to mechanical stability."

In essence, the bentonite (and bentonite mixture with sand) seem to be simply "space-filling" attributes not tied to the chemical properties of the bentonite.

With respect to a sorption safety function, SKB (2014a, Section 5.4.2) states:

> "…radionuclides released [from waste packages] to the connecting tunnels will be retarded by sorption on the materials in the plugs. The greatest retention capacity for the radionuclides is found in cementitious materials… [it] should, however, be noted that the safety assessment also credits retention in other materials in the repository (such as bentonite) in the radionuclide transport calculations."

SKB (2014a, Section 5.1) states, however, that:

> "… no criteria for the safety function indicators have been defined in this [SR-PSU] assessment."

This is taken to mean specific, quantitative criteria are not defined.

Chemical and mineralogical properties of bentonite that may affect such safety functions are assessed in Section 4.2, with attention devoted to SKB's conceptual model for bentonite behavior under relevant SFR conditions. The results of this review are then applied to SKB's initial state evaluation of bentonite-bearing components in SFR's silo, plugs/ transition zone, access tunnels and boreholes/shaft seals.

10

3.2. Overview of Safety Functions of Bentonite as Related to Chemical Properties and Processes

Explicit bentonite-bearing *components* include compacted bentonite below and around waste vaults (typically as a layer between cementitious *vault* containing waste and surrounding host rock), bulk bentonite as tunnel backfilling material, parts of tunnel plugs, and parts of sealing in investigation boreholes. The requirements (safety functions) on a given bentonite-bearing component, therefore, will be different depending on the specific purpose of the component.

As an example, an important safety function can be to limit advective groundwater flow into waste-containing vaults via the natural swelling process of montmorillonite (an expanding clay) as bentonite becomes saturated with water. Another safety function can be to reduce transport of radionuclides from waste vaults, both by assuring diffusive transport and additional sorptive retardation of some radionuclides. A basic function of some bentonite-bearing components in SFR is to assist in mechanical stability of emplaced vaults through the swelling pressure of bentonite as it transitions from dry to saturated conditions. However, bentonite must not jeopardize safety functions of other SFR components by chemical or mechanical interactions. Finally, bentonite-bearing components have to retain their designated safety functions over set time intervals. This means that the bentonite-bearing component has to stay in place and that no significant mineralogical changes occurs over that time interval. This includes possible mineralogical transformation of montmorillonite, but also might include consideration of possible dissolution of soluble accessory minerals and diffusion out of the bentonite, potentially leading to lower bentonite density and thereby reduced sealing properties. Karnland et al. (2006), for example, describe and discuss SKB's basic conceptual model for assessing coupling between bentonite mineralogy and the physio-chemical properties of different bentonites.

3.2.1. Safety Function Associated with Swelling Pressure and Hydraulic Conductivity Behavior

The basic montmorillonite crystal structure is shown in Figure 3-2 (left-hand side), composed of alternating tetrahedral and octahedral sheets. A characteristic of montmorillonite particles is that they typically have negatively charged surfaces arising from substitutions in the crystal structure of Mg or Fe(II) for Al in the octahedral sheet, and also Al or Fe(III) for Si in the tetrahedral sheet.

In aqueous solutions, the negatively charged surfaces attract cations as charge-compensating ions to the interlayer spacing between montmorillonite particles. Charge-compensating cations cannot freely diffuse away from the negatively charged montmorillonite layers because of the strong electrostatic attraction. Water, however, does move to this interlayer region of charge-compensating ions (Figure 3-2, right-hand side) in order to equalize chemical potential, causing the distance between the montmorillonite layers to increase (i.e., swell).
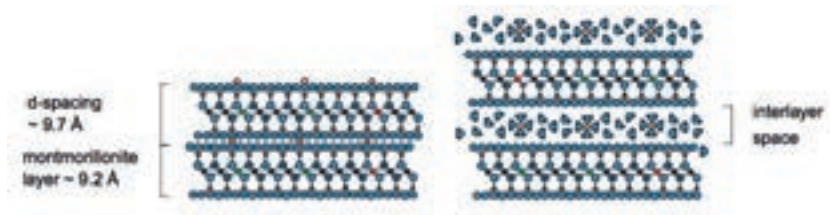
Figure 3-2   Schematic structure of dry montmorillonite (left) and hydrated montmorillonite (right). Expanded interlayer-space contains both charge-compensating cations and water molecules. (from Figure 5-5, Karnland et al, 2006).

Such water uptake will continue until chemical potentials equilibrate across the entire system (e.g., bentonite + host rock + waste- vault system). Since the rock and vault are assumed to be rigid regions, the swelling of the bentonite in its confinement between these rigid regions exerts a stabilizing pressure, usually referred to as *swelling pressure*. The behavior of different bentonites as a function of temperature, initial dry density, and groundwater compositions have been studied by SKB in the laboratory and field tests as well (Karnland et al., 2006).

The swelling properties of bentonite is strongly dependent on the valence of the exchangeable cations, leading to a general classification of bentonites into Na and Ca-types. At high bulk density, the sealing properties of *both* types of bentonite are similar, but the potential to form colloidal particles is strongly reduced at a high calcium content. Which cation dominates in the interlayer space is controlled over time by (1) the presence of accessory minerals in bentonite, and (2) the composition of the contacting groundwater.

Bentonite to be used in the SFR must have high montmorillonite content (>70%) compacted to *high* density. Increasing density generally leads to an increase in the final swelling pressure and a matching, nearly proportional decrease in hydraulic conductivity. Thus, the factors that determine swelling pressure are also applicable to deriving the hydraulic-conductivity "safety function" for bentonite-containing materials. Lower hydraulic conductivity (i.e., higher swelling pressure) of an intervening bentonite-barrier can inhibit advective flow between host rock and waste vaults. This basically decouples the waste-vault from uncertainties in future hydrological flow-conditions in the host rock.

3.2.2. Safety Function Associated with Sorption Behavior

With respect to sorption behavior, the bentonite used in assessment for the SR-PSU has the trade name GEKO/QI and is a calcium-montmorillonite product, transformed to the sodium form. In particular, the bentonite is used in the ILW Silo part of the repository, either in an unmixed form or mixed with 90% sand.

For the currently installed bentonite parts for the Silo, the Silo rests on a 1.5-meter (m) thick bed made of 90% sand and 10% bentonite. The 0.85-m diameter space between the Silo and rock wall is filled with pure granulated bentonite that has been poured into the space. The top part of the Silo, which will be installed when the repository closes, will also consist of a mixture of 90% sand and 10% bentonite GEKO/QI. As noted earlier, the safety functions of the top, bottom and walls of bentonite layers in the silo are mainly to prevent a high hydraulic flow through the Silo repository, but also to retard the diffusion of ILW radionuclides through sorption by bentonite minerals. The bentonite barrier also serves as mechanical stabilizer between the rock and the Silo.

Because "bentonite" is composed of accessory minerals in addition to the predominate montmorillonite, the exact sorption behavior of a bentonite will depend on its mineralogical abundances, plus any admixtures of additional materials such as sand. With respect to the reversible-sorption behavior of montmorillonite, Birgersson and Karnland (2009) have argued for a homogeneous-mixture model (HMM) in which all water, montmorillonite, and dissolved aqueous species are assumed to form a single homogeneous mixture. At the macroscopic level at which HMM is applied, this "mixture" in essence constitutes a single "phase." The remaining constituents (accessory minerals, etc.) are "suspended" in the montmorillonite/water mixture. These authors argue that the notion of exchangeable cations in the interlayer space demonstrates that such exchange is not a true sorption process. Given the empirical "K_d" basis of SKB's analysis of bentonite sorption in SF-PSU (SKB, 2014f; 2014h) and the relative low reliance on sorption by bentonite, the details of the HMM for montmorillonite behavior does not seem to be a vital consideration with respect to the chemically based sorption function. For a more complete discussion on HMM, see Birgersson and Karnland (2009).

Thus, there are two basic chemical processes that might affect the initial-state sorption "K_d" value for the SF-PSU bentonite-bearing materials. The first process would be mineralogical transformation/ alteration of montmorillonite, which is >75 wt.% of the bentonite. The second process would be preferential dissolution of the more soluble accessory phases in the bentonite, such as gypsum.

Unfortunately, the geochemical models employed by SKB apparently do not include alumino-silicate hydrolysis reactions. Thus, known reactions involving dissolution and precipitation of alumino-silicate minerals (especially clays) under evolving near-field conditions do not appear to be included in SDF-PSU geochemical considerations. In the past, there has been concern about smectite transformation to illite. External review (Savage, 2016) suggests that other transformations, including smectite to zeolite under elevated pH conditions, and smectite to more iron-rich clays during reducing conditions may be of greater concern. Unfortunately, SKB current geochemical models are intrinsically incapable of evaluating stability relationships and possible clay transformations.

3.2.3. Safety Function Associated with Mechanical Stability/ Erosion

Adverse impacts on the 'space-filling' mechanical stability safety-function of bentonite-containing barriers from changes in chemical properties of the bentonite itself are likely negligible.

The onset and rate of erosion of bentonite material arise from changes in the chemical properties of the contacting groundwater in the host rock (enabling or preventing formation of suspended colloidal material) and groundwater flow rate, respectively. One chemical aspect of bentonite is the long-term ion-exchange of Na^+ for Ca^{2+} in montmorillonites, with the Ca-form being less susceptible to erosion

Erosion from scouring of bentonite by high groundwater flow-rates during initial construction periods imposing strong hydraulic gradients may be a greater concern than the potential long-term formation and removal of colloidal from bentonite-containing barriers.

13

3.3. Bentonite in the Silo: initial state affecting safety functions

Among all the parts of SFR (Figure 3-1), the Silo containing ILW has the greatest degree of inclusion of bentonite-containing barriers. For the Silo, waste packages are embedded in concrete grout which, together with the compartment walls and the walls of reinforced concrete, constitute the Silo's concrete barriers.

The bentonite used for barriers in the Silo is a bentonite from Greece (Milos), with 80 wt% montmorillonite (~72% of which is converted (Pusch, 2003) from its original Ca-form to the Na-state by soda treatment). The product name of the bentonite is GEKO/QI. The concrete structure of the Silo rests on a bed of a mixture of 10% finely ground GEKO/QI bentonite and 90% sand. The bed material was applied in several layers and compacted to get the required density. By contrast, pure GEKO/QI bentonite granulate (grain size ranging between 0.1 and 20 millimeters [mm]) filled the gap between the Silo concrete walls and the surrounding host rock, although the bentonite was not compacted. Frequent measurements and tests were made of as-installed bentonite material-properties (Pusch, 2003).

SKB calculated that it would take ~25 years for water to fully saturate the bentonite and concrete portions of the Silo (Holmén and Stigsson, 2001). Thus, the water composition in the bentonite surrounding the Silo would be expected to be influences by both the surrounding groundwater composition (Auqué et al., 2013) and the high-pH pore water of the concrete, both of which can evolve over time, especially as the initially high pH concrete pore water would gradually be neutralized toward lower, albeit still highly alkaline, pH levels.

The hydraulic conductivity of the pure bentonite at the walls of the Silo is expected to vary from the bottom to the top depending on the degree of self-compacting. Pusch (2003) concluded that the hydraulic conductivity will be less than about $1 \cdot 10^{-10}$ meters per second (m/s) for all parts of the wall fill. The lower part has a hydraulic conductivity of about $9 \cdot 10^{-12}$ m/s and the upper part about $9 \cdot 10^{-11}$ m/s, while the hydraulic conductivity of the sand/bentonite in the bottom and top of the Silo will be less than $1 \cdot 10^{-9}$ m/s (Pusch, 2003).

As noted previously, the SR-PSU assumes the vast majority of radionuclides released from cement-solidified waste or concrete-embedded waste will be retarded by sorption on these cementitious materials, as well as by the surrounding host rock for certain radionuclides (SKB 2014a, g).

3.4. Bentonite in plugs and other closure components: initial state affecting safety functions

3.4.1. Bentonite in plugs

SKB (2014d, Section 3.2.6) notes that no unambiguous safety function for the plugs, backfilling and other bentonite-containing "closure components" has been defined at this stage, although it is vaguely asserted that the expectation is that such plugs and closure components will "perform well." There are noted requirements for such

14

components, however. With respect to performance and duration, SKB (2014d, Section 3.2.6) states:

- "The plugs shall limit the flow through the caverns and the silo. The design and location of the plugs shall result in a resistance of $> 2 \cdot 10^9$ s.
- The plugs shall uphold their function for at least 10,000 years. It is an advantage if they can uphold their function until the end of next glacial cycle, i.e. about 70,000 years.
- The hydraulic conductivity of the material used for backfilling tunnels and caverns shall be 10^{-5} m/s or higher."

The closure of SFR tunnel sections, by temporary or permanent tunnel plugs, will be performed by filling the tunnel sections with bentonite that are confined, in most positions, by concrete plugs for mechanical support. The function of the bentonite-filled sections is to act as hydraulic seals. The function of the mechanical seals is to confine the bentonite sections. The requirements on the bentonite in such barriers is basically to exert an expandable seal in case of fractures or volume changes in the plug bulk material, which usually is cement. A further requirement on initial conditions of such plugs is resistance to erosion ("piping"), as relatively high flow rates in adjacent rock fractures are foreseen as a consequence of initial strong pressure-gradients over the plugs.

Initially, these bentonite-containing components will be saturated by the groundwater that surrounds the SFR repository. SKB asserts reducing conditions will prevail in the SFR shortly after closure arising from the corrosion of iron-bearing materials present in the repository (Duro et al., 2012). For components also containing, or in close proximity to, cement/concrete, the composition of pore water will also be affected by the high pH pore water of such cementitious materials. The potential for accelerated mineralogical transformation of montmorillonite to non-swelling reaction products is discussed in Section 4 of this report. For plugs, the high pH conditions induced by the cement, in combination with the relatively small volumes of bentonite compared to cement in such plugs, it is judged such mineralogical alteration on expected long-term requirements is a concern for further evaluation by SKB.

The vast majority of radionuclides released from the waste vaults via the plugs will be limited by sorption in the bentonite-filled sections outside the mechanical plugs and the macadam or other backfill material in the connecting tunnels.

3.4.2. Bentonite in tunnels

The main functions of the backfilling access tunnels with bentonite are to reduce possible advective groundwater flow and radionuclide transport in the tunnels. The requirements on the bentonite material in access tunnel backfilling are basically the same as for the near-field bentonite barriers surrounding waste from a qualitative point of view, but generally lower qualitatively. This is in part because tunnel volumes are orders of magnitude larger than the near-field bentonite barriers.

With respect to the specific properties intended for tunnel backfill containing bentonite, SKB states the following (SKB, 2014b, page 113):

> "The hydraulic conductivity of the bentonite in the connecting tunnels (brown in Figure 1-4) is assumed to be less than 10^{-10} m/s, i.e. the same as

the hydraulic conductivity for the deposition tunnels in the repository for spent fuel (SKB 2010, p 151). Possible initial hydraulic conductivity is as low as $10^{-13} - 10^{-12}$ m/s (SKBdoc 1358612)[2]. The hydraulic conductivity of the low hydraulic conductivity sections in the access tunnels…is calculated from the requirement of a resistance of at least $2 \cdot 10^9$ s that correspond to $5 \cdot 10^{-10}$ m/s for a 1 m section."

Concerns about time-*dependent* impacts from mineralogical transformation of montmorillonite in bentonite of tunnel backfill would likely depend on the proximity to cementitious materials of the SFR.

3.4.3. Bentonite in borehole seals

Bentonite in borehole backfill constructions has essentially the same "low hydraulic conductivity" function as for tunnel plugs, comprised of a hydraulically tight section with bentonite surrounded by upper and lower concrete plugs for mechanical support. Vertical shafts connecting different parts of the repository need to be closed and plugged. SKB's aim is to inhibit/ prevent formation of "fast pathways" in the SFR structure within the host rock.

As summarized by SKB in qualitative terms (SKB, 2014b, pages 95-97), to accomplish this goal, the portions of the host rock with low hydraulic conductivity, the borehole seal must also have low hydraulic conductivity. In the case of positions along boreholes where the rock has high hydraulic conductivity (fractures and deformation zones), borehole sealing material requirements are only defined for mechanical stability (i.e., resistance to scoring erosion). Thus, highly compacted bentonite is planned to be used where low hydraulic conductivity sections are needed and cement-stabilized plugs are cast where the boreholes pass through fracture zones. SKB (2014b, page 96) envisions that the design of borehole seals (and other closures) can be further developed and optimized before closure of SFR.

SKB envisions the requirements are the same with respect to chemical stability, but the sealing capacity may be lower, since high pressure gradients are not foreseen. As with other bentonite-containing components, the reviewers judge that concern over possible accelerated montmorillonite transformation to non-swelling materials under high pH conditions will depend on proximity to cementitious materials in the SFR.

3.5. Chemical Processes Potentially Affecting Safety Functions of Bentonite-containing Components in SFR

This Section summarizes the chemical properties of bentonite-containing barriers as they affect safety functions or requirements for the planned expansion of the low- and intermediate-level waste SFR facility. SKB (2014a) addresses SKB's views on safety functions of barriers for the SFR:

---

[2] "SKBdoc 1358612" refers to SKB's unpublished Closure Plan, "SFR förslutningsplan" [in Swedish] (SKB, 2014a, page 392).

> *"The use of safety functions and indicators is an aid in the evaluation of safety but is not sufficient to demonstrate that an acceptable level of safety has been achieved. Nor is safety necessarily compromised if a safety function is violated, this is rather an indication that more in-depth analyses are needed to evaluate safety. Quantitative calculations are required to show compliance with the risk criterion irrespective of whether none, one or several safety functions are violated."k*

Indeed, SKB's application of safety functions seems to focus on using uncertainties in future repository evolution possibly affecting/ degrading safety functions as a basis for scenario descriptions. Table 5-2 of SKB (2014a) states the safety functions associated with bentonite-containing barriers as:

- Mechanical stability
- Limited advective transport (via assurance of low hydraulic conductivity)
- Sorption

However, no specific safety-function criteria are set, only general requirements regarding how low should be the hydraulic conductivity of various bentonite-containing components. The most notable in this regard, are hydraulic conductivities for the bentonite wall, floor and top of the Silo containing ILW.

One chemical process that could significantly affect the swelling pressure of bentonite-containing components is the chemical transformation of the swelling-clay montmorillonite, which is the dominant mineral in bentonite and results in low hydraulic conductivity. Under ambient natural conditions for the near-surface SFR, including low temperature and relatively dilute, mildly alkaline groundwater, the metasomatic transformation (i.e., requiring the additional supply of chemical components such as potassium and aluminum) of montmorillonite to non-swelling illite, is expected to take greater than 100,000 years, based on extrapolation of laboratory tests as well as the presence and persistence of such clays both within Forsmark fractures and in other comparable locations.

There are, however, several additional considerations that could possibly accelerate the mineralogical transformation of montmorillonite, with a corresponding diminishment in swelling capacity, and degradation of the "limited advective transport" safety function. These include

- *In situ* redox reactions involving Fe(II) and Fe(III) in montmorillonite lattice sites,
- Microbial mediation of inorganic reactions, and
- Elevated pH conditions arising from the presence and close proximity of massive amounts of cementitious materials within the SFR (examined in Section 4 of this report).

The lability of reducing redox-reactions converting Fe (III) to Fe (II) in octahedral positions within montmorillonite/ smectite clay has been studied since at least the 1980s (Stucki et al., 1984). Figure 3-3 shows this situation schematically. The role of bacteria in catalyzing such reactions at ambient surface temperatures has been demonstrated more recently (Kostka et al., 1999; Jinwook et al., 2004; and Vorhies and Gaines, 2009). The key point of such studies is that the reduction of octahedral Fe(III) in montmorillonite/ smectite clays to octahedral Fe(II) causes a de-stabilization in the clay, and a lowering of swelling pressure. Early studies to evaluate this impact used chemical means of reducing Fe (III) (Stucki et al., 1984).
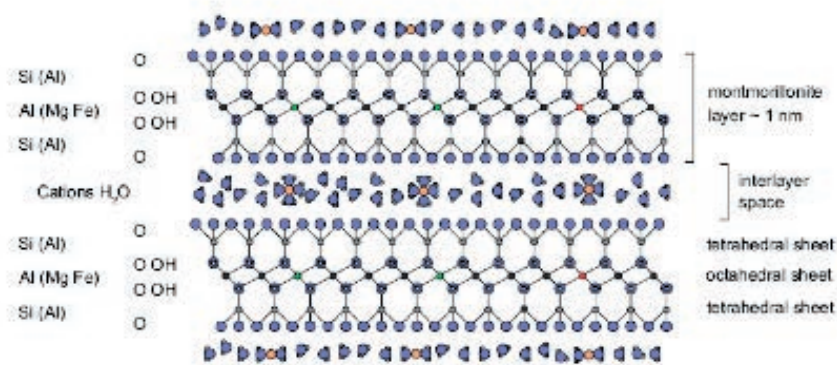
Figure 3-3   Framework structure of montmorillonite clay with initial Fe(III) ions in octahedral sites. Under reducing conditions, as argued for in SKB (2014-TR-2014-04) for the SFR, the Fe(III) ions can be reduced to Fe(II), leading to possible destabilization of the clay. (from SKB. 2006b. Buffer and backfill process report for the safety assessment SR-Can. SKB TR-06-18, Swedish Nuclear Fuel and Waste Management Co., Stockholm, Sweden).

More recently, indigenous bacteria isolated from soils and sediments have been shown to catalyze the rapid reduction of structural Fe(III) in the smectite clay minerals at Earth-surface conditions (Kostka et al., 1999). The extent of Fe(III) reduction can be large, from 46% to >90%. Furthermore, the impacts of structural Fe(III) reduction by bacteria on swelling pressure of reduced smectites can be significant, with decreases by 40% to 44% in smectites reduced by bacteria as compared to unaltered or reoxidized smectites. Clay surface areas decreased by 26% to 46% in response to bacterial reduction, while the surface charge density as measured by the ratio of cation exchange capacity to specific surface area increased. The valence state of Fe in the octahedral layer of smectite was measured through reflectance spectra, correlated to the amount of Fe(III) reduced in bacterial cultures, indicating the mechanism of intervalence electron transfer in bacterially reduced clay minerals. The extent of reduction and surface chemical effects catalyzed by bacteria found by Kostka et al. (1999) was approximately the same as previously observed for potent inorganic reductants.

Subsequent studies have extended the understanding of impacts and wide-spread occurrence in nature of microbially-catalyzed Fe(III) reduction in smectites. Kim et al. (2004) show that the classic understanding of temperature, pressure, and time thought to control the diagenetic smectite-to-illite (S-I) reaction utilized in petroleum exploration now needs to also consider the role of bacteria. They demonstrated that microorganisms can promote the S-I reaction by dissolving smectite through reduction of structural Fe(III) at room temperature and 1atmosphere within 14 days. To be observed in a laboratory context, this same S-I reaction typically requires conditions of 300° to 350°C, 100 megapascals, and 4 to 5 months in the absence of microbial activity. Vorhies and Gaines (2009) present natural analogue evidence that such bacterially-mediated catalysis under Earth-surface conditions may be more widespread than previously considered.

Taken together, these various microbial studies challenge the conventional concept of extremely slow S-I reaction kinetics. They suggest that microbially catalyzed Fe(III) reduction in montmorillonite might play an important role in the long-term chemical stability and properties of montmorillonite in the SFR, perhaps adversely

18

affecting the safety function of high swelling pressure/ low hydraulic conductivity. SKB (2014d, page 235) recognizes this vulnerability:

> *"Microbial destabilization of montmorillonite due to iron reduction could be considered. It has been readily demonstrated that this process can occur with ferruginous nontronile-type clays (Kostka et al. 2002, Kim et al. 2004). It is not known to what extent a similar process can proceed with the type of clays to be used in the Silo."*

The statement of *"…could be considered…"* is, however, rather vague and disconcerting, given the importance of the low-hydraulic conductivity property assumed for bentonite in barriers for the ILW Silo and tunnel/ shaft plugs. Attempting to make a distinction between SFR montmorillonite and "ferruginous nontronite-type clays", hardly a key difference since both montmorillonite and nontronite are dioctahedral smectites, does not squarely address this concern. A more direct and confidence-building response would be to replicate both the cited Fe (II/Fe(III) and microbial studies on possible accelerated alteration of SFR montmorillonite. Such studies should be rather easy to be conducted. Instead, the apparent focus of recent and current SKB microbial studies seem to be limited to (1) sulfate reduction, and (2) degradation of cement waste forms under high pH conditions. While such studies are also of worth, investigating possibly more rapid degradation of the safety function of initially low hydraulic conductivity of bentonite-containing barriers seems of even higher priority. This same concern over degradation of low conductivity via more rapid degradation of montmorillonite in bentonite-containing barriers equally applies to concerns over the impact of elevated pH conditions within the SFR (see Section 4).

4. Bentonite-Interactions with Cementitious materials and Possible Degradation of Bentonite

Bounding calculations by SKB estimate that it will take ~25 years for water to fully saturate the silo, surrounded with bentonite (Holmén and Stigsson, 2001). At the same time, the cement-conditioned waste will also be saturated, as modeled by Holmén and Stigsson (2001). Cronstrand (2014) provides a somewhat simplistic reactive-transport analysis of the evolution of pH in the SFR, modeling the system as a homogeneous mixing tank with advective flow, assuming thermodynamic equilibrium between different solid materials. Based on these rather conservative assumption (i.e., neglect of reaction kinetics and evolution in advective flow conditions), the pH throughout the SFR is predicted to be remain buffered above 12 for at least 10,000 years. The one exception is the BLA, in which a combination of higher flow rates and low content of cement and concrete leads to a more rapid decline (although still remaining strongly alkaline) pH evolution for BLA than for the other parts of the SFR.

To reiterate, bentonite-containing barriers of the SFR achieves "low hydraulic conductivity" safety functions due to the swelling of montmorillonite. Transformation of montmorillonite (a smectite clay) to non-swelling minerals such as illite (S-to-I) is observed in nature, but occurring only after time periods greater than 100,000 years under near-surface conditions in the Earth. As noted in Section 3, however, there are certain chemical (strongly reducing conditions) and biochemical factors that have been found that can possibly accelerate such mineralogical transformation of montmorillonite.

In addition, high pH, alkaline conditions can also accelerate this mineralogical transformation (Koskinen, 2013). It has long been recognized from experimental studies that the conversion of smectite to illite-smectite can occur in a matters of days, weeks to months at low temperature in high-pH solutions (Eberl et al., 1993; Fernández et al., 2009b). The possible "accelerant" role of high pH, arising from groundwater reacting with cementitious portions of the SFR, is therefore of concern. This could be a key chemical-reactivity factor to be considered for the Silo of SFR, for example, given the contact of bentonite-containing barriers that surround the inner cementitious ILW.

The chemical reactions between cementitious materials and pore water for the SFR are thoroughly examined by Savage (2016).

SKB's views on this concern are presented in SKB (2014d). It is acknowledged that montmorillonite transformation is relevant for bentonite in the presence of highly alkaline solutions. SKB asserts that resolution of this concern, however, is difficult because of great uncertainty regarding reaction pathways and products, as well as regarding kinetic controls on the transformation reaction.

In response to these uncertainties and complexities, SKB notes that cement–clay interactions have been studied in the EU-project ECOCLAY-II (EC, 2005). Based on these studies, it is asserted (2014d, page 223) that SKB's *"simplified but reasonably realistic view"* of the transformation process considers that montmorillonite dissolution in highly alkaline solutions liberates Al, Si, Mg and Na ions. Under closed-system (metamorphic) conditions, these released elements can then re-precipitate in the form of a range of silicates and aluminosilicates (Gaucher

20

et al., 2005). These minerals will have different properties from the original montmorillonite, in particular lower swelling properties and higher molar volumes, which act in opposite ways with respect to possible changes in hydraulic conductivity of the original bentonite material.

In the reviewers' judgement, SKB's ability to assess exactly what phases might form is confounded by the Ostwald Step-rule, a well-known empirical observation in low-temperature geochemistry (e.g., Dibble and Tiller, 1981). Simply stated, at the low-temperature, near-surface conditions of the Earth, it is observed that the dissolution of unstable mineral phases initially leads to precipitation of metastable assemblages of minerals/solids, rather than precipitation of the most thermodynamically stable assemblage of minerals. Therefore, depending on pore-water composition and kinetics, a wide range of possible metastable assemblages may form, in many cases complex solid-solution phases with variable degrees of crystallinity. Open-system (metasomatic) conditions, with the influx of additional dissolved elements (i.e., K, Ca) supplied by dissolution of cementitious solid phases or from groundwater of the site, further complicates the ability to confidently assess through thermodynamic modeling the initial reaction products from montmorillonite dissolution.

Relying on the ECOCLAY-II results and interpretations by Gaucher et al. (2005), SKB (2008; 2014d) advocates the following general reaction-pathway for the case of for montmorillonite dissolution when exposed to highly alkaline solutions (with a low potassium content) as follows (see SKB 2008):

montmorillonite
↓
beidellite (a clay mineral of the smectite type)
↓
saponite (also a 2:1 clay mineral); chlorite (clinochlore)
↓
zeolites (hydrated aluminosilicates such as analcime, chabazite, mordenite and phillipsite)
↓
gismondine (hydrated aluminosilicate, also of the zeolite type); gyrolite (silicate without aluminum)

SKB acknowledges that this reaction pathway must be viewed as one out of several possible sequences of reactions, given the uncertainties noted above. SKB also notes that if the alkaline fluid is rich in potassium, illite can be formed, possibly followed by formation of phillipsite.

As to the performance assessment impacts on the 'low hydraulic conductivity' safety-functions of bentonite-containing materials in SFR, SKB (2014d, page 228) finishes by stating:

> *"In comparison to the originally present montmorillonite, the secondary phases according to the above summary have a high molar volume, which presumably would tend to reduce or block the available porosity. On the other hand, these minerals do not possess the ability to swell, which would lead to a drop in, or complete loss of, swelling pressure. Depending to which degree the discussed transformations take place, a loss of barrier functions cannot be excluded. The modelling by Gaucher et al. (2005) indicates a nearly complete disappearance of montmorillonite in the long term, while other studies (Cronstrand 2007, Fernández et al. 2009a)*

indice a significantly smaller effect (see model studies/experimental studies."

Given this acknowledged uncertainty in current data, a more complete analysis of factors leading to such disparate results ought to be evaluated by SKB.

SKB speculates (Section 6.6.2 of the Main Report) that zeolites that may form more strongly sorb radionuclide cations, so that these replacement phases should be as good or better sorbants than the original bentonite. By 17,500 years, SKB expects that more than one third of the total quantity of montmorillonite in the bentonite may be transformed to other minerals (SKB, 2014a, Section 6.6.), and all the montmorillonite is expected to be altered after 100,000 years (SKB, 2014a, Section 6.6.). However, confidence in estimating rates of montmorillonite transformation based on studies such as Gaucher et al., (2005) is severely undercut by two acknowledged limitations to their model and input data:

- There is no consideration of any evolution of the porosity, which would affect the rate of diffusion of chemical components into the bentonite pore water, and
- There is no consideration of the dissolution kinetics of the clays, zeolites and cement phases, admittedly due to sparse kinetic-reaction-rate data for some of these phases.

SKB (2014d) cites Smellie (1998) regarding possible insights to clay reactions under natural high pH conditions in the Maqarin (Jordan) natural analogue site. Of course, the "clay" at the Maqarin site is a non-swelling clay phase as a minor phase in a limestone matrix. Hence, the analogy to the SFR may be a bit of a reach, and is also somewhat at odds with SKB's (2014d) earlier attempt to make a distinction between SFR "montmorillonite" and "nontronite-type clays" used in microbial alteration studies, given that both montmorillonite and nontronite are dioctahedral smectites.

Finally, there is the consideration of how pH conditions might affect the sorption safety function of bentonite-containing barriers. In general, cations sorb more strongly at higher pHs because of negatively charged surfaces of minerals, while the opposite is generally true for anions. The presence of organic ligands and carbonate can complicate this view, because such ligands form negatively charged complexes cations, thus mitigating their sorption potential. However, the high pH and high calcium concentrations in cementitious materials necessarily means that the carbonate concentration is low, because it is controlled by the calcite precipitation. In the similar manner, high pH values and high calcium concentrations can constrain the concentration of other ligands, such as oxalate, to low values. Still other ligands, such as α-isosaccharinic acid, sorb to cement, perhaps from complexation with calcium-rich solid phases. Overall cement-pore water reactions attenuate the concentrations of ligands that might otherwise inhibit the sorption of numerous radionuclides. Until and unless the minerals of the cement matrix are completely reacted, the pH in cement pore waters can be expected to be higher than about 10.5, where high pH should promote favorably high sorption properties in the SFR.

5. Phase Changes/Freezing Potential Considerations on Bentonite-Bearing

Permafrost formation and possible mechanical effects on bentonite-containing materials is first treated in the global warming variant of SKB's main scenario. It assumes the onset of permafrost at 52,000 years, with additional episodes of permafrost occurring before the end of the assessment timeframe at 100,000 years. It is assumed there would be no groundwater flow or radionuclide transport during permafrost periods (Section 8.3.1 of the Main Report). As a further exploration of possible permafrost effects, SKB also considers an early periglacial variant of the main scenario arising during a period of minimum insolation between 17,500 years and 20,500 years. The basic boundary-condition assumptions are identical to the global warming variant, with the exception that conditions during this early periglacial period are considered to be less cold than during later periglacial periods, such that permafrost is discontinuous rather than continuous. This assumption leads to consideration of that groundwater flow is only reduced but not completely stopped, with groundwater discharge restricted to taliks. The treatment of permafrost scenarios for the SR-PSU is thoroughly reviewed by SSM (Klos et al., 2016).

If permafrost reaches the repository, an ice lens may form in the bentonite-containing barriers of the Silo at SFR. SKB considers (SKB, 2014a, Section 6.6.2) that ice-lens formation could occur during either early or later (colder) periglacial periods. SKB (2014d, pages 47-48) considers a wide range of factors that may affect the actual freezing point and rate of freezing of sub-surface structures at the SFR, including freezing point of water decreasing with increasing pressure, freezing point depression due to concentration of solutes, freezing point depression due to small confining volume, and effects of pre-melting and temperature gradients related to frost heaving and repeated cycles of freezing and thawing may cause particle sorting which would likely change hydraulic properties. SKB (2014d, page 49) also notes coupling of freezing processes with other processes such as heat-transfer, elevated stresses from overburden and liquid pressure, and water transport. The complex set of interactions of mechanical forces and resulting physical deformations in porous media from permafrost/ ice-lens heaving are well-summarized by Remple (2010).

SKB developed and tested a thermodynamic model of freezing in saturated bentonite (e.g., Birgersson et al., 2008; Birgersson et al., 2010).The model predicts a strong temperature-dependence of changes in swelling pressure at temperatures below 0°C due to entropy differences between the clay-water system and a reference system consisting of liquid water and ice. This dependence affects the freezing-point temperature in a manner that is analogous to the effects of freezing-point depression in salt solutions, where freezing point temperatures decrease with increasing salt content. Because the temperature-dependence of the equilibrium vapor pressure in an ice-water system differs from that in a clay-water system, a critical temperature exists where the two pressures are equal. SKB's model predicts that the swelling pressure is completely lost at this critical temperature. Water is transported out of the clay below this temperature to form a discrete ice phase, or ice "lens" (Norrish and Rausell-Colom, 1962).

SKB's thermal/freezing modeling of permafrost (SKB, 2014d, Section 5.1) envisions that the bentonite-containing barriers in the Silo will gradually be mechanically displaced or otherwise physically disrupted as ice lens grow. With climatic warming, ice lens will melt, but the swelling properties of the bentonite are expected to be locally degraded. SKB cites simulations that show an order of magnitude increase in water flow in the affected bentonite volume. SKB further

asserts, however, that a limited change of this magnitude in the Silo bentonite-containing structures would still effectively limit the amount of water that can penetrate to the waste. In part, this assertion seems to be based on considerations of heterogeneity in the freezing phenomena within SFR structures, and on the assumption that flow properties of concrete barriers will not be mechanically degraded during the early period of permafrost.

With respect to any degradation in the swelling pressure properties of bentonite, however, bentonite samples tested up to seven freezing/thawing cycles showed the decreases (becoming zero at the critical freezing temperature for bentonite) and increases in swelling pressure due to temperature changes show such changes in swelling pressure to be fully reversible (Birgersson et al., 2010). Thus, the physical impacts of freeze/thaw from a permafrost event on the low hydraulic conductivity of bentonite-containing materials seems to be relatable only to physical displacements of the bentonite rather than to any permanent change in the bentonite swelling properties.

In the reviewers estimation, all of these permafrost processes represent, however, *physical changes* (i.e., a change not involving a change in the substance's chemical identity), rather than *chemical changes* (i.e., initial solids are not changed into new compounds). The hydraulic conductivity and probably mechanical stability safety functions of bentonite-containing barriers of the Silo may be degraded from permafrost conditions. The occurrence of permafrost conditions and associated physical modification of such barriers, however, has nothing to do with any change in chemical properties or processes. Degradation in hydraulic conductivity arising from physical damage/ deformation of the bentonite, not any mineralogical transformation or degradation of montmorillonite. There is no change in the sorption properties of deformed bentonite-containing barriers, although there may changes in the physical shape and dimensions in transport pathways that need to be considered in subsequent modeling of sorption in such deformed barriers.

There is a potential geochemical impact from the migration of a freezing front through the SFR, potentially leading to increased salinity of groundwater through 'salt exclusion' (SKB, 2014e; Section 5.11). Increased salinity of pore water in bentonite-containing materials would slightly decrease its swelling pressure, hence, low hydraulic conductivity safety function. Furthermore, the increase concentrations in dissolved species in bentonite pore-water below the freezing front (hence, capable of radionuclide transport) might lead to some decrease in the sorption properties of the bentonite through 'competitive-ion' effects. However, the SR-PSU safety analysis does not assign much credit to sorption by bentonite, except for the LILW Silo portion of the SFR. Addressing such possible chemical impacts of increased salinity on swelling pressure and sorption properties could be easily assessed from current test data on bentonite, perhaps supported by confirmatory tests where appropriate.

6. Formation of, Stability of, and Possible Enhancement of Radionuclide Transport by Bentonite Colloids

SKB judges (SKB 2014, TR-2014-04, Sections 5.4.5, 6.4.4, 7.4.5, 8.4.4 and 9.4.4) radionuclide-bearing colloids will not be stable within pore waters of cementitious waste forms which have high ionic strength and high dissolved Ca^{2+} concentrations. Furthermore, the transport of any radionuclide-bearing colloids through barriers containing compacted bentonite is deemed negligible, because of the low hydraulic conductivity and small pore-sizes of such barriers.

More importantly, SKB (2014d, Sections 7.4.12 and 10.4.9) examines the bentonite-colloid formation and so-called "chemical erosion" for bentonite-containing barriers of the SFR Silo and "plugs and other closure components", respectively. The SKB conceptualization of "chemical erosion" is summarized as (SKB 2014d, page 233):

> *"Openings in the confining walls (e.g. intersecting fractures) mean a local loss of swelling restriction, and localised swelling may continue into such openings until a thermodynamic equilibrium is reached. Such free swelling may lead to separation of individual clay platelets (or of small stacks of platelets), resulting in a dispersion of the clay. Depending on flow conditions, the dispersed portions of the clay could be transported away with the groundwater as individual colloidal particles.*
>
> *The dispersion behaviour of montmorillonite is strongly dependent on the valence and concentration of the ions in the porespace. Dispersion (formation of a clay sol) from aggregated clay (clay gel) is mainly relevant in the presence of dilute groundwaters and especially at low concentrations of divalent groundwater cations (Ca, Mg). For the parameter space of simple mono- and divalent cations (with a monovalent counter-anion), Birgersson et al. (2011) outlined the compositional field where the formation of clay dispersions is possible. They identify two limiting conditions for avoiding the formation of a clay sol (see Figure 7-2):*
>
> - *The ionic strength of the external solution needs to be ≥ 25 mM.*
> - *The fraction of the divalent ion in the clay needs to be $\geq 90\%$."*

Figure 6-1 summarizes these two constraints regarding the chemical-environmental conditions in which an erodible sol-gel of bentonite colloids might be removed into flowing fractures intersecting a bentonite-containing barrier. According to SKB, the yellow region represents the region in which sol-gel formation can occur, and for chemical conditions outside of this region no "erodible" sol can form and persist.
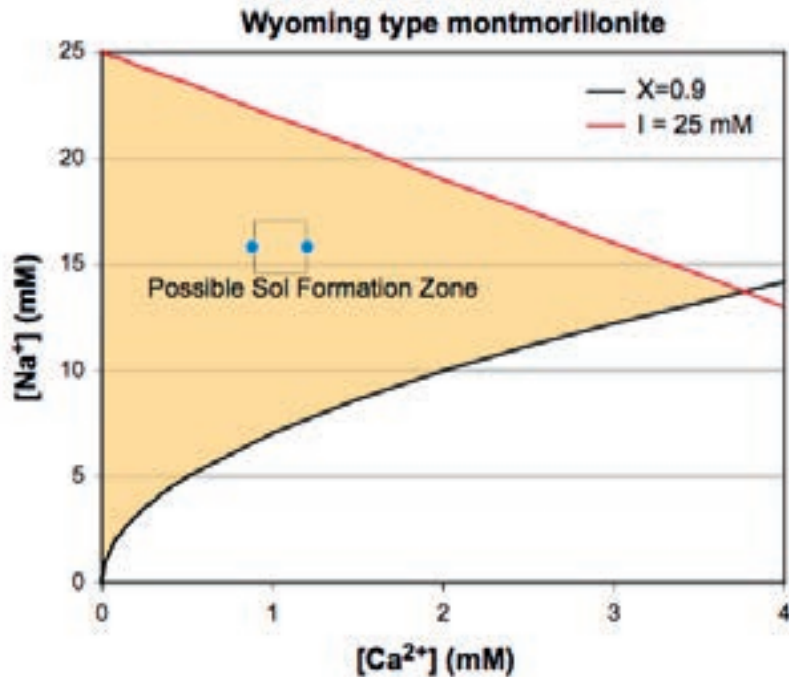
Figure 6-1.   Outline of the parameter space for the possible formation of a disperse sol of Wyoming type montmorillonite in equilibrium with an external Ca/Na-chloride solution. The lower curve (X=0.9) represents a Ca fraction ≥ 0.9 in the clay, the upper curve represents an ionic strength ≥ 25 mM (which is the CCC for Wyoming-type montmorillonite in NaCl solution (Birgersson et al. 2010, 2011). [Caption is the direct quote for Figure 7-2 in SKB (2014d)].

In addition to attempting to outline a colloid-stability region for chemical erosion as illustrated in Figure 6-1, SKB (2005) also developed a "force-balance model" based physical (including rheological) factors to estimate the rate of such erosion into flowing fractures having dilute groundwater. The chemical and physical bases for colloid stability and "chemical erosion" rate have been previously reviewed for SSM, including implications as to long-term safety (Apted et al., 2010). The formation of bentonite colloids for SKB's model is based on the DLVO theory (Kruyt, 1952; Neretnieks et al., 2009). This theory assumes that the stability of an aqueous colloidal system is controlled by a balance between electrostatic forces, which tend to repel particles of like charge, and attractive forces arising from van der Waals interactions. Both the limitations and conservative aspects of the DLVO theory as applied to bentonite used in geological disposal systems are reviewed in Apted et al (2010). The consensus view was that the conceptual basis of DLVO theory is substantially correct and appropriate for use as outlined by SKB, but that the DLVO theory oversimplifies the properties of real colloids, and omits certain factors that might be important under certain circumstances. As one example, montmorillonite colloids carry a net negative charge on faces oriented parallel to the dominant tetrahedral-octahedral-tetrahedral layering, and, depending on pH, net positive or negative charges on edges that are oriented normal to this layering. Thus, edge-face attractive forces might lead to particle agglomeration (i.e., loss of colloidal dispersion) even in dilute groundwater conditions (Birgersson et al. 2010).

For the SR-PSU, SKB (2014d, page 233) evaluates the formation of bentonite colloids as unlikely for several reasons. The first reason is that even for time periods up to 100,000 years after repository closure, SKB asserts that the cement-modeling results of Gaucher et al. (2005) indicate that Ca^{2+} concentrations at the bentonite–shotcrete (fractured host-rock) interface of the SFR Silo are expected to be well above the concentration necessary to suppress the dispersion of clay to form a sol (i.e., far to the right of the intersection of the black and red lines in Figure 6-1). This a key point, because it is intended to apply broadly, both in time (out 100,000 years) and space within the SFR.

However, the authors of this report have the opinions that the modeling approach adopted by Gaucher et al. (2005) provides a rather limited basis on which to assure confidence in this important claim by SKB. Gaucher et al. (2005) has been criticized on a number of issues (Savage, 2016). A far more reliable basis for SKB assertion of high Ca^{2+} concentrations would seem to the modeling study by Höglund (2013). This report is a more thorough treatment of concrete degradation processes (chemical and physical) based on the PHAST code (Parkhurst et al., 2004) to model the reactions of concrete in the different waste vaults at SFR with different groundwater types. As noted by Savage (2016), Höglund (2013) is a major improvement on the previous Gaucher et al. (2005) SFR study. Höglund (2013) takes into account different thermodynamic databases (e.g., MinteqCem2001 - Höglund, 2001; Cemdata07 - Matschei et al., 2007), making it a much more robust approach regarding concrete degradation. Clearly, although Höglund (2013) also supports the view of elevated Ca^{2+} concentrations necessary to prevent stability of bentonite colloids, there remain uncertainties regarding the degree of reactions over different temporal and spatial scales, that are acknowledged and evaluated by Höglund (2013) in a transparent manner.

In addition to the evaluation and argumentation of by Höglund (2013), there is a second reason that SKB (2014d, page 233) argues will limit, if not exclude, chemical erosion of bentonite-containing materials in the SFR. Recent experimental test data from Birgersson et al. (2011) show that the upper boundary of the sol formation zone (red line shown in Figure 6-1) should be much lower, shrinking the chemical conditions under which erodible bentonite-colloid sols can form. The test results are extensive and provide more convincing evidence than in past experiments.

Independent laboratory tests by the Finnish disposal program evaluating bentonite barriers also finds that Ca-bentonite is particularly resistive to chemical erosion (Posiva 2012; 2016).

7. Summary

This review addresses chemical properties, together with processes that involve or impact such properties, of bentonite-containing barriers for the planned expansion of the low- and intermediate-level waste SFR facility. Relevant reports that are part of SKB's overall SR-PSU safety analysis are the basis of this review.

The review has been conducted with regard to:

- Scientific soundness,
- Technical reliability, and
- Pedagogical quality

The SR-PSU reports reviewed provide clear and traceable documentation regarding possible processes effects on safety functions of bentonite-bearing barriers. The laboratory, field and analogue evidence presented in the various SR-PSU reports on these processes are of high scientific quality, and use of multiple lines of arguments enhances the reliability of the interpretations that SKB has made.

Bentonite is used in different parts of the SFR, due to its unique physical and mechanical properties, as well as its relative stable chemical properties in the disposal environment. There are three basic safety functions associated with bentonite-containing barriers within the SFR:

- Low hydraulic conductivity,
- Sorption, and
- Mechanical stability.

This report reviews chemically based properties of bentonite/ montmorillonite, and possible chemical and mineralogical changes that might arises to change such retardation safety-functions.

Bentonite is dominantly composed of montmorillonite which displays a high swelling pressure. This property is directly linked to the safety function of "low hydraulic conductivity" for bentonite-containing barriers, assuring low solute diffusivity. Low hydraulic conductivity is of particular importance for the LILW Silo of the SFR, as well as plugs and other closure barriers.

Bentonite also contributes sorptive-retardation for certain cationic radionuclides potentially released from various waste-disposal sites within the SFR. In particular, the LILW Silo portion of the SFR uses bentonite as a fill between the concrete waste and the wall of the bedrock, and relies on this sorption safety function of bentonite to a greater extent than other waste-disposal sites within the SFR.

The third safety function is mechanical stability. Bentonite-containing materials are used as space-filling materials with low hydraulic conductivity to stabilize waste vaults, tunnels, plugs and seals.

The SR-PSU scenario analyses on "bentonite degradation" examine several types of processes potentially degrading the safety functions of bentonite-containing barriers:

- Mineralogical transformation of montmorillonite enhanced by microbial catalysis or contact with high pH pore water from SFR cementitious wastes,

- Freeze/thaw and potential development of ice-lens within bentonite from future glacial conditions, and
- Erosion of bentonite colloids, formed upon contact with dilute groundwater, into flowing fractures intersecting bentonite.

Enhanced rates of mineralogical transformation of montmorillonite from microbial catalysis is acknowledged based on experimental studies reported in peer-review literature, but definitive tests replicating these experiments using the specific montmorillonite from the planned SFR bentonite have not been conducted, nor were any plans identified to do so. SKB's approach to enhanced montmorillonite transformation in high pH solutions seems to rest on reactive-chemical modeling. The potential role of reduction of Fe(III) ions to Fe(II) under expected SFR conditions, thereby destabilizing the initial montmorillonite, has not been identified, however.

With respect to ice lens formation, there are chemical aspects affects the rate and spatial extent of freezing. However, the actual impacts on safety functions arise from purely physical processes and changes, not chemical changes, in the bentonite.

Regarding the potential for 'chemical erosion' of bentonite colloids into host rock-fractures, SKB basically presents the same empirical model used for the safety assessment of its spent fuel repository (Neretnieks et al., 2009). This involves (1) consideration of the necessary dilute chemical environment under which bentonite (clay) colloids can stably form, and (2) a force-balance model for estimating the rate of removal of such colloids into flowing fractures. With respect to attaining the necessary chemical environment within the SFR, SKB supporting reports argue that (1) concentrated, Ca^{2+} pore water from adjoining cementitious waste will prevent colloid formation, and (2) recent experimental studies show the actual chemical environment in which bentonite colloids can stably form is much more restricted (i.e., extremely dilute) than previously presumed.

It is concluded from this review that (1) the SKB reports and analyses regarding reported chemical properties of bentonite-containing barriers, and processes that involve or impact such properties, within the planned SFR expansion are of good scientific quality, with reasonable, transparent and traceable treatment of uncertainties for the models and data that are reported; (2) with respect to completeness, however, there is under-representation and lack of appropriate attention for certain chemical processes and biologically mediated montmorillonite transformation that might impact the long-term chemical/ mineralogical properties, hence safety functions, of bentonite-containing barriers in the SFR. Based on published SR-PSU safety analyses, for example, degradation in the sorption safety-function of bentonite-containing barriers is likely to be of minor safety significance. This is because of the relatively short path lengths of such bentonite-containing barriers compared to sorption safety-functions arising from spatially larger cement and host-rock barriers. As a further caution, it also noted that the time-scales over which such potential additional chemical and bio-chemical processes might occur could be relatively long with respect to the expected duration of the safety functions for bentonite-bearing barriers. Thus, in the absence of such data, it is not possible to state the degree to which such additional impacts might, or might not, be safety significant over relevant regulatory timescales.

Based on this review, the following chemical processes/ properties affecting bentonite-containing barriers in the SFR should be considered for further confirmation to enhance regulatory confidence in SKB's safety assessment:

- Processes affecting dissolution and/or transformation of montmorillonite/ smectite (the key swelling clay that is in bentonite) at relevant SFR conditions, especially the (1) role of microbially catalyzed reactions, (2) role of reducing conditions on Fe(III) reduction to Fe(II) in octahedral sites of montmorillonite, and (3) role of cement-derive high pH pore water, with possible resulting impacts on swelling pressure and sorption properties.
- SKB's thermodynamic and structural model for water in bentonite (e.g., Birgersson et al., 2008; 2010), in which montmorillonite and the associated water are considered as a homogeneous-mixture model (HMM), differs from the views of other repository programs that are also evaluating bentonite-containing barriers (e.g., Nagra, 2014). Further independent evaluations by SSM to compare and identify possible, different long-term performance impacts among credible alternative models may be warranted.

References

Apted, M., R. Arthur., D. Bennett D. Savage, G. Sällfors and H. Wennerström (2010) Buffer erosion: An overview of concepts and potential safety consequences, SSM 2010:31, Swedish Radiation Safety Authority, Stockholm, Sweden.

Auqué L., M. Gimeno, P. Acero, J. B. Gómez (2013) Composition of groundwater for SFR and its extension, during different climatic cases, SR-PSU. SKB R-13-16, Swedish Nuclear Fuel and Waste Management Company, Stockholm, Sweden.

Birgersson M., M. Hedström, O. Karnland (2011) Sol formation ability of Ca/Na-montmorillonite at low ionic strength. *Physics and Chemistry of the Earth, Parts A/B/C*, 36, 1572–1579.

Birgersson M., O. Karnland, U. Nilsson (2008) Freezing in saturated bentonite-A thermodynamic approach, *Physcis and Chemsitry of the Earth*, 33, 5527 – 5530.

Birgersson M., O. Karnland (2009) Ion equilibrium between montmorillonite interlayer space and an external solution – Consequences for diffusional transport. *Geochimica et Cosmochimica Acta*, 73, 1908–1923.

Birgersson, M., O. Karnland, U. Nilsson (2010) Freezing of bentonite: Experimental studies and theoretical considerations, SKB Technical Report TR-10-40, Swedish Nuclear Fuel and Waste Management Co., Stockholm, Sweden.

Cronstrand, P. (2007) Modelling the long-time stability of the engineered barriers of SFR with respect to climate changes, SKB Report R-07-51, Swedish Nuclear Fuel and Waste Management Company, Stockholm, Sweden.

Cronstrand, P. (2014) Evolution of pH in SFR 1, SKB Report R-14-01, Swedish Nuclear Fuel and Waste Management Company, Stockholm, Sweden.

Dibble, W. and W. Tiller (1981) Kinetics model of zeolite paragenesis in tuffaceous sediments. *Clay and Clay Minerals*, 29(5), 323-330.

Duro, L., C. Dominech, M. Grivé, G. Roman-Ross, J. Bruno, K. Källström, K. (2014) Assessment of the evolution of the redox conditions in a low and intermediate level nuclear waste repository (SFR1, Sweden). *Applied Geochemistry*, 49, 192-205.

Eberl, D., B. Velde and T. McCormick (1993) Synthesis of illite-smectite from smectite at earth surface temperatures and high pH, *Clay and Clay Minerals*, 28, 49-60 C, 2005.

Fernández R., J. Cuevas, U. Mäder (2009a) Modelling concrete interaction with a bentonite barrier. *European Journal of Mineralogy*, 21, 177–191.

Fernández R., U. Mäder,M. Rodríguez, R. Vigil De La Villa, J. Cuevas (2009b) Alteration of compacted bentonite by diffusion of highly alkaline solutions. *European Journal of Mineralogy*, 21, 725–735.

Gaucher, E. C., C. Tournassat, and C. Nowak (2005) Modelling the geochemical evolution of the multi-barrier system of the Silo of the SFR repository, SKB Report

R-05-80, Swedish Nuclear Fuel and Waste Management Company, Stockholm, Sweden.

Höglund, L. (2001) Project SAFE. Modelling of long-term concrete degradation processes in the Swedish SFR repository, SKB Report R-01-08, Swedish Nuclear Fuel and Waste Management Company, Stockholm, Sweden.

Höglund, L. (2013) The impact of concrete degradation on the BMA barrier functions, SKB Report R-13-40, Swedish Nuclear Fuel and Waste Management Company, Stockholm, Sweden.

Holmén, J. G. and M. Stigsson (2001) Modelling of future hydrogeological conditions at SFR. SKB R-01-02, Svensk Kärnbränslehantering AB.

Karnland, O., S. Olsson, A. Dueck, M. Birgersson, U. Nilsson., T. Hernan-Hakansson, A.K. Pedersen, S. Nilsson, T.E. Eriksen, B. Rosborg (2009) Long term test of buffer material at the sp Hard Rock Laboratory, LOT project. Final report on the A2 test parcel, SKB Report TR-09-29, Swedish Nuclear Fuel and Waste Management Company, Stockholm, Sweden.

Karnland, O., S. Olsson, U. Nilsson, P. Sellin (2006) Mineralogy and sealing properties of various bentonites and smectite-rich clay materials, SKB Report TR-06-30, Swedish Nuclear Fuel and Waste Management Company, Stockholm, Sweden, 2006.

Jinwook Kim, Hailiang Dong, Jennifer Seabaugh, Steven W. Newell, Dennis D. Eberl (2004) Role of microbes in the smectite-to-illite reaction, *Science*, 303 (5659), 830-832.

Klos, R., A. Wörman, and G. Shaw (2016) SR-PSU Review of dose assessment landscape models, in in SSM's External Experts' Reviews of SKB's Safety Assessment SR-PSU- Radionuclide transport, dose assessment, and safety analysis methodology, SSM Technical Note 2016-09, Swedish Radiation Safety Authority, Stockholm, Sweden.

Koskinen, K. (2013) Effects of cementitious leachates on the EBS, Posiva Report 2013-04, Posiva Oy, Eurajoki, Finland.

Kostka, J., J. Wu, K. Nealson, and J. Stucki (1999) The impact of structural Fe(III) reduction by bacteria on the surface chemistry of smectite clay minerals, *Geochimica et Cosmochimica Acta*, 63, 3705–3713.

Kruyt, H. R. (ed.) (1952). *Colloid Science*. Elsevier, New York.

Matschei, T., B. Lothenbach, F. Glasser (2007) Thermodynamic properties of Portland cement hydrates in the system CaO-Al2O3-SiO2-CaSO4-CaCO3-H2O. *Cement and Concrete Research*, 37, 1379-1410.

Nagra (2014) Montmorillonite stablity under near-field conditions, Technical Report NTB 14-12, National Cooperative for the Disposal of Radioactive Waste, Wettingen, Switzerland.

Neretnieks, I., L. Liu, L. Moreno (2009) Mechanisms and models for bentonite erosion. SKB TR-09-35, Swedish Nuclear Fuel and Waste Management Co., Stockholm, Sweden.

Norrish, K. J. Rausell-Colom (1962) Effect of freezing on the swelling of clay minerals, *Clay Minerals Bulletin*, 5, 9-16.

Parkhurst, D. L., K. Kipp, P. Engesgaard, P., S. Charlton. (2004) PHAST - A program for simulating ground-water flow, solute transport, and multicomponent geochemical reactions, Techniques and Methods 6-A8, US Geological Survey. Posiva (2012) Buffer erosion in dilute water, Posiva Report 2012-44, Posiva Oy, Eurajoki, Finland.

Posiva (2016) Buffer Erosion in Sloped Fracture Environments. Posiva Report 2016-13, Posiva Oy, Eurajoki, Finland.

Pusch, R. (2003) Design, construction and performance of the clay-based isolation of the SFR silo. SKB R-03-30, Swedish Nuclear Fuel and Waste Management Co, Stockholm, Sweden.

Reardon, E. J. (1990) An ion interaction model for the determination of chemical equilibria in cement/water systems. *Cement and Concrete Research*, 20, 175-192,

Reardon, E. J. (1995) Anaerobic corrosion of granular iron: measurement and interpretation of hydrogen evolution rates. *Environmental Science and Technology*, 29, 2936-2945.

Rempel, A. (2010) Frost Heave, *Journal of Glaciology*, 56 (200) 1122-1128.

Savage, D., (2012) Initial review of chemical and erosional processes within the buffer and backfill - geochemical processes, SSM Technical Note 2012:28, Swedish Radiation Safety Authority, Stockholm, Sweden.

Savage, D. (2016) Review of chemical evolution in rock and engineered barrier systems in SFR according to the safety assessment SR-PSU, in SSM's External Experts' Reviews of SKB's Safety Assessment SR-PSU- Hydrological and Chemical Aspects, Initial Review Phase, SSM Technical Note 2016-08, Swedish Radiation Safety Authority, Stockholm, Sweden.

SKB (2006) Buffer and backfill process report for the safety assessment SR-Can. SKB Report TR-06-18, Swedish Nuclear Fuel and Waste Management Company, Stockholm, Sweden.

SKB (2008) Safety analysis SFR 1. Long-term safety. SKB R-08-130, Swedish Nuclear Fuel and Waste Management Co, Stockholm, Sweden.

SKB (2011) Site description of the SFR area at Forsmark at completion of the site investigation phase SDM-PSU Forsmark. SKB Report TR-11-04, Swedish Nuclear Fuel and Waste Management Company, Stockholm, Sweden.

SKB (2014a) Safety analysis for SFR. Main report for the safety assessment SR-PSU. SKB Report TR-14-01, Swedish Nuclear Fuel and Waste Management Company, Stockholm, Sweden.

SKB (2014b) Initial state report for the safety assessment SR-PSU. SKB TR-14-02 Swedish Nuclear Fuel and Waste Management Company, Stockholm, Sweden.

SKB (2014c) Waste form and packaging process report for the safety assessment SR-PSU. SKB Report TR-14-03, Swedish Nuclear Fuel and Waste Management Company, Stockholm, Sweden.

SKB (2014d) Engineered barrier process report for the safety assessment SR-PSU. SKB Report TR-14-04, Swedish Nuclear Fuel and Waste Management Company, Stockholm, Sweden.

SKB (20014e) Geosphere process report for the safety assessment SR-PSU. SKB Report TR- 14-05, Swedish Nuclear Fuel and Waste Management Company, Stockholm, Sweden.

SKB (2014f) Data report for the for the safety assessment SR-PSU. SKB Report TR 14-10, Swedish Nuclear Fuel and Waste Management Company, Stockholm, Sweden.

SKB (2014g) Model summary report for the safety assessment SR-PSU. SKB TR-14-11, Swedish Nuclear Fuel and Waste Management Company, Stockholm, Sweden.

SKB (2014h) Input data report for the safety assessment SR-PSU. SKB TR-14-12, Swedish Nuclear Fuel and Waste Management Company, Stockholm, Sweden.

Stucki, J., D. Golden, and C. Roth (1984) Effects of reduction and reoxidation of structural iron on the surface charge and dissolution of dioctahedral smectites, *Clays and Clay Minerals*, 32 (5), 350-356).

Vorhies, J. and R. Gaines (2009) Microbial dissolution of clay minerals as a source of iron and silica in marine sediments, *Nature Geoscience*, 2.

Appendix 1 Coverage of SKB Reports

Birgersson, M., O. Karnland, U. Nilsson (2010) *Freezing of bentonite: Experimental studies and theoretical considerations*, SKB Technical Report TR-10-40, Swedish Nuclear Fuel and Waste Management Co., Stockholm, Sweden.

Gaucher, E. C., C. Tournassat, and C. Nowak (2005) *Modelling the geochemical evolution of the multi-barrier system of the Silo of the SFR repository*, SKB Report R-05-80, Swedish Nuclear Fuel and Waste Management Company, Stockholm, Sweden.

Höglund, L., (2013) *The impact of concrete degradation on the BMA barrier* functions, SKB Report R-13-40, Swedish Nuclear Fuel and Waste Management Company, Stockholm, Sweden.

SKB (2008) *Safety* analysis *SFR 1. Long-term safety*. SKB R-08-130, Swedish Nuclear Fuel and Waste Management Co, Stockholm, Sweden.

SKB (2011) Site *description of the SFR area at Forsmark at completion of the site investigation phase SDM-PSU Forsmark*. SKB Report TR-11-04, Swedish Nuclear Fuel and Waste Management Company, Stockholm, Sweden.

SKB (2014a) *Safety analysis for SFR. Main report for the safety assessment SR-PSU*. SKB Report TR-14-01, Swedish Nuclear Fuel and Waste Management Company, Srockholm, Sweden.

SKB (2014b) Initial *state report for the safety assessment SR-PSU*. SKB TR-14-02 Swedish Nuclear Fuel and Waste Management Company, Srockholm, Sweden.

SKB (2014c) *Waste form and packaging process report for the safety assessment SR-PSU*. SKB Report TR-14-03, Swedish Nuclear Fuel and Waste Management Company, Stockholm, Sweden.

SKB (2014d) *Engineered barrier process report for the safety assessment SR-PSU*. SKB Report TR-14-04, Swedish Nuclear Fuel and Waste Management Company, Stockholm, Sweden.

SKB (20014e) *Geosphere process report for the safety assessment SR-PSU*. SKB Report TR- 14-05, Swedish Nuclear Fuel and Waste Management Company, Stockholm, Sweden.

SKB (2014f) *Data report for the for the safety assessment SR-PSU*. SKB Report TR 14-10, Swedish Nuclear Fuel and Waste Management Company, Stockholm, Sweden.

SKB (2014g) *Model summary report for the safety assessment SR-PSU*. SKB TR-14-11, Swedish Nuclear Fuel and Waste Management Company, Stockholm, Sweden.

SKB (2014h) *Input data report for the safety assessment SR-PSU*. SKB TR-14-12, Swedish Nuclear Fuel and Waste Management Company, Stockholm, Sweden.

2017:28

The Swedish Radiation Safety Authority has a comprehensive responsibility to ensure that society is safe from the effects of radiation. The Authority works to achieve radiation safety in a number of areas: nuclear power, medical care as well as commercial products and services. The Authority also works to achieve protection from natural radiation and to increase the level of radiation safety internationally.

The Swedish Radiation Safety Authority works proactively and preventively to protect people and the environment from the harmful effects of radiation, now and in the future. The Authority issues regulations and supervises compliance, while also supporting research, providing training and information, and issuing advice. Often, activities involving radiation require licences issued by the Authority. The Swedish Radiation Safety Authority maintains emergency preparedness around the clock with the aim of limiting the aftermath of radiation accidents and the unintentional spreading of radioactive substances. The Authority participates in international co-operation in order to promote radiation safety and finances projects aiming to raise the level of radiation safety in certain Eastern European countries.

The Authority reports to the Ministry of the Environment and has around 300 employees with competencies in the fields of engineering, natural and behavioural sciences, law, economics and communications. We have received quality, environmental and working environment certification.